

# **COMPUTATIONAL INVESTIGATION OF THERMOELECTRIC PROPERTIES IN SELECTED TWO- AND THREE-DIMENSIONAL MATERIALS**

**A Thesis Submitted  
in Partial Fulfilment of the Requirements  
for the Degree of**

**DOCTOR OF PHILOSOPHY**

by

**SANGEETA**  
(2K20/PHDAP/02)

**Under the Supervision of  
Dr. MUKHTIYAR SINGH**

**Assistant Professor  
Department of Applied Physics  
Delhi Technological University**



**Department of Applied Physics**

**DELHI TECHNOLOGICAL UNIVERSITY**  
(Formerly Delhi College of Engineering)  
Shahbad Daultpur, Main Bawana Road, Delhi-110 042, India

**April 2025**

**©Delhi Technological University-2025**

**All rights reserved.**

***This Thesis is  
Dedicated to My Loving Family***

## ACKNOWLEDGMENTS

I would like to express my gratitude to many wonderful people who have helped me throughout the Ph.D. journey.

First and foremost, I am profoundly grateful to my esteemed Ph.D. supervisor, **Dr. Mukhtiyar Singh**, for his remarkable guidance, encouragement, and unwavering support that allowed me to grow as a researcher. His belief in my abilities, even when I doubted myself, has been a tremendous source of motivation. His punctuality, dedication, and scientific intuition have exceptionally inspired. I will remain forever obliged for his continuous support. I am also grateful for his prompt assessment of my manuscripts and thesis chapters. I would like to thank **Mrs. Harmeet Kaur**, **Yashkaran Singh**, and **Nimrat Kaur** for their warmth, for making me feel like part of their family, and for the many delightful dinner gatherings that brought comfort and joy during my journey.

I would like to express my respect to **Prof. Prateek Sharma** (Vice-Chancellor, DTU), **Prof. Vinod Kumar** (HoD, AP), **Prof. Suresh C Sharma** (DRC Chairperson), and **Prof. A. S. Rao** (former DRC Chairperson and HoD, AP), for providing the necessary resources to facilitate the research activity. I further thank the experts and members of the SRC and DRC for dedicating their valuable time to serve on my committee and providing support. Also, I would like to thank **all other faculty and staff members** of the Department for their help and cooperation.

I would like to acknowledge **Delhi Technological University (DTU)** for providing me with financial assistance. I also wish to acknowledge **National Supercomputing Mission (NSM)** for providing computing resources of '**PARAM SEVA**' at IIT Hyderabad, '**PARAM SMRITI**' at NABI Mohali, and '**PARAM SIDHI**' at C-DAC Pune, which are implemented by **C-DAC** and supported by the *Ministry of Electronics and Information Technology (MeitY)* and *Department of Science and Technology (DST), Government of India*.

I wish to acknowledge all my school and college teachers, I would not have been here without their guidance, blessings, and support. I also wish to acknowledge **Prof. Manish K Kashyap** (JNU, Delhi) for his unwavering support, appreciation, and motivation. I sincerely thank **Dr. Payal Wadhwa** (*Payal Di*) for her inspiring presence, creativity, and kind support.

I am deeply grateful to my senior lab member, **Dr. Rajesh Kumar**, for sharing his expertise, creating a family-like environment in the lab, and supporting me throughout. His mentorship and encouragement kept me motivated at every step. I also would like to thank my current lab members, **Ramesh Kumar**, **Kulwinder Kumar**, **Chinmaya Datt**, **Deepanshi**, and **Deepika**, for their constant support, stimulating discussions, shared responsibilities, endless fun, and care. I



want to thank my PhD friends and roommates, **Dr. Jyoti** and **Dr. Ananya Pandey**, for being my closest companions through all the ups and downs. I am also grateful to my batchmates, especially **Dr. Ankit** and **Dr. Anu**, for their friendship and shared experiences. I am grateful to my seniors and juniors, **Rajesh Sir, Jyoti Didi, Umang Sharma Ma'am, Harender Mor Sir, Rajat Bajaj Sir, Kulwinder, Lokesh Ahlawat, Manisha Mor, and Deepanshi Deswal** for the fun, the spontaneous tea breaks, and the cheerful parties.

I thank my dearest friend, **Vijeta (Devi Vishnupriya ji)**, for always believing in me, loving me selflessly, and praying for my happiness. Her devotion to *God* inspires me every day, I'm truly blessed to have her in my life. I would like to thank my post-graduation friends, my closest ones, **Priya Rana** and **Manisha**, for their friendship, words of encouragement, and for always checking in. I also thank my other friends from school and college, **Amrit Kaur, Anuraj Chahal, Ranjana Nain, Priyanka Dhanda, Sushila, Sushma, Aarti, and Sonam Sagwal**, for being a part of a special time in my life that I still hold dear.

Finally, I thank the foundation of my life, the reason for my every achievement- **My Family**. I thank my parents, **Mr. Ramraji Dhull** and **Mrs. Mamo Devi**, for their unconditional love, support, blessings, and belief in me. I would like to thank my brother, **Vikas Dhull**, and **Sheetal Bhabhi**, who always encouraged me to pursue my dreams. I am immensely grateful to my sister, **Preeti**, and **Amit Sindher Jiju** for their constant encouragement, love, and support.

A big thank to my little champs, **Tanjil Dhull, Bhavreet Sindher, Anayra Dhull, Kowin Dhull, and Reeva Sindher**, for giving me many reasons to smile in hard times. Their presence has been a constant source of comfort throughout the journey.

A heartfelt thanks to my late **Nana ji, Nani ji, Mama Ji, and Mami Ji** for their blessings, care, and support. I also extend my love and thanks to **Khushboo Goyat, Nakul Goyat, and Ankush Goyat**, whose presence and affection have always brought me joy and strength.

Above all, I thank *God* for giving me the perseverance and strength to show up at my lab each day and work through the ups and downs of my Ph.D. journey.

Sangeeta  
2K20/PHDAP/02



# DELHI TECHNOLOGICAL UNIVERSITY

(Formerly Delhi College of Engineering)

Shahbad Daulatpur, Main Bawana Road, Delhi-42

## **CANDIDATE'S DECLARATION**

I **Sangeeta (2K20/PHDAP/02)** hereby certify that the work which is being presented in the thesis entitled "**Computational Investigation of Thermoelectric Properties in Selected Two- and Three-Dimensional Materials**" in partial fulfillment of the requirements for the award of the Degree of Doctor of Philosophy, submitted in the Department of Applied Physics, Delhi Technological University is an authentic record of my own work carried out during the period from **August 2020** to **April 2025** under the supervision of **Dr. Mukhtiyar Singh, Department of Applied Physics, Delhi Technological University.**

The matter presented in the thesis has not been submitted by me for the award of any other degree of this or any other Institute.

**Candidate's Signature**

This is to certify that the student has incorporated all the corrections suggested by the examiners in the thesis and the statement made by the candidate is correct to the best of our knowledge.

**Signature of Supervisor**

**Signature of External Examiner**



# DELHI TECHNOLOGICAL UNIVERSITY

(Formerly Delhi College of Engineering)

Shahbad Daulatpur, Main Bawana Road, Delhi-42

## **CERTIFICATE BY THE SUPERVISOR**

Certified that **Sangeeta** (2K20/PHDAP/02) has carried out her research work presented in this thesis entitled **“Computational Investigation of Thermoelectric Properties in Selected Two- and Three-Dimensional Materials”** for the award of **Doctor of Philosophy** from Department of Applied Physics, Delhi Technological University, Delhi, under my supervision. The thesis embodies results of original work, and studies are carried out by the student herself and the contents of the thesis do not form the basis for the award of any other degree to the candidate or to anybody else from this or any other University/Institution.

**Dr. Mukhtiyar Singh**

(Supervisor)

Assistant Professor

Department of Applied Physics

Delhi Technological University

Date:

## **ABSTRACT**

Thermoelectricity has emerged as one of the potential green energy harvesting technologies that provide clean and sustainable energy solutions. This technology relies on the materials that efficiently convert waste heat into useful electricity, known as thermoelectric (TE) materials, which have a wide span of applications ranging from wearable devices to space applications. In recent years, the search for novel TE materials has been extended to the classes of materials that simultaneously have decoupled transport parameters with inherently low lattice thermal conductivity. We have discussed four such classes of materials, i.e., Zintl phases, half-Heusler (HH) compounds, Li-transition-metal nitrides, and pnictide monolayers, and conducted extensive first-principles calculations followed by semiclassical Boltzmann transport theory to explore their thermoelectric properties of these materials.

In the first problem, we realized that the carrier concentration optimization is an effective way to enhance the TE performance of a material. We have explored the TE properties of the *p*-type  $\text{RbZn}_4\text{P}_3$  and *n*-type  $\text{RbGaSb}_2$  Zintl compounds at different hole and electron doping concentrations, respectively. A peak  $ZT$  value of 0.78 (0.87) at 700 K (900 K) for optimal hole (electron) doping concentration of  $2 \times 10^{20} \text{ cm}^{-3}$  ( $2 \times 10^{19} \text{ cm}^{-3}$ ) has been obtained for  $\text{RbZn}_4\text{P}_3$  ( $\text{RbGaSb}_2$ ). The key advantages of using Zintl compounds are their complex crystal structure, potential rattling of Rb cations, and presence of heavy elements. We have obtained low lattice thermal conductivities of both compounds,  $\text{RbZn}_4\text{P}_3$  and  $\text{RbGaSb}_2$ . This low thermal conductivity allows for the efficient conversion of heat into electricity, making them potential candidates for TE applications. In the second problem, we analysed and compared the electronic, transport, phononic, and thermal properties of 8 valence electron count (VEC) Li-based HH compounds  $\text{LiCaX}$  ( $X = \text{As, Sb}$ ). The value of the Seebeck coefficient has been found to be higher in *p*-type  $\text{LiCaX}$  than that of *n*-type due to flat VB edges. TE performance is slightly enhanced with an increase in atomic weight of X atom owing to low  $\kappa_l$  and significant power factor ( $PF$ ). The remarkably low  $\kappa_l$  of 8-VEC HH compounds  $\text{LiCaX}$  ( $X = \text{As, Sb}$ ) has been understood in terms of different phonon modes and optimization of carrier concentration, resulting in an improved  $ZT$  at higher temperatures. The optimized carrier concentration ( $\sim 10^{20} \text{ cm}^{-3}$  for *p*-type carriers and  $\sim 10^{19} \text{ cm}^{-3}$  for *n*-type carriers) of the investigated compounds was found to be comparable to the experimentally estimated value for other 8-VEC Li-based HH. Our study has predicted that the *p*-type HH alloys  $\text{LiCaX}$  are promising TE materials. In the third problem, we understood the role of lattice dynamics in

realizing high TE performance in an already experimentally synthesized layered materials  $\text{Li}_2\text{MN}_2$  ( $\text{M} = \text{Zr}$  and  $\text{Hf}$ ). We have analyzed how replacing Zr with the relatively heavy element Hf in  $\text{Li}_2\text{MN}_2$  leads to an increase in thermal conductivity instead of a decrease, which is against the common notion. We have obtained a lower lattice thermal conductivity ( $1.52 \text{ Wm}^{-1}\text{K}^{-1}$ ), compared to  $\text{Li}_2\text{HfN}_2$ , along the  $a$ -axis at 1000 K for  $\text{Li}_2\text{ZrN}_2$  which has been attributed to the rattling behaviour of Zr that leads to shorter phonon lifetimes. Moreover, the anisotropic character owing to the layered structure of  $\text{Li}_2\text{MN}_2$  has enabled tuning their transport properties. Therefore, a high  $PF$  has been obtained along the  $a$ -axis for both compounds, which resulted in high  $ZT$  in this direction. The high figure of merit (1.07) of  $\text{Li}_2\text{ZrN}_2$  along the  $a$ -axis has unravelled its potential for high-temperature TE application. These calculations have provided valuable insights into the vibrational properties, including the phonon group velocities, phonon lifetime, and phonon frequencies that govern the thermal conductivity and the phonon-mediated heat transport.

In the fourth problem, we explored structural, electronic, and TE properties of 2D YX ( $\text{X} = \text{N}, \text{P}, \text{As}$ ) rare-earth pnictide monolayers. The monolayers are found to exhibit high anisotropy in the electronic transport properties, which is attributed to their unique crystallographic and electronic structure. The dimensionality reduction in these semiconducting materials with strong  $p$ - $d$  hybridization led to high electron conductivities, thereby resulting in high  $ZT$ . The phonon band structure shows enhanced coupling between the low-frequency optical and acoustic modes. Accordingly, low  $\kappa_l$  obtained, with values 3.335, 1.779, and  $1.648 \text{ Wm}^{-1}\text{K}^{-1}$  for YN, YP, and YAs monolayers, respectively, at 500 K. For the  $p$ -type materials, the highest  $ZT$  is achieved in the order  $\text{YN} < \text{YP} < \text{YAs}$  in the  $y$ -direction, while for  $n$ -type materials, it is in order  $\text{YN} > \text{YP} > \text{YAs}$  in the  $x$ -direction. The monolayers YN, YAs, and YP are found to exhibit a maximum figure of merit of 2.02, 1.39, and 1.18, respectively, at 500 K, showing excellent TE performance.

Our study outlines some effective approaches for enhancing the TE performance of materials, which include carrier concentration optimization, phonon engineering, and dimensional reduction. It may open new avenues for future experimental realization of these materials for energy harvesting applications in a wide temperature range. This thesis underlines the effective use of computational techniques to screen efficient materials for desired applications. These techniques save valuable resources and help experimentalists to synthesize the proposed materials without resorting to trial-and-error methodology in the wet lab.

## LIST OF PUBLICATIONS

### THESIS WORK

1. **Sangeeta**, Ramesh Kumar, and Mukhtiyar Singh, “Realizing high thermoelectric performance in  $p$ -type  $\text{RbZn}_4\text{P}_3$  Zintl compound: a first-principles investigation”, *Journal of Materials Science* **57**, 10691 (2022). <https://doi.org/10.1007/s10853-022-06953-y>.
2. **Sangeeta** and Mukhtiyar Singh, “Augmented thermoelectric performance of  $\text{LiCaX}$  ( $X = \text{As, Sb}$ ) Half Heusler compounds via carrier concentration optimization”, *Journal of Physics and Chemistry Solids* **174**, 111182 (2023). <https://doi.org/10.1016/j.jpcs.2022.111182>.
3. **Sangeeta**, Rajesh Kumar, Ramesh Kumar, Kulwinder Kumar, and Mukhtiyar Singh, “Unravelling the ultralow Thermal Conductivity of Ternary Antimonide Zintl Phase  $\text{RbGaSb}_2$ : A First-principles Study”, *Indian Journal of Pure & Applied Physics* **61**, 731, (2023). <https://doi.org/10.56042/ijpap.v61i9.3152>.
4. **Sangeeta**, Mukhtiyar Singh, “Computational study of the thermoelectric properties and lattice dynamics of  $\text{Li}_2\text{MN}_2$  ( $M = \text{Zr or Hf}$ )”, *Materials Research Bulletin* **172**, 112650 (2024). <https://doi.org/10.1016/j.materresbull.2023.112650>.
5. **Sangeeta**, Rajesh Kumar, Mukhtiyar Singh, “In-silico realization of  $\text{YX}$  ( $X = \text{N, P, As}$ ) pnictide monolayers as highly efficient thermoelectric materials”, *Surfaces and Interfaces*, **55**, 105442 (2024). <https://doi.org/10.1016/j.surfin.2024.105442>.

### OTHERS

1. Rajesh Kumar, **Sangeeta**, Ramesh Kumar, Ramesh K. Bibiyan, Mukhtiyar Singh, and Ankush Vij, “An ab-initio study of induced half metallic ferromagnetism in  $\text{Hf-Nb}$  alloy oxides”, *European Physical Journal Plus* **138**, 561 (2023). <https://doi.org/10.1140/epjp/s13360-023-04179-8>.
2. Rajesh Kumar, Ramesh Kumar, **Sangeeta**, Kulwinder Kumar, and Mukhtiyar Singh, “Insights into Structural, Electronic and Thermoelectric Properties of  $\text{ZnTMN}_2$  ( $\text{TM} = \text{Zr and Hf}$ ): A First-Principles Study”, *Indian Journal of Pure & Applied Physics* **61**, 910 (2023). <https://doi.org/10.56042/ijpap.v61i11.3151>.
3. Ramesh Kumar, Rajesh Kumar, **Sangeeta**, and Mukhtiyar Singh, “Pressure Induced Surface States and Wannier Charge Centers in Ytterbium monoarsenide”, *Indian*

*Journal of Pure & Applied Physics* **61**, 735 (2023).

<https://doi.org/10.56042/ijpap.v61i9.3148>.

4. Stephen Shaiju Mathew, **Sangeeta**, Rajesh Kumar, Mukhtiyar Singh, Manish K. Kashyap, “Optimizing carrier concentration for enhanced thermoelectric performance in AgSbS<sub>2</sub> monolayer. *Ionics* **30**, 8647–8657 (2024). <https://doi.org/10.1007/s11581-024-05844-3>.
5. Sumedha Yadav, **Sangeeta**, Kulwinder Kumar, Mukhtiyar Singh, “Optimizing Thermoelectric Performance of Halide Perovskite Ca<sub>3</sub>AsBr<sub>3</sub> Through Strain Engineering” *Physics Letters A*, **551**, 130625, (2025). <https://doi.org/10.1016/j.physleta.2025.130625>.

## **TABLE OF CONTENTS**

<b>ACKNOWLEDGMENTS .....</b>	<b>iv</b>
<b>CANDIDATE'S DECLARATION.....</b>	<b>vi</b>
<b>CERTIFICATE BY THE SUPERVISOR .....</b>	<b>vii</b>
<b>ABSTRACT.....</b>	<b>viii</b>
<b>LIST OF PUBLICATIONS .....</b>	<b>x</b>
<b>TABLE OF CONTENTS .....</b>	<b>xii</b>
<b>LIST OF TABLES .....</b>	<b>xvi</b>
<b>LIST OF FIGURES.....</b>	<b>xvii</b>
<b>LIST OF SYMBOLS.....</b>	<b>xxi</b>
<b>LIST OF ABBREVIATIONS.....</b>	<b>xxii</b>
<b>CHAPTER 1: INTRODUCTION.....</b>	<b>1-13</b>
1.1 Overview of Thermoelectricity .....	1
1.2 Application Areas of Thermoelectric Materials .....	2
1.3 Thermoelectric effects.....	3
1.3.1 Seebeck effect .....	3
1.3.2 Peltier effect .....	4
1.3.3 Thomson effect .....	4
1.4 Thermoelectric figure of merit and efficiency .....	4
1.4.1 Challenges Pertaining to Efficient Thermoelectric Materials.....	5
1.4.2 Strategies to optimize Figure of merit .....	5
1.4.2.1 Band Structure Engineering .....	6
1.4.2.2 Dimensionality Reduction .....	6
1.4.2.3 Phonon Engineering.....	7
1.5 Thermoelectric materials .....	7
1.5.1 Zintl Compounds .....	7
1.5.2 Half Heusler Compounds.....	8
1.5.3 Layered Materials .....	9
1.5.4 Two-Dimensional Materials .....	10
1.6 Objectives of the thesis .....	10
1.7 Scope of the thesis .....	10
1.7.1 Structure of the thesis.....	11
<b>CHAPTER 2: THEORETICAL METHODOLOGY .....</b>	<b>14-34</b>
2.1 Introduction to Many-Body Problem.....	14
2.1.1 Born-Oppenheimer approximation .....	14
2.1.2 Hartree Approximation .....	15
2.1.3 Hartree-Fock approximation.....	16



2.2	Density functional theory.....	17
2.2.1	Hohenberg-Kohn Theorems.....	17
2.2.2	Kohn-Sham Approach .....	18
2.3	Exchange-Correlation Functionals.....	20
2.3.1	Local Density Approximation.....	20
2.3.2	Generalized Gradient Approximation.....	21
2.3.3	Tran-Blaha modified Becke-Johnson potential .....	21
2.3.4	Hybrid Functionals.....	22
2.4	Electron-Ion Interactions .....	23
2.4.1	All-electron scheme .....	23
2.4.2	Pseudopotential method .....	24
2.4.3	Projector Augmented Wave Method .....	24
2.5	Numerical Aspects .....	25
2.5.1	Energy Cut-off .....	25
2.5.2	$k$ -mesh Sampling.....	26
2.6	Transport in Solids.....	26
2.6.1	Boltzmann Transport Equation.....	26
2.6.2	Electronic Transport.....	28
2.6.2.1	Deformation Potential Theory .....	29
2.6.3	Phonon Transport.....	30
2.7	Ab initio Molecular Dynamics.....	31
2.8	Computational Packages.....	32
2.8.1	WIEN2k .....	32
2.8.2	Vienna Ab initio Simulation Package.....	32
2.8.3	BoltzTaP .....	33
2.8.4	Phonopy .....	33
2.8.5	Phono3py .....	34
2.9	Summary .....	34
<b>CHAPTER 3: THERMOELECTRIC PROPERTIES OF <math>p</math>-TYPE RbZn<sub>4</sub>P<sub>3</sub> AND <math>n</math>-TYPE RbGaSb<sub>2</sub> ZINTL COMPOUNDS .....</b>		<b>35-51</b>
3.1	Introduction.....	35
3.2	Computational Details .....	36
3.3	Results and Discussion .....	37
3.3.1	Structural Properties.....	37
3.3.2	Stability of RbZn <sub>4</sub> P <sub>3</sub> compound.....	39
3.3.2.1	Thermodynamical .....	39
3.3.2.2	Dynamical .....	39
3.3.2.3	Mechanical.....	39
3.3.3	Electronic Structure Properties .....	41
3.3.4	Transport properties of RbZn <sub>4</sub> P <sub>3</sub> .....	44
3.3.5	Transport properties of RbGaSb <sub>2</sub> .....	48

3.4	Summary .....	51
<b>CHAPTER 4: AUGMENTED THERMOELECTRIC PERFORMANCE OF LiCaX</b>		
<b>(X=As, Sb) HALF HEUSLER COMPOUNDS .....</b>		<b>52-68</b>
4.1	Introduction.....	52
4.2	Computational Details .....	53
4.3	Results and Discussion .....	54
4.3.1	Structural properties and Thermal stability.....	54
4.3.2	Dynamical stability .....	56
4.3.3	Electronic Structure Properties .....	58
4.4	Thermoelectric Properties .....	60
4.4.1	Seebeck Coefficient .....	60
4.4.2	Electrical and Electronic Thermal Conductivity.....	61
4.4.3	Power Factor .....	63
4.4.4	Lattice thermal conductivity .....	63
4.4.5	Figure of Merit.....	65
4.5	Summary .....	68
<b>CHAPTER 5: THERMOELECTRIC PROPERTIES AND LATTICE DYNAMICS OF</b>		
<b>Li<sub>2</sub>MN<sub>2</sub> (M = Zr, Hf) .....</b>		<b>69-79</b>
5.1	Introduction.....	69
5.2	Computational Details and Methodology .....	70
5.3	Results and Discussion .....	70
5.3.1	Structural Properties.....	70
5.3.2	Electronic Properties.....	73
5.3.3	Transport Properties.....	75
5.4	Summary .....	79
<b>CHAPTER 6: REALIZATION OF YX (X = N, P, As) Pnictide Monolayers as</b>		
<b>Highly Efficient Thermoelectric Materials.....</b>		<b>81-103</b>
6.1	Introduction.....	81
6.2	Computational Details .....	82
6.3	Results and discussion .....	84
6.3.1	Structural properties.....	84
6.3.2	Stability.....	85
6.3.3	Electronic properties .....	88
6.3.4	Transport properties .....	90
6.3.4.1	Seebeck coefficient .....	90
6.3.4.2	Electrical and Electronic Thermal Conductivity.....	92
6.3.4.3	Power factor .....	96
6.3.4.4	Lattice thermal conductivity .....	96
6.3.4.5	Figure of merit .....	101
6.4	Summary .....	103
<b>CHAPTER 7: CONCLUSION, FUTURE SCOPE, AND SOCIAL IMPACT .....</b>		<b>104-106</b>

7.1	Conclusions.....	104
7.1.1	Thermoelectric performance in <i>p</i> -type RbZn <sub>4</sub> P <sub>3</sub> and <i>n</i> -type RbGaSb <sub>2</sub> Zintl compounds.....	104
7.1.2	Augmented thermoelectric performance of LiCaX (X = As, Sb) Half Heusler compounds via carrier concentration optimization .....	105
7.1.3	Thermoelectric properties and lattice dynamics of Li <sub>2</sub> MN <sub>2</sub> (M = Zr or Hf) .	105
7.1.4	Realization of YX (X = N, P, As) pnictide monolayers as highly efficient thermoelectric materials .....	105
7.2	Future Scope .....	106
7.3	Social Impact .....	106
<b>REFERENCES.....</b>		<b>107</b>
<b>LIST OF PUBLICATIONS AND THEIR PROOFS .....</b>		<b>121</b>

## LIST OF TABLES

<b>Table 3.1</b> Calculated structural parameters ( $a$ and $c$ in Å and $V$ in Å <sup>3</sup> ) and bond lengths (in Å) of RbZn <sub>4</sub> P <sub>3</sub> in comparison with available experimental values. ....	37
<b>Table 3.2</b> Calculated lattice parameters, volume, and total energy. ....	38
<b>Table 3.3</b> Calculated elastic coefficients $C_{ij}$ ( $i, j = 1-6$ ), bulk modulus ( $B$ ), shear modulus ( $G$ ), Young's modulus ( $Y$ ), all in units of GPa, and Poisson ratio ( $\nu$ ). ....	40
<b>Table 4.1</b> Possible Wyckoff positions of atoms for the LiCaX ( $X = \text{As, Sb}$ ) HH compounds. ....	54
<b>Table 4.2</b> Calculated optimized volume ( $V_0$ ), bulk modulus ( $B$ ), pressure derivative ( $B_p$ ), and total energy ( $E_0$ ) of both LiCaAs and LiCaSb compounds. ....	55
<b>Table 4.3</b> Calculated elastic constants $C_{ij}$ (GPa), Bulk modulus $B$ (GPa), and melting temperature $T_m$ (K). ....	56
<b>Table 4.4</b> Relative contributions of acoustic and optical phonon modes to the lattice thermal conductivity ( $\kappa_l$ ) at room temperature and 800 K for both compounds LiCaAs and LiCaSb. ....	64
<b>Table 4.5</b> The elastic modulus ( $C_\beta$ ), deformation potential constant ( $E_\beta$ ), and relaxation time ( $\tau$ ) at 300, 600, and 800 K of electrons and holes for LiCaAs and LiCaSb. ....	66
<b>Table 4.6</b> Figure of merit of LiCaAs and LiCaSb for both type of carriers at optimized carrier concentration. ....	67
<b>Table 5.1</b> The optimized lattice parameters (in Å) and bond lengths (in Å) of Li <sub>2</sub> MN <sub>2</sub> ( $M = \text{Zr or Hf}$ ), along with available experimental values. ....	71
<b>Table 6.1</b> The obtained structural parameters of YX monolayers, the lattice constant (in Å) comparable with previous work, buckling height ( $h$ ), bond lengths (in Å), and bond angles (in degree) based on PBE functional. ....	85
<b>Table 6.2</b> Carrier effective masses $m^*$ in units of free electron mass ( $m_0$ ), in-plane stiffness $C_{2D}$ (Nm <sup>-1</sup> ), Deformation potential constant $E_d$ (eV), and relaxation time $\tau$ (s) at 300 and 500 K for YN, YP, and YAs. ....	93
<b>Table 6.3</b> Comparison of $\kappa_l$ (in units of Wm <sup>-1</sup> K <sup>-1</sup> ) for monolayer YN, YP, and YAs found by solving the fPBTE and based on the RTA approach in $x$ -direction ( $xx$ ) and $y$ -direction ( $yy$ ) at 300 and 500 K. ....	99
<b>Table 6.4</b> Peak figure of merit, $ZT$ in the $x$ -direction, $y$ -direction, and their average values for $p$ - and $n$ -type YX ( $X = \text{N, P, As}$ ) monolayers at two different temperatures 300 and 500 K at optimized carrier concentration. ....	102

## LIST OF FIGURES

<b>Figure 1.1</b> Sources of the waste heat energy. ....	2
<b>Figure 1.2</b> A diverse range of domains where the application of thermoelectric materials can prove to be effective. ....	3
<b>Figure 1.3</b> Electronic DOS for different dimensionality. Low-dimensional materials showing sharp DOS. ....	6
<b>Figure 2.1</b> Flow chart for self-consistent density functional calculations. ....	20
<b>Figure 2.2</b> Muffin Tin Approximation .....	23
<b>Figure 3.1</b> Crystal structure of <b>(a)</b> RbZn <sub>4</sub> P <sub>3</sub> and <b>(b)</b> RaGaSb <sub>2</sub> compound .....	38
<b>Figure 3.2</b> The optimization of total energy as a function of deviation from experimental <i>c/a</i> ratio. The curve is fitted up to a fourth-order polynomial .....	38
<b>Figure 3.3</b> <b>(a)</b> Phonon dispersion curve and <b>(b)</b> phonon density of state of RbZn <sub>4</sub> P <sub>3</sub> compound .....	40
<b>Figure 3.4</b> The electronic band structure and DOS of RbZn <sub>4</sub> P <sub>3</sub> calculated within TB-mBJ approximation. The Fermi level is set to 0 eV .....	42
<b>Figure 3.5</b> The calculated projected DOS of RbZn <sub>4</sub> P <sub>3</sub> within TB-mBJ approximation. The Fermi level is set to 0 eV .....	42
<b>Figure 3.6</b> Calculated <b>(a)</b> electronic band structure <b>(b)</b> and <b>(c)</b> density of states of RbGaSb <sub>2</sub> using TB-mBJ approximation. ....	43
<b>Figure 3.7</b> The computed charge density (in units of eÅ <sup>-3</sup> ) plot of RbZn <sub>4</sub> P <sub>3</sub> in (010) plane ..	44
<b>Figure 3.8</b> The variation of <b>(a)</b> <i>S</i> <b>(b)</b> $\sigma/\tau$ <b>(c)</b> $\kappa_e/\tau$ and <b>(d)</b> $S^2\sigma/\tau$ with hole doping concentration for RbZn <sub>4</sub> P <sub>3</sub> at different temperatures. ....	46
<b>Figure 3.9</b> Computed Electronic Fitness Function with hole doping concentration at different temperatures. ....	46
<b>Figure 3.10</b> <b>(a)</b> The variation of total thermal conductivity (variation of lattice thermal conductivity with temperature is shown in inset) and <b>(b)</b> Figure of Merit <i>ZT</i> with hole doping concentration at various temperatures .....	48
<b>Figure 3.11</b> Calculated <b>(a-b)</b> Seebeck coefficient and <b>(c-d)</b> power factor in the <i>x</i> - (solid lines) and <i>z</i> - (dotted lines) direction as a function of electron concentration at different temperatures. ....	49
<b>Figure 3.12</b> Calculated <b>(a)</b> $\kappa_l$ <b>(b)</b> $\kappa_t$ <b>(c-d)</b> $\kappa_c$ as a function of frequency and mean free path. ....	50

<b>Figure 3.13</b> Calculated $ZT$ as a function of electron concentration of $\text{RbGaSb}_2$ (a) in the $x$ -direction (b) in the $z$ -direction. ....	50
<b>Figure 4.1</b> Calculated total energy (in Ry) versus volume (in a.u. <sup>3</sup> ) for Type I, Type II, and Type III configurations of $\text{LiCaAs}$ and $\text{LiCaSb}$ .....	55
<b>Figure 4.2</b> The temperature fluctuations versus time for (a) $\text{LiCaAs}$ and (b) $\text{LiCaSb}$ at 400 K and 800 K using AIMD simulations. ....	55
<b>Figure 4.3</b> The obtained phonon dispersion for (a) $\text{LiCaAs}$ and (b) $\text{LiCaSb}$ .....	57
<b>Figure 4.4</b> Calculated phonon density of states of $\text{LiCaAs}$ and $\text{LiCaSb}$ .....	57
<b>Figure 4.5</b> Calculated mode Grüneisen parameter for (a) $\text{LiCaAs}$ and (b) $\text{LiCaSb}$ .....	58
<b>Figure 4.6</b> Calculated electronic band structures of (a) $\text{LiCaAs}$ and (b) $\text{LiCaSb}$ along the high symmetry directions of the BZ as determined using the Tran-Blaha modified Becke-Johnson potential. The Fermi energy is set to 0 eV.....	59
<b>Figure 4.7</b> Calculated total and partial density of states of $\text{LiCaAs}$ and $\text{LiCaSb}$ . The Fermi energy is set to 0 eV. ....	59
<b>Figure 4.8</b> Calculated Seebeck coefficient of (a) $\text{LiCaAs}$ and (b) $\text{LiCaSb}$ as a function of carrier concentration and for temperatures ranging from 300 K to 800 K.....	61
<b>Figure 4.9</b> Calculated electrical conductivity of (a) $\text{LiCaAs}$ and (b) $\text{LiCaSb}$ as a function of carrier concentration and for temperatures ranging from 300 K to 800 K. ....	62
<b>Figure 4.10</b> Calculated electronic thermal conductivity of (a) $\text{LiCaAs}$ and (b) $\text{LiCaSb}$ as a function of carrier concentration and for temperatures ranging from 300 K to 800 K.....	62
<b>Figure 4.11</b> Calculated power factor of (a) $\text{LiCaAs}$ and (b) $\text{LiCaSb}$ as a function of carrier concentration and for temperatures ranging from 300 K to 800 K.....	63
<b>Figure 4.12</b> (a) The lattice thermal conductivity of $\text{LiCaAs}$ and $\text{LiCaSb}$ as a function of temperature (b) The cumulative lattice thermal conductivity as a function of frequency in $\text{LiCaAs}$ and $\text{LiCaSb}$ at different temperatures 300 K and 800 K .....	64
<b>Figure 4.13</b> Calculated $ZT$ values of (a) $\text{LiCaAs}$ and (b) $\text{LiCaSb}$ as a function of carrier concentration within constant relaxation time approximation (i.e., $\tau = 1 \times 10^{-14}$ s) at different temperatures ranging from 300 K to 800 K.....	65
<b>Figure 4.14</b> Calculated $ZT$ values of (a) $\text{LiCaAs}$ and (b) $\text{LiCaSb}$ as a function of carrier concentration using temperature dependent relaxation time of carriers at different temperatures ranging from 300 K to 800 K.....	66
<b>Figure 4.15</b> The variation in Figure of Merit with temperature (a) within constant relaxation time approximation (b) with temperature dependent relaxation time of carriers for $p$ -type and $n$ -type $\text{LiCaAs}$ and $\text{LiCaSb}$ .....	67

<b>Figure 5.1</b> The geometrical structure of $\text{Li}_2\text{MN}_2$ ( $\text{M} = \text{Zr}$ or $\text{Hf}$ ).....	71
<b>Figure 5.2</b> The phonon dispersion curves of <b>(a)</b> $\text{Li}_2\text{ZrN}_2$ and <b>(b)</b> $\text{Li}_2\text{HfN}_2$ . ....	73
<b>Figure 5.3</b> The total and projected phonon density of states of <b>(a)</b> $\text{Li}_2\text{ZrN}_2$ and <b>(b)</b> $\text{Li}_2\text{HfN}_2$ .73	
<b>Figure 5.4</b> The electronic band structure along the high symmetry K-path $\Gamma\text{-M-K-}\Gamma\text{-A}$ of $\text{Li}_2\text{MN}_2$ ( $\text{M} = \text{Zr}$ or $\text{Hf}$ ) calculated using TB-mBJ. The Fermi level is set to 0 eV.....	74
<b>Figure 5.5 (a)-(d)</b> The density of states of $\text{Li}_2\text{MN}_2$ ( $\text{M} = \text{Zr}$ or $\text{Hf}$ ) calculated using TB-mBJ. The Fermi level is set to 0 eV.....	74
<b>Figure 5.6</b> The calculated <b>(a)</b> Seebeck coefficient ( $S$ ), <b>(b)</b> Electrical conductivity ( $\sigma/\tau$ ), <b>(c)</b> Electronic thermal conductivity ( $\kappa_e/\tau$ ), and <b>(d)</b> Power factor ( $S^2\sigma/\tau$ ) of $\text{Li}_2\text{MN}_2$ ( $\text{M} = \text{Zr}$ or $\text{Hf}$ ).....	76
<b>Figure 5.7 (a)</b> Lattice thermal conductivity, <b>(b)</b> average lattice thermal conductivity, <b>(c)</b> , and <b>(d)</b> cumulative lattice thermal conductivity of $\text{Li}_2\text{ZrN}_2$ and $\text{Li}_2\text{HfN}_2$ , respectively. ....	77
<b>Figure 5.8</b> Calculated phonon group velocities of <b>(a)</b> $\text{Li}_2\text{ZrN}_2$ <b>(b)</b> $\text{Li}_2\text{HfN}_2$ at 1000 K. Calculated phonon lifetimes of <b>(c)</b> $\text{Li}_2\text{ZrN}_2$ and <b>(d)</b> $\text{Li}_2\text{HfN}_2$ at 1000 K. The colour bar in the figure represents the phonon density. A brighter colour means a higher phonon density.....	77
<b>Figure 5.9</b> The variation of <b>(a)</b> $ZT$ along $a$ - and $c$ - axes of $\text{Li}_2\text{MN}_2$ ( $\text{M} = \text{Zr}$ or $\text{Hf}$ ) and <b>(b)</b> average $ZT$ with temperature. ....	79
<b>Figure 6.1</b> Crystal structure of tetragonal $\text{YX}$ ( $\text{X} = \text{N}, \text{P}, \text{As}$ ) monolayers. (a) The top view and (b) the side view of the $\text{YX}$ monolayers. ....	84
<b>Figure 6.2</b> AIMD evolution of temperature and energy fluctuations of <b>(a)</b> $\text{YN}$ , <b>(b)</b> $\text{YP}$ , and <b>(c)</b> $\text{YAs}$ monolayers at 500 K. The blue (magenta) solid line is the variation of temperature (energy) with time. The insets are snapshots of monolayer structures before (at 0 fs) and after AIMD simulations (at 5000 fs). ....	87
<b>Figure 6.3</b> Phonon dispersion curves of <b>(a)</b> $\text{YN}$ , <b>(b)</b> $\text{YP}$ and <b>(c)</b> $\text{YAs}$ monolayers. ....	88
<b>Figure 6.4</b> Phonon density of states of $\text{YX}$ ( $\text{X} = \text{N}, \text{P}, \text{As}$ ) monolayers. ....	88
<b>Figure 6.5</b> Calculated electronic structure of <b>(a)</b> $\text{YN}$ , <b>(b)</b> $\text{YP}$ and <b>(c)</b> $\text{YAs}$ monolayers. The Fermi level (shown by dotted black line) is set to 0 eV. ....	89
<b>Figure 6.6</b> The DOS of $\text{YX}$ ( $\text{X} = \text{N}, \text{P}, \text{As}$ ) monolayers in which contribution of different atoms and orbitals are labelled. The Fermi level (shown by dotted orange line) is set to 0 eV. ....	90
<b>Figure 6.7</b> Seebeck coefficient ( $S$ ) versus carrier concentration at 300, 400, and 500 K in both directions of <b>(a)–(c)</b> $p$ -type and <b>(d)–(f)</b> $n$ -type $\text{YX}$ ( $\text{X} = \text{N}, \text{P}, \text{As}$ ) monolayers .....	91

<b>Figure 6.8</b> The energy shifting as a function of uniaxial strain along the $x$ -direction (top panel) and $y$ -direction (bottom panel) of <b>(a and d)</b> YN, <b>(b and e)</b> YP, and <b>(c and f)</b> YAs. The solid lines indicate the parabolic fitting curves. ....	94
<b>Figure 6.9</b> The band edge position shifts of CBM and VBM as a function of uniaxial strain along the $x$ -direction (top panel) and the $y$ -direction (bottom panel) of <b>(a and d)</b> YN, <b>(b and e)</b> YP, and <b>(c and f)</b> YAs. The solid lines indicate the linear fitting curves. ....	94
<b>Figure 6.10</b> The electrical conductivity ( $\sigma$ ) versus carrier concentration at 300, 400, and 500 K in both directions of <b>(a)–(c)</b> $p$ -type and <b>(d)–(f)</b> $n$ -type YX ( $X = N, P, As$ ) monolayers .....	95
<b>Figure 6.11</b> Electronic thermal conductivity ( $\kappa_e$ ) versus carrier concentration from 300 K to 500 K in the $x$ - and $y$ - directions of <b>(a)–(c)</b> $p$ -type and <b>(d)–(f)</b> $n$ -type YX monolayers .....	96
<b>Figure 6.12</b> Power factor ( $S^2\sigma$ ) versus carrier concentration at 300, 400, and 500 K in both directions of <b>(a)–(c)</b> $p$ -type and <b>(d)–(f)</b> $n$ -type YX ( $X = N, P, As$ ) monolayers .....	97
<b>Figure 6.13</b> Lattice thermal conductivities ( $\kappa_l$ ) of <b>(a)</b> YN, <b>(b)</b> YAs, <b>(c)</b> YP monolayers dependent on temperature in the $x$ -direction and $y$ -direction, and <b>(d)</b> Comparison of Average lattice thermal conductivities found using fPBTE and RTA approach at 300 and 500 K. ....	98
<b>Figure 6.14</b> Calculated <b>(a)–(c)</b> group velocity and <b>(d)–(e)</b> phonon lifetime of YX ( $X = N, P, As$ ) monolayers as a function frequency. ....	100
<b>Figure 6.15</b> <b>(a)–(c)</b> Cumulative lattice thermal conductivities ( $\kappa_c$ ) of YX ( $X = N, P, As$ ) monolayers as function frequency at 300 and 500 K in both directions. ....	100
<b>Figure 6.16</b> Thermoelectric figure of merit (ZT) with varying carrier concentrations at 300, 400, and 500 K in the $x$ - and $y$ - directions of <b>(a)–(c)</b> $p$ -type and <b>(d)–(f)</b> $n$ -type YX ( $X = N, P, As$ ) monolayers .....	102



## LIST OF SYMBOLS

$\text{\AA}$	Angstrom ( $10^{-10}$ m)
$eV$	Electron volt ( $1.6 \times 10^{-19}$ J)
$Ry$	Rydberg
$\mu V$	Microvolt ( $10^{-6}$ V)
$m_e$	Mass of electron ( $9.11 \times 10^{-31}$ kg)
$\hbar$	Reduced Planck's constant
$m_e^*$	Effective mass of electron
$m_h^*$	Effective mass of holes
$\sigma$	Electrical conductivity
$S$	Seebeck coefficient
$\kappa$	Thermal conductivity
$\kappa_l$	Lattice thermal conductivity
$\kappa_e$	Electronic thermal conductivity
$PF$	Power Factor
$ZT$	Figure of Merit
$P$	Pressure
$E$	Total Energy
$V$	Volume
$\Delta V$	Potential Difference
$\Delta T$	Temperature Difference
$I$	Electric Current
$Q$	Heat
$\Pi$	Peltier Coefficient
$\eta$	Efficiency
$\tau$	Relaxation time
$\Gamma$	Gamma
$V_H$	Hartree Potential
$V_{ext}$	External Potential

## **LIST OF ABBREVIATIONS**

TE	Thermoelectric
3D	Three-Dimensional
2D	Two-Dimensional
TEG	Thermoelectric Generator
DOS	Density of States
HH	Half Heusler
VEC	Valence Electron Count
DFT	Density Functional Theory
HF	Hartree-Fock
KS	Kohn-Sham
BZ	Brillouin Zone
LDA	Local Density Approximation
GGA	Generalized Gradient Approximation
TB-mBJ	Tran Blaha modified Becke Johnson
FPLAPW	Linearized Augmented Plane Wave
MT	Muffin-tin
PP	Pseudopotential
PAW	Projector Augmented Wave
IBZ	Irreducible Brillouin Zone
BTE	Boltzmann Transport Equation
DPT	Deformation Potential Theory
ADP	Acoustic Deformation Potential
DFPT	Deformation Potential Perturbation Theory
SMRT	Single Mode Relaxation Time
LBTE	Linearized Phonon Boltzmann Equation
EFF	Effective Fitness Function
AIMD	Ab initio Molecular Dynamics
SCF	Self-Consistent Field
IFC	Interatomic Force Constant
CRTA	Constant Relaxation Time Approximation
RBA	Rigid Band Approximation

CBM	Conduction Band Minima
VBM	Valence Band Maxima
VASP	Vienna Ab initio Simulation Package
PBE	Perdew, Burke, and Ernzerhof functional
HSE	Heyd-Scuseria-Ernzerhof functional
SOC	Spin-Orbit Coupling

# CHAPTER 1: INTRODUCTION

---

## 1.1 Overview of Thermoelectricity

Energy is the backbone of modern society, powering everything from the smartphones in our hands to the vehicles we travel in and the homes we live in. As technology becomes deeply embedded in our daily lives, the ever-increasing demand for energy highlights the pressing need for more efficient utilization of resources through modern science and technology. The global quest for clean and sustainable energy is rapidly growing due to the extensive use of non-renewable energy resources [1]. With the increasing global energy demand and the adverse environmental impacts of fossil fuel, which is still a dominant energy source, developing alternative technologies and sustainable energy solutions has become paramount. Energy efficiency is of utmost importance in the battle against climate change and the wise use of resources. Efficient energy use reduces worldwide energy demand and decreases the adverse environmental effects of energy production. Renewable energy resources, such as geothermal, solar, and wind power, are essential for sustainable development. However, these renewable energy resources have their constraints pertaining to weather and location. One of the possible solutions to tackle the emerging energy crisis is the recycling of waste heat into useful energy, which can be realized through the process known as thermoelectricity [2–4].

It is a promising technology that directly converts temperature differences into electrical energy and vice versa. This technology has great potential to provide sustainable solutions to the increasing energy crisis by reducing our dependence on fossil fuels, and the overwhelming problem of global warming, and significantly reduce reliance on renewable energy resources. Thermoelectric (TE) materials can directly convert waste heat- commonly released from industrial processes, vehicle engines, and household appliances (as shown in **Figure 1.1**) into useful electricity [5–7]. This energy recovery approach conserves resources and addresses thermal management challenges across various applications. The TE generators (TEGs) possess unprecedented advantages, including eco-friendliness, long working life, a simple structure, silent, containing no moving parts, pollution-free, easy maintenance, and high reliability. They hold the potential to play a vital role in achieving energy sustainability, particularly when integrated with emerging technologies in nanostructured materials such as three-dimensional (3D) and two-dimensional (2D) materials, which have shown promising results in increasing TE performance [8].

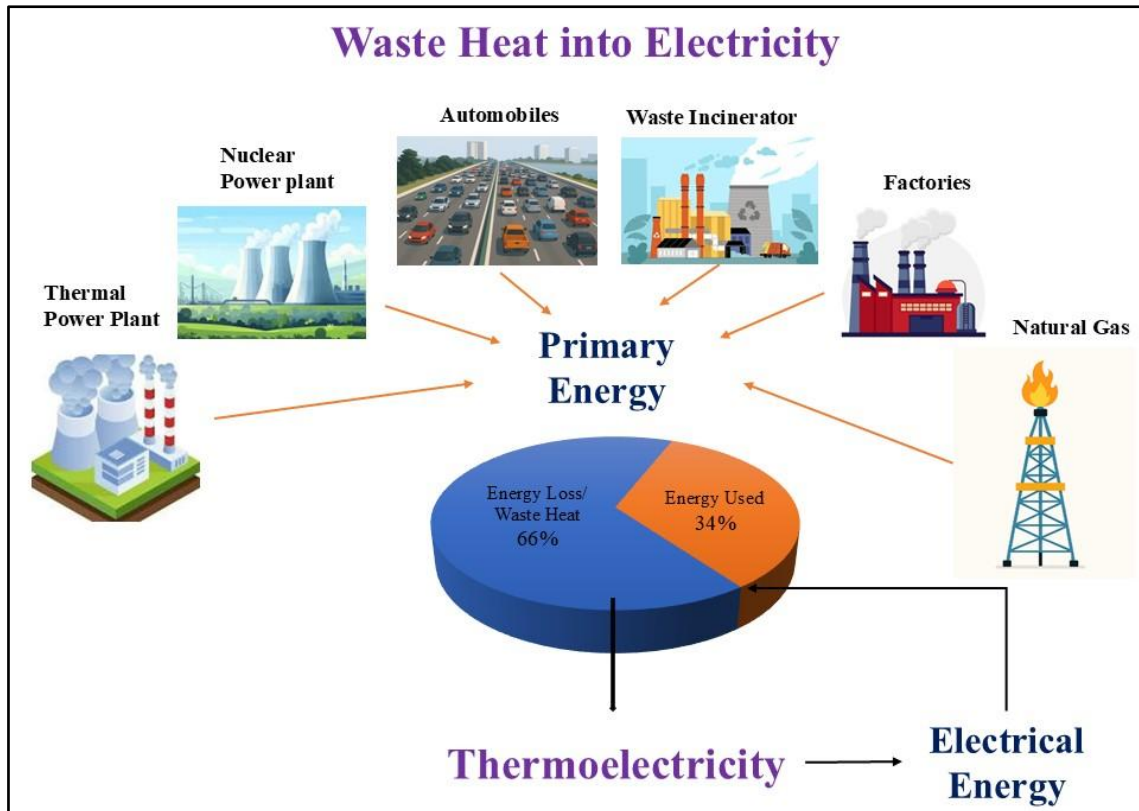


**Figure 1.1** Sources of the waste heat energy.

## 1.2 Application Areas of Thermoelectric Materials

Thermoelectric materials has multiple applications: waste heat recovery, power generation, cooling applications, and wearable and portable electronics [5,9–11]. Waste heat recovery is one of the most substantial applications, where TEGs convert industrial waste heat, vehicular output, etc., into useful electricity. By converting this heat into power, TE materials help improve energy efficiency and reduce operational costs. TEGs provide reliable, maintenance-free power sources and are especially useful in remote or extreme environments where traditional power sources are impractical. For example, they are deployed in spacecraft, remote sensors, and deep-sea exploration. They provide silent, vibration-free cooling, which is crucial for high-performance computing, sensitive laboratory equipment, and optical devices. These materials are used in small cooling devices, from consumer electronics to advanced aerospace applications. In some portable devices, TE materials can power small electronics using body heat, emphasizing the potential for self-powered devices. **Figure 1.2** illustrates the potential application that can be explored in this field.



**Figure 1.2** A diverse range of domains where the application of thermoelectric materials can prove to be effective.

### 1.3 Thermoelectric effects

Thermoelectricity is based upon three different effects: the Seebeck, Peltier, and Thomson effects.

#### 1.3.1 Seebeck effect

In 1821, Thomas Seebeck discovered this effect. He found that when different types of materials joined together and were subjected to temperature gradient, an electromotive force is produced. The potential difference ( $\Delta V$ ) generated is directly proportional to the temperature difference ( $\Delta T$ ) of the two junctions. Seebeck coefficient ( $S$ ) is the proportionality constant and is given by

$$S = -\frac{\Delta V}{\Delta T} \quad (1.1)$$

The negative sign indicates that the material is *n*-type semiconductor and the electrons diffuse from hot end to cold end. The reverse sign is for *p*-type semiconductors in which holes move from the hot to the cold end.

### 1.3.2 Peltier effect

In 1834, Jean Charles Peltier found this effect which is the reverse of the Seebeck phenomenon. When an electric current ( $I$ ) passes through the junction of two dissimilar conducting materials, A and B, heat ( $Q$ ) may be absorbed or released at the junction depending on the direction of the current. Peltier coefficient ( $\Pi$ ) is the proportionality constant

$$\Pi = \frac{Q}{I} \quad (1.2)$$

### 1.3.3 Thomson effect

In 1851, William Thomson (also known as Lord Kelvin) discovered the third TE effect, which combines both the Peltier and Seebeck effects. He found that the Seebeck and Peltier coefficients are related through thermodynamics. The Peltier coefficient is simply the Seebeck coefficient times absolute temperature, i.e.,  $\Pi = ST$ . This relation led Thomson to predict a third TE effect, known as the Thomson effect. In this effect, heat is absorbed or released when current flows in a material with a temperature gradient ( $\Delta T$ ). The heat is proportional to both the electric current and the temperature gradient. The proportionality constant, known as the Thomson coefficient ( $\gamma$ ) is given

$$\gamma = \frac{\Delta Q}{I \Delta T} \quad (1.3)$$

## 1.4 Thermoelectric figure of merit and efficiency

Figure of merit (FOM) is a dimensionless quantity, denoted by  $ZT$ , which is equal to  $S^2 \sigma T / (\kappa_e + \kappa_l)$ , where  $S$ ,  $\sigma$ ,  $T$ ,  $\kappa_e$ , and  $\kappa_l$  are the Seebeck coefficient, electrical conductivity, absolute temperature, and electronic and thermal contributions to the thermal conductivity, respectively.

The efficiency of an ideal TE material is given by

$$\eta = \left(1 - \frac{T_c}{T_h}\right) \left\{ \frac{\sqrt{1 + ZT} - 1}{\sqrt{1 + ZT} + (T_c/T_h)} \right\} \quad (1.4)$$

Where  $T_c$  and  $T_h$  are the temperatures at the cold and hot sides, respectively.

### 1.4.1 Challenges Pertaining to Efficient Thermoelectric Materials

A few of the challenges highlighted and shown below are based on the dedicated literature review in the field of thermoelectricity.

- The efficiency of any TE material is measured by the dimensionless quantity, the figure of merit, denoted by  $ZT$ , which is equal to  $S^2\sigma T/(\kappa_e + \kappa_l)$ , where  $S$ ,  $\sigma$ ,  $T$ ,  $\kappa_e$ , and  $\kappa_l$  are the Seebeck coefficient, electrical conductivity, absolute temperature, and electronic and thermal contributions to the thermal conductivity, respectively. Achieving a high  $ZT$  is difficult, as optimizing these parameters simultaneously is challenging. Many current materials do not have a high enough  $ZT$  value to be viable for large-scale applications. Therefore, researchers are constantly looking for new materials having high  $ZT$  and effective strategies that can enhance the TE performance of existing materials [12].
- High-performance TE materials often face issues with stability, especially at elevated temperatures. For instance, materials like  $\text{Bi}_2\text{Te}_3$ , while efficient at room temperature, degrade at higher temperatures, which limits their use in high-heat applications [13]. Developing materials that are both efficient and stable over a wide temperature range is a crucial area of research.
- For efficient TE performance, materials need low lattice thermal conductivity ( $\kappa_l$ ) to sustain a temperature gradient. However, managing  $\kappa_l$  is complex. Therefore, innovations in nanostructuring and low-dimensional materials show potential in addressing this issue by introducing phonon scattering centers but maintaining mechanical and chemical stability remains a challenge [14,15].

### 1.4.2 Strategies to optimize Figure of merit

Over the years various strategies have been used to improve transport properties resulting in high  $ZT$ , which is an important parameter for TE applications. The most effective way to enhance the electronic transport properties is through carrier optimizations by band engineering and defects, which effectively decouple  $\sigma$  and  $S$  and simultaneously have high values that lead to achieving a higher TE power factor ( $PF$ ). Generally, the optimum carrier concentration for mostly excellent TE materials lies in the range  $10^{19}$  to  $10^{21} \text{ cm}^{-3}$ , and the corresponding Fermi level is close to the band edge [16]. Another way is to reduce the  $\kappa_l$  without affecting the electronic transport properties, so that enhanced  $ZT$  can be achieved.



The transport parameters  $S$ ,  $\sigma$ , and  $\kappa$  that affects TE performance are directly related via the following relationships:

#### 1.4.2.1 Band Structure Engineering

The band structure engineering can be done by doping, strain, and external fields [17–20]. The dopant in the host can create new energy levels in the material, resulting in the modification of the electronic band structure. This leads to an increase in the effective mass of the electron or hole and leads to an increase in available states around the Fermi level, which increases the  $S$  and hence  $ZT$ . The influence of the dopant also increases the charge carrier type ( $n$ -type and  $p$ -type) and carrier concentration in the material. Doping increases phonon scattering through the additional disorder in the crystal structure [21]. Isovalent elemental doping induces mass disorder in the structure, which reduces the lattice thermal conductivity without significantly altering the electronic parameters [22]. Lattice strain can arise from the difference in the atomic size of dopants, which affects the electronic band structure and phonon scattering [17,23].

#### 1.4.2.2 Dimensionality Reduction

It is possible to reduce the interrelation among the transport coefficients by modifying the dimensionality of the material. Once the material size decreases to a nanometre length, it can offer quasi-independent control to  $S$ ,  $\sigma$ , and  $\kappa$  due to the quantum confinement. Reducing the dimensionality from three-dimensional (3D) to two-dimensional (2D), then one-dimensional (1D), and finally from 1D to zero-dimensional (0D), as demonstrated in **Figure 1.3**, enhances the electronic DOS in the vicinity of the Fermi level, leading to an increased  $S$  value. The quantum confinement opens new opportunities to decouple the dependence of key TE parameters and tune them separately. The developments in the direction of obtaining high performance TE materials gained a new motivation following Hicks' and Dresselhaus' suggestion that significant increases in TE performance can be achieved by developing TE materials with quantum-well superlattice structures [24,25]. A review paper by Li et al. highlights the recent progress in 2D materials with high TE performance [15].

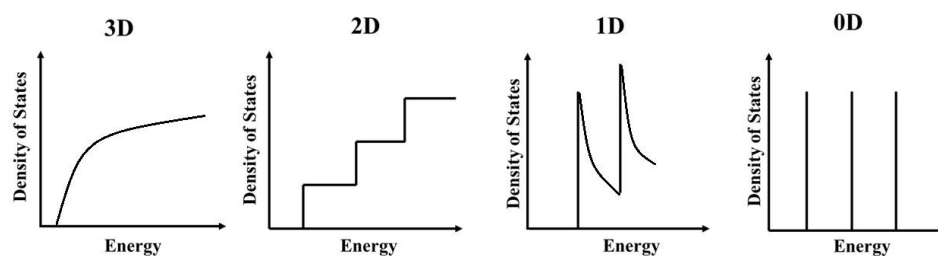


**Figure 1.3** Electronic DOS for different dimensionality. Low-dimensional materials showing sharp DOS.

### 1.4.2.3 Phonon Engineering

In recent years, more and more methods for engineering the phonon transport have been reported. For example, the multi-scale scattering centre introduced by defect engineering could help shorten the phonon mean free path [26], thus decreasing the  $\kappa_l$ . From the dimensionality perspective, in general, defects can be categorized into 0D (point defect), 1D (dislocation), 2D (grain boundary), and 3D (nano inclusion or secondary phase) [27]. Point defects, including vacancy [28,29], alloying or doping [30], and interstitial atoms [31] can scatter high-frequency phonons efficiently. High-density dislocations can scatter mid-frequency phonons, which can be introduced via plastic deformation of the samples. A large number of grain boundaries can be introduced via nano-structuring, thus forming high-density grain boundary scattering centers that can scatter low-frequency phonons. However, it should be noted that the high-density grain boundary scattering center not only scatters the low-frequency phonon but also the charge carriers, having a negative effect on the electronic performance. Introducing these kinds of defects in a system, one can construct multi-scale and multi-frequency scattering centers, thus realizing the reduction in phonon transport properties. Additionally, the  $\kappa_l$  can also be effectively reduced via a porous structure [32,33], complex crystal structure [34], lattice anharmonicity [35] and introducing heavy elements or weak chemical bonding [36].

## 1.5 Thermoelectric materials

The attempt to improve  $ZT$  is either made by discovering new materials or by tuning the existing TE materials. As discussed in the previous section, the components of  $ZT$  are interconnected. Therefore, it is difficult to modify one parameter without affecting the other. This section provides a quick review of potential candidates for thermoelectricity, and we focus on selected 3D and 2D materials for their unique properties and promising TE performance. Also, literature on recent advances in the TE properties of these materials is briefly discussed to provide insights relevant to our work.

### 1.5.1 Zintl Compounds

Zintl phases follow valence rules to achieve stable electronic configurations [37,38]. ‘Zintl’ is named after the scientist Eduard Zintl, who made the binary phases by the combination of main group metalloid, electropositive alkali and alkaline metal. Unlike alloys, where electrons are shared collectively, Zintl phase compounds exhibit well-defined oxidation states, with electron transfer occurring from electropositive to electronegative elements. However, in many cases, the octet rule remains unfulfilled, leading to the formation of anionic covalent networks that

ensure closed-shell configurations. The bonding in these systems follows the Zintl-Klemm concept, where electropositive elements such as alkali and alkaline earth metals donate electrons, and electronegative elements form covalent structures [39].

Zintl compounds have been studied for the last few years to achieve high TE performance. These compounds offer an excellent balance between high PF and low thermal conductivity, resulting in remarkable TE performance [40,41]. They exhibit a well-balanced combination of covalent and ionic bonding, resulting in a favorable electronic structure that supports high Seebeck coefficients. Their semiconducting nature is ideal for TE applications. Many Zintl compounds have shown high TE efficiency due to intrinsically low lattice thermal conductivity [42]. This is attributed to their complex crystal structures, which scatter phonons effectively. Thus, these compounds exhibit phonon glass electron crystal behaviour. Zintl compounds such as binary, ternary, and quaternary are currently under extensive investigation both at experimental and theoretical fronts [43–46]. In the present thesis, we have carried out calculations to investigate the TE properties of both *p*-type and *n*-type Zintl compounds.

### 1.5.2 Half Heusler Compounds

In 1903, Dr. F. Heusler found that the alloy  $\text{Cu}_2\text{MnAl}$  is ferromagnetic, even though the constituent elements are non-magnetic in nature [47]. This was a groundbreaking discovery of that time. Half-Heusler (HH) compounds are a kind of material that falls on the borderline between alloys and compounds. They possess some vacant lattice sites, allowing for tunable compositions similar to alloys, while the covalent nature of the lattice characterizes them as compounds. Later, O. Heusler and Bradley defined the crystal structure of Heusler compounds as a structure made from four interpenetrating FCC lattices [48,49]. Nowotny and Juza discovered the ternary counterparts of these compounds, known as HH or semi-Heusler compounds [50,51]. HH compounds are unique in the sense that the nature of the band structure can be determined just by finding the number of valence electrons in the compounds. HH compounds having 8 or 18 valence electrons are found to be semiconducting in nature [27,28]. Generally, HH compounds crystallize in cubic structures having a space group  $F\bar{4}3m$  (216). These structures exhibit XYZ stoichiometry 1:1:1 and the atoms X and Y have cationic characters, with Z being the anionic counterpart. Also, in a given formula, the elements are arranged from the most electropositive to the most electronegative. The electropositive elements (X and Y) can be a transition metal, main group element, or rare earth metal, while the electronegative element (Z) is typically a main group element, primarily from the p-block. The tunable and covalent nature of HH compounds makes them a promising candidate in a

variety of fields. Over the decade, HH compounds have made considerable development in TE conversion technology [52–55]. These compounds are known for their high thermal stability, making them suitable for applications in high-temperature environments. Their robust mechanical properties also make them attractive for integration into TE modules. HH compounds with 18 valence electrons are semiconducting in nature such as TiCoSb, ZrNiSn, and HfNiSn and were found to have significant values of the Seebeck coefficient and power factor, which are essential for TE efficiency of a material [56,57]. The reason behind this is their unique electronic and structural properties. Most of the research focussed on the TE performance on 18 valence electron HH compounds. While a few HH compounds have 8 valence electrons, they are also semiconductors and can exhibit good TE performance [58]. The present thesis includes the TE properties of 8 valence electron count (VEC) HH compounds.

### 1.5.3 Layered Materials

The main benefit of layered structured materials for TE purposes and applications is that they can separate the interrelated electrical and thermal conductivity to improve their contribution to TE energy conversion [59]. The anisotropic electronic and phonon transport properties in layered materials are the key driving forces behind the increasing attention for this kind of materials. Layered materials, such as SnSe, Bi<sub>2</sub>Te<sub>3</sub>, and BiCuSeO, have really transformed the TE research [60,61]. Strong in-plane and weak out-of-plane bonding in layered materials cause bonding heterogeneity, and the subsequent lattice anharmonicity brings down the  $\kappa_l$ . Also, weak interactions among layers results in many low-dimensional features in electronic transport, such as the quantum confinement of free charge carriers leading to an augmented  $S$  value. The correspondence of lattice anharmonicity and low-dimensional electronic features, making the layered materials perfect for realizing high TE performance as their anisotropic phonon and electronic transport properties offer imperative fundamental insights as well. Further, nitride semiconductors are highly attractive owing to their potential for environmental sustainability, utilization of readily available elements, and desirable electronic properties [62]. Extensive research has been conducted to explore the early-transition metal nitrides, such as ScN and CrN, and various methods implemented to enhance their performance for their potential use in TE applications [63]. And layered nitrides are of much interest regarding TE energy conversion as they favour anisotropic properties that ultimately enable the tuning of transport properties [64,65].

### 1.5.4 Two-Dimensional Materials

2D materials, such as graphene, transition metal dichalcogenides, phosphorene, etc., benefited from quantum confinement effects, which enhance their Seebeck coefficient and electronic properties [15]. Reduced dimensionality from 3D to 2D leads to enhanced phonon scattering and ultralow lattice thermal conductivity, which are vital for achieving high  $ZT$ . 2D materials can demonstrate lower  $\kappa_l$ , making them highly promising for TE devices. In general, decreasing the dimensionality of materials can significantly reduce the average distance that phonons can travel freely and increase the scattering of phonons at interfaces. This ultimately limits the ability of these materials to transport heat and, consequently, good TE performance. The 2D systems, such as transition metal chalcogenides, MXenes, and h-BN, rare-earth monolayers with anisotropic properties, have gained extensive consideration as efficient TE materials [64,66–68]. Further, strain engineering is also a powerful tool for tuning the electronic, phononic, and TE properties of 2D materials [69]. The application of strain induces structural and electronic changes, which can enhance or suppress specific material properties. By combining the unique properties of 2D materials with the tunability offered by strain engineering, one can achieve unprecedented control over TE performance. This synergy enables efficient, flexible, and application-specific TE device design.

## 1.6 Objectives of the thesis

The main objectives of the work presented in the thesis are as follows:

- To investigate the structural, electronic, and thermoelectric properties of some Zintl compounds.
- To understand the thermoelectric properties of Heusler-based materials.
- To unravel the thermoelectric properties and lattice dynamics of layered materials.
- To optimize the carrier concentration of some existing two-dimensional materials for enhancing their thermoelectric performance.

## 1.7 Scope of the thesis

The importance of the search for novel TE materials is discussed clearly in the previous sections. This study outlines some effective approaches for enhancing the TE performance of materials, which include carrier concentration optimization, phonon engineering, and dimensional reduction. It may open new avenues for future experimental realization of these materials for energy harvesting applications in a wide temperature range (from near room temperature to moderate temperature to high temperature). This thesis underlines the effective

use of computational techniques to screen efficient materials for desired applications without resorting to trial-and-error methodology in the wet lab, which results in saving valuable resources. We have explored the TE properties of few selected materials that belong to well-established emerging materials systems, such as Zintl phase, Heusler alloys, layered materials, and two-dimensional materials within the framework of Density Functional Theory (DFT) and Boltzmann transport equations. These classes of materials have been selected due to their promising electronic band structures and tunable thermal transport properties, which are crucial for achieving high TE efficiency. We proposed strategies to achieve a high TE figure of merit. Moreover, this thesis focuses on the tuning of transport parameters such as electrical conductivity and thermopower and reports the possible ways to enhance TE parameters. The findings contribute to the broader development of sustainable technologies for waste heat recovery and energy-efficient devices for different temperature applications. Experimental synthesis of presented materials and large-scale device implementation are beyond the scope of this thesis but remain important avenues for future research.

### 1.7.1 Structure of the thesis

This thesis is divided into seven chapters as described below:

**Chapter 1** gives the origin of TEs and the introduction to 3D and 2D TE materials. It also describes the basic concepts involved in determining the transport properties of a material. We discussed challenges pertaining to efficient TE materials and focused on parameters involved in optimizing the TE efficiency and figure of merit. Moreover, it provides an overview of the background history, motivation, and objective of the thesis work.

**Chapter 2** discusses the theoretical methodology used to carry out the research work. The main emphasis is given to the DFT to solve body problems. It briefly introduces the functional used, electron-ion interactions, the concept of full-electron scheme, projector augmented wave, and pseudopotentials. Different numerical aspects of k-mesh sampling, plane wave cut-off energy, etc. In addition, the underlying theory involved in the electronic and thermal transport of solids. The TE transport coefficient calculation was carried out using density functional theory and semiclassical Boltzmann transport theory. It provides the details of all the computational packages used in this thesis to carry out the electronic structure calculations, electronic transport, and lattice transport properties.

**Chapter 3** reports the first-principles investigation of high TE transport properties of the *p*-type  $\text{RbZn}_4\text{P}_3$  and *n*-type  $\text{RbGaSb}_2$  Zintl compounds. It elaborates on phonon glass electron

crystal behaviour in the Zintl compound. Charge density analysis shows the coexistence of ionic and covalent bonding. The electronic band structure calculations reveal that both compounds are moderate direct bandgap semiconductors. The high  $ZT$  values for a widely studied temperature range make these compounds quite promising for future TE material. TE investigations suggest that optimizing carrier concentration enhances  $ZT$ . As a result, the findings in this chapter offer a theoretical foundation for experimental investigations of thermoelectricity in the Zintl compound.

**Chapter 4** focuses on the detailed physical insight into the structural, electronic, and transport properties of 8-valence electron count (VEC) half Heusler compounds  $\text{LiCaX}$  ( $X = \text{As}, \text{Sb}$ ). Our findings validate the high thermal stability and dynamical stability of these compounds. Further, it presents and compares the  $ZT$  under the constant relaxation time approximation and temperature-dependent relaxation time for both hole and electron carriers. We realize the high figure of merit of  $\text{LiCaAs}$  and  $\text{LiCaSb}$  for both optimal hole and electron carrier doping. Also, the  $ZT$  was found to be comparable to experimentally synthesized 8 VEC HH compounds. This indicates that these compounds are promising candidates for the 8 valence electron HH family and carry huge potential for thermoelectric energy harvesting applications.

**Chapter 5** examines the lattice dynamics of  $\text{Li}_2\text{MN}_2$  ( $M = \text{Zr}, \text{Hf}$ ) layered nitrides to unravel the factors contributing to their unique thermal transport properties using first-principles calculations. We analyse how replacing Zr with the relatively heavy element Hf in  $\text{Li}_2\text{MN}_2$  leads to an increase in thermal conductivity instead of a decrease.  $\text{Li}_2\text{ZrN}_2$  possesses a low lattice thermal conductivity owing to the significant reduction in phonon lifetime caused by the rattling behaviour of Zr. Moreover, the anisotropic character owing to the layered structure of  $\text{Li}_2\text{MN}_2$  has enabled tuning their transport properties. These findings on the electronic and lattice transport properties of  $\text{Li}_2\text{MN}_2$  may open new horizons for the design and synthesis of more efficient nitride-based TEs. It also provides valuable insights into exploring the role of lattice dynamics in minimizing the lattice thermal conductivity of transition metal nitrides and their prospective energy harvesting applications.

**Chapter 6** explores the thermoelectric properties of yttrium pnictides  $\text{YX}$  ( $X = \text{N}, \text{P}, \text{As}$ ) monolayers. We show that the dimensionality reduction in these semiconducting materials with strong  $p$ - $d$  hybridization led to dispersive band edges and, consequently, high carrier mobilities in these semiconductors. We present a detailed investigation highlighting the merit of yttrium pnictides monolayer-based materials for TE applications. High power factor for optimal carrier

doping YX monolayers in both the  $x$ - and the  $y$ -direction is obtained. This, in conjunction with low to moderate lattice thermal conductivities of these monolayers at 500 K, leads to high  $ZT$ s. The high TE performance of these materials by breaking the  $ZT \sim 1$  barrier at 500 K suggests the prospect of developing yttrium pnictides monolayer-based materials for energy applications. The room-temperature performance of these monolayers is limited, which leaves scope for further material optimization.

**Chapter 7** presents the conclusion of the research work done and possible future direction and social impact. We summarized all the results of chapters 3-6. In the outlook, we provide the future directions, where experimentalists can confirm our findings to develop new members for TE applications.



# CHAPTER 2: THEORETICAL METHODOLOGY

---

## 2.1 Introduction to Many-Body Problem

In Quantum mechanics, it is well known that the Schrödinger equation for one body problem like a Hydrogen atom, can be solved exactly [70]. However, the many-body problem has never been solved precisely using this equation. So, what prohibits the solution for the system having more than one electron? How to deal with the dynamics of electrons in solids? To answer these questions, let us consider a many-body Schrödinger equation

$$\hat{H}\psi(\vec{R},\vec{r}) = E\psi(\vec{R},\vec{r}) \quad (2.1)$$

where  $\hat{H}$  and  $\psi(\vec{R},\vec{r})$  are the many-body Hamiltonian and wave function of the system, respectively.  $\vec{R}$  and  $\vec{r}$  are the position coordinates of the nucleus and electrons, respectively.  $E$  is the corresponding energy eigenvalue of the system. On ignoring the relativistic effects, the Hamiltonian can be written as

$$\hat{H} = -\frac{\hbar^2}{2} \sum_I \frac{\nabla_I^2}{m_I} - \frac{\hbar^2}{2m_e} \sum_i \nabla_i^2 + \sum_I \sum_{J>I} \frac{Z_I Z_J e^2}{|\vec{R}_I - \vec{R}_J|} - \sum_I \sum_i \frac{Z_I e^2}{|\vec{r}_i - \vec{R}_I|} + \sum_j \sum_{i>j} \frac{e^2}{|\vec{r}_i - \vec{r}_j|} \quad (2.2)$$

1<sup>st</sup> and 2<sup>nd</sup> terms are the kinetic energy of the nuclei and electrons, respectively. 3<sup>rd</sup>, 4<sup>th</sup>, and 5<sup>th</sup> terms represent the potential energies from the interactions among nuclei-nuclei, electrons-nuclei, and electrons-electrons, respectively.

The electrons are quantum mechanical entities; hence, it is impossible to locate their position due to the associated wave nature. Due to the uncertainty in the position of electrons, the distance ( $\vec{r}_{ij}$ ) between them cannot be determined exactly, and subsequently, the Hamiltonian. Here, the situation is even more complicated since we are dealing with solids having multiple electrons interacting with multiple nuclei. Several approximations were made for solving the many-body problem and are described as follows:-

### 2.1.1 Born-Oppenheimer approximation

In 1927, Born and Oppenheimer made an assumption that nuclei can be considered fixed in comparison to electrons due to the huge difference between their masses ( $m_I \sim 2000 m_e$ ) [71]. As a result, from the prospect of electronic motion, nuclei are no longer variable, but only fixed parameters. In the background of moving electrons, the nucleus appears to be frozen, like honey

bees around an elephant. It allows the decoupling of the nuclear and electronic motion, therefore, the total wave function in equation 2.1 can be written as the product of electronic and nuclear wave functions

$$\psi(\vec{R}, \vec{r}) = \psi_{el}(\vec{R}, \vec{r}) \psi_N(\vec{R}) \quad (2.3)$$

where  $\psi_{el}(\vec{R}, \vec{r})$  and  $\psi_N(\vec{R})$  represent the electronic and nuclear part of the wavefunction.

This approximation is known as Born-Oppenheimer approximation that reduces many-body equation to

$$(\hat{H}_{el} \psi_{el}(\vec{R}, \vec{r}) = E_{el} \psi_{el}(\vec{R}, \vec{r}) \quad (2.4)$$

where,

$$\hat{H}_{el} = \frac{\hbar^2}{2m_e} \sum_i \nabla_i^2 + \sum_I \sum_{J>I} \frac{Z_I Z_J e^2}{|\vec{R}_I - \vec{R}_J|} - \sum_I \sum_i \frac{Z_I e^2}{|\vec{r}_i - \vec{R}_I|} + \sum_J \sum_{i>j} \frac{e^2}{|\vec{r}_i - \vec{r}_j|} \quad (2.5)$$

Despite having been simplified, solving  $\hat{H}_{el}$  is still a challenge. Thus, more approximations are required to solve the equation as discussed in the next section.

### 2.1.2 Hartree Approximation

In 1928, Hartree proposed a method to solve the many-body system, where each electron is moving independently [72]. He assumed the  $N$ -electron system as a set of  $N$  non-interacting one-electron systems, where each electron feels an average electrostatic potential due to other electrons. According to this approximation, the Schrödinger wave equation (in atomic units) can be written as

$$\left( -\frac{1}{2} \sum_i \nabla_i^2 - V_{ext} + V_H \right) \psi(\vec{r}) = E \psi(\vec{r}) \quad (2.6)$$

Here,  $V_{ext} = \sum_I \sum_i \frac{Z_I}{|\vec{r}_i - \vec{R}_I|}$  i.e., the attractive potential among the nuclei and the electrons, and

$V_H$  is the Hartree potential due to electron-electron Coulomb interaction and given by

$$V_H = \int \frac{\rho(\vec{r}')}{|\vec{r} - \vec{r}'|} d\vec{r}' \quad (2.7)$$

This approximation is also known as an independent electron approximation, and the total energy ' $E$ ' can be written as a sum of  $N$  one-electron energies:

$$E = E_1 + E_2 + E_3 + \dots + E_N \quad (2.8)$$

However, Hartree theory neglects the effect of electron-electron correlation and also violates the wave function's antisymmetric requirements on their exchange, hence requires further approximations.

### 2.1.3 Hartree-Fock approximation

In 1930, Fock improved the Hartree theory based on the mean-field approach by taking spin into consideration and writing the one-electron wave function in the form of Slater determinant as given below [73]

$$\psi(\vec{r}_1, \vec{r}_2, \vec{r}_3, \dots, \vec{r}_N) = \frac{1}{\sqrt{N!}} \begin{vmatrix} \psi_1(1) & \psi_1(2) & \dots & \psi_1(N) \\ \psi_2(1) & \psi_2(2) & \dots & \psi_2(N) \\ \cdot & \cdot & \cdot & \cdot \\ \psi_N(1) & \psi_N(2) & \dots & \psi_N(N) \end{vmatrix} \quad (2.9)$$

Here,  $\frac{1}{\sqrt{N!}}$  is a normalization factor. The total wave function written in the form of a determinant takes care of the anti-symmetric nature of the fermions, i.e., the sign is changed when any two columns or rows are interchanged which ensures the anti-symmetric nature of the total wave function. Moreover, suppose any two rows or columns are identical. In that case, the determinant is zero, implying that the electronic state having electrons of the same spatial and spin coordinates does not exist, thus satisfying the Pauli exclusion principle.

Now, equation 2.6 is modified as:

$$\left( -\frac{1}{2} \sum_i \nabla_i^2 - V_{ext} + V_{ij} \right) \psi(\vec{r}) = E \psi(\vec{r}) \quad (2.10)$$

Essentially,  $V_{ij}$  is driven by two interactions: Coulomb interaction between electron coordinates  $i$  and  $j$ , and an exchange interaction caused by the Slater determinant's anti-symmetrical nature. Since exchange interaction will give negative exchange energy, the total energy in Hartree and Fock (HF) approximation will be much closer to the ground state energy, which is minimized using the variational principle:

$$\delta \left( \int \psi^*(\vec{r}) \hat{H} \psi(\vec{r}) d\vec{r} \right) = 0 \quad (2.11)$$

Now, the total energy under HF approximation is written as:

$$E = T + E_{ext} + E_H + E_x \quad (2.12)$$

where 1<sup>st</sup>, 2<sup>nd</sup>, 3<sup>rd</sup>, and 4<sup>th</sup> terms are the kinetic energy of electrons, external energy due to the interaction between nuclei and electrons, Hartree energy, and the exchange energy. HF theory incorporates the exchange interaction but did not consider the electron correlation. The neglected correlation was included in the density approach method known as Density functional theory (DFT), which is discussed in the next section.

## 2.2 Density functional theory

Solving many-electron systems through the wave function approach is very tedious and computationally expensive. The self-consistency scheme used in HF theory makes an initial guess on the wave function, which depends on  $3N$  variables for  $N$ -electrons. DFT is a powerful quantum mechanical method used to explore the electronic structure of many-electron systems [74]. It enables us to determine the properties of such systems based on the electron density, denoted as  $\rho(\vec{r})$ , thus reducing the  $3N$  variables problem to 3 coordinates ( $x, y, z$ ) only. Solving many-electron systems through the spatially dependent electron density in comparison to the wave function approach is a remarkably versatile method and computationally inexpensive. The framework of DFT mainly includes the Hohenberg-Kohn theorem and Kohn-Sham equations, which are discussed in subsequent sections.

### 2.2.1 Hohenberg-Kohn Theorems

Hohenberg and Kohn in 1964 introduced two fundamental theorems on which the theoretical foundation of DFT relies, and are given as [75]

**Theorem I** states that the ground state energy,  $E$ , of a system of interacting electrons, is uniquely determined by electron density i.e.,  $E[\rho(\vec{r})]$ .

**Theorem II** states that the  $\rho(\vec{r})$  can be minimized w.r.t energy using the variational principle. If and only if the input density is the real ground-state density ( $\rho_0(\vec{r})$ ), the energy functional that yields the ground-state energy of the system would have the lowest energy.

Using the above two theorems, the total energy for many-electron system can be written as

$$\hat{H} = -\frac{1}{2} \sum_i \nabla_i^2 - V_{ext}(\vec{r}_i) + \sum_{i \neq j} \frac{1}{|\vec{r}_i - \vec{r}_j|} \quad (2.13)$$

here  $V_{ext}$  represents the external potential, which includes the interaction between the electrons and the nuclei. Using these theorems, Kohn and Sham considered a fictitious system of one electron that can replace the  $N$ -electron system [76]. The methodology is discussed in detail in the next section.

### 2.2.2 Kohn-Sham Approach

In 1965, Kohn and Sham showed that a many-electron problem can be converted into a problem of non-interacting particles, where each particle is moving under an effective Kohn-Sham (KS) potential and described by a single-particle Schrodinger equation, and the total energy within the DFT formalism is written as [77]:

$$E_{KS} = T[\rho(\vec{r})] + E_{ext}[\rho(\vec{r})] + E_H[\rho(\vec{r})] + E_{xc}[\rho(\vec{r})] \quad (2.14)$$

As per KS scheme,  $T[\rho(\vec{r})]$  represents the independent particle kinetic energy and is expressed in terms of the KS orbitals ( $\phi_i$ ) as

$$T[\rho(\vec{r})] = -\frac{1}{2} \sum_{i=1}^N \phi_i^*(\vec{r}) \nabla^2 \phi_i(\vec{r}) \quad (2.15)$$

The square bracket indicates the functional term, implying that energy is a function of electron density, which is dependent on the electronic coordinate  $\vec{r}(x, y, z)$ . The energy derived from the external potential,  $V_{ext}$ , is denoted by  $E_{ext}[\rho(\vec{r})]$  and has the form

$$E_{ext}[\rho(\vec{r})] = \int V_{ext}(\vec{r}) \rho(\vec{r}) d\vec{r} \quad (2.16)$$

The Coulomb interaction between electrons gives rise to Hartree potential,  $V_H$ , which is given by equation 2.7. The Hartree energy corresponding to  $V_H$  is:

$$E_H[\rho(\vec{r})] = \frac{1}{2} \iint \frac{\rho(\vec{r}) \rho(\vec{r}')}{|\vec{r} - \vec{r}'|} d\vec{r} d\vec{r}' \quad (2.17)$$

During the exchange of two particle position, the wave function changes its sign due to their anti-symmetric nature. It is known as the exchange energy ( $E_x$ ), and can be formed as follows:

$$E_x = -\frac{1}{2} \sum_{ij} \iint \frac{\phi_i^*(\vec{r}) \phi_i(\vec{r}') \phi_j^*(\vec{r}) \phi_j(\vec{r}')}{|\vec{r} - \vec{r}'|} d\vec{r} d\vec{r}' \quad (2.18)$$

and the collective interaction of all the electrons of a system with one electron is called electronic correlation, and the corresponding energy is energy  $E_c$ . As there is no exact formulation for the correlation energy, the combination of the two ( $E_x + E_c$ ) is together called exchange-correlation energy,  $E_{xc}$ . The exchange-correlation term,  $V_{xc}$  represented as a functional derivative of the exchange correlation energy, is the term that makes DFT efficient and beneficial over HF theory:

$$V_{xc}(\vec{r}) = \frac{\delta E_{xc}(\vec{r})}{\delta \rho(\vec{r})} \quad (2.19)$$

This approach is commonly misunderstood to describe the non-interacting electrons moving in a potential determined by the nuclei. In reality, electrons travel in an effective potential  $V_{eff}$ , which involves electronic interactions, although indirectly. In KS equations, the electron-electron interaction is substituted by the interaction of electrons with a medium that take care of electron-electron interactions. The KS equation in Schrödinger form is represented as:

$$\hat{H}_{KS}\phi(\vec{r}) = E_{KS}\phi(\vec{r}) \quad (2.20)$$

The corresponding Hamiltonian is:

$$\hat{H}_{KS} = -\frac{1}{2}\sum \nabla^2 + V_{eff} \quad (2.21)$$

$V_{eff}$  is the effective potential, which includes three potential terms ( $V_{ext} + V_H + V_{xc}$ ). To solve this Hamiltonian and find the ground state energy and density of the system, an iterative technique is adopted, which is known as the self-consistent method. A flow chart of the self-consistent field cycle is shown in **Figure 2.1**. The initial guess is made on the  $\rho(\vec{r})$ . The trial density at which energy is converged is then used to compute each potential term.  $V_{xc}$  is still not adequately defined leads to more approximations.

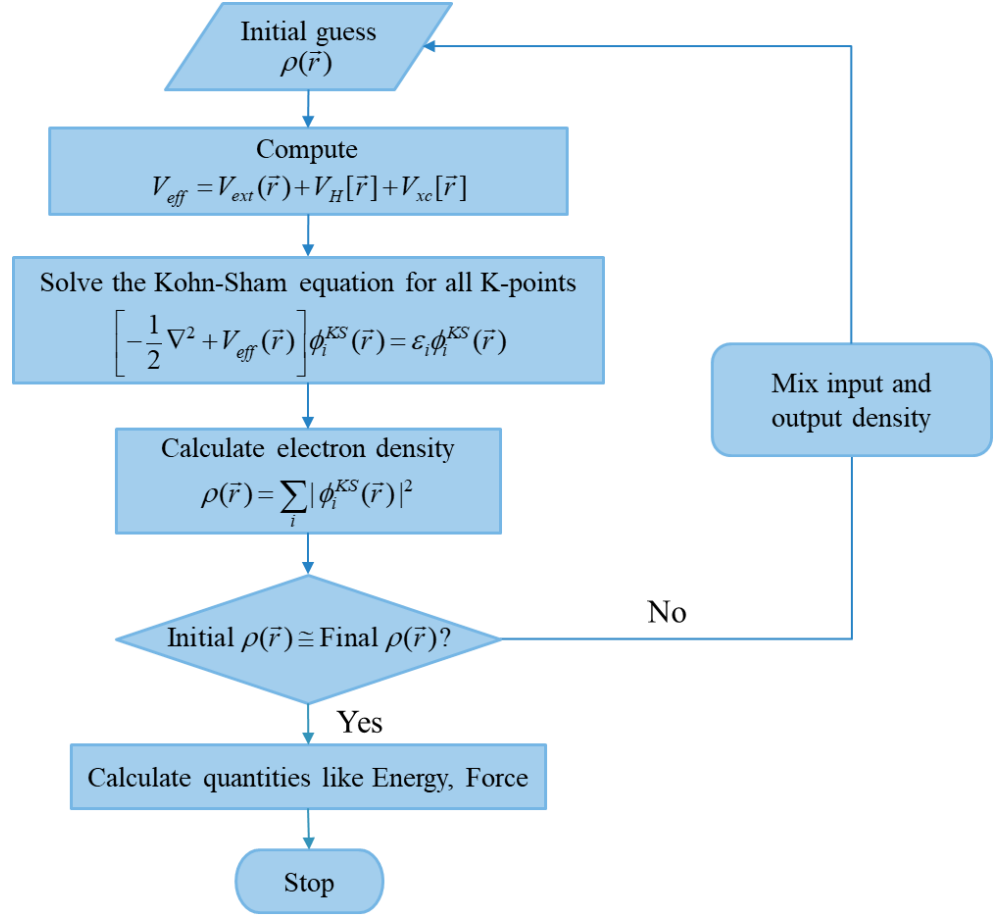


**Figure 2.1** Flow chart for self-consistent density functional calculations.

## 2.3 Exchange-Correlation Functionals

Now we have a workable framework for solving the electronic ground-state problem and, any required property may be determined using KS equations provided the  $\rho(\vec{r})$  is known.

Without knowing the precise form of the exchange-correlation functional,  $E_{xc}$ , a fundamental parameter in DFT, the many-electron problem remains unsolved. Several approximations are made to define  $E_{xc}$  and these functionals can be given as local, semi-local, and non-local approximations. The famous and most frequently used approximations are discussed in sections 2.3.1, 2.3.2, 2.3.3, and 2.3.4.

### 2.3.1 Local Density Approximation

In 1965, Kohn and Sham presented a simple approximation to define exchange correlation functional to achieve a meaningful solution to the many-body problem, called local density approximation (LDA) [75]. The electron density in a system is assumed to vary slowly when compared to spatial coordinates, such that electrons see the entire system in a similar way as

they see it locally. This is similar to the case of a homogeneous gas of free electrons. Under such approximation, exchange correlation is given by:

$$E_{xc}^{LDA}[\rho(\vec{r})] = \int \rho(\vec{r}) \varepsilon_{xc}[\rho(\vec{r})] d^3\vec{r} \quad (2.22)$$

where,  $\varepsilon_{xc}$  denotes the exchange-correlation energy per particle of the interacting free electron gas having density  $\rho(\vec{r})$ . LDA produces good results for metals with uniform electron density. It fails for the cases where density varies rapidly, like in molecules [78].

### 2.3.2 Generalized Gradient Approximation

The generalized gradient approximation technique (GGA) originated from Herman's (1969) proposition that electron density varies as a function of spatial coordinates and that the exchange-correlation energy may be represented as the gradient of electron density [79]. Having gradient density as an additional variable, GGA was considered more accurate functionals than LDA. Its general expression is given by

$$E_{xc}^{GGA}[\rho(\vec{r})] = \int \rho(\vec{r}) \varepsilon_{xc}[\rho(\vec{r}), \nabla(\rho(\vec{r}))] d^3\vec{r} \quad (2.23)$$

Since there is no simpler functional form that accurately captures GGA,  $E_{xc}^{GGA}$  is usually expressed by modifying the LDA functional with an additional term  $F(s)$ , which is nothing but the gradient correction term:

$$E_{xc}^{GGA}[\rho(\vec{r}), s] = \int \varepsilon_{xc}^{LDA}[\rho(\vec{r})] \rho(\vec{r}) F(s) d^3\vec{r} \quad (2.24)$$

Here,  $s = C \frac{|\nabla \rho(\vec{r})|}{\rho^{4/3}(\vec{r})}$ . The usual range of  $s = 0 - 3$  in solids. Under GGA approximation PW91 (proposed by Perdew and Wang in 1992) [80,81] and PBE (proposed by Perdew, Burke, and Ernzerhof in 1996) [82] are most commonly used functionals. As far as the structural properties are concerned, GGA provides better results than LDA. We have used GGA-PBE functionals in the present thesis. However, it somehow underestimates the band gap values, resulting in a misleading prediction of transport properties. So, we need to go beyond GGA. This urged the need to develop approximations leading to more accurate functionals.

### 2.3.3 Tran-Blaha modified Becke-Johnson potential

Tran and Blaha (2009) introduced an effective exchange correlation functional that was subsequently evaluated in various solid materials, including wide band gap insulators, semiconductors, and a few strongly correlated 3d transition metal systems. Their findings



demonstrated the accurate prediction of band gap values, which were found to be in good agreement with experimental results [83]. Several approaches, such as LDA +U and GW, have been presented as extensions to the traditional exchange-correlation functionals LDA and GGA. The TB-mBJ functional has garnered increased attention due to its reduced computational cost. This approach represents a variation of the exchange correlation method first described by Becke and Johnson [84]. It can be mathematically expressed as.

$$v_{x,\sigma}^{MBJ}(\vec{r}) = cv_{x,\sigma}^{BR}(\vec{r}) + (3c-2) \frac{1}{\pi} \sqrt{\frac{5}{12}} \sqrt{\frac{2t_{\sigma}(\vec{r})}{\rho_{\sigma}(\vec{r})}} \quad (2.25)$$

where  $\rho_{\sigma} = \sum_{i,N} |\psi_{i,\sigma}|^2$  and  $t_{\sigma} = -\frac{1}{2} \sum_{i,N_{\sigma}} \nabla \psi_{i,\sigma}^* \cdot \nabla \psi_{i,\sigma}$  represents the electron density kinetic energy, respectively.

$$v_{x,\sigma}^{BR}(\vec{r}) = -\frac{1}{b_{\sigma}(\vec{r})} (1 - e^{-x_{\sigma}(\vec{r})} - \frac{1}{2} x_{\sigma}(\vec{r}) e^{-x_{\sigma}(\vec{r})}) \quad (2.26)$$

is the Becke-Roussel potential.

The factor ‘c’ was chosen as:

$$c = \alpha + \beta \sqrt{\frac{1}{V_{cell}} \int \frac{|\nabla \rho(\vec{r}')|}{\rho(\vec{r}')} d^3 \vec{r}'} \quad (2.27)$$

where,  $\alpha$  and  $\beta$  are the two free parameters and  $V_{cell}$  is the unit cell volume.

The TB-mBJ potential preferably considered in the present work. This potential has shown its applicability in determination of band gap of different oxides and other materials which is consistent with experimental reports.

### 2.3.4 Hybrid Functionals

In Hybrid functionals, the exact energy term is incorporated by considering the HF term, where exchange-correlation energy depends on the orbital-dependent HF and an explicit density functional term [85]. The general expression of hybrid functional can be described as:

$$E_{xc} = \frac{1}{2} (E_{xc}^{HF} + E_{xc}^{LDA \text{ or } GGA}) \quad (2.28)$$

Hybrid functional produce more accurate results in band structure calculations, consequently, the transport properties, but are computationally expensive. To accurately determine the TE properties, we have used HSE06 functional, which was developed by Heyd-Scuseria-Ernzerhof [86].

## 2.4 Electron-Ion Interactions

To solve the KS equations exactly, we need to find the remaining term,  $V_{ext}$ , which is the electron-ion interaction term. Since we are dealing with solids having many electrons, and significant electron oscillations near nuclei, defining  $V_{ext}$ , is difficult. Our main focus is on calculating the properties based on valence electrons; therefore, one can approximate the core behaviour of electrons in the core region while maintaining the behaviour of valence electrons as accurately as possible. The basic approaches used to estimate the electron-ion interactions are the all-electrons scheme and the pseudopotential techniques, which are discussed in the next sections.

### 2.4.1 All-electron scheme

This scheme considers both the core and the valence electrons as spheres centered on atomic sites and interstitial regions, respectively, also known as the Muffin-tin (MT) approximation (**Figure 2.2**). In all-electron scheme, the idea is to consider a basis set where core wave functions are expanded in terms of atomic orbitals and the valence region wave functions expanded in terms of plane waves, having the constraint of coinciding the wave functions at the boundary of the two regions. The method is also known as the Linear Augmented Plane wave method (LPAW) [87]. The MT approximation was frequently used in highly coordinated (metallic) systems, but for covalently bonded systems this approximation leads to inaccuracy in the results. In such cases, the full-potential treatment is essential.

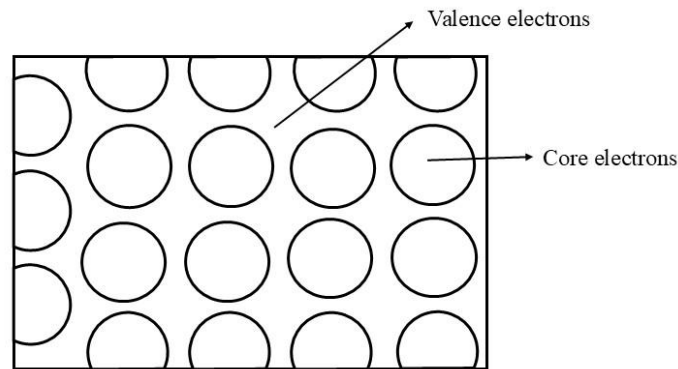


**Figure 2.2** Muffin Tin Approximation

In the full potential approach, the potential and charge density are expanded into the atomic sphere and also in the interstitial region. Thus, they are completely general, so the scheme is treated as full potential calculations [88]:

$$V(r) = \begin{cases} \sum_{LM} V_{LM}(\vec{r}) Y_{LM}(\vec{r}) & \text{Inside sphere} \\ \sum_k V_k \exp(ik \cdot \vec{r}) & \text{Outside sphere} \end{cases} \quad (2.29)$$

In some problems we have employed full potential-LAPW (FPLAPW) method.

#### 2.4.2 Pseudopotential method

Using the pseudopotential (PP) method [89,90], we can reduce a many-electron system to a significant number of electrons that actually participate in bond formation, subsequently reducing the computational cost. Since core electrons are basically localized near the nucleus, they rarely participate while forming solids. In this approach, the nucleus plus core can be considered frozen while only valence electrons are taken into consideration. The chosen wave function used to describe solids may not correspond to the original wave function within the core region, but the pseudo wave function,  $\psi_i^{PP}$ , must coincide with the original wave function beyond a certain cut-off region ( $\vec{r}_c$ ). As per PP approach, KS equations can be rewritten as:

$$\left[ -\frac{1}{2} \nabla^2 + V_{PP}[\rho(\vec{r})] \right] \psi_i^{PP}(\vec{r}) = E_i \psi_i^{PP}(\vec{r}) \quad (2.30)$$

Now the effective potential,  $V_{eff}$ , is replaced by pseudopotential,  $V_{PP}$ , leading to a different charge density having the form:

$$\rho(\vec{r}) = \sum_i |\psi_i^{PP}(\vec{r})|^2 \quad (2.31)$$

#### 2.4.3 Projector Augmented Wave Method

This method was proposed in 1994 by E. Bloch and is a generalization of the LAPW method and pseudopotentials method. This approach is known as the Projector Augmented Wave (PAW) method [91]. The wave function associated with the PAW method has both core ( $\psi_{core}$ ) and valence ( $\psi_{val}$ ) contributions represented by radial and plane wave expansions, respectively. In addition, the overlapping wave function ( $\psi_{net}$ ) is trimmed off to get the final wave function ( $\psi_{PAW}$ ). Thus, it is efficient to calculate exact all-electron properties.

$$\psi_{PAW} = \psi_{val} + \psi_{core} - \psi_{net} \quad (2.32)$$

For some electronic structure computations in this thesis, we employed the PAW technique.

## 2.5 Numerical Aspects

There are several technical parameters, which help to perform exact and efficient DFT calculations, which are discussed below.

### 2.5.1 Energy Cut-off

From Bloch's theorem [92], the solution of a particle moving in a periodic potential is given as

$$\psi_{nk}(\vec{r}) = u_{nk}(\vec{r}) e^{ik \cdot \vec{r}} \quad (2.33)$$

where,  $u_{nk}(\vec{r})$  has periodicity of the crystal lattice, i.e.,

$$u_{nk}(\vec{r}) = u_{nk}(\vec{r} + \vec{R}) \quad (2.34)$$

where,  $\vec{R}$  is lattice translational vector,  $n$  is band index and  $k$  is the wave vector.

Further,  $u_{nk}(\vec{r})$  in terms of Fourier transform of reciprocal space has the form,

$$u_{nk}(\vec{r}) = \sum_G C_{nG}(k) e^{iG \cdot \vec{r}} \quad (2.35)$$

where,  $G$  is the reciprocal lattice vector, and is given by

$$G = n_1 b_1 + n_2 b_2 + n_3 b_3 \quad \forall G \quad (2.36)$$

where,  $G \cdot R = 2\pi m \quad \forall n \in \text{positive integer}$  and  $k$  is wave vector in the first BZ. Thus, equation 2.33 can be redefined as

$$\psi_{nk}(\vec{r}) = \sum C_{n,k+G}(k) e^{i(k+G) \cdot \vec{r}} \quad (2.37)$$

which are called plane wave basis set.

An infinite number of plane waves are required to completely map the whole solid, which is computationally not feasible. This can be avoided by limiting the number of plane waves by defining a cut-off energy parameter [93]. The kinetic energy associated with the plane waves can be expressed as:

$$E_{kin} = \frac{\hbar^2 |k + G|^2}{2m} \quad (2.38)$$

Since, the solutions with lower kinetic energy are more significant than those with higher kinetic energy, we can narrow down the infinite plane waves to a practical limit by introducing cut-off kinetic energy  $E_{cut-off}$

$$\frac{\hbar^2 |k + G|^2}{2m} \leq E_{cut-off} \quad (2.39)$$

where

$$E_{cut-off} = \frac{\hbar^2 G_{cut}^2}{2m} \quad (2.40)$$

and the equation 2.37 becomes:

$$\psi_{nk}(\vec{r}) = \sum_{G+k < G_{cut}} C_{k+G} e^{i(k+G) \cdot \vec{r}} \quad (2.41)$$

This  $E_{cut-off}$  is used as an input parameter while optimizing a particular structure.

### 2.5.2 $k$ -mesh Sampling

A crystalline solid has a periodic arrangement of atoms and is made of unit cells. To deal with the entire solid, first, it is converted to a supercell containing multiple unit cells. The periodic boundary conditions are then used to expand the supercell to infinity, which is then converted into reciprocal space confined within the first Brillouin zone (BZ). In DFT calculations BZ reduces the whole deal of work to integrals of the form

$$g = \frac{V_{cell}}{(2\pi)^3} \int g(k) dk \quad (2.42)$$

where the integral on R.H.S. is defined in reciprocal space that integrates over only possible  $k$  values in the BZ [93]. Monkhorst and Pack given a scheme that generates special  $k$  points in the irreducible BZ (IBZ). IBZ maps the entire solid with the help of symmetry operations, allowing us to reduce the BZ further [94]. The points in an IBZ can be represented by  $k$ -vectors, leading to an infinite number of wave functions. Every  $k$ -point carries information about the wave vector's magnitude, direction, and kinetic energy at that particular point.

## 2.6 Transport in Solids

### 2.6.1 Boltzmann Transport Equation

Boltzmann Transport equation (BTE), a semiclassical approach is a useful technique to gain insights into the charge and heat transport of materials. BTE describes the time evolution of the distribution function  $f(r, k, t)$ , which represents the probability of finding a particle at position  $r$  with wavevector  $k$  at time  $t$ . The total time derivative of  $f(r, k, t)$  is given as

$$\frac{df}{dt} = \frac{\partial f}{\partial t} + \frac{\partial f}{\partial r} \frac{\partial r}{\partial t} + \frac{\partial f}{\partial k} \frac{\partial k}{\partial t} \quad (2.43)$$

where  $\partial r/\partial t$  and  $\hbar \partial k/\partial t$ , respectively, are the velocity ( $v$ ) and the external force ( $F$ ) acting on the particle. Based upon the reasonable assumption that the  $v$  and  $F$  are only related to  $k$  and  $r$ , respectively, we can write

$$\frac{df}{dt} = \frac{\partial f}{\partial t} + \frac{\partial f}{\partial r} v(k) + \frac{\partial f}{\partial k} \frac{F(r)}{\hbar} \quad (2.44)$$

If the scattering between different electronic states is the only mechanism to balance the distribution function change due to external force and electron diffusion, the equation takes the form

$$\left. \frac{\partial f}{\partial t} \right|_{scatt} = \frac{\partial f}{\partial t} + \frac{\partial f}{\partial r} v(k) + \frac{\partial f}{\partial k} \frac{F(r)}{\hbar} \quad (2.45)$$

For an electronic system, the Fermi-Dirac distribution at equilibrium is,

$$f_0 = \frac{1}{\exp\{[E_k - \mu]/k_B T\} + 1} \quad (2.46)$$

where  $E_k$  describes the energy band for the electrons and holes, and  $\mu$  is the chemical potential. At weak  $E$  the distribution function  $f$  is close to  $f_0$ ; therefore, we assume that  $f$  like  $f_0$  depends only on the wavevector, and we can neglect the first and second term on right-hand side of the equation 2.45. For charge transport,  $F(r) = -e_0 E$ , where  $E$  is the electric field. Considering the group velocity  $v(k) = 1/\hbar \times \partial E_k / \partial k$  the equation takes the form

$$\left. \frac{\partial f}{\partial t} \right|_{scatt} = -e_0 E v(k) \frac{\partial f}{\partial \mathcal{E}} \approx -e_0 E v(k) \frac{\partial f_0}{\partial \mathcal{E}} \quad (2.47)$$

This term deals with the shifting of electrons from  $k$  to  $k-k'$  state due to scattering mechanisms. If the scattering rate of moving from  $k$  state to an empty  $k'$  state is  $W_{k-k'}$ , the electron distribution function due to scattering can be expressed as:

$$\left. \frac{\partial f}{\partial t} \right|_{scatt} = \int \left[ f(k') (1-f(k)) W_{k-k'} - f(k) (1-f(k')) W_{k-k'} \right] \frac{d^3 k'}{(2\pi)^3} \quad (2.48)$$

Under the relaxation time approximation (RTA) the scattering term can be expressed as

$$\left. \frac{df}{dt} \right|_{scatt} = -\frac{f(k) - f_0(k)}{\tau(k)} \quad (2.49)$$

where  $\tau(k)$  is the relaxation time, which is defined as the typical time for a system to return to the equilibrium state. This solution forms the foundation for calculating electronic and phonon transport properties.

### 2.6.2 Electronic Transport

In order to calculate transport phenomena, which occur at the electronic level, a model of the transport process is needed to evaluate the transport coefficient. The transport coefficients can be obtained by solving the current density equation, the equation for electric current density ( $J_e$ ) and heat current density due to electrons ( $J_Q$ ) can be written as

$$J_e = \frac{2e}{(2\pi)^3} \int v(k) f(k) dk \quad (2.50)$$

$$J_Q = \frac{2}{(2\pi)^3} \int v(k) [E_k - \mu] f(k) dk \quad (2.51)$$

On substituting the distribution function expression, the above integral becomes:

$$J_e = \frac{2e}{(2\pi)^3} \int v^2(k) \tau(k) \left( \frac{-\partial f_0}{\partial E_k} \right) \left[ eE - \nabla \mu + \frac{E_k - \mu}{T} (-\nabla T) \right] dk = e^2 I_0 E + e \frac{I_1}{T} (-\nabla T) \quad (2.52)$$

$$J_Q = \frac{2}{(2\pi)^3} \int v^2(k) \tau(k) \left( \frac{-\partial f_0}{\partial E_k} \right) \left[ eE - \nabla \mu + \frac{E_k - \mu}{T} (-\nabla T) \right] [E_k - \mu] dk = e I_1 E + e \frac{I_2}{T} (-\nabla T) \quad (2.53)$$

Where,  $I$  is the response function defined as:

$$I_n = \frac{1}{4} \pi^3 \int v^2(k) \tau(k) \left( \frac{-\partial f_0}{\partial E_k} \right) [E_k - \mu]^n dk \quad (2.54)$$

This response function is used to determine different TE parameters of the system as discussed below:

TE transport coefficients have been discussed in Chapter 1. Here, we will see how they are related to the above response functions.

**Thermal conductivity:** When no electric field is applied i.e.,  $E = 0$  the thermal conductivity,  $\kappa$  can be defined by the relation between the heat current density and the temperature gradient:  $J_Q = -\kappa \nabla T$ . Thus, from equations 2.52 and 2.53,  $\kappa = I_2 T$ .

**Electrical conductivity:** Under zero temperature gradient ( $\nabla T = 0$ ) electrical conductivity is defined as the ratio of electric current density to the electric field generated due to voltage gradient:  $J_e = \sigma E$ . Thus, from equations 2.52 and 2.53 we get  $\sigma = e^2 I_0$ .

**Seebeck coefficient:** It is a measure of the open circuit voltage across the semiconductor that has a temperature gradient. So, when,  $J_e = 0$ ,  $S = -V_{oc}/\nabla T$ . This gives  $S = I_1/II_0$ . This becomes more prominent in materials having the asymmetric DOS around the Fermi level.

We have used a semiclassical approach based on solving the BTE within the relaxation time approximation to obtain the above-mentioned transport coefficients. This formalism is implemented in BoltzTraP [95], and in a few chapters we used the latest version BoltzTraP2 [96]; we get  $\sigma$  and  $\kappa_e$  in terms of relaxation time as:  $\sigma/\tau$  and  $\kappa_e/\tau$ . The normally adopted value of  $\tau$  is in the order of  $10^{-14}$  s, but the actual value might vary depending upon the material. So, it is important to calculate  $\tau$  for more accuracy, which affects the results of  $PF$  and  $TE$  FOM, etc.

### 2.6.2.1 Deformation Potential Theory

Deformation potential theory (DPT) was first proposed by Bardeen and Shockley to investigate the role of acoustic phonons on carrier mobilities in semiconductors like Si, Ge, and Te [97]. DPT is a band model that includes only the lattice scattering by the acoustic deformation potential (ADP) because the primary scattering comes from low-frequency acoustic phonons, and the scattering can be approximated by uniform deformation. It is based on the BTE and can be simplified using effective mass approximation; then, one can derive the mobility formula for both 3D and low-dimensional materials. The parameters that are in the mobility formula can be calculated from the first-principles calculations.

Using the effective mass approximation the mobility in the 2D and 3D cases is given as

$$\mu_{2D} = \frac{2e_0 \hbar^3 C_{2D}}{3k_B T m^{*2} 2E_d^2} \quad (2.55)$$



$$\mu_{3D} = \frac{2(2\pi)^{1/2} e_0 \hbar^4 C_{3D}}{3(k_B T)^{3/2} m^{*5/2} E_d^2} \quad (2.56)$$

Where  $C$  is the Elastic modulus of a uniformly deformed crystal,  $m^*$  is effective mass,  $T$  is temperature,  $e$  is the electronic charge  $k_B$  is Boltzmann's constant, and  $E$  is the deformation potential constant.

### 2.6.3 Phonon Transport

The performance of TE materials not only depends upon electronic transport properties but also on the lattice transport properties of the material. Therefore, understanding the transport by lattice vibrations is imperative to design high efficiency TE devices. Under non-equilibrium conditions, the distribution of phonons deviates from its distribution at equilibrium conditions. The transport of phonons is evaluated using the Boltzmann transport formalism. The thermal conductivity calculations are done once the phonon modes are computed, and force constants are calculated using the finite displacement method and density functional perturbation theory (DFPT). In the finite displacement approach, the first-principles calculations on atoms in supercell after introducing finite atomic displacements. Then force constants are calculated from the dataset displacement and forces from any phonon code. On the other hand, in DFPT, direct calculation of force constants at arbitrary wave vector by solving the variation of KS orbitals is obtained followed by the interpolation of force constant in reciprocal space by Fourier transform. The phonon dispersion curve, which is the relation between the phonon frequency and wave vector is thus obtained by either of these methods. All the thermal properties are obtained from this relation and the slope of this dispersion relation gives the phonon group velocity. There is a wide variety of phonon calculation codes, e.g., Phonopy [98], PHONON, ALAMODE [99]. The phonon dispersion curves exhibit two types of phonon modes: acoustic and optical. The contribution to the lattice thermal conductivity mainly comes from the acoustic phonon modes, possessing much higher phonon group velocity. Once we obtain the phonon band structure, the lattice thermal conductivity can be calculated using the relaxation time approximation and iterative method. There are several software packages for lattice thermal conductivity calculations, e.g., Phono3py [100], ShengBTE [101], almaBTE [102], and ALAMODE [99]. In our calculations, we have used the Phono3py package for lattice transport property calculations.

We obtained lattice thermal conductivity, using the single-mode relaxation-time (SMRT) approximation and a full solution of the linearized phonon Boltzmann equation (LBTE) by

performing first-principles anharmonic lattice dynamics calculations. Within the SMRT method,  $\kappa_l$  is calculated as a sum of contributions from individual phonon modes  $\lambda$  according to the equation [100]:

$$\kappa_l = \frac{1}{NV} \sum_{\lambda} C_{\lambda} v_{\lambda} \otimes v_{\lambda} \tau_{\lambda} \quad (2.57)$$

where  $V$  is the volume of the unit cell and  $N$  is the number of phonons wavevectors,  $C_{\lambda}$  are the heat capacities,  $v_{\lambda} \otimes v_{\lambda}$  are the tensor products of the group velocities, and  $\tau_{\lambda}$  are the phonon lifetimes. Since the equation is the simple summation over phonon modes, the lattice thermal conductivity calculation is obviously analyzed in terms of phonon modes. Another method is the direct solution of LBTE, which was developed by Chaput. [103] In this method, huge memory and computation time are required due to the larger matrix size.

## 2.7 Ab initio Molecular Dynamics

The success of DFT can be credited to its scalability over the different systems and sizes and its remarkable accuracy in finding microscopic ground state properties. Then, a question arises: is it possible to study the temperature effect in the system? As a solution, ab initio molecular dynamics (AIMD) simulations are successfully utilized to understand the temperature effect and structural stability. In classical molecular dynamics, the system is typically assumed to consist of rigid and massive point-like nuclei, which are subject to forces derived from empirically devised effective potentials. Then one can obtain the microscopic trajectory of each atom in the system being studied, integrating Newton's equation of motion. AIMD is based on the same consideration, except that the forces calculations are based on electron density obtained by DFT, making this method more accurate. In the present thesis, we carried out AIMD simulations to investigate the structural properties and stability of the material at or above room temperature. Stability is confirmed if the total energy and temperature fluctuate within a small range over time. AIMD simulations are performed under two ensembles. One is a microcanonical ensemble ( $NVE$ ), where the number of particles ( $N$ ), volume ( $V$ ), and energy ( $E$ ) remain constant. The simulation generates spread-out configurations across the phase space, all of which reside on the constant  $E$  hypersurface. Another is the canonical ensemble ( $NVT$ ), where  $N$ ,  $V$ , and the thermal averages are computed under a constant temperature ( $T$ ). In the present thesis, we employed the AIMD ensemble to investigate the structural properties and stability of the material at or above room temperature. We used the Nose-Hoover thermostat to ensure that the system maintained thermal equilibrium by mimicking the coupling

to an external heat bath. We have used the NVT ensemble in AIMD to calculate the thermal stability of the system at room temperature. Thermal stability is crucial for transport studies, as unstable structures may exhibit artificial transport properties. AIMD validates material feasibility before proceeding to electronic and phonon transport calculations.

## **2.8 Computational Packages**

We have mainly used five packages for the calculations presented in the thesis. Each of these packages are discussed in following sections.

### **2.8.1 WIEN2k**

In 1990, Peter Balaha and his team developed a code based on the full potential linearized augmented plane wave that was known as WIEN2k [17]. In this code, no shape approximations are made and the procedure is basically known as the full potential method. To calculate the material properties, first, we relax the crystal structure and optimize the lattice parameters. The RMT and cutoff energy are chosen as there is no charge leakage. The appropriate energy convergence and cutoff energy of the core and valance were fixed before the SCF calculations. The SCF calculations contain all the necessary information regarding total energy, Fermi energy, the distance between the atoms, the charge on the atomic sphere, etc. The SCF cycle consists of the following steps:

LAPW0: generate potential from density

LAPW1: calculates valance bands

LAPW2: compute valance density from the eigen values

LCORE: computes core states and densities

MIXER: mixes input and output densities

### **2.8.2 Vienna Ab initio Simulation Package**

In 1998, George Kresse and his team developed a DFT based package called the Vienna Ab initio Simulation Package (VASP) [104,105]. It uses plane-wave basis sets to represent KS orbitals and the PAW approach to account for the external interactions between electrons and nuclei. In the present thesis, VASP is used to relax the crystal structures, optimize the lattice parameter, determine force constants required in Phonopy and Phono3py, determine the electronic band structures, the density of state calculations, and many more. VASP mainly consists of four input files, which are as follows:

1. **INCAR:** It is a basic “to-do” file, which tells what to do and how to do.
2. **POSCAR:** It involves the geometrical details of the crystal structure, such as the lattice vectors, types of atoms, and their atomic positions.
3. **KPOINTS:** The k-points (Bloch vectors) required to sample the Brillouin zone for the computation are specified in the KPOINTS file. For band-structure calculations, it contains the high symmetry points along which bands are to be plotted.
4. **POTCAR:** This file contains the potential information of every element of the compound. The POTCAR file of the compound is generated by concatenating the POTCARs of each atomic species which is different for different functionals.

### 2.8.3 BoltzTraP

Madsen et al. developed the BoltzTraP package to calculate the Boltzmann Transport Properties [95]. It is based on a semi-classical approach to calculate the electronic transport coefficients such as  $S$ ,  $\sigma$ , and  $\kappa_e$ . It is used as an interface with DFT-based codes such as WIEN2k [95], VASP [105]. In the present thesis, we have used BoltzTraP interfaced with WIEN2k. Since BoltzTraP was originally developed and interfaced with WIEN2k, they share some common input files.

The required files are:

- **Case.intrans:** It contains the information of all the input parameters required to run the transport calculations, such as the temperature range, Fermi energy, energy cutoff, etc. Here, Case is the name of the directory.
- **Case.struct:** The crystal structure information is provided in Case.struct file.
- **Case.energy:** It includes the band structure information needed to run Boltz-TraP code.

### 2.8.4 Phonopy

Before computing any material property using DFT, one must ensure the proposed crystal structure’s dynamical stability, which is carried out using the Phonopy package [98]. It deals with the atom’s response with a thermal perturbation introduced in the system by the supercell approach. This software is based on harmonic and quasi-harmonic approximation included in the density functional perturbation theory (DFPT). The first and second-order force constants are determined using VASP and later are used as an input to find the phonon frequencies at the desired q-points using Phonopy as a post-processing tool.

### **2.8.5 Phono3py**

The phonon-phonon coupling is realized using the Phono3py package [100], which is based on anharmonic lattice approximations. It uses the supercell approach to create displacements in the input structure and then can be used to determine different physical properties related to the phonon-phonon interactions. In our work, we used Phono3py to calculate the lattice thermal conductivity of the half Heusler compounds. The force constants for the supercells are calculated using VASP, which are then treated as inputs to calculate lattice thermal conductivity.

## **2.9 Summary**

In this chapter, we discussed the basic methodology to solve the many-body problem, which further can be extended to condensed matter systems. We mainly emphasize discussing DFT (a first-principles technique) and the associated parameters on which the whole calculations rely. We have also discussed Boltzmann transport theory from which we obtained electronic and thermal transport properties. We have also discussed the details of the terms needed to calculate the TE properties of any system. At the end, we presented a brief discussion of the packages employed to calculate the various electronic and thermal properties mentioned in the thesis.

# CHAPTER 3: THERMOELECTRIC PROPERTIES OF *p*-type $\text{RbZn}_4\text{P}_3$ AND *n*-type $\text{RbGaSb}_2$ ZINTL COMPOUNDS

---

## 3.1 Introduction

In Chapter 1, we briefly discussed the concept of TEs. To realize its practicality and applications, we need to have a high figure of merit. But, it is difficult to achieve high  $ZT$  due to the interdependence of transport parameters. However, the unique properties of some selected efficient TE materials pave a new path to overcome the problems. As discussed in Chapter 1, Zintl compounds are suitable candidates for thermoelectricity. Zintl compounds have been studied for the last few years to achieve high TE performance. These materials offer an excellent balance between large  $PF$  and low thermal conductivity, resulting in impressive TE performance [41,106]. Furthermore, their chemical tunability, complex bonding patterns, low bandgap, and strong anharmonicity make them suitable TE hosts [40,42]. In these compounds, electropositive cations such as alkali and alkaline earth metals donate their valence electrons to the anionic network, which further forms covalent bonding according to the Zintl-Klemm concept to satisfy the valence requirement [39].

A broad class of Zintl compounds, such as binary, ternary, and quaternary, has been studied experimentally and theoretically [43–46]. Among these ternary compounds  $\text{M}_2\text{Zn}_5\text{As}_4$  ( $\text{M} = \text{K}, \text{Rb}$ ) [44], and  $\text{Sr}_3\text{GaSb}_3$ , [45] etc., exhibit good TE performance. A distinguishable characteristic of these TE materials is that they are natively *p*-type semiconductors having moderate to high hole concentrations due to self-doping [107]. It has been seen that As and Sb are used as major, and P is used as the minor substituting element [43,44,107]. Recent studies show that P-based Zintl compounds, such as  $\text{NaSnP}$ ,  $\text{CaIn}_2\text{P}_2$ ,  $\text{Ba}_3\text{Al}_3\text{P}_5$ , and  $\text{Ba}_3\text{Ga}_3\text{P}_5$  have tuneable effective mass and carrier concentration with low lattice thermal conductivity and exhibit intriguing TE properties [108–110]. Experimentally synthesized *p*-type  $\text{RbZn}_4\text{As}_3$  shows a high Seebeck Coefficient of about  $800 \mu\text{VK}^{-1}$  and very high room temperature resistivity [111]. So, we envisaged that replacing As with P in  $\text{RbZn}_4\text{As}_3$  can lead to better TE properties.

The versatile nature of Zintl compounds occurs both in the *n*-type and *p*-type regimes, which makes the widespread use of this in TE applications. Most of the Zintl phases reported in the

literature are *p*-type; however, recently, Gorai et al. [112] computationally predicted ABX *n*-type Zintl compounds. It has been also predicted *n*-type exhibits comparable or even better TE properties than their *p*-type counterparts. Wang et al. [113] experimentally found RbGaSb<sub>2</sub> as an *n*-type semiconductor having negative thermopower at room temperature. They suggested that the enhancement in the carrier concentration effectively boosts the TE performance. So, motivated by the recent experimental synthesis of ternary antimonide RbGaSb<sub>2</sub> [113], we examine the structural, electronic, and transport properties.

In this chapter, two Rb-based Zintl compounds, RbZn<sub>4</sub>P<sub>3</sub> and RbGaSb<sub>2</sub>, are investigated. Interestingly, RbZn<sub>4</sub>P<sub>3</sub> shows good *p*-type TE performance, while RbGaSb<sub>2</sub> exhibits strong *n*-type behavior. This makes them a valuable pair for developing efficient TE modules, which require both *p*-type and *n*-type materials. By comparing their structures and electronic and transport properties, this chapter aims to understand what leads to their different behaviors and how such materials can be designed for better energy conversion efficiency.

### 3.2 Computational Details

The structural, electronic, and TE properties of both compounds were carried out within the framework of DFT using Full potential linearized augmented plane wave as implemented in WIEN2k software [88]. Their structural optimization was carried out by the GGA-PBE [82]. For Brillouin zone sampling, we have used a 20×20×10 and 17×17×9 k-point mesh for RbZn<sub>4</sub>P<sub>3</sub> and RbGaSb<sub>2</sub>, respectively. The number of plane waves in the interstitial region and cut-off energy of core and valence states were set as  $R_{MT} \times K_{max} = 7$  and -6 Ry, respectively. Kohn-Sham equations were solved self-consistently with an energy convergence of 0.0001 Ry. As in most cases, GGA underestimates the band gaps of semiconductors; therefore, we employed TB-mBJ approach to calculate the electronic band structure and transport properties [114]. The thermoelectric properties were calculated by solving the BTE under the CRTA and RBA as implemented in the BoltzTraP code [95]. A denser k-point mesh was used for this calculation. To analyze the extent of decoupling between  $S$  and  $\sigma/\tau$ , we have calculated EFF using transM code for the RbZn<sub>4</sub>P<sub>3</sub> compound [115]. We have obtained the elastic constants of RbZn<sub>4</sub>P<sub>3</sub> using the stress-strain relationship using VASP [105]. To check the dynamical stability, the DFPT was used to calculate the phonon dispersion of RbZn<sub>4</sub>P<sub>3</sub> by building a 3×3×1 supercell and using a 9×9×5 k-point mesh employing the Phonopy code [98]. The Phono3py code [100] is used for the computation of anharmonic third-order interatomic force constants of RbGaSb<sub>2</sub>, taking interactions up to the fifth nearest neighbour.

### 3.3 Results and Discussion

#### 3.3.1 Structural Properties

RbZn<sub>4</sub>P<sub>3</sub> Zintl compound crystallizes in the tetragonal structure having space group  $P4/mmm$  and has a framework of  $[Zn_4P_3]^-$  layers with  $Rb^+$  atoms between the layers. The unit cell of the RbZn<sub>4</sub>P<sub>3</sub> compound is shown in **Figure 3.1 (a)**. The Rb atom occupies the Wyckoff position  $1b$  (0, 0, 1/2), Zn and P1, P2 atoms are located at  $4i$  (0, 1/2, 0.1577) and  $2h$  (1/2, 1/2, 0.2864),  $1a$  (0, 0, 0), respectively. Each unit cell is made up of four distinct ions due to the varied locations of the Phosphorus atoms. We have performed structural optimization of this compound and calculated its equilibrium lattice parameters. The optimized structural parameters and bond length are listed in **Table 3.1**, which are in good agreement with the available experimental results [111].

**Table 3.1** Calculated structural parameters ( $a$  and  $c$  in Å and  $V$  in Å<sup>3</sup>) and bond lengths (in Å) of RbZn<sub>4</sub>P<sub>3</sub> in comparison with available experimental values.

	Structural Parameters			Bond lengths (Å)			
	$a$ (Å)	$c$ (Å)	$V$ (Å <sup>3</sup> )	Rb-Zn	Rb-P1	Zn-P1	Zn-P2
<b>Present work</b>	4.080	10.230	170.41	4.068	3.635	2.423	2.591
<b>Expt. Work</b> [111]	4.059	10.069	165.92	3.999	3.586	2.408	2.577

On the other hand, RbGaSb<sub>2</sub> ternary antimonide Zintl phase crystallizes in a tetragonal structure with space group  $P4_2/nmc$  (space group no. 137). The crystal structure of the investigated compound (as shown in **Figure 3.1 (b)**) comprises two-dimensional  $[GaSb_2]^-$  tetrahedral layers separated by layer of  $Rb^+$  cations. There are two  $[GaSb_2]^-$  layers in the unit cell that are shifted along the  $[010]$  direction. This structure results in a high degree of anisotropy. The calculated total energy versus deviation from the experimental  $c/a$  ratio is shown in **Figure 3.2**. The initial value of  $c/a$  ratio is taken from experimental data (1.857), and the optimized value is 1.841. The optimized crystal structure parameters and comparison with the experimental ones are presented in **Table 3.2**. The optimized structure is further used to evaluate the electronic and transport properties.



**Table 3.2** Calculated lattice parameters, volume, and total energy.

	$a=b$ (Å)	$c$ (Å)	Volume (Å <sup>3</sup> )	Total energy (Ry)
<b>This work</b>	8.359	15.390	1075.56	-286007.0047
<b>Exp. [113]</b>	8.335	15.483	1075.60	-

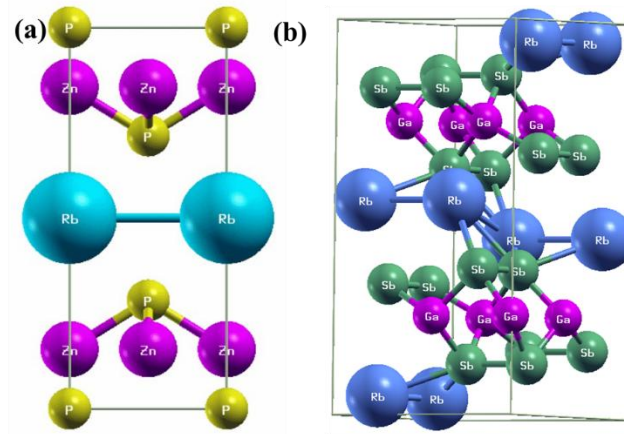


**Figure 3.1** Crystal structure of (a) RbZn<sub>4</sub>P<sub>3</sub> and (b) RaGaSb<sub>2</sub> compound

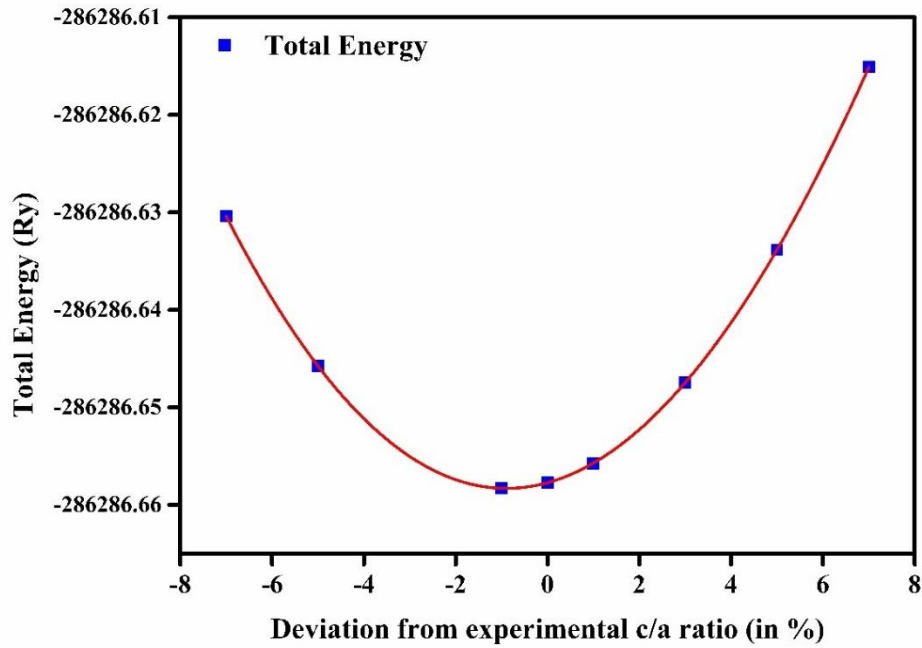


**Figure 3.2** The optimization of total energy as a function of deviation from experimental  $c/a$  ratio. The curve is fitted up to a fourth-order polynomial

### 3.3.2 Stability of RbZn<sub>4</sub>P<sub>3</sub> compound

#### 3.3.2.1 Thermodynamical

To check the stability of the compound, we have calculated the formation energy  $E_{for}$  using the following equation

$$E_{for} = \frac{[E_{RbZn_4P_3} - (E_{Rb} - 4E_{Zn} - 3E_P)]}{N} \quad (3.1)$$

where  $E_{RbZn_4P_3}$  is the ground state energy of RbZn<sub>4</sub>P<sub>3</sub>,  $N$  is the total number of atoms in the unit cell, and  $E_{Rb}$ ,  $E_{Zn}$ , and  $E_P$ , respectively, are the total energy per atom for Rb, Zn, and P in bulk form. The calculated  $E_{for}$  is found to be -1.9108 eV/atom, indicating that this compound is thermodynamically stable.

#### 3.3.2.2 Dynamical

Further to determine the dynamical stability, we have obtained the phonon dispersion along with R- $\Gamma$ -X-M- $\Gamma$  high symmetry direction in the Brillouin zone, which is presented in **Figure 3.3 (a)** using the DFPT approach [98]. Since there are eight atoms per unit cell in RbZn<sub>4</sub>P<sub>3</sub>, hence there are total 24 phonon branches in the phonon dispersion curve, out of which three are acoustic, and 21 are optical branches. The lower branches in the dispersion spectra correspond to acoustic branches, and the upper branches represent the optical branches with the corresponding frequency range (0-25 cm<sup>-1</sup>), and (25-144 cm<sup>-1</sup>), respectively. It can be seen that there are no negative frequencies, thereby confirming that the tetragonal phase of the RbZn<sub>4</sub>P<sub>3</sub> compound is dynamically stable. Also, no phonon gap between optical and acoustic branches is observed, indicating a strong coupling of acoustic-optical phonon modes, which might provide a material with low lattice thermal conductivity [116]. The calculated total and projected phonon density of states are also shown in **Figure 3.3 (b)**. It can be seen that the projected phonon density of states in the uppermost optical phonon density region is mainly contributed by the vibrational motion of P-atoms, whilst in the lower optical region, the coupled vibrational motion of Rb- and Zn-atoms is dominated.

#### 3.3.2.3 Mechanical

The elastic constants of the tetragonal RbZn<sub>4</sub>P<sub>3</sub> compound have been obtained by stress-strain relationship. Because of its tetragonal symmetry, this compound possesses six independent elastic constants:  $C_{11}$ ,  $C_{12}$ ,  $C_{13}$ ,  $C_{33}$ ,  $C_{44}$ , and  $C_{66}$ , as listed in **Table 3.3**. To check whether this compound is mechanically stable, we need to verify the Born stability criteria given as [117]:

$$C_{11} > 0, C_{33} > 0, C_{44} > 0, C_{66} > 0, (C_{11} - C_{12}) > 0, (C_{11} + C_{33} - 2C_{13}) > 0 \text{ and } (2C_{11} + C_{33} + 2C_{12} + 4C_{13}) > 0 \quad (3.2)$$

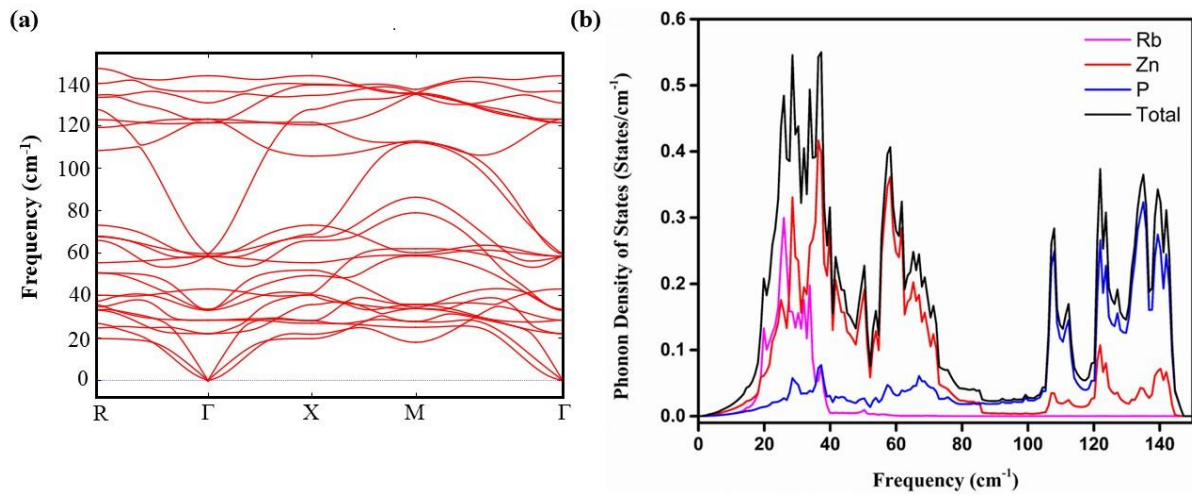


**Figure 3.3** (a) Phonon dispersion curve and (b) phonon density of state of RbZn<sub>4</sub>P<sub>3</sub> compound

**Table 3.3** Calculated elastic coefficients  $C_{ij}$  ( $i, j = 1-6$ ), bulk modulus ( $B$ ), shear modulus ( $G$ ), Young's modulus ( $Y$ ), all in units of GPa, and Poisson ratio ( $\nu$ ).

Parameter	$C_{11}$	$C_{12}$	$C_{13}$	$C_{33}$	$C_{44}$	$C_{66}$	$B$	$G$	$Y$	$\nu$
RbZn <sub>4</sub> P <sub>3</sub>	1017.4	126.3	132.6	500.4	205.5	124.3	350.7	229.1	567.5	0.2
	2	8	6	2	0	0	8	5	3	3

All calculated elastic parameters completely satisfied the Born mechanical stability criteria for tetragonal structure, indicating the mechanical stability of the compound under ambient conditions. Further, we have calculated various mechanical properties such as bulk modulus ( $B$ ), shear modulus ( $G$ ), Young's modulus ( $Y$ ), and Poisson ratio ( $\nu$ ), using the elastic parameters in order to determine physical properties like stiffness, strength, hardness and ductile or brittleness behaviour of RbZn<sub>4</sub>P<sub>3</sub>. These mechanical parameter values are also reported in Table 2, along with elastic constants. We have used the Voigt-Reuss-Hill approximation (VRH) to estimate  $B$  and  $G$  [118]. The mechanical stability is dominated by shear modulus as  $G$  is smaller than  $B$ . Young's modulus provides the degree of stiffness of a compound; the higher value of  $Y$  indicates that RbZn<sub>4</sub>P<sub>3</sub> is stiffer. The value of Poisson's ratio is less than the threshold value ( $\nu = 0.26$ ), which predicts the brittle nature of RbZn<sub>4</sub>P<sub>3</sub> [119]. Apart from these, we have also

determined Debye temperature ( $\theta_D$ ), an essential parameter for calculating lattice thermal conductivity. It is linked to elastic constants via average sound velocity ( $v_m$ ) as:

$$\theta_D = (h/k_B) \left[ \left( \frac{3n}{4\pi} \right) (N_A \rho / M) \right]^{\frac{1}{3}} v_m \quad (3.3)$$

where  $h$  is Planck's constant,  $k_B$  is Boltzmann's constant,  $N_A$  is Avogadro's number,  $n$  is the number of atoms in the unit cell,  $\rho$  is the density and  $M$  is the molecular weight of the compound. The average sound velocity is computed using transverse ( $v_t$ ) and longitudinal sound velocity ( $v_l$ ) using elastic constants as expressed by the following equations [120]:

$$v_m = \left[ \frac{1}{3} \left( \frac{2}{v_t^3} + \frac{1}{v_l^3} \right) \right]^{-\frac{1}{3}} \quad (3.4)$$

$$v_l = \sqrt{\frac{G}{\rho}} \quad (3.5)$$

$$v_t = \sqrt{\frac{3B + 4G}{\rho}} \quad (3.6)$$

The obtained values of  $v_l$ ,  $v_t$ ,  $v_m$ , and  $\theta_D$  for  $\text{RbZn}_4\text{P}_3$  are  $7.30 \text{ kms}^{-1}$ ,  $12.36 \text{ kms}^{-1}$ ,  $8.09 \text{ kms}^{-1}$ , and  $870.03 \text{ K}$ , respectively.

### 3.3.3 Electronic Structure Properties

The electronic band structure along with the density of states (DOS) of the compound is calculated using the TB-mBJ approach and shown in **Figure 3.4**. Our calculations have predicted a direct bandgap of  $1.02 \text{ eV}$  at the  $\Gamma$ -point. The projected density of states (PDOS) shows that the P atom contributes the most to the valence band (VB), followed by a minor contribution from the Zn atom and a very feeble contribution from the Rb atom. In the conduction band (CB),  $s$ -orbitals of P atom are dominant from  $1.5 \text{ eV}$ – $3.5 \text{ eV}$ , and above this energy range, its  $p$ -orbital is prevalent over the Zn and Rb atoms as presented in **Figure 3.5**. Therefore, we can see clearly from PDOS that the top of the VB is formed mainly by P- $p$  and Zn- $p$ ,  $s$  orbitals, and the bottom of the conduction band is composed of P- $s$  and Zn- $p$  orbitals. We obtained that the sharp peak at the top of the VB, which indicates that the large Seebeck coefficient and hence the good TE transport properties can be observed for the  $p$ -type considered material.

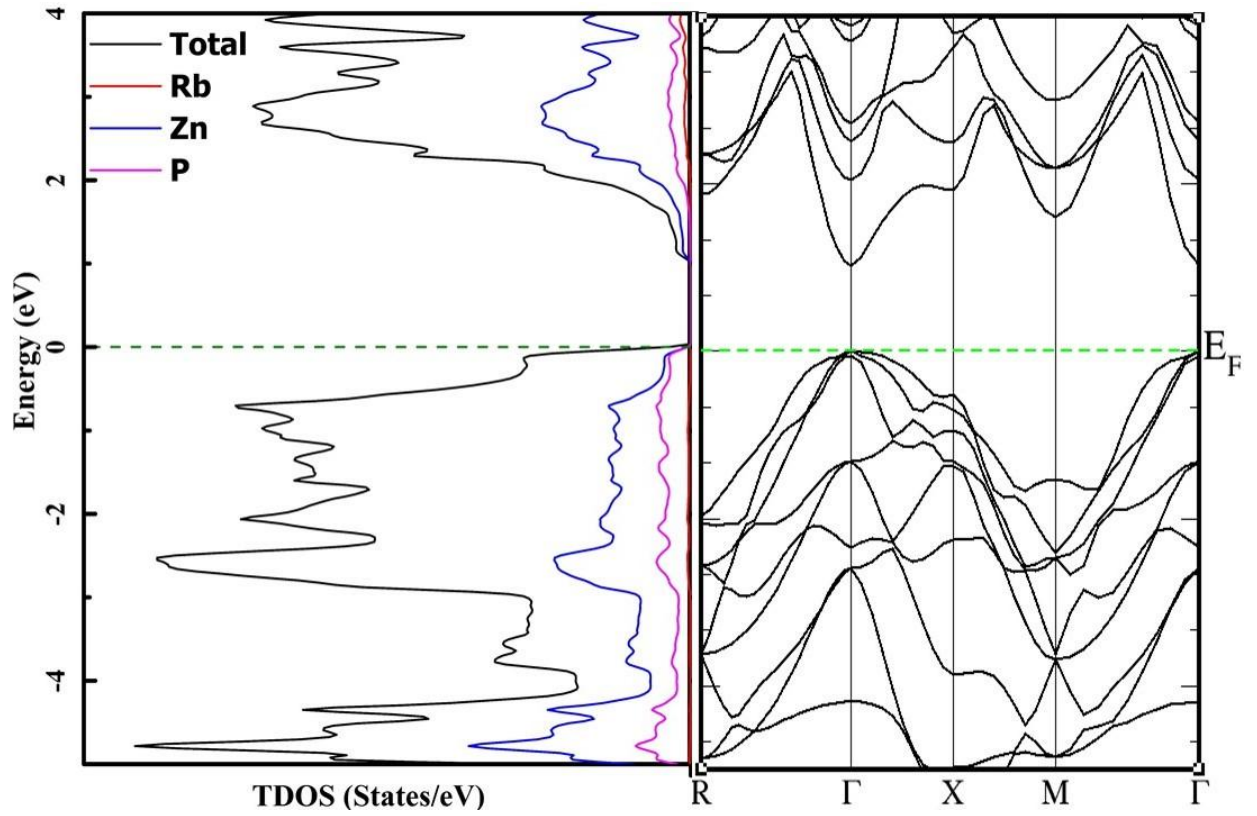


**Figure 3.4** The electronic band structure and DOS of  $\text{RbZn}_4\text{P}_3$  calculated within TB-mBJ approximation. The Fermi level is set to 0 eV

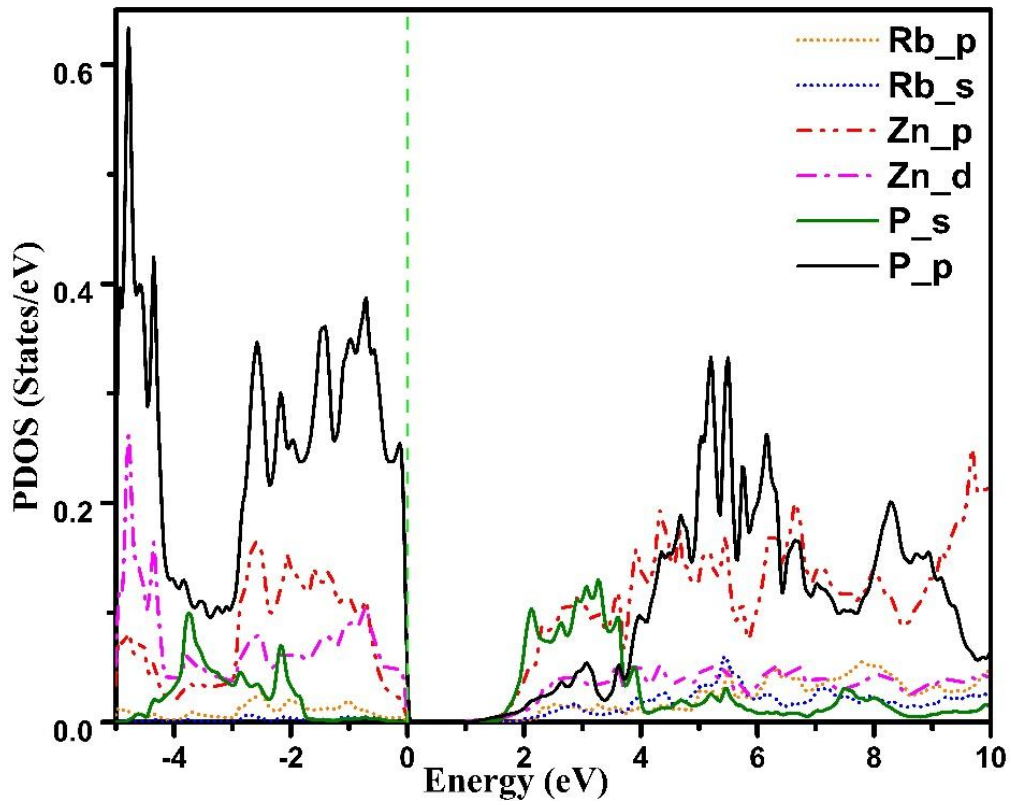


**Figure 3.5** The calculated projected DOS of  $\text{RbZn}_4\text{P}_3$  within TB-mBJ approximation. The Fermi level is set to 0 eV

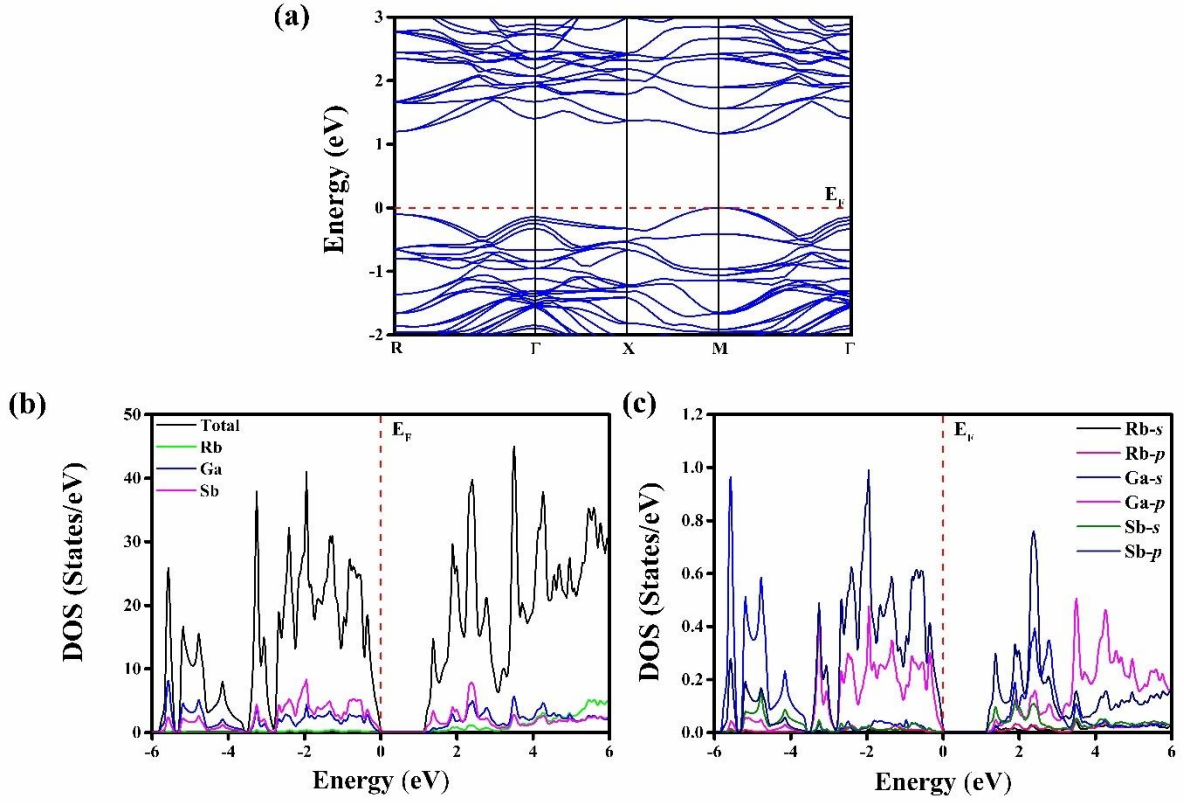


**Figure 3.6** Calculated (a) electronic band structure (b) and (c) density of states of RbGaSb<sub>2</sub> using TB-mBJ approximation.

The electronic band structure of RbGaSb<sub>2</sub> obtained using TB-mBJ is shown in **Figure 3.6 (a)**. The conduction band minima (CBM) and the valence band maxima (VBM) are both present at M, indicating a direct band gap. The calculated energy band gap of 1.17 eV is close to previously estimated value of 1.0 eV. It is experimentally found that RbGaSb<sub>2</sub> tends to form *n*-type semiconductor near room temperature [113], therefore we only focus on the lower part of CB that can determine the transport properties of *n*-type RbGaSb<sub>2</sub>. The band structure exhibits less dispersion at the M k-point in the lower part of CB, suggesting that the electron effective mass is large and high *S* can be obtained. The density of states is obtained as shown in **Figure 3.6 (b and c)**. Both VB and CB are predominantly contributed by Sb atoms, while negligible contribution of Rb atoms is observed. The sharp peaks are observed at VBM and CBM. Also, the upper part of VB and the lower part of CB are mainly contributed by the *p* orbital of Sb atoms.

Next, we have calculated the charge density (in units of eÅ<sup>-3</sup>) of RbZn<sub>4</sub>P<sub>3</sub> in the (010) plane, which is shown in **Figure 3.7**. The purple color shows the large accumulation of electrons in the region, while the red color shows the charge depleted region. The charge density analysis shows the transfer of electrons among Rb, Zn, and P, which is useful in determining the bonding



properties of the compound [121]. The distribution of valence charge density around the Rb atom shows that it donates its valence electrons to the network  $[\text{Zn}_4\text{P}_3]^-$ , and indicates that balancing of valence charge is maintained as  $(\text{Rb}^+)$ ,  $(\text{Zn}^{2+})$ ,  $(\text{P}^{3-})$  within its configuration, which allows the separation of electron energy bands needed to form a bandgap. Both the VB maxima and CB minima are derived from hybridized P and Zn orbitals, which corresponds to the significant contribution of covalent Zn-P bonds. Therefore, covalent bonds are present in the polyanionic network, which interacts with the electropositive metal cations through ionic bonds. Covalent and ionic bonds coexist in the various Zintl phase compounds [21,44], which is compatible with the bonding picture. As seen in the PDOS, the major contribution of P and Zn atoms is also reflected in the charge density contour plot.

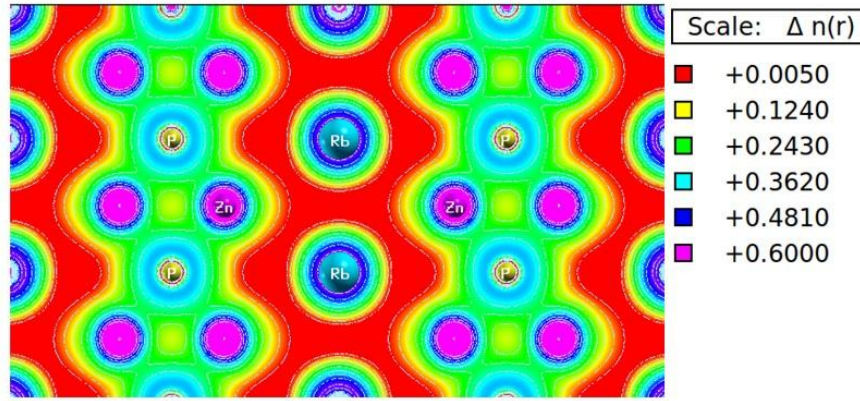


**Figure 3.7** The computed charge density (in units of  $\text{e}\text{\AA}^{-3}$ ) plot of  $\text{RbZn}_4\text{P}_3$  in  $(010)$  plane

### 3.3.4 Transport properties of $\text{RbZn}_4\text{P}_3$

We have used CRTA, which means  $S$  is independent of scattering rate ( $\tau$ ), and RBA, which assumes that doping concentrations and temperature do not affect electronic band structure [95]. We have studied the effect of hole doping concentration and temperature on thermoelectric properties.

The Seebeck coefficient can be expressed as:

$$S = \frac{8\pi^2 k_B^2}{3eh^2} m^* T \left( \frac{\pi}{3n} \right)^{\frac{2}{3}} \quad (3.7)$$

where  $m^*$  is effective mass,  $n$  is the carrier concentration, and  $T$  is the absolute temperature. As the doping concentration of hole ( $n$ ) increases from  $1 \times 10^{18} \text{ cm}^{-3}$  to  $1 \times 10^{21} \text{ cm}^{-3}$ ,  $S$  decreases as depicted in **Figure 3.8 (a)** at different temperatures from 300 K to 700 K. It has been observed that the positive value of Seebeck coefficient sharply decreases with increase in the hole doping concentrations at fixed temperatures. The maximum observed value of  $S$  is  $735.43 \text{ }\mu\text{VK}^{-1}$  at

700 K, 725.75  $\mu\text{VK}^{-1}$  at 600 K, 708.58  $\mu\text{VK}^{-1}$  at 500 K, 683.41  $\mu\text{VK}^{-1}$  at 400 K, and 641.72  $\mu\text{VK}^{-1}$  at 300 K. It implies that for all doping concentrations, the Seebeck coefficient increases as the temperature increases. This shows that the material has *p*-type semiconducting nature. The calculated value of  $S$  for  $\text{RbZn}_4\text{P}_3$  is comparable with the experimentally measured value of a similar Zintl compound [111]. The effective mass of electrons and holes is calculated along  $\Gamma$ -X direction, which is 0.14  $m_e$  in the CB and 0.47  $m_e$  (light hole), 1.31  $m_e$  (heavy hole) in the VB. The high effective mass of holes leads to a high  $S$  value of  $\text{RbZn}_4\text{P}_3$ .

The calculated  $\sigma/\tau$  increases with an increase in hole doping concentration for the entire studied doping range (which as per the relation,  $\sigma = ne\mu$ ) as shown in **Figure 3.8 (b)**. It remains almost constant up to  $1 \times 10^{19} \text{ cm}^{-3}$  and then slightly increases up to  $5 \times 10^{19} \text{ cm}^{-3}$ ; after that, it abruptly increases and reaches a maximum value of  $25.43 \times 10^{18} \Omega^{-1} \text{ m}^{-1} \text{ s}^{-1}$  at concentration  $1 \times 10^{21} \text{ cm}^{-3}$ . The observed value of  $\sigma/\tau$  versus hole concentration is nearly the same for all temperatures, indicating its weak dependence on  $T$ . The electronic contribution to thermal conductivity ( $\kappa_e/\tau$ ) is shown in **Figure 3.8 (c)**. It has a similar behavior to  $\sigma/\tau$ , as  $\kappa_e$  and  $\sigma$  are interrelated by the Wiedemann-Franz law,  $\kappa_e = L\sigma T$  where  $L$  is the Lorentz number, but highly temperature dependent [122].

The variation of  $PF$  for hole doping concentration at different temperatures is shown in **Figure 3.8 (d)**. As carrier concentration increases from  $1 \times 10^{18} \text{ cm}^{-3}$  to  $1 \times 10^{19} \text{ cm}^{-3}$ ,  $PF$  increases slightly first, and after that, it increases sharply for all temperatures and attains a maximum value between  $4 \times 10^{20} \text{ cm}^{-3}$  and  $7 \times 10^{20} \text{ cm}^{-3}$ . The calculated highest values of  $PF$  are  $5.57 \times 10^{11} \text{ Wm}^{-1} \text{ K}^{-2} \text{ s}^{-1}$  at 700 K,  $4.89 \times 10^{11} \text{ Wm}^{-1} \text{ K}^{-2} \text{ s}^{-1}$  at 600 K,  $4.19 \times 10^{11} \text{ Wm}^{-1} \text{ K}^{-2} \text{ s}^{-1}$  at 500 K,  $3.46 \times 10^{11} \text{ Wm}^{-1} \text{ K}^{-2} \text{ s}^{-1}$  at 400 K, and  $2.65 \times 10^{11} \text{ Wm}^{-1} \text{ K}^{-2} \text{ s}^{-1}$  at 300 K. It can be seen that the optimum carrier concentration for  $\text{RbZn}_4\text{P}_3$  is of the order of  $10^{20} \text{ cm}^{-3}$ .

We have computed the electronic fitness function (EFF), using transM code [115], which is given by the formula  $(S^2 \sigma / \tau) (N/V)^{-2/3}$ . Based on the complexity of electronic structure, EFF helps to detect high-performance TE material. As discussed above,  $S$  and  $\sigma/\tau$  are correlated, and the degree of correlation is to be identified in order to manipulate these parameters independently [123,124]. In **Figure 3.9**, we have plotted EFF with hole doping concentration at different temperatures. The maximum observed value is  $6.4 \times 10^{-20} \text{ W}^{5/3} \text{ ms}^{-1/3} \text{ K}^{-2}$  at 700 K for optimum doping concentration ( $1 \times 10^{20} \text{ cm}^{-3}$ ), which indicates that there is a strong decoupling between  $S$  and  $\sigma/\tau$ . The high value of EFF signifies the good TE behaviour of a material.



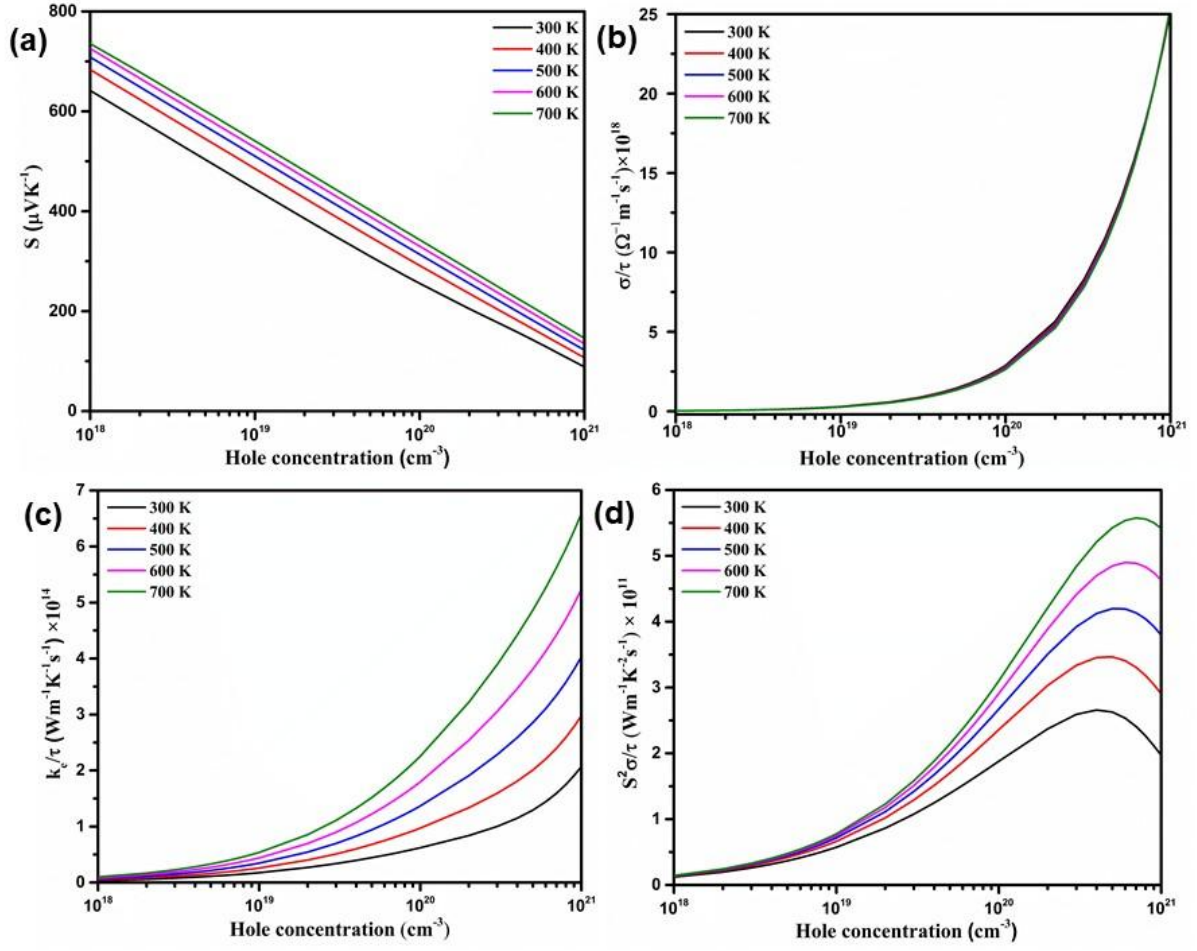


**Figure 3.8** The variation of (a)  $S$  (b)  $\sigma/\tau$  (c)  $\kappa_e/\tau$  and (d)  $S^2\sigma/\tau$  with hole doping concentration for RbZn<sub>4</sub>P<sub>3</sub> at different temperatures.

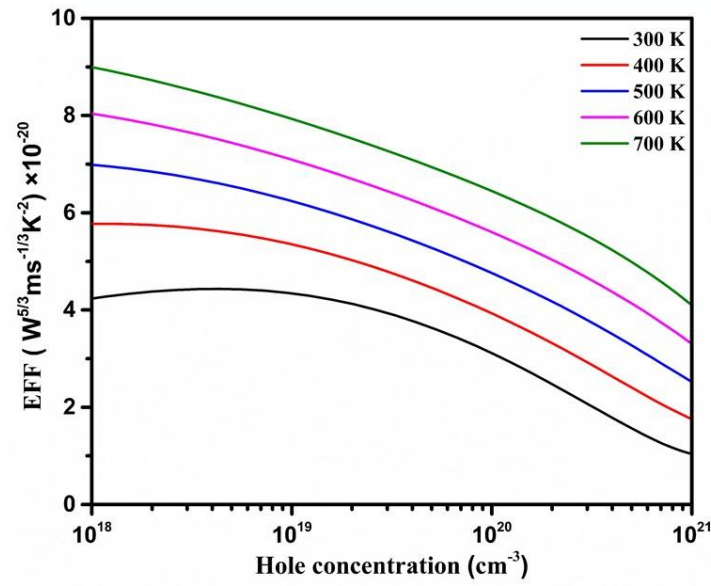


**Figure 3.9** Computed Electronic Fitness Function with hole doping concentration at different temperatures

In order to calculate the total thermal conductivity ( $\kappa_t$ ), we have determined the lattice thermal conductivity ( $\kappa_l$ ) of RbZn<sub>4</sub>P<sub>3</sub> using Slack's equation [125]:

$$\kappa_l = \frac{AM_a\delta n^{1/3}\theta_D^3}{\gamma^2 T} \quad (3.8)$$

where  $M_a$  denotes the average atomic mass of atoms in the unit cell,  $\delta$  is the cube root of the average volume of the unit cell,  $\gamma$  is the Grüneisen parameter,  $\theta_D$  is the Debye temperature and  $A$  is calculated using  $\gamma$  [126] as:

$$A = \frac{2.43 \times 10^{-8}}{1 - 0.514\gamma^{-1} + 0.228\gamma^{-2}} \quad (3.9)$$

Further, we have calculated  $\gamma$ , which is related to Poisson's ratio as given by the following relation

$$\gamma = \frac{3}{2} \left( \frac{1+\nu}{2-3\nu} \right) \quad (3.10)$$

The Grüneisen parameter can partially address the issue of anharmonicity of phonon-phonon interaction [109,127]. A high Grüneisen parameter implies strong anharmonic phonon-phonon scattering. The calculated  $\gamma$  value (1.42) is comparable to that of Bi<sub>2</sub>Te<sub>3</sub> [128]. **Figure 3.10 (a)**, inset, shows the variation of lattice thermal conductivity with temperature. It is found that  $\kappa_l$  decreases as temperature increases. The observed value of  $\kappa_l$  at room temperature is estimated to be 1.32 Wm<sup>-1</sup>K<sup>-1</sup>, and it decreases to 0.56 Wm<sup>-1</sup>K<sup>-1</sup> at a temperature of 700 K. This reduction in  $\kappa_l$  is beneficial for yielding high thermoelectric conversion efficiency of the compound.

Finally,  $\kappa_e$  has been obtained using  $\frac{\kappa_e}{\tau} \times \tau$  ( $\tau = 10^{-14}$  s) and  $\kappa_l$ , as shown in **Figure 3.10 (a)**.

The calculated value of  $\kappa_t$  is 2.15 Wm<sup>-1</sup>K<sup>-1</sup> at room temperature for optimum carrier concentration, 10<sup>20</sup> cm<sup>-3</sup>.

The variation of  $ZT$  with hole doping concentration at all temperatures ranging from 300 K to 700 K is shown in **Figure 3.10 (b)**. At a fixed temperature,  $ZT$  increases with the increase in hole carrier concentration and reaches its maximum value at  $\sim 2 \times 10^{20}$  cm<sup>-3</sup>, then decreases significantly. Hence, we have obtained the enhanced FOM for our optimum hole doping concentration ( $\sim 2 \times 10^{20}$  cm<sup>-3</sup>). Moreover, at a fixed doping concentration,  $ZT$  increases as temperature increases from 300 K to 700 K. The maximum observed  $ZT$  values at optimum hole doping concentration are 0.78, 0.72, 0.65, 0.52, and 0.33 at temperatures 700 K, 600 K,

500 K, 400 K, and 300 K, respectively. This shows RbZn<sub>4</sub>P<sub>3</sub> as a promising candidate for future thermoelectric applications. The observed high  $ZT$  of this compound is contributed by the low  $\kappa_l$  and a high value of  $PF$ .

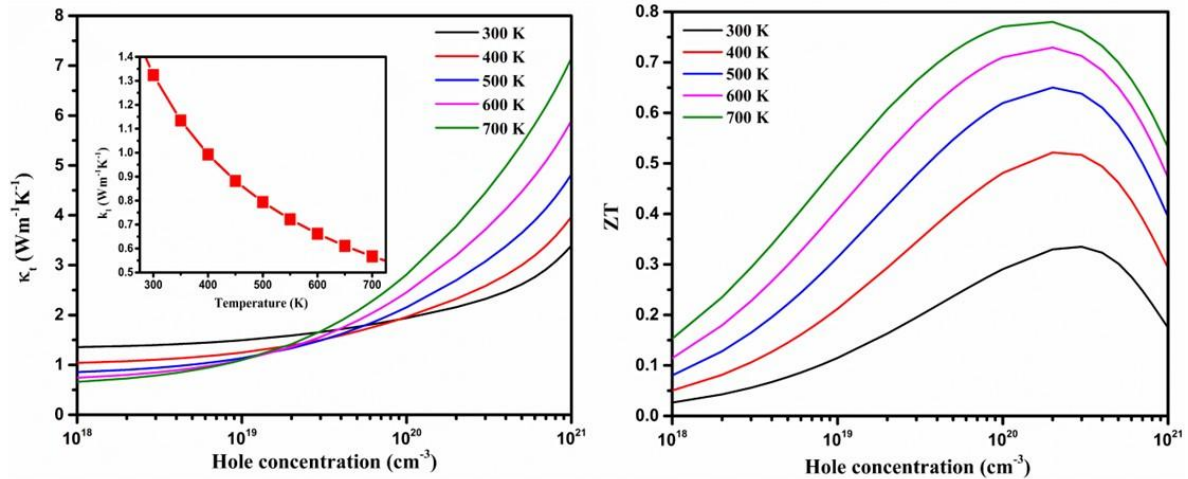


**Figure 3.10 (a)** The variation of total thermal conductivity (variation of lattice thermal conductivity with temperature is shown in inset) and **(b)** Figure of Merit  $ZT$  with hole doping concentration at various temperatures

### 3.3.5 Transport properties of RbGaSb<sub>2</sub>

The transport parameters of RbGaSb<sub>2</sub> are also computed through the solution of the BTE. We employed rigid band approximation, which assumes that temperature and doping concentration have no impact on electronic band structure, and constant relaxation time approximation, which states that  $S$  is independent of scattering rate. We have investigated how temperature and electron concentration affect TE coefficients. The variation of the  $S$ ,  $\sigma$ ,  $\kappa_e$  and  $ZT$  is obtained as functions of electron concentration for both  $n$ -type RbGaSb<sub>2</sub> in the range  $10^{18}$ - $10^{21}$  cm<sup>-3</sup> along the [100] ( $x$ -direction) and [001] ( $z$ -direction) crystallographic directions for temperature 300, 600, and 900 K.

The  $S$  value decreases with carrier concentration in both directions, as shown in **Figure 3.11 (a-b)**. The negative value of  $S$  signifies the  $n$ -type behaviour of RbGaSb<sub>2</sub>. The maximum  $S$  value obtained is  $-633.66 \mu\text{VK}^{-1}$  in the  $x$ -direction at 900 K for electron concentration of  $1 \times 10^{18}$  cm<sup>-3</sup>. Further utilizing the values of electrical conductivity and  $S$  we calculated power factor ( $PF$ ) in terms of relaxation time ( $\tau$ ) at 300, 600, and 900 K in both directions. The  $PF/\tau$  first increases with the increase in electron concentration and then reaches a maximum value, as shown in **Figure 3.11 (c-d)**. High  $PF$  is obtained in the  $x$ - than the  $z$ -direction. The optimized  $PF/\tau$  values at  $4 \times 10^{20}$  cm<sup>-3</sup> are  $3.13 \times 10^{11}$  ( $x$ -direction) and  $0.25 \times 10^{11}$  ( $z$ -direction) at 900 K.

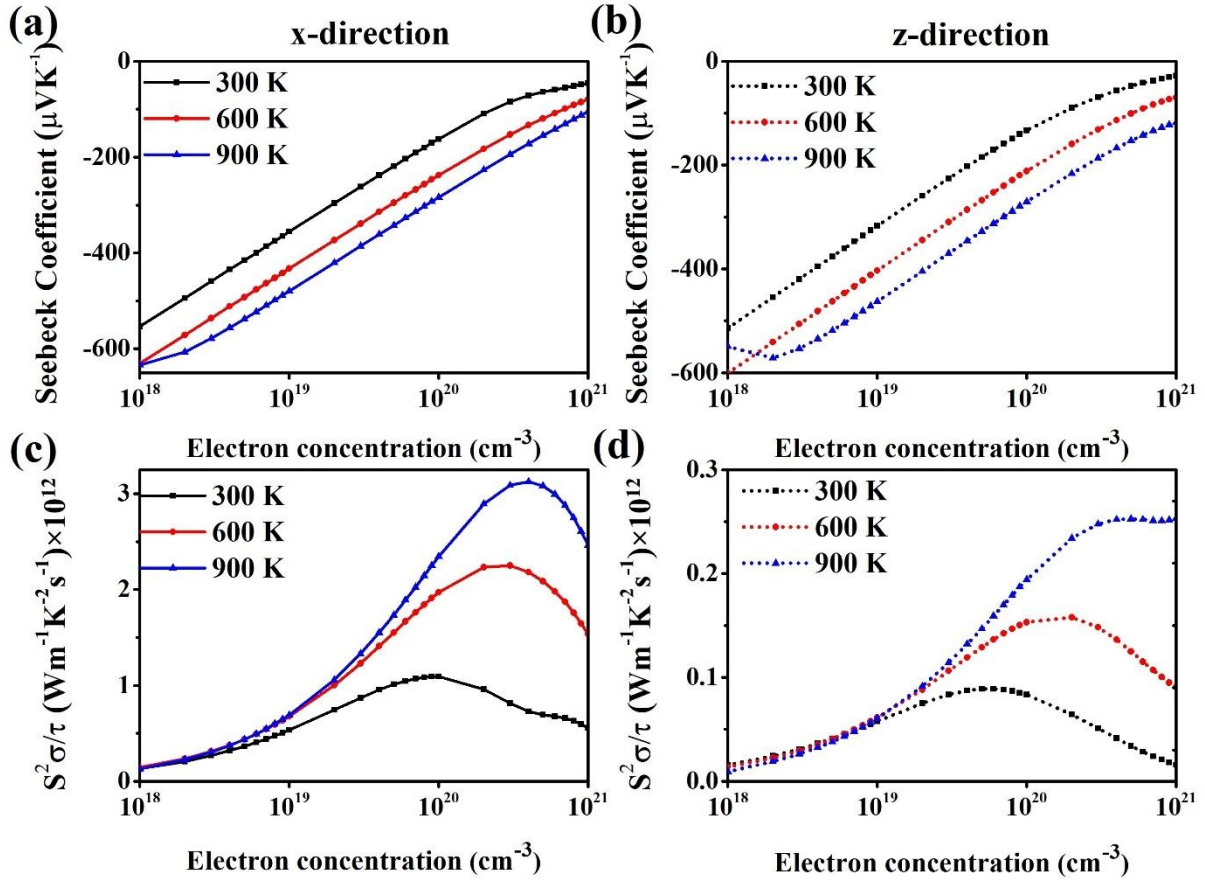


**Figure 3.11** Calculated (a-b) Seebeck coefficient and (c-d) power factor in the x- (solid lines) and z- (dotted lines) direction as a function of electron concentration at different temperatures.

Further, to evaluate  $ZT$ , we calculate  $\kappa_l$  that decreases with the increase in temperature in both directions, as shown in **Figure 3.12 (a)**. This decrease in  $\kappa_l$  at higher temperatures is attributed to the phenomenon of Umklapp phonon-phonon scattering. The total thermal conductivity,  $\kappa_l$  (**Figure 3.12 (b)**) of  $\text{RbGaSb}_2$  was found to be  $0.38 \text{ Wm}^{-1}\text{K}^{-1}$  at a temperature of 300 K and found within the range of previously reported values for antimony-based TE [129]. The complex crystal structure, rattling behavior of Rb cation, and the presence of heavy elements lead to ultralow thermal conductivity of  $\text{RbGaSb}_2$  [130].

The calculated frequency-dependent cumulative lattice thermal conductivity ( $\kappa_c$ ) shown in **Figure 3.12 (c)** reveals that low-frequency phonon modes contribute most to  $\kappa_l$  in the x-direction and then increases slightly. **Figure 3.12 (d)** shows the  $\kappa_c$  depends on the mean free path. The variation of  $ZT$  with electron concentration at different temperatures is shown in Fig. 4. At a constant temperature,  $ZT$  for both directions increases with electron concentration and

it reaches optimum value at  $\sim 10^{19} \text{ cm}^{-3}$ , after that significantly decreases. The maximum  $ZT$  values at optimized electron concentration are found to be 0.90 (in the  $x$ -direction) and 0.85 (in the  $z$ -direction) at 900 K. The high  $ZT$  value of  $\text{RbGaSb}_2$  is obtained by ultralow  $\kappa_l$  and large value of power factor.

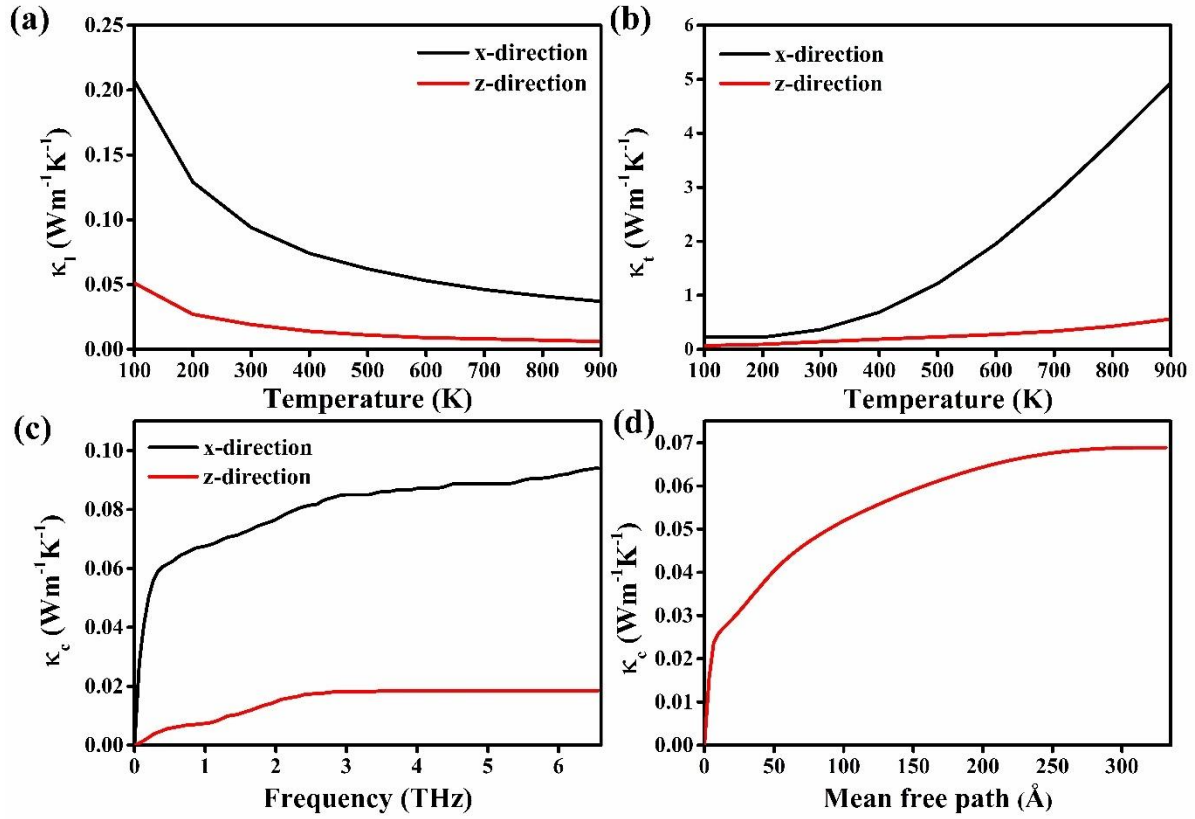


**Figure 3.12** Calculated (a)  $\kappa_l$  (b)  $\kappa_t$  (c-d)  $\kappa_c$  as a function of frequency and mean free path.

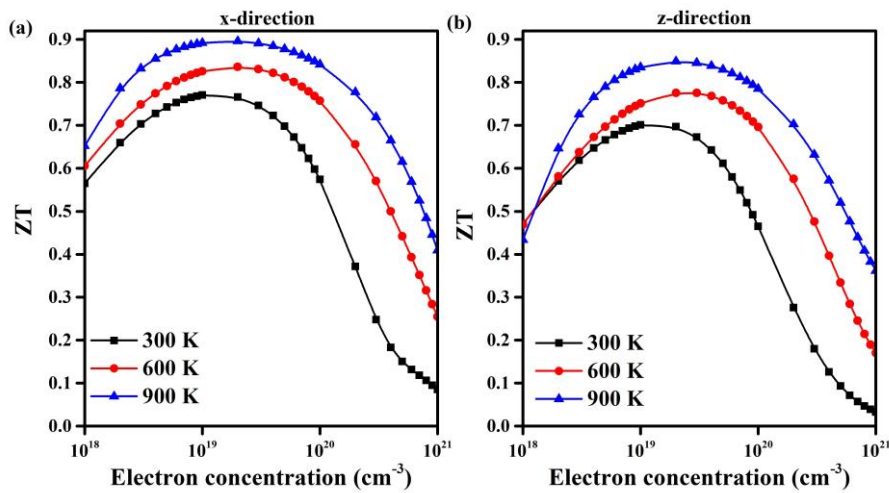


**Figure 3.13** Calculated  $ZT$  as a function of electron concentration of  $\text{RbGaSb}_2$  (a) in the  $x$ -direction (b) in the  $z$ -direction.

### 3.4 Summary

In this chapter, we have explored the TE properties of  $\text{RbZn}_4\text{P}_3$  and  $\text{RbGaSb}_2$ , respectively at different hole and electron doping concentrations using first-principles calculations in combination with semi-classical Boltzmann transport theory. The obtained structural parameters and bond lengths of both compounds are in good agreement with the experimentally measured values. The formation energy, phonon dispersion, and elastic properties have confirmed that  $\text{RbZn}_4\text{P}_3$  is stable thermodynamically, dynamically, and mechanically, respectively. Charge density analysis shows the Rb atom completely transfers its valence electron to the covalently bonded cluster  $[\text{Zn}_4\text{P}_3]^-$ , thus confirming the coexistence of ionic and covalent bonding in  $\text{RbZn}_4\text{P}_3$ . The electronic band structure calculations reveal that  $\text{RbZn}_4\text{P}_3$  is a moderate bandgap semiconductor. For  $\text{RbZn}_4\text{P}_3$ , a peak  $ZT$  value of 0.78 at 700 K for optimal hole doping concentration ( $2 \times 10^{20} \text{ cm}^{-3}$ ) has been obtained. The key advantage of  $\text{RbGaSb}_2$  as TE material is attributed to the complex crystal structure, the potential rattling of Rb cations, and the presence of heavy elements. This low thermal conductivity allows for the efficient conversion of heat into electricity, making it a potential candidate for TE applications. The high  $ZT$  values for a widely studied temperature range make these compounds quite promising for future TE material. The  $p$ -type  $\text{RbZn}_4\text{P}_3$  and  $n$ -type  $\text{RbGaSb}_2$  make them a valuable pair for developing efficient TE modules. We believe that this study would pave the way for future experimental TE energy harvesting studies on these materials.

# CHAPTER 4: AUGMENTED THERMOELECTRIC PERFORMANCE OF LiCaX (X=As, Sb) HALF HEUSLER COMPOUNDS

---

## 4.1 Introduction

HH compounds have emerged as promising TE materials due to their favorable combination of electrical and thermal transport properties. As discussed in the Chapter 1, their intrinsic structural and electronic features make them well-suited for mid-to-high-temperature TE applications. This chapter explores the TE performance of HH materials, examining their crystal structure, electronic properties, and potential for optimizing energy conversion efficiency. Numerous studies are existing in the literature that shows enhancement in TE performance of HH alloys realized through optimizing the carrier concentration via doping [131], heavy element substitution [132,133], and strain [134]. Rausch et al. [132] have synthesized *p*-type HH alloy  $\text{Ti}_{0.3}\text{Zr}_{0.35}\text{Hf}_{0.35}\text{CoSb}_{1-x}\text{Sn}_x$  and attained a maximum ZT value of 0.8 (for  $x = 0.15$ ) corresponding to an optimal carrier concentration of  $1.4 \times 10^{21} \text{ cm}^{-3}$  thereby proving that the carrier concentration can be an efficient way for improving TE properties. El-Khouly et al. [131] have reported that co-doping Hf-Ti in FeVSb increased the ZT value by 20% as compared to the pristine compound at 873 K. Recently, Shen et al. [135] and Serrano-Sánchez et al. [136] have demonstrated improved TE performance of NbFeSb and NbCoSn, respectively, by doping with heavy elements as it optimizes the PF and reduces the  $\kappa_l$  by causing high scattering of phonons.

Among the anticipated HH alloys, the Li-based 8-VEC HH compounds exhibit good mechanical, dynamical stability, and transport properties [58,137–140]. Few studies have been carried out in recent times focussing on their TE properties [141–143]. Very recently, Xiong et al. have achieved a significant enhancement in the figure of merit using carrier concentration optimization in Li-based 8-VEC HH compounds at 673 K. They have concluded that this compound may be very promising for TE energy harvesting if the thermal conductivity can be reduced significantly [144]. This motivated us to look for a unique combination of Li-based 8-VEC HH compounds with low thermal conductivity, which can be achieved by using heavy *p*-block elements such as Antimony (Sb) as it may increase the phonon–phonon scattering rates and reduces the phonon group velocities. We observed that all the reported studies on Li-based

8-VEC HH compounds lack a crucial thorough investigation of lattice thermal conductivity. Moreover, as these Li-based compounds are not experimentally synthesized yet, a clear guidance for the experimentalist is missing in reported works, i.e., the thermal stability at higher temperatures and phonon dynamics.

We used the DFT to probe the electronic structure of LiCaX (X = As, Sb) compounds. We assessed the thermal stability at different temperatures using AIMD simulations, which suggests that these compounds can be used for high-temperature applications. We then employed the semiclassical Boltzmann transport theory to calculate TE parameters at different temperatures for a given carrier concentration. In order to accurately predict the TE properties, a true value of  $\kappa_l$  is obtained and understood the role of acoustic and optical phonon modes in determining  $\kappa_l$ . This work shows that the  $ZT$  values of the LiCaAs and LiCaSb could be significantly enhanced with optimized carrier concentration, which results in making these Li-based 8-VEC HH compounds very promising candidates for high-temperature TE applications.

## 4.2 Computational Details

The structural properties of LiCaX were obtained using DFT as implemented in the VASP [145]. The GGA-PBE was used for the exchange-correlation potential [82]. For electron-ion interactions, we employed the projector augmented plane wave approach [105]. The Brillouin zone (BZ) was sampled using a Gamma-centred  $11 \times 11 \times 11$  k-point mesh, and a plane-wave kinetic energy cut-off of 650 eV was used. The geometric structure was fully optimized with a convergence threshold of  $10^{-8}$  eV for energy and  $-0.001$  eV/Å for the force. The AIMD simulation was employed, over a  $2 \times 2 \times 2$  supercell, to check the high-temperature stability of the proposed materials [146]. These calculations were carried out in a canonical ensemble (NVT) at temperatures 400 and 800 K using a time step of 1 fs, which lasted for 5000 fs.

The electronic structure and transport properties were calculated using the Full potential linearized augmented plane wave method implemented in the WIEN2k [147]. The cut-off energy was set to -6 Ry for the core and valence states, and the plane wave cut-off was decided by  $\text{RMT} \times \text{Kmax} = 7$ . The Kohn-Sham equation was solved self-consistently with an energy convergence of 0.0001 Ry/cell. We used TB-mBJ potential for the accurate prediction of band gap and transport properties [114]. The TE parameters were estimated via solving the BTE under the constant relaxation time approximation, which is implemented in the BoltzTraP code [95]. In order to ensure precise TE properties, a dense k-mesh of  $34 \times 34 \times 34$  was used for the BZ.



The Phonopy code [98] was used to obtain the second-order harmonic interatomic force constants (IFCs) and phonon structure via the DFPT method [148] using a  $2 \times 2 \times 2$  supercell on an  $8 \times 8 \times 8$  k-mesh. With the same supercell, the Phono3py code [100] was used to calculate anharmonic third-order IFCs. Interactions up to the fifth-closest neighbour were taken into consideration for the third-order IFCs. The phonon BTE was solved self-consistently to obtain the lattice thermal conductivity using a dense  $20 \times 20 \times 20$  q-mesh.

## 4.3 Results and Discussion

### 4.3.1 Structural properties and Thermal stability

The HH LiCaX crystallizes in the cubic structure, having a space group  $F\bar{4}3m$  (no. 216), where Li atoms occupy positions  $4b$  ( $1/2, 1/2, 1/2$ ), Ca atoms occupy positions  $4a$  ( $0, 0, 0$ ), and X (As and Sb) occupy  $4c$  ( $1/4, 1/4, 1/4$ ). Thus, the crystal structure can be viewed as a zinc blende type structure  $(\text{CaX})_4$ , partially filled by  $\text{Li}^+$  ions [149]. Thomas et al. have conducted extensive ab-initio investigations for the crystal structures of a variety of HHs and have observed the above-mentioned structure to be the most favourable for I–II–V HHs [150]. To further verify this, we have carried out the total energy calculations of different possible configurations (Type I, Type II, and Type III) whose Wyckoff positions are listed in **Table 4.1**. The total energies obtained from the self-consistent calculations for these configurations for both compounds are plotted as a function of cell volume **Figure 4.1** and curves are fitted in accordance with the Birch-Murnaghan equation of states [151]. The results show that the Type I configuration corresponds to the minimum energy and thus the most stable for both HH compounds. The calculated lattice constants of LiCaAs ( $6.67 \text{ \AA}$ ) and LiCaSb ( $6.96 \text{ \AA}$ ) are found to be in good agreement with previous studies [143,152]. The computed volume, bulk modulus, and its pressure derivative, and ground state energy for both compounds are presented in **Table 4.2**.

**Table 4.1** Possible Wyckoff positions of atoms for the LiCaX (X = As, Sb) HH compounds.

	Type I	Type II	Type III
<b>Li</b>	$4b$	$4c$	$4a$
<b>Ca</b>	$4a$	$4a$	$4b$
<b>X</b>	$4c$	$4b$	$4c$

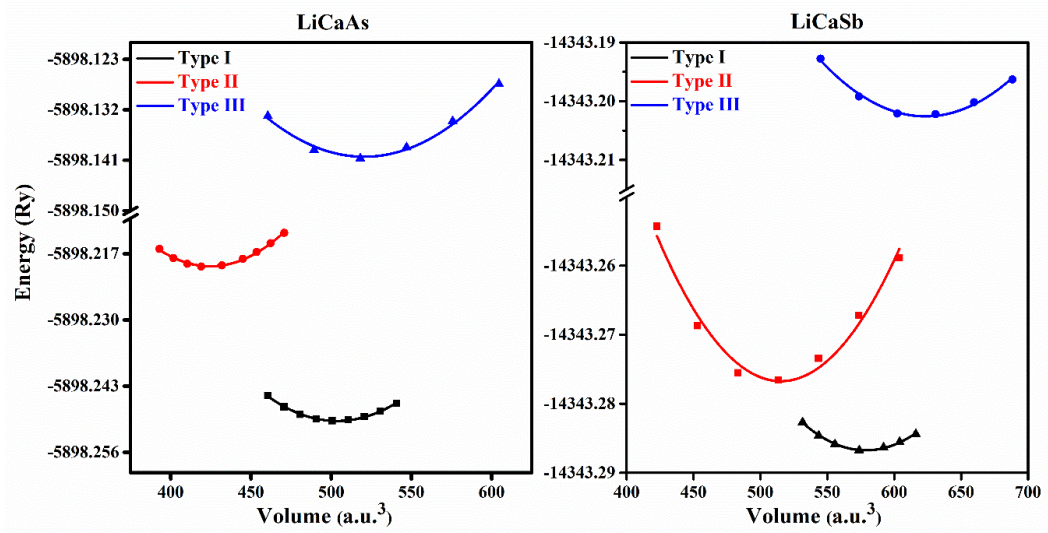


**Figure 4.1** Calculated total energy (in Ry) versus volume (in a.u.<sup>3</sup>) for Type I, Type II, and Type III configurations of LiCaAs and LiCaSb

**Table 4.2** Calculated optimized volume ( $V_0$ ), bulk modulus ( $B$ ), pressure derivative ( $B_p$ ), and total energy ( $E_0$ ) of both LiCaAs and LiCaSb compounds.

	$V_0$ (a.u. <sup>3</sup> )	$B$ (GPa)	$B_p$	$E_0$ (Ry)
<b>LiCaAs</b>	501.94	37.5093	3.5402	-5898.249798
<b>LiCaSb</b>	573.23	30.6543	3.5741	-14343.286715

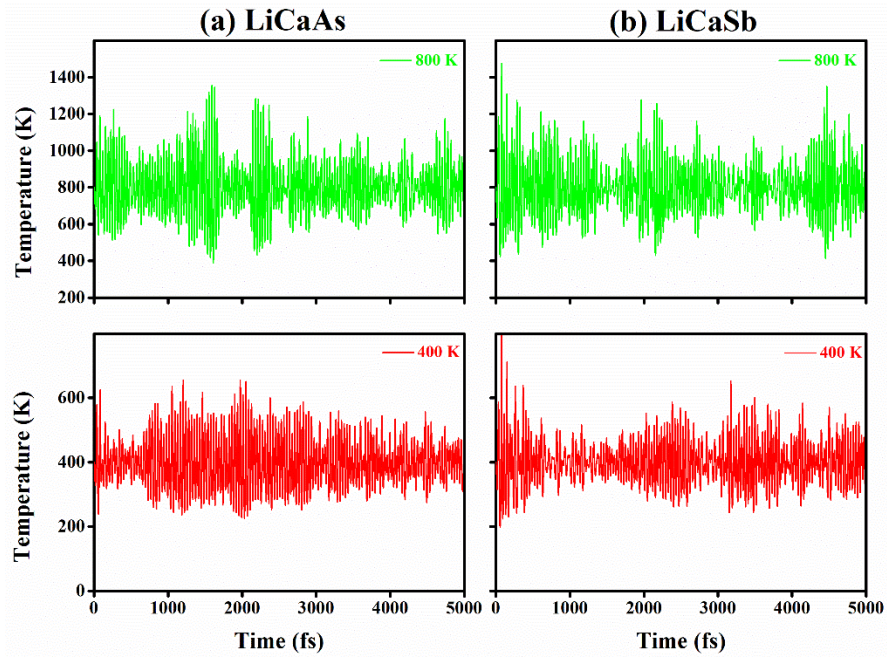


**Figure 4.2** The temperature fluctuations versus time for (a) LiCaAs and (b) LiCaSb at 400 K and 800 K using AIMD simulations.

Thermal stability is a crucial parameter for any material to be used for TE applications. We have probed the thermal stability of LiCaX by AIMD simulations using canonical ensemble at 400 K and 800 K, as shown in **Figure 4.2**. It is visible that the temperature fluctuations are very trivial throughout the 5000 fs AIMD simulations at 400 K and 800 K. These results indicate that the structures are thermally stable at ambient as well as elevated temperatures.

We have also obtained the melting temperature ( $T_m$ ) of LiCaX using an empirical relation [46]:  $T_m = 553 \text{ K} + (5.91/\text{GPa}) C_{11} \pm 300 \text{ K}$ . This relation has also been used for other similar Li-based 8 VEC HH compounds [153]. We have used the elastic package, implemented in WIEN2k software, to calculate the elastic constants for cubic systems in order to obtain the value of  $C_{11}$ . The obtained results are presented in **Table 4.3**. The value of the bulk modulus ( $B$ ) is obtained by fitting the Birch-Murnaghan equation of states [151].

**Table 4.3** Calculated elastic constants  $C_{ij}$  (GPa), Bulk modulus  $B$  (GPa), and melting temperature  $T_m$  (K).

	$C_{11}$	$C_{12}$	$C_{44}$	$B$	$T_m$
<b>LiCaAs</b>	62.305	25.252	28.220	37.026	921.22
<b>LiCaSb</b>	53.730	18.346	24.996	30.137	870.54

#### 4.3.2 Dynamical stability

To confirm the dynamical stability, we have calculated frequency-dependent phonon band structure using DFPT as presented in **Figure 4.3**. The presence of all positive frequency phonon modes shows that the structures under investigation are stable. In their primitive cell, there are three atoms that give rise to nine different phonon modes, three of which are acoustic (low-frequency phonon modes) and six of which are optical (high-frequency phonon modes). The highest frequencies for LiCaAs and LiCaSb are 10 THz and 8.5 THz, respectively. There is a band gap from 6.5 THz to 7.5 THz in LiCaAs, between 5.6 THz to 6.8 THz and slightly from 3.3 THz to 4.0 THz in LiCaSb. It can be seen that in the entire frequency range the dispersion of phonon modes shrinks with an increase in atomic weight of the X atom. This suggests a reduction in the corresponding group velocity, which further leads to low lattice thermal conductivity [154].

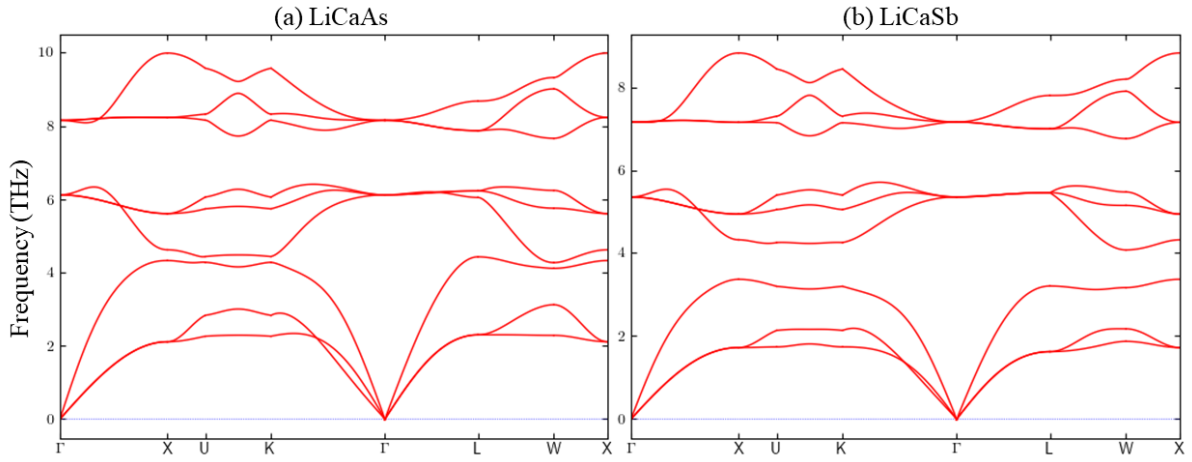


**Figure 4.3** The obtained phonon dispersion for **(a)** LiCaAs and **(b)** LiCaSb

It can be seen from **Figure 4.4** that the optical phonon modes above the band gap are predominantly contributed from the vibrations of Li atoms. This characteristic is the same for both structures LiCaAs and LiCaSb. The primary factor separating the phonon DOS of these two structures is the vibrations of As and Sb atoms. Owing to the large atomic mass of Sb, its vibrational frequencies mainly dominate up to 3 THz in LiCaSb. On the other hand, in the case of LiCaAs, the vibrational frequencies dominate up to 5 THz. Also, the minor contribution of Ca ions can be seen in the low frequency modes; however, the mid frequency phonon modes are largely contributed by the vibrations of Ca ions.

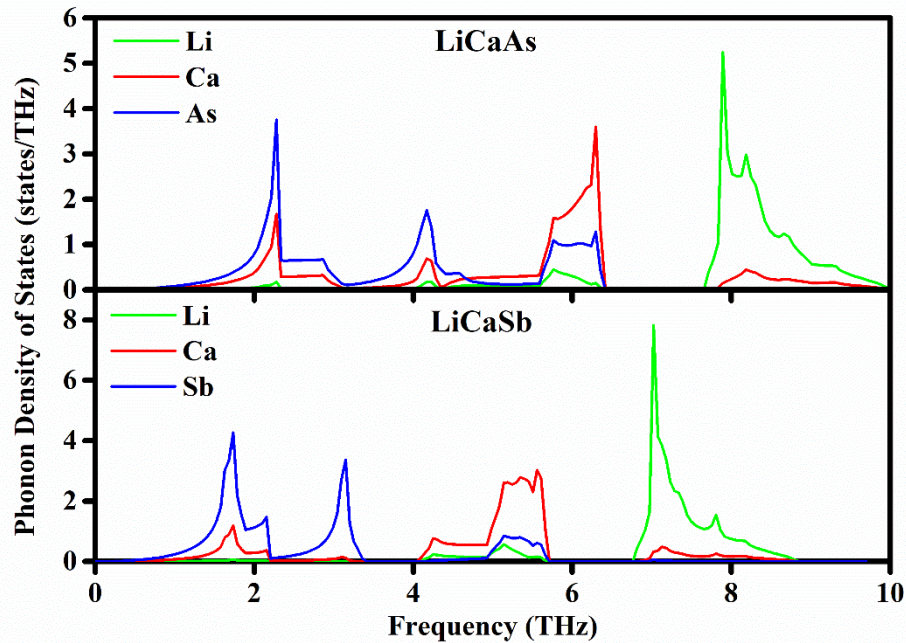


**Figure 4.4** Calculated phonon density of states of LiCaAs and LiCaSb

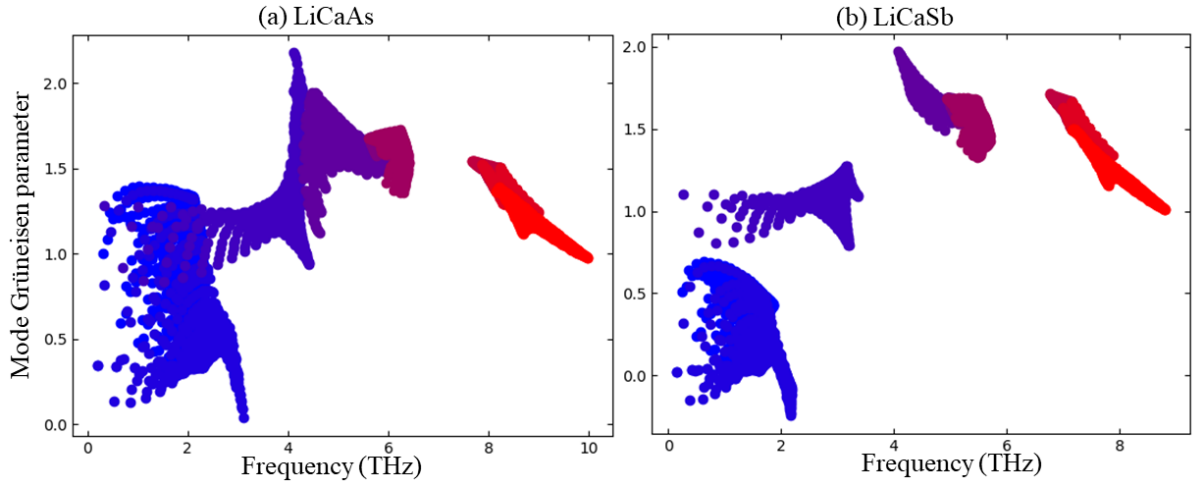


**Figure 4.5** Calculated mode Grüneisen parameter for **(a)** LiCaAs and **(b)** LiCaSb

The Grüneisen parameter ( $\gamma$ ) as a function of frequency is shown in **Figure 4.5**, its value is positive for all modes. It is a measure of anharmonicity, therefore large  $\gamma$  reflects the strong anharmonicity, thus the low lattice thermal conductivity. The average value  $\gamma$  for LiCaAs and LiCaSb is 1.28 and 1.20, respectively, smaller than that of other HH alloys [154,155] but comparable to promising thermoelectric material PbTe [125].

### 4.3.3 Electronic Structure Properties

**Figure 4.6** shows the energy band structure of LiCaAs and LiCaSb, which is obtained using the TB-mBJ potential. The CBM and the VBM of both alloys are found at the  $X$ -point and the  $\Gamma$ -point in the BZ, respectively. Therefore, both are found to be indirect band gap semiconductors. The band gaps of LiCaAs and LiCaSb are calculated to be 1.82 (2.52) eV and 1.52 (2.09) eV using GGA (TB-mBJ), respectively. The calculated value of the band gap for LiCaAs is comparable to previous DFT calculations [143,152]. The band gap of LiCaX decreases from As to Sb. Thus, a higher value of the Seebeck coefficient can be expected for LiCaAs. Also, the VB edges are flat, indicating strongly localized holes, on the contrary, the CB edges are dispersed, showing free electrons. Therefore, we foresee superior TE performance for the  $p$ -type compounds in comparison to the  $n$ -type ones.

The total and partial DOS of LiCaX HH alloys are depicted in **Figure 4.7**. It is noticeable that the VB is primarily dominated by X (i.e., As and Sb) atoms, and the CB is majorly composed of Ca atoms for LiCaX HH alloy. Li atoms give negligible contribution both in CB and VB. It is also found that the DOS in the VB is higher than that in the CB. As a result, we anticipate superior TE performance in the  $p$ -type doping than in the  $n$ -type counterpart.



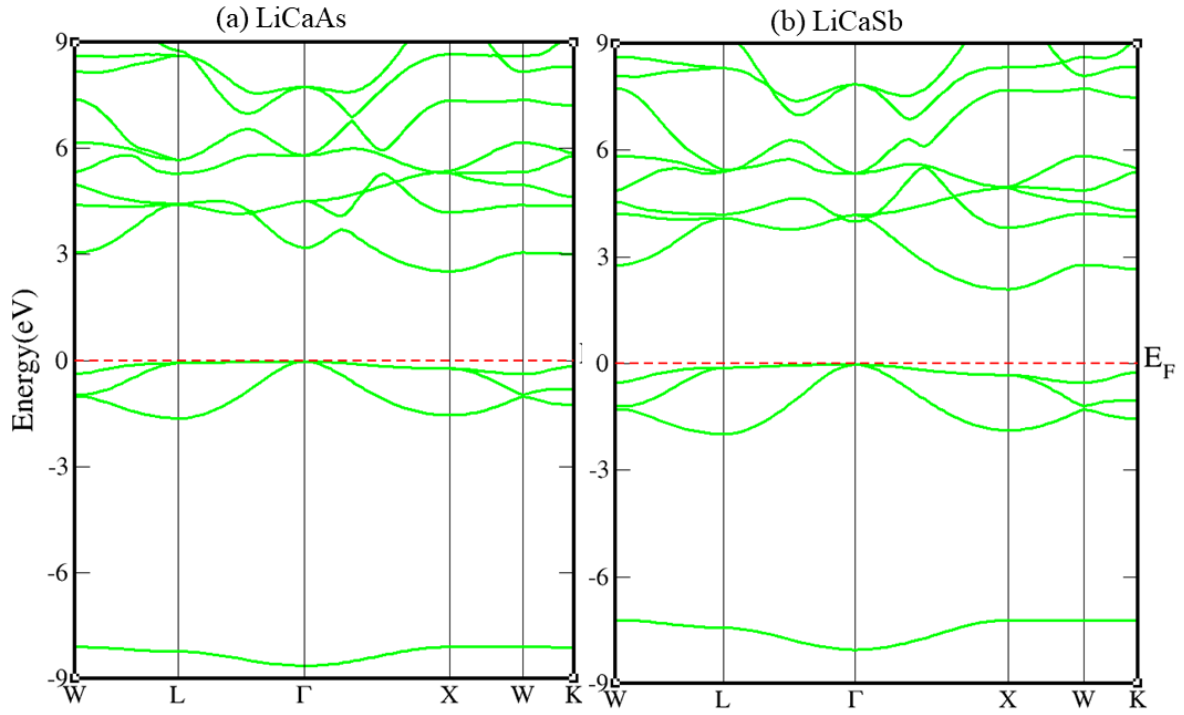


**Figure 4.6** Calculated electronic band structures of (a) LiCaAs and (b) LiCaSb along the high symmetry directions of the BZ as determined using the Tran-Blaha modified Becke-Johnson potential. The Fermi energy is set to 0 eV.

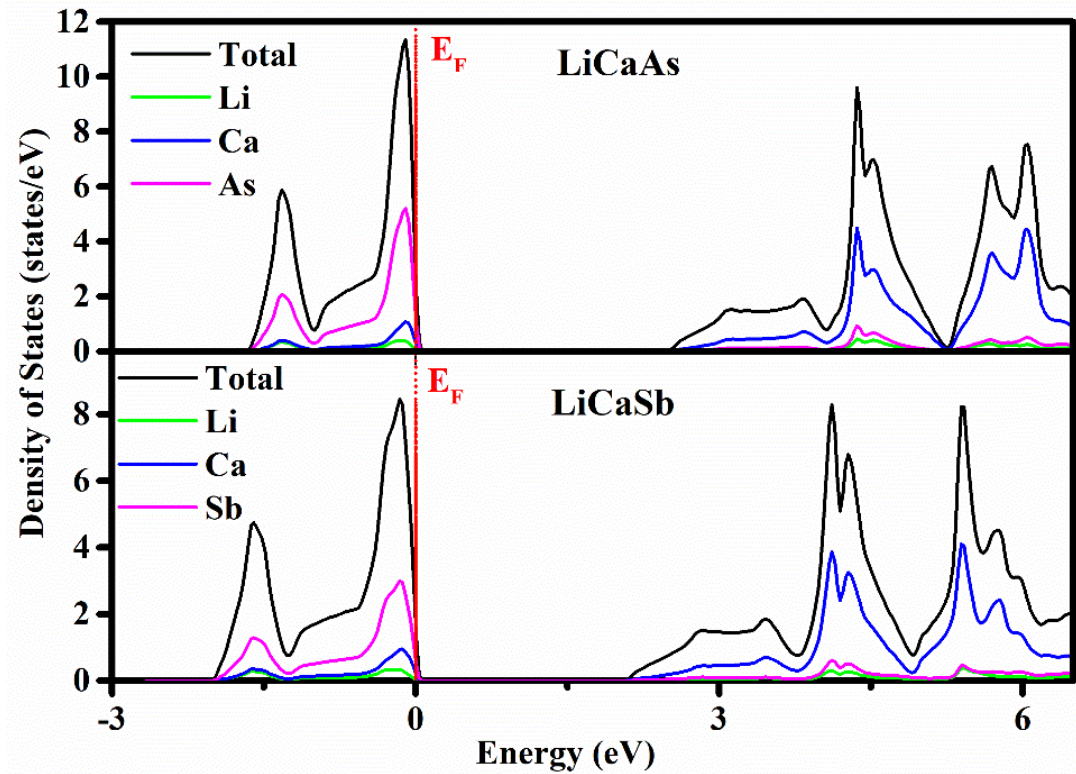


**Figure 4.7** Calculated total and partial density of states of LiCaAs and LiCaSb. The Fermi energy is set to 0 eV.

## 4.4 Thermoelectric Properties

The TE parameters  $S$ ,  $\sigma$ , and  $\kappa_e$  are calculated by the following relations [95]:

$$S_{\alpha\beta}(\mu, T) = \frac{1}{eT\sigma_{\alpha\beta}(\mu, T)} \int \sigma_{\alpha\beta}(\varepsilon)(\varepsilon - \mu) \left( -\frac{\partial f(T, \varepsilon, \mu)}{\partial \varepsilon} \right) d\varepsilon \quad (4.1)$$

$$\kappa_{\alpha\beta}^e(\mu, T) = \frac{1}{e^2 T \Omega} \int \sigma_{\alpha\beta}(\varepsilon)(\varepsilon - \mu)^2 \left( -\frac{\partial f(T, \varepsilon, \mu)}{\partial \varepsilon} \right) d\varepsilon \quad (4.2)$$

$$\sigma_{\alpha\beta}(\mu, T) = \frac{1}{\Omega} \int \sigma_{\alpha\beta}(\varepsilon) \left( -\frac{\partial f(T, \varepsilon, \mu)}{\partial \varepsilon} \right) d\varepsilon \quad (4.3)$$

where  $\Omega$  is the reciprocal space volume,  $f$  is the Fermi distribution function,  $e$  is the electron charge,  $\varepsilon$  is the carrier energy.  $\sigma_{\alpha\beta}(\varepsilon)$  is conductivity tensor can be expressed as:

$$\sigma_{\alpha\beta}(\varepsilon) = \frac{1}{N} \sum_{i,k} \sigma_{\alpha\beta}(i, k) \frac{\delta(\varepsilon - \varepsilon_{i,k})}{d\varepsilon} \quad (4.4)$$

The transport properties are calculated as a function of temperature and with varying carrier concentration ( $n$ ) ranging from  $1 \times 10^{19} \text{ cm}^{-3}$  to  $1 \times 10^{22} \text{ cm}^{-3}$ , which is an optimum range for good TE performance [21], with constant relaxation time for the HH alloys LiCaX (X = As and Sb). Considering that these compounds are stable at higher temperatures, thereby we calculated the transport properties up to 800 K.

### 4.4.1 Seebeck Coefficient

**Figure 4.8** depicts the  $S$  as a function of carrier concentration ( $1 \times 10^{19} \text{ cm}^{-3}$  to  $1 \times 10^{22} \text{ cm}^{-3}$ ) at temperatures ranging from 300 K to 800 K. The absolute value, i.e.,  $|S|$ , decreases with the increase in carrier concentration, which is consistent with the fact that  $S$  is inversely proportional to  $n$ . The  $S$  of  $p$ -type LiCaAs and LiCaSb is significantly greater than that for the  $n$ -type because of flat bands in the VB and dispersed bands in CB (which leads to a higher effective mass of holes than that of electrons). This indicates that the TE performance of the  $p$ -type LiCaX is better than that of the  $n$ -type. We calculated the effective mass ( $m^*$ ) of hole and electron carriers using the relation  $m^* = \hbar^2 / [\partial^2 E / \partial k^2]$ . The calculated value of  $m^*$  of holes is  $11.86 m_e$ , and  $5.55 m_e$ , respectively, for LiCaAs, and LiCaSb, whereas the corresponding effective mass of electron is  $0.63 m_e$  and  $0.54 m_e$ , here  $m_e$  is the mass of free electron. The maximum obtained value of  $S$  for  $p$ -type LiCaAs, and LiCaSb, respectively, are  $727.31 \mu\text{VK}^{-1}$  and  $704.08 \mu\text{VK}^{-1}$  at 800 K, whereas the corresponding  $S$  values for  $n$ -type are  $-501.54 \mu\text{VK}^{-1}$  and  $-475.14 \mu\text{VK}^{-1}$ , respectively. The larger  $S$  is obtained for  $p$ -type variants, throughout the studied carrier concentration range and temperature, of both compounds, which might be

because of the higher effective mass of holes than electrons. The optimum carrier concentration for which maximum  $|S|$  is obtained is  $1 \times 10^{19} \text{ cm}^{-3}$ .

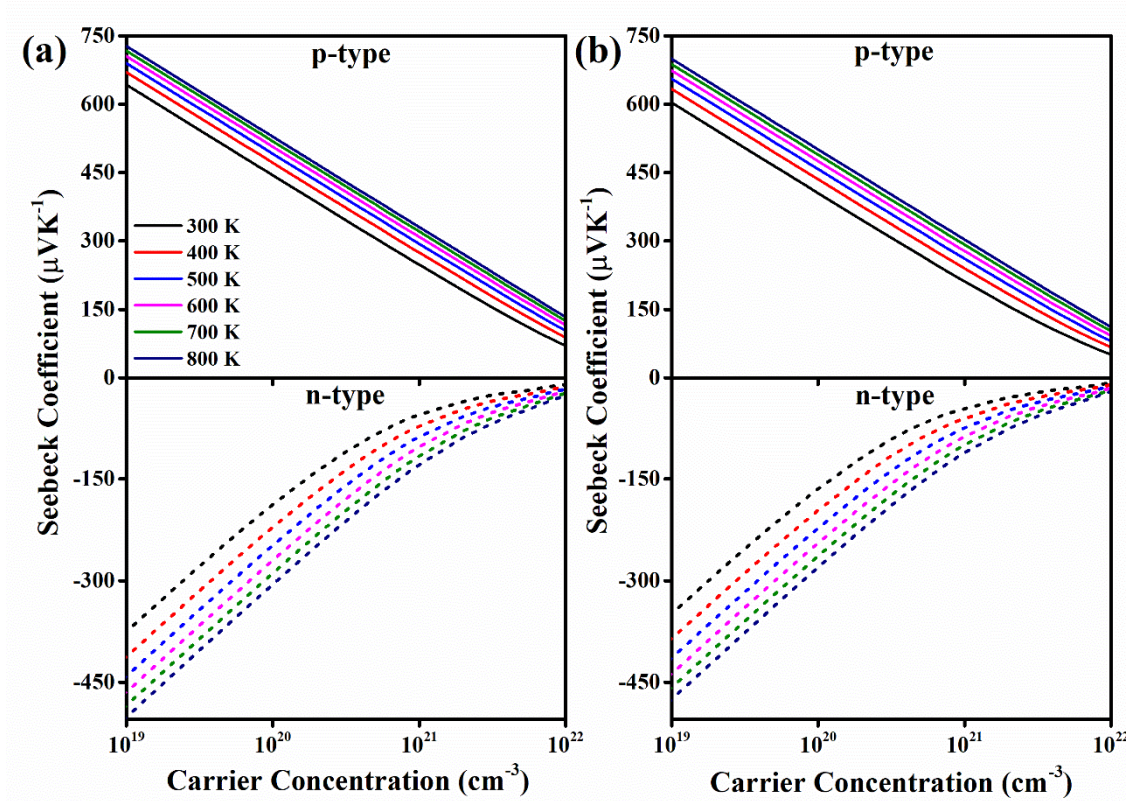


**Figure 4.8** Calculated Seebeck coefficient of (a) LiCaAs and (b) LiCaSb as a function of carrier concentration and for temperatures ranging from 300 K to 800 K.

#### 4.4.2 Electrical and Electronic Thermal Conductivity

The magnitude of  $\sigma/\tau$  increases with the carrier concentration for both *n*-type and *p*-type nature of the investigated compounds. **Figure 4.9** shows that  $\sigma/\tau$  increases sharply beyond carrier concentration  $\sim 1 \times 10^{21} \text{ cm}^{-3}$ . Also, it can be noted that electrical conductivity shows weak dependence on temperature. The value of  $\sigma/\tau$  is higher in the *n*-type than in the *p*-type due to parabolically dispersed CB edges. The thermal conductivity includes both lattice and electronic contribution; its electronic component is described by Wiedemann Franz's law [122] that states that  $\kappa_e$  varies linearly with the temperature and electrical conductivity. The obtained electronic contribution to thermal conductivity, with respect to relaxation time, i.e.,  $\kappa_e/\tau$  presented in **Figure 4.10**, reveals that for the same carrier concentration, the values for LiCaSb are greater than those for LiCaAs, and the change in  $\kappa_e/\tau$  with the carrier concentration is similar to that of  $\sigma/\tau$ .



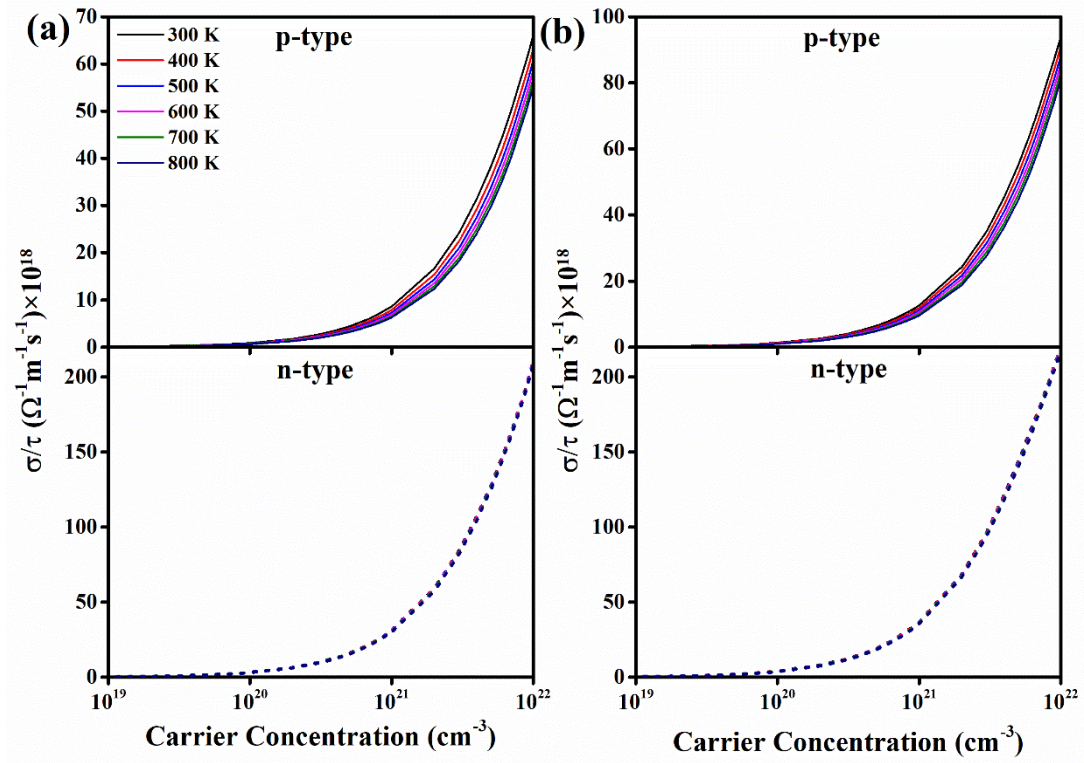


**Figure 4.9** Calculated electrical conductivity of (a) LiCaAs and (b) LiCaSb as a function of carrier concentration and for temperatures ranging from 300 K to 800 K.

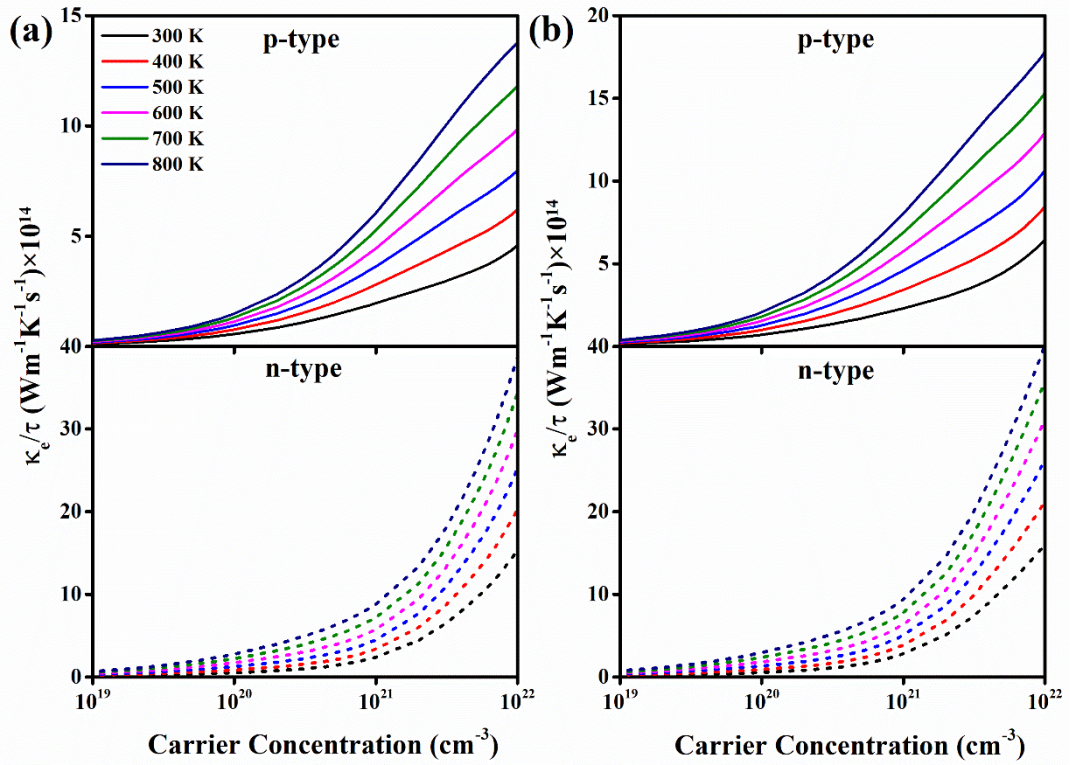


**Figure 4.10** Calculated electronic thermal conductivity of (a) LiCaAs and (b) LiCaSb as a function of carrier concentration and for temperatures ranging from 300 K to 800 K.

#### 4.4.3 Power Factor

The optimization of the carrier concentration substantially improves the  $PF$  of LiCaX HH compounds as given in **Figure 4.11**. With the increase in carrier concentration, the value of  $PF$  first increases reaches a maximum value, and then starts decreasing. We estimated that the optimum carrier concentration for  $n$ -type compounds is relatively lower than  $p$ -type. For LiCaAs, the optimal  $p$ -type and  $n$ -type  $PF/\tau$  values are around  $10.95 \times 10^{11} \text{ Wm}^{-1}\text{K}^{-2}\text{s}^{-1}$  at a carrier concentration of  $5 \times 10^{21} \text{ cm}^{-3}$  and  $4.99 \times 10^{11} \text{ Wm}^{-1}\text{K}^{-2}\text{s}^{-1}$  at  $9 \times 10^{20} \text{ cm}^{-3}$ , respectively, whereas corresponding values for LiCaSb are  $12.53 \times 10^{11} \text{ Wm}^{-1}\text{K}^{-2}\text{s}^{-1}$  at  $4 \times 10^{21} \text{ cm}^{-3}$  and  $5.30 \times 10^{11} \text{ Wm}^{-1}\text{K}^{-2}\text{s}^{-1}$  at  $8 \times 10^{20} \text{ cm}^{-3}$ . The comparison of  $PF/\tau$  shows that  $p$ -type LiCaSb has a relatively higher value. Therefore, one can expect better TE performance in the case of the  $p$ -type LiCaSb compound.

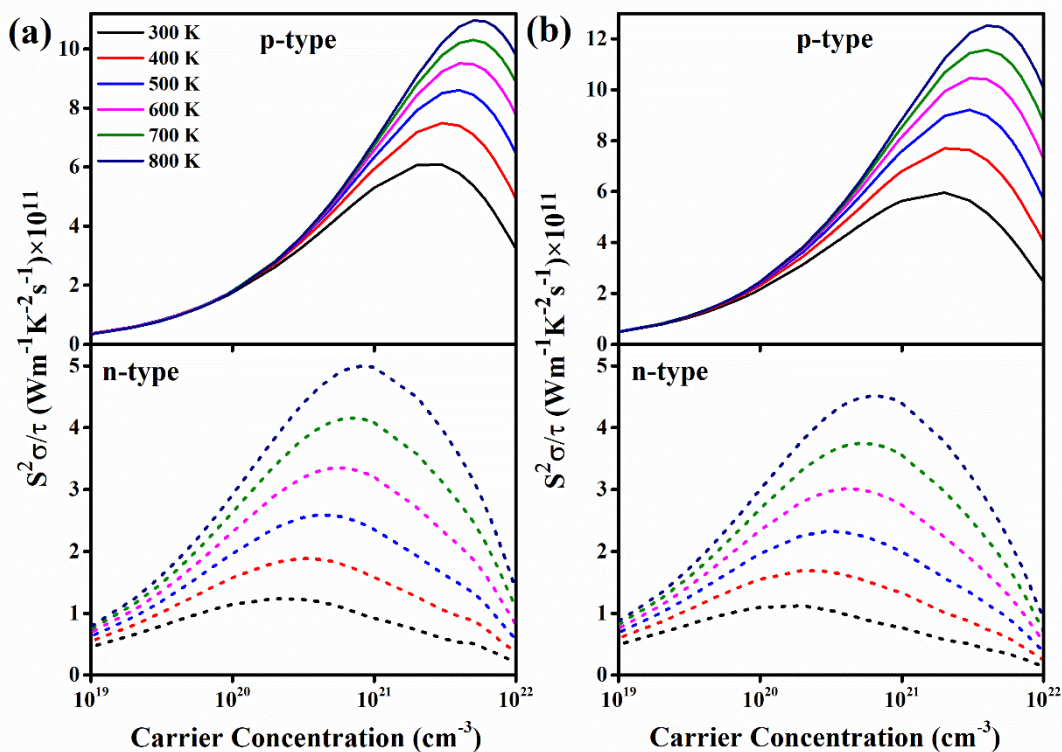


**Figure 4.11** Calculated power factor of (a) LiCaAs and (b) LiCaSb as a function of carrier concentration and for temperatures ranging from 300 K to 800 K.

#### 4.4.4 Lattice thermal conductivity

To understand the behaviour of  $\kappa_l$  in LiCaAs and LiCaSb, it is crucial to understand the phonon dynamics of both HH alloys. From **Figure 4.3**, it can be noticed that the LiCaSb has overall lower frequencies than that of LiCaAs. Therefore, low  $\kappa_l$  is expected for LiCaSb. This also reflects in its low value of lattice thermal conductivity than that of LiCaAs. The calculated temperature-dependent lattice contribution to the thermal conductivity of these HH alloys is

shown in **Figure 4.12 (a)**. The room temperature  $\kappa_l$  values for LiCaSb, and LiCaAs are  $1.42 \text{ Wm}^{-1}\text{K}^{-1}$  and  $1.90 \text{ Wm}^{-1}\text{K}^{-1}$ , respectively, but these values decrease  $0.66 \text{ Wm}^{-1}\text{K}^{-1}$  and  $0.88 \text{ Wm}^{-1}\text{K}^{-1}$  at 800 K. These compounds have an intrinsically low value of  $\kappa_l$  than that of TaFeSb based ( $\kappa_l = 3.1 \text{ Wm}^{-1}\text{K}^{-1}$  for  $\text{Ta}_{0.84}\text{Ti}_{0.16}\text{FeSb}$  and  $2.3 \text{ Wm}^{-1}\text{K}^{-1}$  for  $\text{Ta}_{0.74}\text{V}_{0.1}\text{Ti}_{0.16}\text{FeSb}$ ), which is amongst the high-performance TE material, [156] and  $\text{Ti}_{0.5}\text{Hf}_{0.5}\text{NiSn}$  with  $3.2 \text{ Wm}^{-1}\text{K}^{-1}$  [155] HH alloys. These obtained values of  $\kappa_l$  at room temperature are comparable to conventional promising TE candidates like PbTe ( $2.2 \text{ Wm}^{-1}\text{K}^{-1}$ ) [157] and  $\text{Bi}_2\text{Te}_3$  ( $1.6 \text{ Wm}^{-1}\text{K}^{-1}$ ) [158]. The value of the lattice thermal conductivity of LiCaSb is lower than that of LiCaAs.

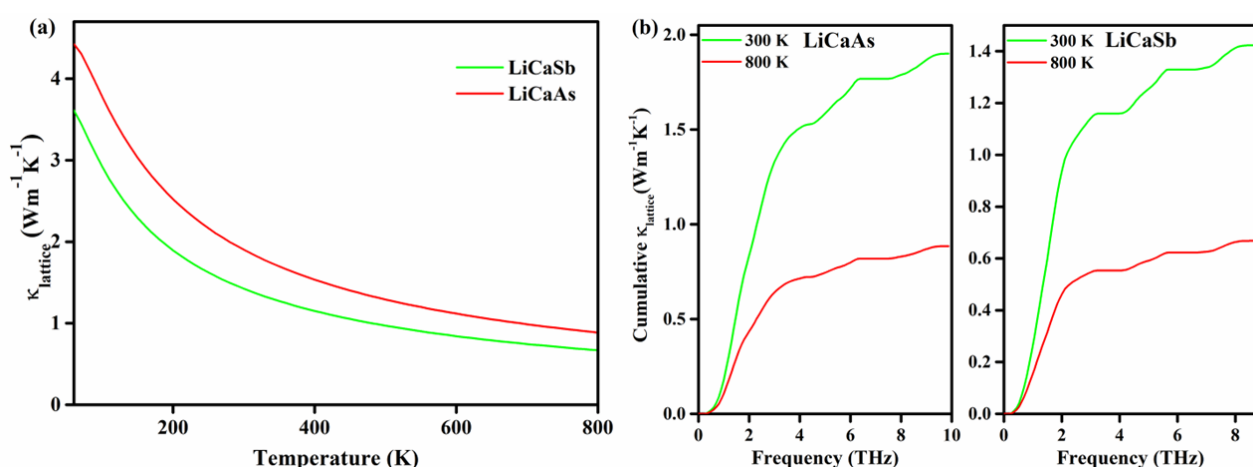


**Figure 4.12 (a)** The lattice thermal conductivity of LiCaAs and LiCaSb as a function of temperature **(b)** The cumulative lattice thermal conductivity as a function of frequency in LiCaAs and LiCaSb at different temperatures 300 K and 800 K

Further, we have calculated the cumulative thermal conductivity of LiCaAs and LiCaSb at 300 K and 800 K as a function of frequency (**Figure 4.12 (b)**). It increases rapidly in the low-frequency acoustic phonon modes (1 – 4 THz), and this part of the phonons contributes more than 80% of the lattice thermal conductivity. Therefore, the high-frequency optical phonon modes have a minor contribution (less than 20%) to the thermal conductivity. The relative contribution of these phonon modes of both compounds to  $\kappa_l$  is presented in **Table 4.4**.

**Table 4.4** Relative contributions of acoustic and optical phonon modes to the lattice thermal conductivity ( $\kappa_l$ ) at room temperature and 800 K for both compounds LiCaAs and LiCaSb.

	Temperature (K)	$\kappa_l$ ( $\text{Wm}^{-1}\text{K}^{-1}$ )	Contribution of acoustic modes (%)	Contribution of optical modes (%)
<b>LiCaAs</b>	300	1.90	80.26	19.73
	800	0.88	81.03	18.96
<b>LiCaSb</b>	300	1.42	81.49	18.50
	800	0.66	83.17	17.18



#### 4.4.5 Figure of Merit

The dependence of transport parameters on the carrier concentration and temperature suggests that a high FOM can be obtained by tuning the carrier concentration and increasing the temperature. As depicted in **Figure 4.13**, FOM is calculated as a function of carrier concentration and for the temperature range 300–800 K in HH LiCaAs and LiCaSb by incorporating the  $PF$  and  $\kappa_l$ . It is observed that the room temperature  $ZT$  values are higher for  $p$ -type LiCaAs and LiCaSb than those of  $n$ -type. It can be seen that the  $ZT$  improved at higher temperatures at optimized carrier concentrations ( $\sim 10^{21} \text{ cm}^{-3}$  for  $p$ -type carriers and  $\sim 10^{20} \text{ cm}^{-3}$  for  $n$ -type carriers for both the investigated compounds). The similar values of carrier concentrations have been experimentally observed in other Li-based 8 VEC HH compounds [144]. It is obvious that as we move towards higher atomic weight element,  $\kappa_l$  suppressed by 24%, resulting in an augmentation of TE performance of LiCaSb. However, the final  $ZT$  value of the two compounds is nearly identical because of the large  $S$  value of LiCaAs compared to LiCaSb. The low  $\kappa_l$  and high  $PF$  of LiCaX compounds result in high  $ZT$  value at higher temperatures. This shows that these HH compounds are worthy candidates for further experimental investigations. The TE properties of  $p$ -type are superior to those of  $n$ -type; therefore, hole doping seems to be good for improving the performance of these compounds.

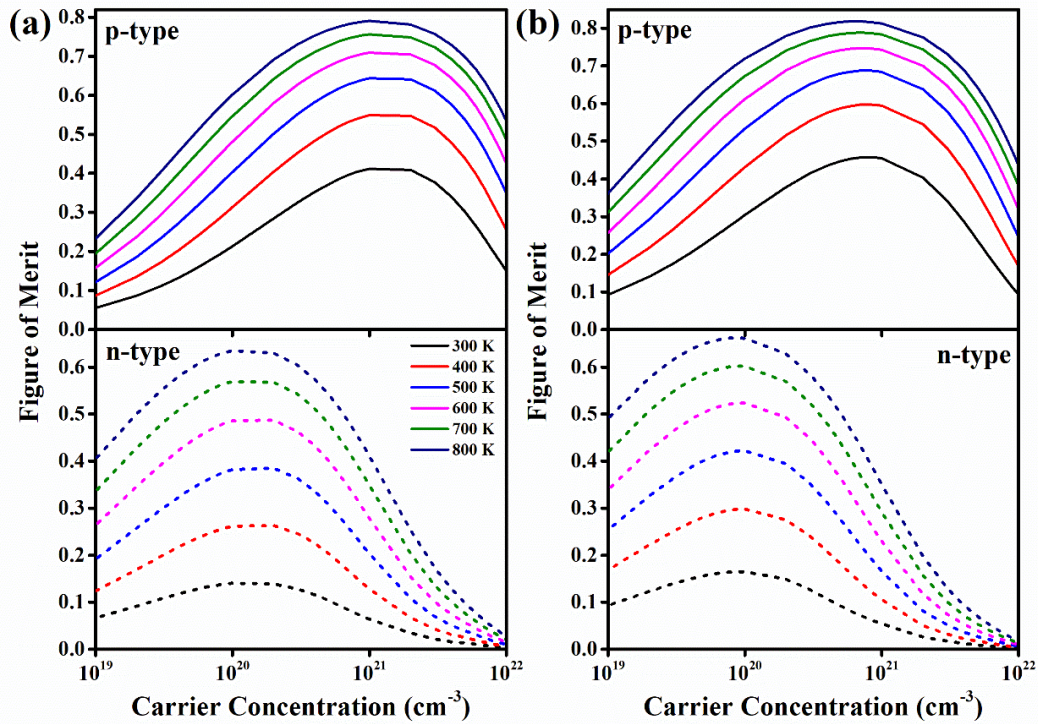


**Figure 4.13** Calculated  $ZT$  values of (a) LiCaAs and (b) LiCaSb as a function of carrier concentration within constant relaxation time approximation (i.e.,  $\tau = 1 \times 10^{-14} \text{ s}$ ) at different temperatures ranging from 300 K to 800 K

Further to determine the figure of merit accurately, the temperature-dependent  $\tau$  of the charge carriers, i.e., electrons and holes has evaluated using the deformation potential theory developed by Bardeen and Shockley [97], according to which  $\tau$  is given by the following:

$$\tau = \frac{2\sqrt{2}\pi C_{\beta}\hbar^4}{3(k_B T m^*)^{3/2} E_{\beta}^2} \quad (4.5)$$

Where,  $C_{\beta}$  is the elastic modulus along  $\beta$  axis,  $m^*$  is the effective mass of charge carriers,  $k_B$  is Boltzmann's constant, and  $E_{\beta}$  is the deformation potential constant along  $\beta$  axis. The  $m^*$  values are written in the text (section 4.4.1) and other parameters-  $C_{\beta}$ ,  $E_{\beta}$ , and  $\tau$  of charge carriers i.e., electrons and holes for both compounds at different temperatures are listed in **Table 4.5**.

**Table 4.5** The elastic modulus ( $C_{\beta}$ ), deformation potential constant ( $E_{\beta}$ ), and relaxation time ( $\tau$ ) at 300, 600, and 800 K of electrons and holes for LiCaAs and LiCaSb.

		LiCaAs		LiCaSb	
Carriers type		electron	hole	electron	hole
$C_{\beta}$ (eV/Å <sup>3</sup> )		0.070146	0.070146	0.063437	0.063437
$E_{\beta}$ (eV)		1.73353	0.20233	1.58507	0.20083
$\tau$ (s)	300 K	$2.56 \times 10^{-13}$	$2.30 \times 10^{-13}$	$3.49 \times 10^{-13}$	$6.60 \times 10^{-13}$
	600 K	$9.06 \times 10^{-14}$	$8.14 \times 10^{-14}$	$1.23 \times 10^{-13}$	$2.33 \times 10^{-13}$
	800 K	$5.88 \times 10^{-14}$	$5.29 \times 10^{-14}$	$8.02 \times 10^{-14}$	$1.52 \times 10^{-13}$

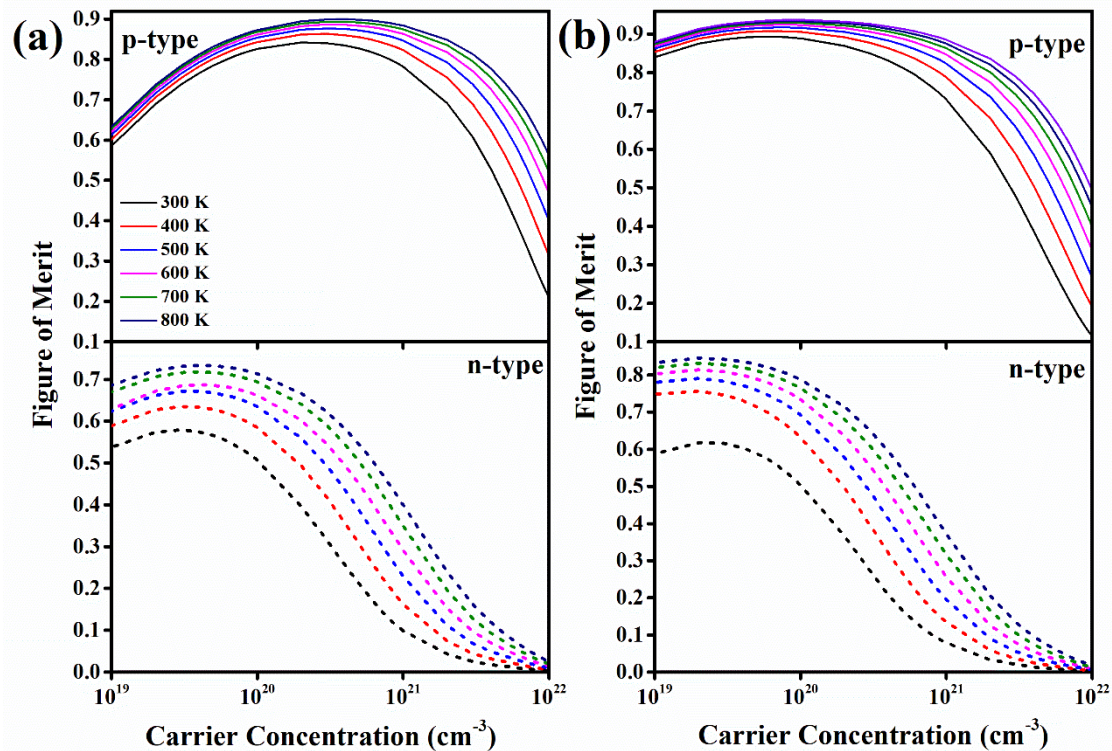


**Figure 4.14** Calculated  $ZT$  values of (a) LiCaAs and (b) LiCaSb as a function of carrier concentration using temperature dependent relaxation time of carriers at different temperatures ranging from 300 K to 800 K

When the temperature-dependent  $\tau$  is used the increase in FOM is observed as shown in **Error! Reference source not found.** in comparison to constant  $\tau = 1 \times 10^{-14}$  s. The calculated FOM values at optimized carrier concentration for both *p*-type and *n*-type compounds at 300 and 800 K are listed in **Table 4.6**.

The variation of  $ZT$  with the temperature at the optimum carrier concentration using constant  $\tau$  approximation and temperature dependent  $\tau$  of charge carriers is also shown in **Figure 4.15**. It is found that the optimum carrier concentration for *p*-type LiCaAs and LiCaSb offers better TE performance than the *n*-type counterparts.

**Table 4.6** Figure of merit of LiCaAs and LiCaSb for both types of carriers at optimized carrier concentration

Figure of merit at optimized carrier concentration					
		LiCaAs		LiCaSb	
		300 K	800 K	300 K	800 K
With constant $\tau$	<i>p</i> -type	0.41 $1 \times 10^{21} \text{ cm}^{-3}$	0.79 $1 \times 10^{21} \text{ cm}^{-3}$	0.46 $8 \times 10^{20} \text{ cm}^{-3}$	0.82 $7 \times 10^{20} \text{ cm}^{-3}$
	<i>n</i> -type	0.14 $1 \times 10^{20} \text{ cm}^{-3}$	0.64 $1 \times 10^{20} \text{ cm}^{-3}$	0.16 $1 \times 10^{20} \text{ cm}^{-3}$	0.66 $9 \times 10^{19} \text{ cm}^{-3}$
Without Constant $\tau$	<i>p</i> -type	0.84 $4 \times 10^{20} \text{ cm}^{-3}$	0.90 $4 \times 10^{20} \text{ cm}^{-3}$	0.89 $1 \times 10^{20} \text{ cm}^{-3}$	0.93 $1 \times 10^{20} \text{ cm}^{-3}$
	<i>n</i> -type	0.58 $3 \times 10^{19} \text{ cm}^{-3}$	0.73 $4 \times 10^{19} \text{ cm}^{-3}$	0.62 $2 \times 10^{19} \text{ cm}^{-3}$	0.84 $2 \times 10^{19} \text{ cm}^{-3}$

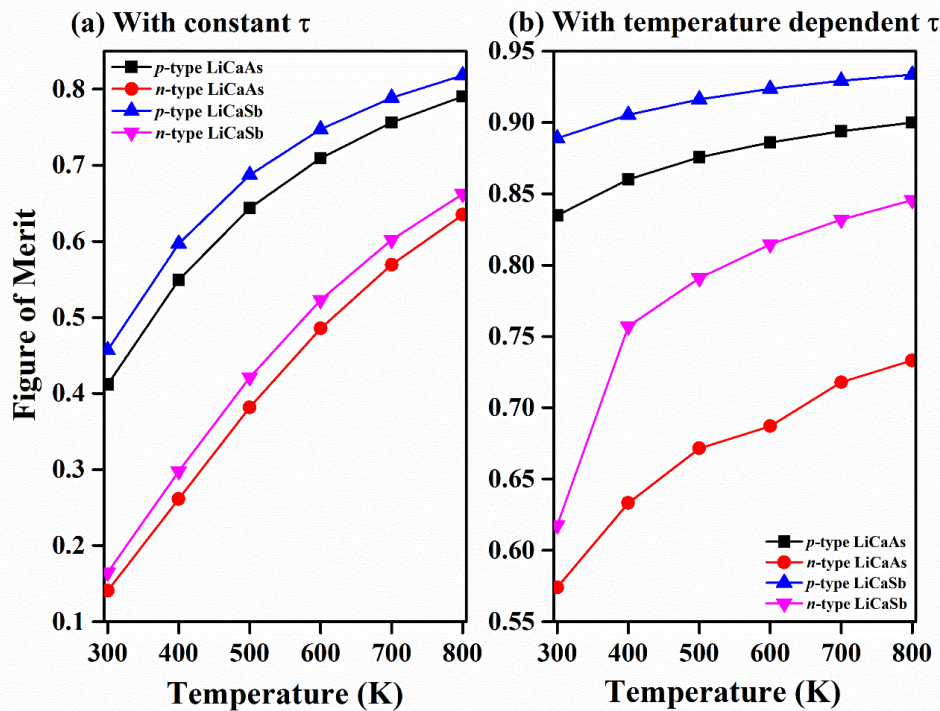


**Figure 4.15** The variation in Figure of Merit with temperature (a) within constant relaxation time approximation (b) with temperature dependent relaxation time of carriers for *p*-type and *n*-type LiCaAs and LiCaSb

## 4.5 Summary

We have used first-principles calculations in conjunction with semi-classical Boltzmann approach, density functional perturbation technique and *ab-initio* molecular dynamics to explore electronic, transport, phononic, and thermal properties of 8-VEC Li-based HH compounds LiCaX (X = As, Sb). We have also calculated temperature-dependent relaxation time using deformation potential theory. Our calculations have validated the high temperature stability and dynamical stability of these compounds. We found that both LiCaAs and LiCaSb are indirect band gap semiconductors having band gaps, respectively, of 2.52 eV and 2.09 eV estimated using TB-mBJ potential. The value of the Seebeck coefficient is found to be higher in *p*-type LiCaX than that of *n*-type due to flat VB edges. TE performance is slightly enhanced with an increase in atomic weight of X atom owing to low  $\kappa_l$  and significant power factor. The room temperature  $\kappa_l$  values for LiCaSb and LiCaAs have found to be 1.42 Wm<sup>-1</sup>K<sup>-1</sup> and 1.90 Wm<sup>-1</sup>K<sup>-1</sup>, respectively, but these values have decreased to 0.66 Wm<sup>-1</sup>K<sup>-1</sup> and 0.88 Wm<sup>-1</sup>K<sup>-1</sup> at 800 K. The remarkably low  $\kappa_l$  of 8-VEC HH compounds LiCaX (X = As, Sb), which has been understood in terms of different phonon modes, and optimization of carrier concentration resulted into an improved ZT at higher temperature. The optimized carrier concentration ( $\sim 10^{20}$  cm<sup>-3</sup> for *p*-type carriers and  $\sim 10^{19}$  cm<sup>-3</sup> for *n*-type carriers) of the investigated compounds have found to be comparable to experimentally estimated value for other 8-VEC Li-based HH. Our calculations have predicted that the *p*-type HH alloys LiCaX are promising thermoelectric materials. We are optimistic that this work could lead to future experiments to investigate the thermoelectric properties of proposed Li-based half-Heusler alloys.



# CHAPTER 5: THERMOELECTRIC PROPERTIES AND LATTICE DYNAMICS OF $\text{Li}_2\text{MN}_2$ ( $\text{M} = \text{Zr}, \text{Hf}$ )

---

## 5.1 Introduction

As discussed in Chapter 1, it is difficult to manipulate the transport parameters simultaneously due to their interdependence. Therefore, researchers are constantly looking for new materials having high  $ZT$  and/or effective strategies that can enhance the TE performance of existing materials [12]. Heusler alloys [159–161], Zintl compounds [162–164], oxides- and nitrides-based materials [63,165–167] are under intense research for their TE properties. Among these, nitride semiconductors are highly attractive owing to their potential for environmental sustainability, utilization of readily available elements, and desirable electronic properties [62]. Extensive research has been conducted to explore the early-transition metal nitrides, such as ScN and CrN, and various methods implemented to enhance their performance for their potential use in TE applications [168–170]. Investigations have been carried out into the TE properties of epitaxial ScN films deposited by magnetron sputtering onto MgO (001) substrates [171]. Enhanced transport properties in ScN have been achieved through electronic structure engineering via stoichiometry tuning and doping. Saha et al. have examined the temperature-dependent thermal and TE properties of n- and p-type  $\text{Sc}_{1-x}\text{Mg}_x\text{N}$  thin film alloys up to 850 K [172]. Furthermore, a high  $ZT$  value of 1.5 has been attained in a ZrN/ScN superlattice [173]. These studies shed light on the crucial role of nitride semiconductors in TE applications, offering potential improvements in energy conversion efficiency and sustainability. Further, layered nitrides are of much interest regarding TE energy conversion as they favour anisotropic properties that ultimately enable the tuning of transport properties [64,65]. In a study, Ohkubo et al. have found that the transport properties of  $\text{NaTaN}_2$ , which exhibits an anisotropic character are potentially superior to that of isotropic  $\text{KTaO}_3$  [174].

This chapter aims to investigate the TE properties of Zr- and Hf-based nitride (i.e.,  $\text{Li}_2\text{MN}_2$ ) to analyze their structural properties, electronic structures, transport properties, and potential for utilization in TE applications. Furthermore, it is interesting to see the effect of Hf replacing the transition metal (M) Zr. Generally, the heavy elements result in a reduced frequency of acoustic phonons [175,176], decreased group velocity, and suppressed lattice thermal conductivity.



Previous studies identified heavy element usage as a viable approach to suppress lattice thermal conductivity and, consequently, the enhanced  $ZT$  value [177,178]. However, materials containing heavy elements don't always need to have lower lattice thermal conductivity than those containing light elements. The lattice thermal conductivity depends on both the phonon group velocity, which is associated with mass, and the phonon relaxation time, associated with anharmonicity and scattering rate. Our results reveal the underlying mechanisms responsible for the high thermal transport properties observed in materials containing heavy elements and offer an alternative way to design materials with low lattice thermal conductivity for TE applications.

## 5.2 Computational Details and Methodology

The first-principles calculations were performed using the full potential linearized augmented plane wave method implemented in the WIEN2k code [147]. The exchange correlational functional GGA-PBE was used for structural optimization [82]. A Gamma-centred k-mesh of  $17 \times 17 \times 9$  was used to sample the Brillouin zone (BZ). The cut-off energy of valence and core states was set to -6 Ry. The Kohn-Sham equations were solved self-consistently until an energy convergence of 0.0001 Ry/cell was achieved. The more accurate TB-mBJ functional was used for electronic and transport properties, as in most cases, GGA underestimates the band gap of semiconductors [114]. The TE properties were calculated by solving the BTE under the constant relaxation time approximation as implemented in the BoltzTraP code. We employed the finite displacement method to derive the second-order harmonic interatomic force constants (IFCs) and the phonon structure. A  $3 \times 3 \times 1$  supercell was utilized on an  $8 \times 8 \times 3$  k-mesh, and the phonopy code [179] was interfaced with the VASP [145] for this purpose. The Phono3py code [179] was used to evaluate anharmonic third-order IFCs, and the interactions up to the fourth-closest neighbour were taken. The phonon Boltzmann equations were solved self-consistently using a dense  $20 \times 20 \times 20$   $q$ -mesh to calculate the lattice thermal conductivity.

## 5.3 Results and Discussion

### 5.3.1 Structural Properties

$\text{Li}_2\text{MN}_2$  ( $\text{M} = \text{Zr}$  or  $\text{Hf}$ ) crystallizes in the anti- $\text{La}_2\text{O}_3$  trigonal structure [180,181] with the  $P\bar{3}m1$  space group (no. 164). The M atoms occupy Wyckoff positions  $1a$  (0, 0, 0), whereas the Li and N atoms occupy the Wyckoff positions  $2d$  (2/3, 1/3, 0.381139) and  $2d$  (2/3, 1/3, 0.775853), respectively, as shown in **Figure 5.1**.  $\text{Li}^{1+}$  is bonded to four equivalent  $\text{N}^{3-}$  atoms to form distorted  $\text{LiN}_4$  tetrahedra, having three shorter and one longer Li–N bond length.  $\text{M}^{4+}$  is bonded

to six equivalent  $\text{N}^{3-}$  atoms to form  $\text{MN}_6$  octahedra, with all M–N having the same bond lengths. The bond length, Zr–N, is 2.267 Å, greater than the sum of Zr and N covalent radii, i.e., 2.23 Å, which indicates that the Zr atom is located over the  $\text{ZrN}_6$  octahedra. As a result, the Zr atoms act as a heavy rattler that will strongly scatter the acoustic phonons. On the other hand, the Hf–N bond length is smaller than that of Hf and N covalent radii (2.25 Å); therefore, it is expected that  $\text{Li}_2\text{ZrN}_2$  will have superior lattice transport properties. The optimization of total energy vs. strain (deviation from initial structure) gives the optimized lattice constants and unit cell volume. In **Table 5.1**, we summarize our optimized structural data for both materials and compare them with the available experimental data. The structural parameters (such as the bond lengths and lattice parameters) agree with the previously reported experimental values [180]. We used the optimized structures for further calculations.

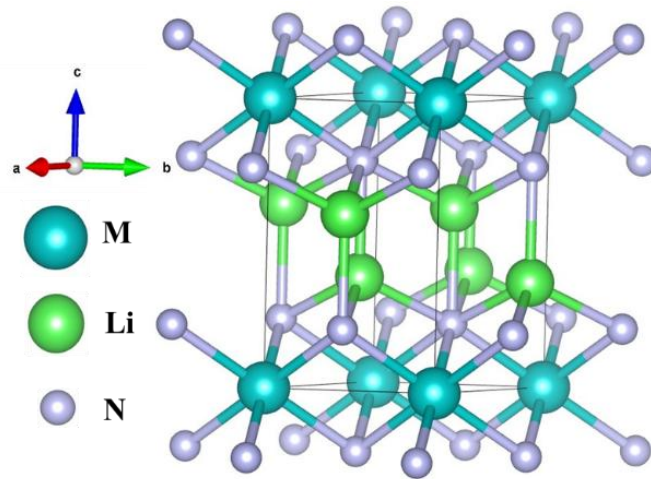


**Figure 5.1** The geometrical structure of  $\text{Li}_2\text{MN}_2$  (M = Zr or Hf).

**Table 5.1** The optimized lattice parameters (in Å) and bond lengths (in Å) of  $\text{Li}_2\text{MN}_2$  (M = Zr or Hf), along with available experimental values.

System		$a=b$	$c$	Bond Lengths		
				Li-N	M-N	M-Li
$\text{Li}_2\text{ZrN}_2$	Present work	3.299	5.489	2.090, 2.167	2.267	2.829
	Experiment [180]	3.285	5.461	2.098, 2.268	2.253	2.840
$\text{Li}_2\text{HfN}_2$	Present work	3.261	5.474	2.080, 2.180	2.235	2.813
	Experiment [180]	3.246	5.427	-	-	-

### 3.2 Stability Analysis

Following the structural optimization, we examine the thermodynamic stability of  $\text{Li}_2\text{MN}_2$  ( $\text{M} = \text{Zr}$  or  $\text{Hf}$ ) by computing their formation energies ( $E_{for}$ ) using the equation [182] given as:

$$E_{for} = \frac{[E_{\text{Li}_2\text{MN}_2} - (2E_{\text{Li}} - E_{\text{M}} - 2E_{\text{N}})]}{n} \quad (5.1)$$

where  $E_{\text{Li}_2\text{MN}_2}$  is the ground state energy of  $\text{Li}_2\text{MN}_2$ ,  $E_{\text{Li}}$ ,  $E_{\text{M}}$ , and  $E_{\text{N}}$  are total energy per atom for Li, M, and N, respectively, in their solid form, and  $n$  denotes the total number of atoms in their unit cell. The calculated  $E_{for}$  for  $\text{Li}_2\text{ZrN}_2$  and  $\text{Li}_2\text{HfN}_2$  are found to be -1.148 and -1.230 eV/atom, respectively, indicating that both the compounds are energetically stable.

Next, to investigate the dynamical stability of the proposed structures, we computed the phonon dispersion spectra using the finite displacement method. The results are shown in **Figure 5.2**; the absence of negative frequencies in both structures confirms that they are dynamically stable. There are five atoms in each unit cell, which means there is a total of 15 phonon branches, of which 3 are low-frequency acoustic branches (in-plane Longitudinal Acoustic (LA) and Transverse Acoustic (TA) and out-of-plane Transverse Acoustic (ZA)) and 12 are optical branches. The  $\text{D}_{3h}$  symmetry of both structures results in nondegenerate and twofold-degenerate modes at the  $\Gamma$  point. As shown in **Figure 5.2**, there are six distinct eigenmodes that can be used to describe the optical spectrum. The four optical modes are nondegenerate (A modes), and four are twofold-degenerate (E modes) for both compounds. The overall characteristics of the phonon dispersion of both compounds are almost similar, with only a slight frequency shift. Additionally, no phonon bandgap is observed, which suggests a coupling between the acoustic LA mode and low-frequency optical modes. A coupling between the modes indicates that phonons scatter more easily between the acoustic and optical branches, resulting in a lower phonon lifetime and, consequently, a low lattice thermal conductivity. This coupling is observed more in  $\text{Li}_2\text{ZrN}_2$  owing to the proximity of its LA branch at 8.6 THz and low-frequency optical branch at 5.7 THz. Further, to analyse the atomic contribution to the acoustic and optical modes, the phonon density of states is obtained, as shown in **Figure 5.3**. The high-frequency region is mainly attributed by the oscillations of light-mass Li and N atoms. Both Zr and Hf contribute to the low-frequency acoustic modes due to heavier atomic mass. Also, the coupling between acoustic and optical branches in frequency range 5.5-8.5 THz in  $\text{Li}_2\text{ZrN}_2$  is primarily contributed by the oscillations of Zr atoms, that might lead to low lattice thermal conductivity.

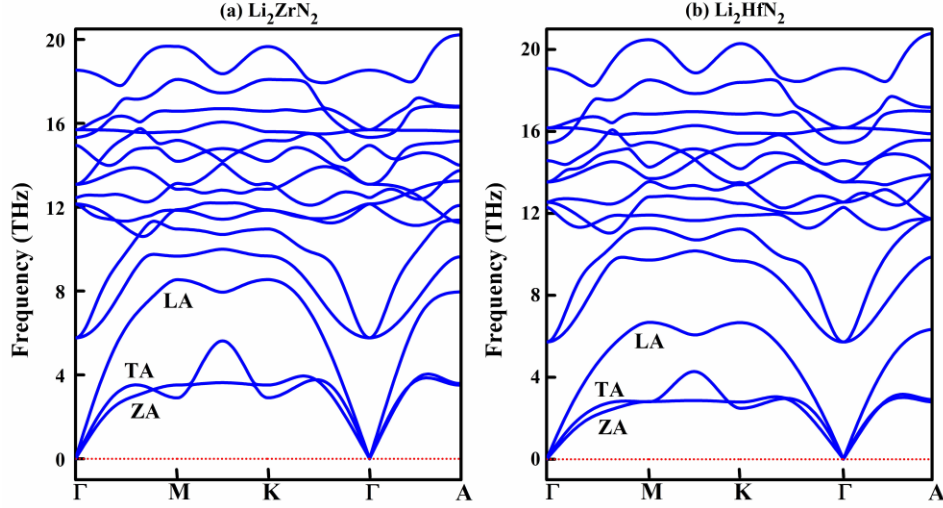


**Figure 5.2** The phonon dispersion curves of (a)  $\text{Li}_2\text{ZrN}_2$  and (b)  $\text{Li}_2\text{HfN}_2$ .

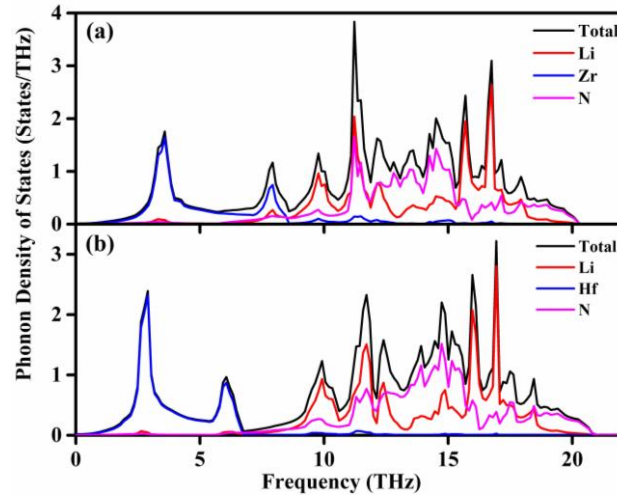


**Figure 5.3** The total and projected phonon density of states of (a)  $\text{Li}_2\text{ZrN}_2$  and (b)  $\text{Li}_2\text{HfN}_2$ .

### 5.3.2 Electronic Properties

The electronic band structure calculated using TB-mBJ of the investigated systems reveals that both are semiconductors, as shown in **Figure 5.4**. The conduction band minima are located at the high symmetry M point. In contrast, the valence band maxima are present at the  $\Gamma$  point. Therefore, an indirect band gap of 2.402 eV and 2.963 eV is observed for  $\text{Li}_2\text{ZrN}_2$  and  $\text{Li}_2\text{HfN}_2$ , respectively, which are found even smaller than other nitrides such as  $\text{Ca}_5\text{Sn}_2\text{N}_6$  (3.55 eV),  $\text{Sr}_5\text{Ge}_2\text{N}_6$  (3.15) [183],  $\text{ZnZrN}_2$  (2.77 eV), and  $\text{ZnHfN}_2$  (3.31 eV) [184] that have shown good TE performance. Because of the indirect band gap, these materials must absorb a low-energy phonon with high directional momentum to pass electrons through the band gap. The significant band gap value obtained will help to reduce the bipolar effect in TE.

To gain further insight in the electronic properties of these compounds, the density of states is obtained as depicted in **Figure 5.5 (a)-(d)**. In both compounds, the valence band (VB) is mainly

contributed by the N atom, while the conduction band (CB) is primarily contributed by the M (Zr and Hf) atoms. The sharp peaks at VB maxima for both compounds are observed, which indicates that the high Seebeck coefficient might be observed. The slight contribution of Zr in VB and N in CB, and the negligible contribution of Li atoms are observed in both CB and VB. Further, the orbital contribution can be analyzed from projected DOS (**Figure 5.5 c and d**). The N-*p* and the M-*d* majorly contribute to the top of VB and the bottom of the CB, respectively.

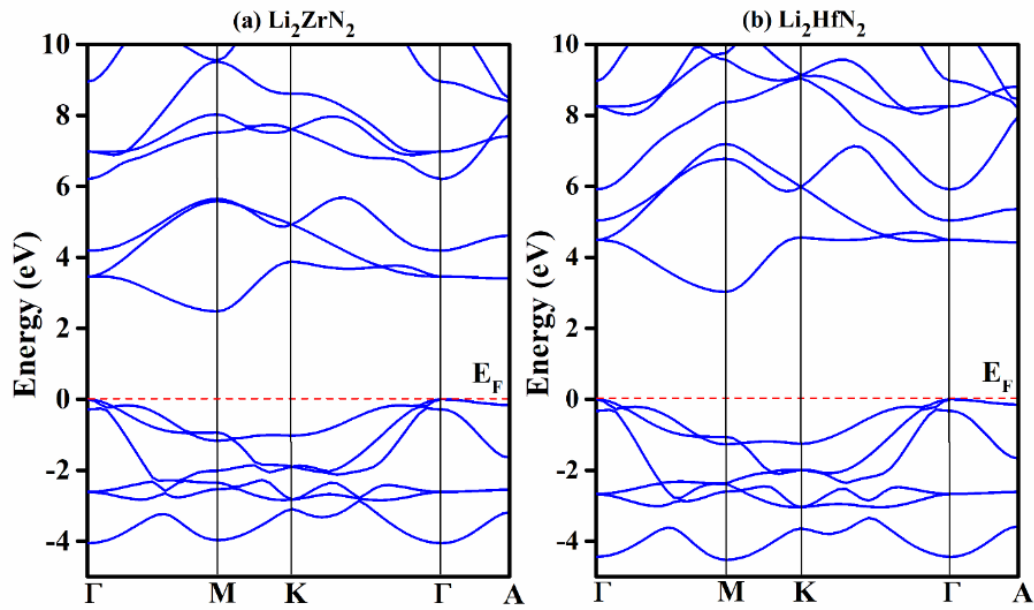


**Figure 5.4** The electronic band structure along the high symmetry K-path  $\Gamma$ -M-K- $\Gamma$ -A of  $\text{Li}_2\text{MN}_2$  (M = Zr or Hf) calculated using TB-mBJ. The Fermi level is set to 0 eV.

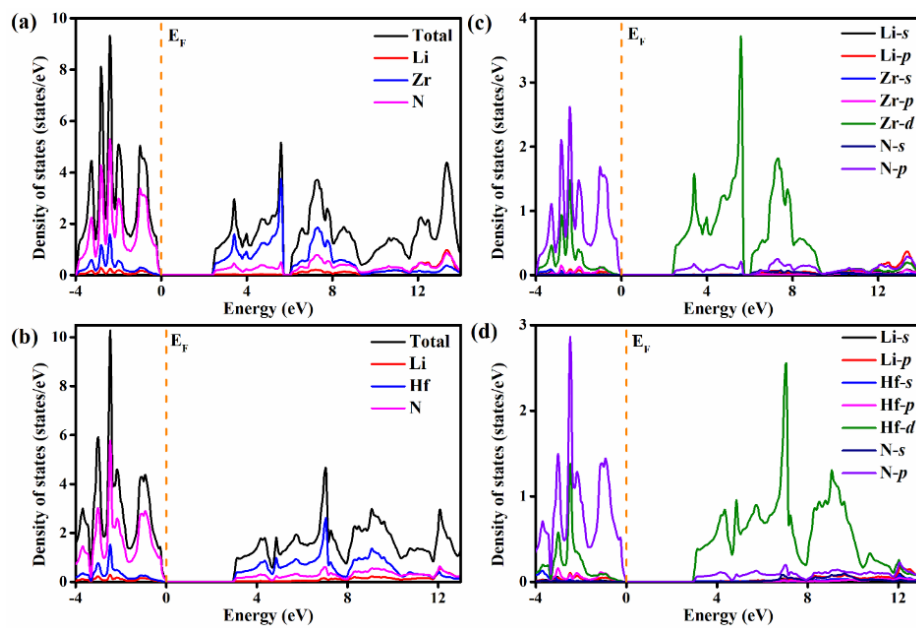


**Figure 5.5** (a)-(d) The density of states of  $\text{Li}_2\text{MN}_2$  (M = Zr or Hf) calculated using TB-mBJ. The Fermi level is set to 0 eV.

### 5.3.3 Transport Properties

The transport properties of  $\text{Li}_2\text{MN}_2$  are calculated via Boltzmann transport theory along the *a*- and the *c*-axes as a function of temperature from 300 K to 1000 K. **Figure 5.6 (a)–(d)** illustrates the graphical representation of TE parameters with temperature. It can be observed that these parameters exhibit strong anisotropic behaviour for both systems. The variation in  $S$  with temperature (**Figure 5.6 (a)**), for both compounds, is trivial along the *a*-axis, whereas it is quite noticeable along the *c*-axis. The maximum values observed for  $\text{Li}_2\text{ZrN}_2$  and  $\text{Li}_2\text{HfN}_2$  are 306.71 and 326.91  $\mu\text{VK}^{-1}$ , respectively, at 1000 K along the *c*-axis. These values are found to be larger than those previously reported for nitride compounds of the type  $\text{AMN}_2$ , where  $A = \text{Ca, Sr, and Ba}$ , and  $M = \text{Ti, Zr, Hf}$  ( $\sim 150 \mu\text{VK}^{-1}$ ) [64], as well as for compounds like  $\text{Sr}_3\text{SbN}$  (257  $\mu\text{VK}^{-1}$ ),  $\text{Sr}_3\text{BiN}$  (142  $\mu\text{VK}^{-1}$ ) [167], and  $\text{ZnTMN}_2$  with  $\text{TM} = \text{Zr and Hf}$  (with values ranging from 220 to 275  $\mu\text{VK}^{-1}$ ) [184]. The electrical conductivity of both compounds increases with the increase in temperature, as illustrated in **Figure 5.6 (b)**. Strong anisotropy in the electrical conductivity of both compounds is observed, with  $\sigma/\tau$  values along the *a*-axis much higher than that along *c*. Moreover,  $\sigma/\tau$  of  $\text{Li}_2\text{HfN}_2$  along the *a*-axis is slightly greater than  $\text{Li}_2\text{ZrN}_2$ . At room temperature, the  $\sigma/\tau$  values for  $\text{Li}_2\text{HfN}_2$  and  $\text{Li}_2\text{ZrN}_2$  are 0.23 and  $0.21 \times 10^{19} \Omega^{-1}\text{m}^{-1}\text{s}^{-1}$ , respectively. These values increase to 1.45 and  $1.43 \times 10^{19} \Omega^{-1}\text{m}^{-1}\text{s}^{-1}$ , respectively, when the temperature is raised to 1000 K. The  $\kappa_e/\tau$  of  $\text{Li}_2\text{ZrN}_2$  exhibits a positive correlation with temperature, as shown in **Figure 5.6 (c)** because with rising temperature, the electrons undergo thermal excitations which results in their thermal conductivity augmentation. A slight variation in  $\kappa_e/\tau$  values of both systems is observed along the *a*-axis, whereas this variation is significant along the *c*-axis. The room temperature values of  $\kappa_e/\tau$  along the *c*-axis are 0.09 and  $0.02 \times 10^{14} \text{Wm}^{-1}\text{K}^{-1}\text{s}^{-1}$  for  $\text{Li}_2\text{ZrN}_2$  and  $\text{Li}_2\text{HfN}_2$ , respectively. The power factor ( $S^2\sigma/\tau$ ) values show a positive relationship with rising temperature, as depicted in **Figure 5.6 (d)**. The anisotropic trend between the *a*- and *c*- axes, as observed in the electrical and thermal conductivity, is also visible here. Our findings show that  $\text{Li}_2\text{ZrN}_2$  has slightly higher PF values than  $\text{Li}_2\text{HfN}_2$  at higher temperatures. The promising PF is observed for both compounds along the *a*-axis. Also, at higher temperatures, it is found that the PF are significantly increased, indicating that these compounds are appropriate for high-temperature TE applications. At 1000 K, the  $\text{Li}_2\text{ZrN}_2$  and  $\text{Li}_2\text{HfN}_2$  materials exhibit maximum values of  $0.84 \times 10^{12}$  and  $0.89 \times 10^{12} \text{Wm}^{-1}\text{K}^{-2}\text{s}^{-1}$ , respectively, along the *a*-axis.

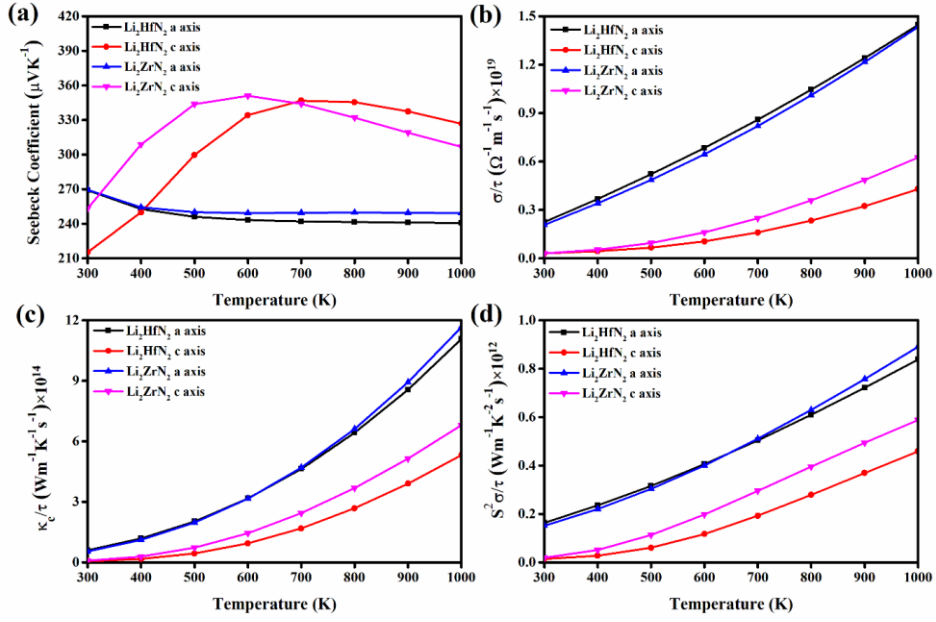


**Figure 5.6** The calculated (a) Seebeck coefficient ( $S$ ), (b) Electrical conductivity ( $\sigma/\tau$ ), (c) Electronic thermal conductivity ( $\kappa_e/\tau$ ), and (d) Power factor ( $S^2\sigma/\tau$ ) of  $\text{Li}_2\text{MN}_2$  ( $M = \text{Zr}$  or  $\text{Hf}$ ).

To evaluate the precise TE figure of merit, it is imperative to elucidate the lattice dynamics of investigated compounds by calculating the lattice thermal conductivity and other associated properties. Using the single-mode relaxation-time approximation,  $\kappa_l$  is calculated as a sum of contributions from individual phonon modes  $\lambda$  according to the equation [100]:

$$\kappa_l = \frac{1}{NV} \sum_{\lambda} C_{\lambda} v_{\lambda} \otimes v_{\lambda} \tau_{\lambda} \quad (5.2)$$

where  $V$  is the volume of the unit cell and  $N$  is the number of phonons wavevectors,  $C_{\lambda}$  are the heat capacities,  $v_{\lambda} \otimes v_{\lambda}$  are the tensor products of the group velocities, and  $\tau_{\lambda}$  are the lifetimes. Therefore, we analysed the phonon dispersion and calculated lattice thermal conductivity, group velocity and phonon lifetime for both compounds. The effect of temperature on the lattice thermal conductivity of  $\text{Li}_2\text{MN}_2$  is shown in **Figure 5.7 (a and b)**. The  $\kappa_l$  and average  $\kappa_l$  decrease with the increase in the temperature because of Umklapp scattering at higher temperature. The findings indicate that  $\text{Li}_2\text{ZrN}_2$  exhibits intrinsic lattice thermal conductivity values of 1.52 and 0.93  $\text{W m}^{-1}\text{K}^{-1}$  along the  $a$ - and  $c$ - axes, respectively, at a temperature of 1000 K, and the corresponding values 1.97 and 0.93  $\text{W m}^{-1}\text{K}^{-1}$  for  $\text{Li}_2\text{HfN}_2$ . The average value of  $\kappa_l$  at 1000 K is observed as 1.22 and 1.45  $\text{W m}^{-1}\text{K}^{-1}$  for  $\text{Li}_2\text{ZrN}_2$  and  $\text{Li}_2\text{HfN}_2$ , respectively. The value of  $\kappa_l$  is found to be much lower than that of other anisotropic nitride materials, such



as NaTa<sub>2</sub>N<sub>2</sub> (11.42 Wm<sup>-1</sup>K<sup>-1</sup>), NaNbN<sub>2</sub> (13.37 Wm<sup>-1</sup>K<sup>-1</sup>), CuTa<sub>2</sub>N<sub>2</sub> (9.59 Wm<sup>-1</sup>K<sup>-1</sup>), and CuNbN<sub>2</sub> (10.86 Wm<sup>-1</sup>K<sup>-1</sup>) [174]. It is also comparable to or less than oxide materials like BaTiO<sub>3</sub>, PbTiO<sub>3</sub>, KNbO<sub>3</sub>, KTaO<sub>3</sub>, and NaNbO<sub>3</sub>, whose thermal conductivity have been measured from 2 to 390 K [185].

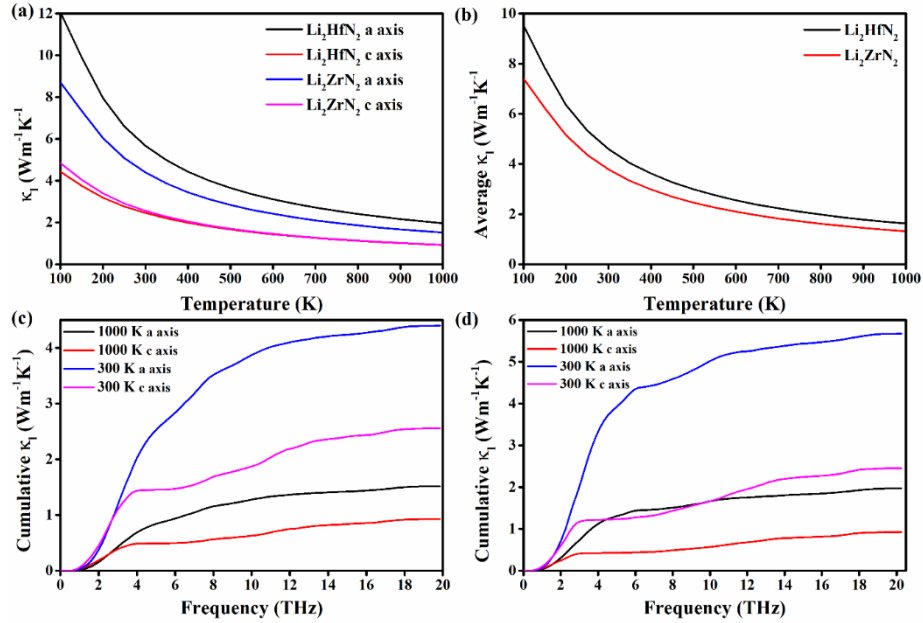


**Figure 5.7** (a) Lattice thermal conductivity, (b) average lattice thermal conductivity, (c), and (d) cumulative lattice thermal conductivity of Li<sub>2</sub>ZrN<sub>2</sub> and Li<sub>2</sub>HfN<sub>2</sub>, respectively.

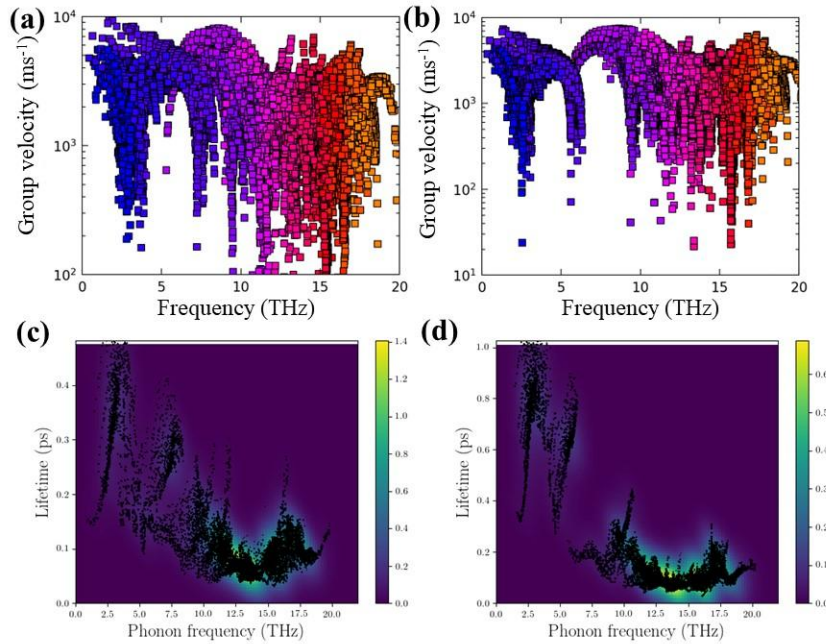


**Figure 5.8** Calculated phonon group velocities of (a) Li<sub>2</sub>ZrN<sub>2</sub> (b) Li<sub>2</sub>HfN<sub>2</sub> at 1000 K. Calculated phonon lifetimes of (c) Li<sub>2</sub>ZrN<sub>2</sub> and (d) Li<sub>2</sub>HfN<sub>2</sub> at 1000 K. The colour bar in the figure represents the phonon density. A brighter colour means a higher phonon density.



We have obtained the cumulative  $\kappa_l$  (**Figure 5.7 c and d**) to explore the origin of the low value of  $\kappa_l$ . For  $\kappa_l$  at 300 K along the *a*- and *c*-axes, the frequency-dependent cumulative  $\kappa_l$  shows a sharp increase originating from the acoustic phonon modes, followed by a slight increase from the low-frequency optical modes and then converges. Further investigations suggest that the optical phonons contribute over 35% and 50% to the lattice thermal conductivity of  $\text{Li}_2\text{ZrN}_2$  and  $\text{Li}_2\text{HfN}_2$ , respectively. It indicates the presence of a coupling effect between acoustic and low-lying optical phonon modes, resulting in a restriction of the contribution of acoustic phonons to lattice thermal conductivity.

To unravel the unusual phenomenon that  $\text{Li}_2\text{MN}_2$  compound containing light element has a lower  $\kappa_l$  than a heavy element, we first calculated their group velocity as shown in **Figure 5.8 (a and b)**. The group velocities of  $\text{Li}_2\text{HfN}_2$  are comparatively lower than those of  $\text{Li}_2\text{ZrN}_2$ , consistent with their masses. However, it fails to account for the unusual lattice thermal conductivities exhibited by these materials. Therefore, the frequency-dependent phonon lifetimes are calculated to gain insight into the low and unusual thermal conductivity observed in  $\text{Li}_2\text{ZrN}_2$  than  $\text{Li}_2\text{HfN}_2$ . From **Figure 5.8 (c and d)**, it can be observed that the phonon lifetime of low-frequency phonon modes is much longer than that of high-frequency modes for both compounds. It means that the acoustic phonon modes contribute mainly to thermal transport, which is also consistent with the analysis of the frequency contribution to  $\kappa_l$ . Based on the outcomes of frequency-dependent lattice thermal conductivities, it can be inferred that a shorter lifetime contributes to the comparatively lower thermal conductivity of  $\text{Li}_2\text{ZrN}_2$  compared to  $\text{Li}_2\text{HfN}_2$ . The shorter lifetime in  $\text{Li}_2\text{ZrN}_2$  is due to the Zr atoms acting as a heavy rattler that will strongly scatter the acoustic phonons. The lanthanide contraction, which causes strong interatomic bonding, leads to a greater phonon lifetime. It means the substitution of Zr with the heavier element Hf in  $\text{Li}_2\text{ZrN}_2$  does not result in a reduction of the lattice thermal conductivity. On the contrary, it leads to a notable increase in  $\kappa_l$  of  $\text{Li}_2\text{HfN}_2$ . The relatively higher lattice thermal conductivity in  $\text{Li}_2\text{HfN}_2$  is primarily ascribed to the significant rise in phonon lifetime as lanthanide contraction causes strong interatomic bonding. This unusual behaviour is also shown in previously reported Zr- and Hf-based nitride halides [186]. Thus, even though  $\text{Li}_2\text{ZrN}_2$  exhibits higher phonon group velocities, its lattice thermal conductivity is lower than that of  $\text{Li}_2\text{HfN}_2$ .

We determined the  $ZT$  using values of  $S$ ,  $\sigma$  and  $\kappa_t$  for both compounds along the two different crystallographic axes, as shown in **Figure 5.9**. As BoltzTraP code [95] is based on constant relaxation time approximation, it gives  $\sigma$  and  $\kappa_e$  in terms of  $\tau$ . In our study, we obtained  $\sigma$  and  $\kappa_e$  by employing  $\sigma/\tau$  and  $\kappa_e/\tau$ , respectively, using  $\tau = 10^{-14}$  s. This value has been utilized in previous studies as well [159,163,166,167]. The  $\kappa_t$  is computed by combining the contributions from both the electronic and lattice parts of thermal conductivity. We observe that the  $ZT$  of  $\text{Li}_2\text{ZrN}_2$  is higher than that of  $\text{Li}_2\text{HfN}_2$ , owing to its low lattice thermal conductivity. Also, it is observed that in  $\text{Li}_2\text{ZrN}_2$ , the  $a$ -axis shows a higher  $ZT$  value compared to the  $c$ -axis showing a strong anisotropy. The  $ZT$  value reached 1.07 and 0.64 along the  $a$ -axis at 1000 K for  $\text{Li}_2\text{ZrN}_2$  and  $\text{Li}_2\text{HfN}_2$ , respectively. Despite the large power factor of  $\text{Li}_2\text{HfN}_2$ , it could not benefit high  $ZT$  because of its unusual high lattice thermal conductivity.  $\text{Li}_2\text{ZrN}_2$  appears as an intriguing alternative to well-established TE materials since its  $ZT$  value exceeds 1. As shown in **Figure 5.9 (b)**, the average  $ZT$  increases with the increasing temperature, and the maximum value of  $ZT$  at 1000 K for  $\text{Li}_2\text{ZrN}_2$  and  $\text{Li}_2\text{HfN}_2$  are 0.92 and 0.68, respectively. The high  $ZT$  value is higher than other ternary nitride materials [167,172]. This indicates  $\text{Li}_2\text{MN}_2$  as efficient materials for future TE applications.

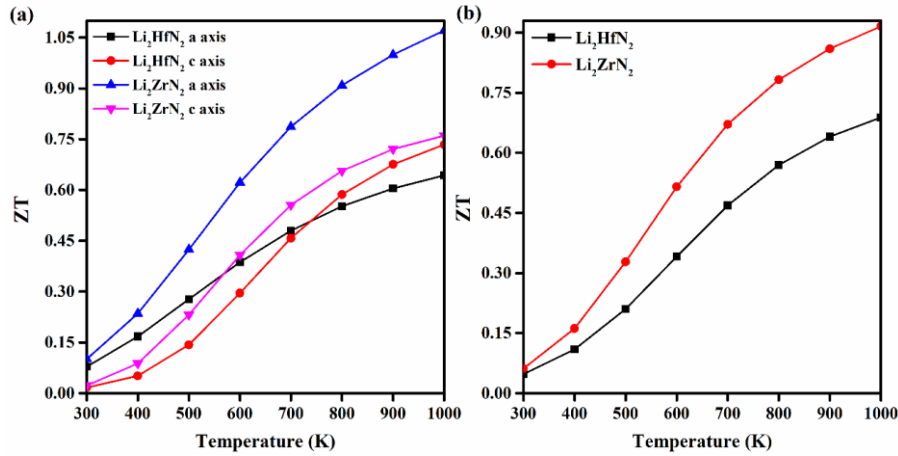


**Figure 5.9** The variation of (a)  $ZT$  along  $a$ - and  $c$ - axes of  $\text{Li}_2\text{MN}_2$  ( $M = \text{Zr}$  or  $\text{Hf}$ ) and (b) average  $ZT$  with temperature.

## 5.4 Summary

In conclusion, we have explored the role of lattice dynamics on thermal transport in transition metal nitrides  $\text{Li}_2\text{MN}_2$  ( $M = \text{Zr}$  and  $\text{Hf}$ ). These materials have been synthesized long ago, but no study is available regarding their thermoelectric properties. We have used first-principles calculations in conjunction with Boltzmann transport theory to understand the role of lattice dynamics in realizing high thermoelectric performance in  $\text{Li}_2\text{MN}_2$ . We have analyzed how

replacing Zr with the relatively heavy element Hf in  $\text{Li}_2\text{MN}_2$  leads to an increase in thermal conductivity instead of a decrease, which is against the common notion. The calculated cell parameters and various bond lengths are in accordance with previous experimental study. The thermodynamic and dynamical stability has been ascertained before calculating the electronic and transport properties of both systems. We have obtained a lower lattice thermal conductivity ( $1.52 \text{ Wm}^{-1}\text{K}^{-1}$ ), compared to  $\text{Li}_2\text{HfN}_2$ , along  $a$ -axis at 1000 K for  $\text{Li}_2\text{ZrN}_2$  which has been attributed to the rattling behaviour of Zr that leads to shorter phonon lifetimes. Moreover, the anisotropic character owing to the layered structure of  $\text{Li}_2\text{MN}_2$  has enabled tuning their transport properties. Therefore, a high power factor has been obtained along the  $a$ -axis for both compounds, which resulted in high  $ZT$  in this direction. The high figure of merit (1.07) of  $\text{Li}_2\text{ZrN}_2$  along the  $a$ -axis has unravelled its potential for high-temperature thermoelectric application. These calculations have provided valuable insights into the vibrational properties, including the phonon group velocities, phonon lifetime and phonon frequencies that govern the thermal conductivity and the phonon-mediated heat transport. Our findings on the electronic and lattice transport properties of  $\text{Li}_2\text{MN}_2$  may open new horizons for the design and synthesis of more efficient nitride-based thermoelectrics.

# CHAPTER 6: REALIZATION OF YX (X = N, P, As) PNICTIDE MONOLAYERS AS HIGHLY EFFICIENT THERMOELECTRIC MATERIALS

---

## 6.1 Introduction

In Chapter 1, we discussed reducing the dimensionality has been considered an important approach for enhancing TE performance and it was proposed first by Hicks and Dresselhaus [24,187]. Since the discovery of graphene, two-dimensional (2D) systems have gained extensive attention because of their interesting electronic, mechanical, transport, and optical properties and their promising applications in optoelectronics, energy storage and conversion devices [15,188–190]. The 2D systems with anisotropic properties have gained extensive consideration as efficient TE materials [15,67,68,191–195]. Beginning from the later part of the last decade, several computational studies have suggested the potential for developing  $d'$  transition metal pnictides into a new family of prospective TE materials owing to the strong  $p$ - $d$  hybridization in these materials, which leads to dispersive band edges and consequently, high carrier mobilities in these semiconductors. Specifically, Kaur et al. have found ultra-high to high carrier mobility that gives rise to large  $\sigma$  ( $\sim 10^8 \text{ S m}^{-1}$ ) and low to moderate intrinsic lattice thermal conductivities in puckered ScP and ScAs monolayers [196]. Also, the study of Zheng et al. reveals high carrier mobilities in the hexagonal phase of YN, with hole (electron) mobility reaching  $10^3$  ( $10^4$ )  $\text{cm}^2\text{V}^{-1}\text{s}^{-1}$  [193]. Recently, Loyal et al. reported the rare-earth semiconducting YbN thin films, exhibiting a large TE power factor ( $PF$ ) of  $1.93 \text{ mWm}^{-1}\text{K}^{-2}$ , attributed to high  $\sigma$  and a moderately high  $S$  at 750 K [197]. Additionally, rare-earth-based 2D materials possess high thermal and mechanical stability, which advocates their room temperature and elevated-temperature TE applications. For example, ScX (X= N, P, As, Sb) have been extensively studied for their strong anisotropic mechanical, electronic and TE properties [63,170,171,195,196,198]. 2D monoclinic, hexagonal, and orthorhombic phases of ScN have been predicted to have high dynamical and thermal stability, indicating the practicability of experimental synthesis of these phases. In addition, hexagonal and monoclinic ScN, respectively, exhibit ultrahigh electron mobilities  $1.22 \times 10^4$  and  $3.09 \times 10^4 \text{ cm}^2 \text{ V}^{-1} \text{ s}^{-1}$ . Further particularly, orthorhombic ScN has been found to be a promising 2D ferroelastic and auxetic system [198]. Liu et al. found that monolayer ScN (110), bilayer ScN (100), monolayer YN (110), and bilayer YN (100), structures are stable thermodynamically. They exhibit

semiconducting properties, having band gaps ranging from 0.6 to 2.2 [199]. Experimentally, it has been found that ScN thin-film exhibits  $S$  of value  $-86 \mu\text{VK}^{-1}$  and a low resistivity of  $2.94 \mu\Omega\text{m}$ , resulting in a high  $PF$  of  $2.5 \text{ mWm}^{-1}\text{K}^{-2}$  [170]. Kerdsonpanya et al. have conducted both theoretical and experimental investigations into the  $\kappa_l$  of ScN thin films. The most significant influence observed is the reduction in  $\kappa_l$  associated with domain size, as indicated by the obtained values of  $20 \text{ Wm}^{-1}\text{K}^{-1}$  for single crystal and ranging from 4 to  $13 \text{ Wm}^{-1}\text{K}^{-1}$  for domain sizes 5–20 nm [200]. Recently, the 2D tetragonal YN monolayer has been identified as the ferroelastic semiconductor exhibiting low direct band gap. The ferroelasticity indicates that the anisotropies of this monolayer can be further influenced through the application of external stress. The effective mass anisotropic ratios across the two directions are 2.94 for electrons and 2.10 for holes, respectively [201]. In addition, Babaee Touski et al. have examined the structural, electronic, and optical tetragonal scandium- and yttrium-based pnictides monolayers, finding them as promising materials [202].

Motivated by these developments, we proposed similar rare-earth 2D TE materials: tetragonal-structured yttrium pnictides (YX; X = N, P, As) monolayers. The bulk of these materials have a rock-salt-like structure with  $\text{Fm}\bar{3}\text{m}$  space group. Amongst these, YN is an indirect band gap semiconductor, and rest are metals. It has been reported that 2D YX monolayers can be obtained from their bulk structure when exfoliated along the [110] direction [199,201,203]. In this chapter, we also show that carrier doping is an effective means to enhance the TE performance of YX (X = N, P, As). Furthermore, the insights gained into the electronic structure, lattice dynamics, and overall, TE performance of YX monolayers offer important strategies for designing novel 2D materials with improved TE performance. The results obtained can also pave the way for more focused studies on rare-earth-based monolayers for TE applications. We predicted large ZT values at 500 K, but the room-temperature performance of these monolayers is limited, which leaves scope for further material optimization.

## 6.2 Computational Details

The calculations were carried out using DFT, as implemented in VASP [145]. The projector augmented wave method was used to deal with the electron-ion interactions. The generalized gradient approximation within the parametrization of PBE was used for structural relaxation [82]. The HSE06 hybrid functional was used to compute the accurate electronic structure of YX (X = N, P, As) monolayers [86]. The cutoff energy for plane wave basis functions was set at 520 eV, and a width of 0.001 eV for Gaussian smearing was used. A vacuum of 20 Å was

used along  $z$ -axis to avoid inter-layer interactions. The BZ for these monolayers was sampled with  $13 \times 15 \times 1$  Monkhorst-Pack (MP)  $k$ -mesh. All the monolayers were relaxed completely till the force on each atom reaches less than  $0.001 \text{ eV \AA}^{-1}$ . To ensure accuracy, a strict convergence criterion for energy was fixed to  $1 \times 10^{-8} \text{ eV}$  for the self-consistent calculations. The harmonic phonon calculations for affirming the dynamical stability of the studied monolayers were performed employing a finite differences approach. For each of the studied materials, displaced structures corresponding to the  $4 \times 4 \times 1$  supercells of the materials were generated using the Phonopy package [179]. The sets of forces associated with the atoms of the displaced structures were found by performing self-consistent field calculations employing  $5 \times 5 \times 1$  MP meshes for BZ sampling. The thus obtained force sets for each material were used to extract the respective second-order interatomic force constants (IFCs) using Phonopy. To ensure the accuracy of the harmonic phonon analysis, particularly in the light of the 2D structure of these materials and the limitation of force constant extraction procedure of the Phonopy code, these originally extracted second order IFCs were corrected as a post-processing step by enforcing rotational sum rules, following the approach of Eriksson et al, using the Hiphive code [204]. The AIMD were performed using a  $5 \times 5 \times 1$  supercell to observe thermal and energy fluctuations, utilizing a time step of 1 fs using the NVT ensemble and with a Nose-Hoover thermostat for all three monolayers [146]. The electronic transport properties for YX ( $X = \text{N, P, As}$ ) monolayers were calculated using the semiclassical BTE under the CRTA and RBA utilizing BoltzTraP2 [96]. The charge carrier relaxation times at the considered temperatures were determined within the DPT of Bardeen and Shockley. [97]. The lattice thermal conductivities and other anharmonic phonon properties of YN monolayers were evaluated for the temperature 300-900 K. For the evaluation of second and third-order force constants to be used in these anharmonic phonon calculations, displaced structures corresponding to  $4 \times 4 \times 1$  supercells of the materials were created using the Phono3py code [32]. The self-consistent field calculations for obtaining Hellmann-Feynman forces on the atoms of the displaced structures were performed by employing  $5 \times 5 \times 1$  MP meshes for BZ sampling. The thus obtained force sets were used to extract second and third-order IFCs for each monolayer with the help of the Phono3py code. The work of Taheri et al. [205] illustrates the importance of accurately capturing the characteristics of the flexural acoustic (ZA) mode in the long wavelength limit to attain reliable prediction of lattice thermal conductivities [205,206]. Therefore, to ensure the reliability of calculated lattice thermal conductivities, we have applied corrections to these originally extracted force constants following the approach of Erikson et al., as implemented in the Hiphive [204]. In this approach, the parametrization for the interatomic potential based

on the originally extracted force constants is projected onto the correct subspace respecting the symmetries of the crystal structure, to get a new force constant potential from which the corrected force constants can be extracted. Finally, the  $\kappa_l$  of monolayers were obtained, with both single-mode relaxation time approximation (RTA) and solving full Peierls–Boltzmann transport equation (fPBTE) employing Phono3py for both cases [100,179]. We solved the fPBTE by directly diagonalizing the phonon collision matrices [103]. For both cases, we solved phonon BTE using a  $60 \times 60 \times 1$   $q$ -mesh to sample the BZ.

## 6.3 Results and discussion

### 6.3.1 Structural properties

2D YX (X=N, P, As) monolayers are having orthorhombic crystal structure with space group no. 59 ( $Pmmn$ ), exhibiting  $D_{2h}$  symmetry, as displayed in **Figure 6.1 (a)–(b)**. This structure consists of two Y atoms and two N atoms per unit cell and refers to (110) plane of their bulk crystal structure. The optimized lattice parameters of the monolayers obtained using the DFT/PBE method are specified in **Table 6.1**, which agree well with the previously reported values [199,201,203]. Along the  $y$ -axis, YX systems are buckled into a zigzag line, while along the  $x$ -axis, they possess a bilayer structure. These monolayer shows anisotropy because of their buckled structure. As the lattice parameter along the  $x$ -direction is greater than that in  $y$ , the bond length of Y–X is longer in the  $x$ -direction than that in the  $y$ -direction.

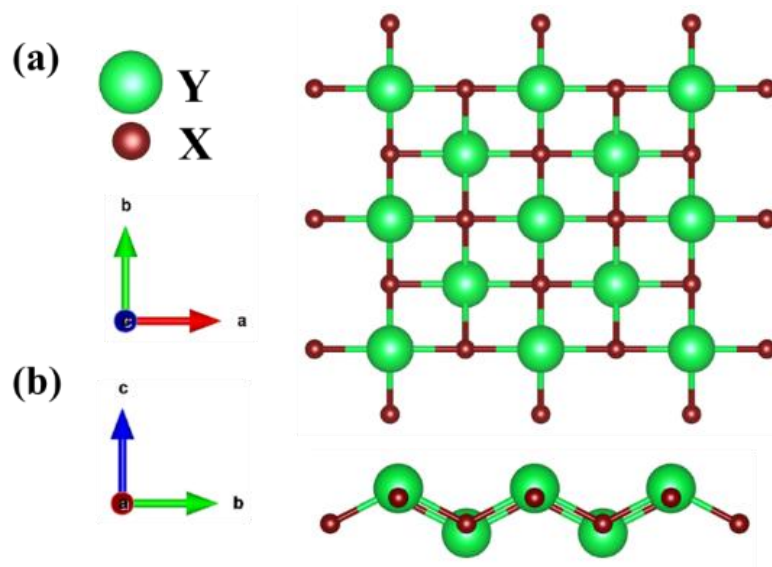


**Figure 6.1** Crystal structure of tetragonal YX (X= N, P, As) monolayers. (a) The top view and (b) the side view of the YX monolayers.

**Table 6.1** The obtained structural parameters of YX monolayers, the lattice constant (in Å) comparable with previous work, buckling height ( $h$ ), bond lengths (in Å), and bond angles (in degree) based on PBE functional.

Monolayer	Lattice Constant		$h$	Bond lengths Y–X	Bond angles
	This work	Other work			
YN	$a = 4.618$	$a = 4.647^a, 4.605^b, 4.63^c, 4.567^d$	1.305	along $x = 2.325$	Y1–N2–Y1 = 125.226
	$b = 3.982$	$b = 3.974^a, 4.024^b, 3.98^c, 4.068^d$		along $y = 2.242$	Y1–N1–Y1 = 166.506
YP	$a = 5.442$	$a = 5.44^c, 5.221^d$	1.710	along $x = 2.748$	Y1–N2–Y1 = 121.759
	$b = 4.749$	$b = 4.75^c, 5.217^d$		along $y = 2.718$	Y1–N1–Y1 = 163.810
YAs	$a = 5.557$	$a = 5.56^c, 5.353^d$	1.912	along $x = 2.826$	Y1–N2–Y1 = 120.345
	$b = 4.874$	$b = 4.87^c, 5.341^d$		along $y = 2.809$	Y1–N1–Y1 = 159.016

<sup>a</sup>Ref. [199], <sup>b</sup>Ref. [201], <sup>c</sup>Ref. [203], and <sup>d</sup>Ref. [202]

### 6.3.2 Stability

Keeping in mind the possible experimental synthesis of these monolayers, we explored various thermal and dynamical stability criteria. The cohesive energy per atom is calculated as  $E_C = (2E_Y + 2E_X - E_{YX})/4$ , where  $E_Y$ , and  $E_X$ , respectively, are energies of isolated Y and X atom;  $E_{YX}$  is the total energy of YX monolayers. The calculated  $E_C$  are 5.56, 4.25, and 3.96 eV per atom for YN, YP, and YAs, respectively, which are consistent with earlier literature results [201,203]. The obtained results for  $E_C$  indicate that the investigated monolayers are energetically favourable structures and these values are comparable with the previously reported stable monolayers, like pentagonal tellurene (2.93) [207], phosphorene (3.42) [208], low-buckled germanene (4.15) [209], low-buckled silicene (5.16) [209], ScN (5.98) [203], and MoSi<sub>2</sub>N<sub>4</sub> (6.51) [210]; all values are in eV per atom.

The AIMD evolution of energy and temperature fluctuations as functions of time, as illustrated in **Figure 6.2**, examines the thermal stability of all three considered monolayers. The temperature profiles of the YN, YP, and YAs monolayers display no significant temperature



fluctuations over a range of 0 to 5000 fs at 500 K. This indicates the thermal stability of monolayers as no structural phase changes or chemical bond breaking are observed during the entire AIMD calculations, confirming that there are ample chances that these monolayers can be sustained even above room temperature. Furthermore, the energy fluctuation, as shown by the magenta solid line, is below 1.0 eV, which is acceptable and consistent with previous findings [211].

The phonon calculations for YX pnictide monolayers were computed to get the second-order IFCs using the finite difference method, with the displaced atomic configurations generated by Phonopy [179]. To enforce rotational sum rules, these force constants were subsequently corrected using the Hiphive code, following the methodology outlined by Eriksson et al. [204]. The quadratic nature of the lowermost acoustic branch in the long-wavelength limit is apparent from the high symmetry path plot of phonon dispersion (as illustrated in **Figure 6.3**) resulting from the corrected IFCs near to  $\Gamma$ -point. The absence of imaginary phonon frequencies confirms that the investigated systems are dynamically stable. Four atoms exist in the unit cell of YX monolayers; therefore, total 12 vibrational frequencies are present in their phonon dispersion. Three acoustics are low-frequency branches and nine optical are high-frequency branches. The maximum frequencies observed in YN, YP and YAs are 19, 10.5 and 7.8 THz, respectively, which follows the usual trend, i.e., the phonon frequency decreases with the atomic mass.

A significant coupling between the low-frequency optical and acoustic branches is observed in all investigated systems, which indicates that phonons will scatter more easily resulting in low phonon lifetime and, subsequently, low  $\kappa_l$ . This type of behaviour has been observed in other materials [212–215]. To get further insights into the phonon dynamics, the atomic contribution of phonon is analysed from the phonon DOS, as depicted in **Figure 6.4**. The contribution to the low-frequency phonon branches mainly arises from Y atoms, and the high-frequency phonon branches are contributed by the pnictide atoms in case of YN and YP. Whereas Y and As contributed almost equally to both low-frequency acoustic and high-frequency phonon modes. Also, the main difference in the phonon DOS of three monolayers is the vibration of pnictides. Due to the smaller atomic mass of N atoms, frequencies are up to 19 THz in YN, while the phonon modes of P and As ions are up to 10.5 and 7.8 THz, respectively, in YP and YAs monolayers.

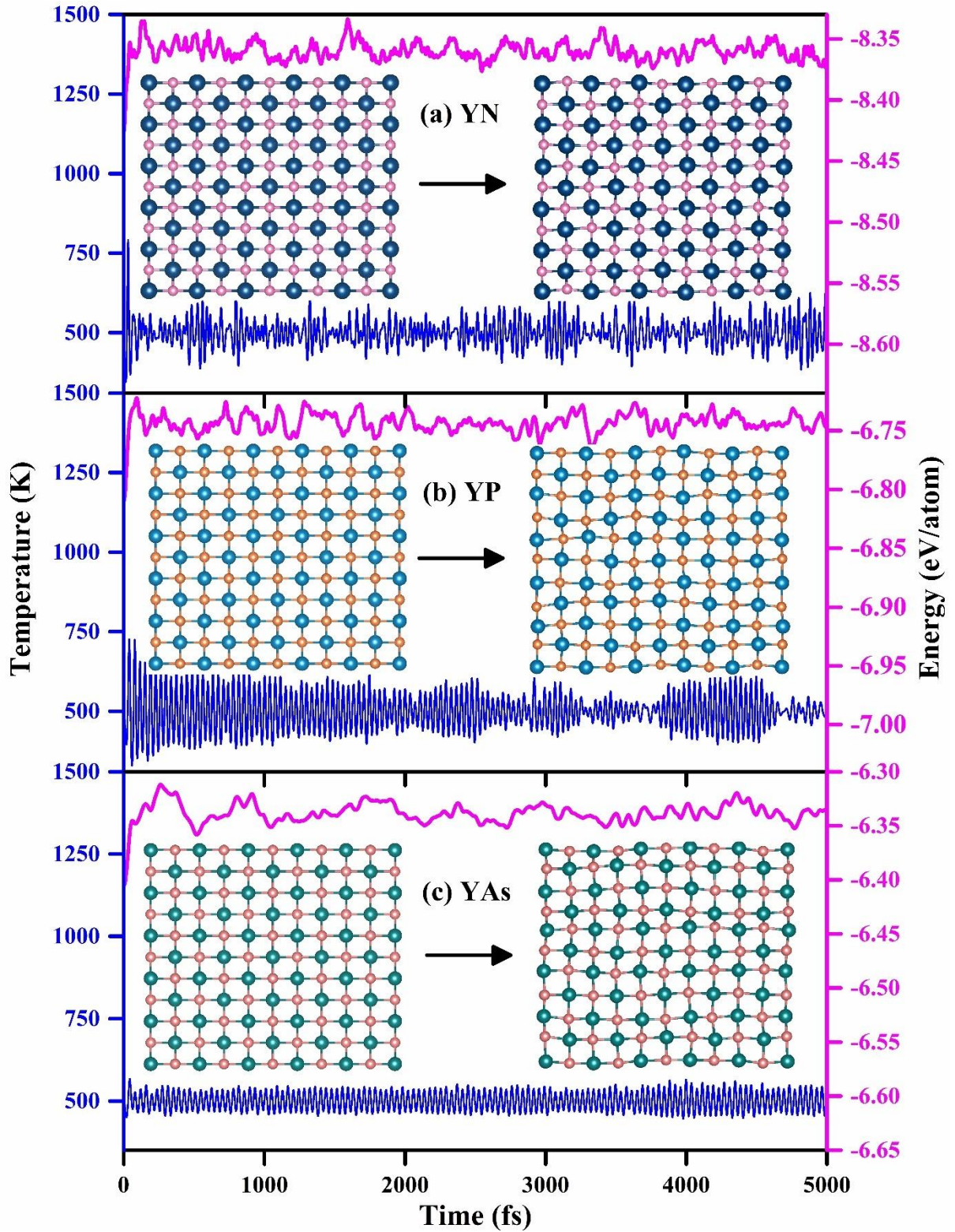


**Figure 6.2** AIMD evolution of temperature and energy fluctuations of (a) YN, (b) YP, and (c) YAs monolayers at 500 K. The blue (magenta) solid line is the variation of temperature (energy) with time. The insets are snapshots of monolayer structures before (at 0 fs) and after AIMD simulations (at 5000 fs).

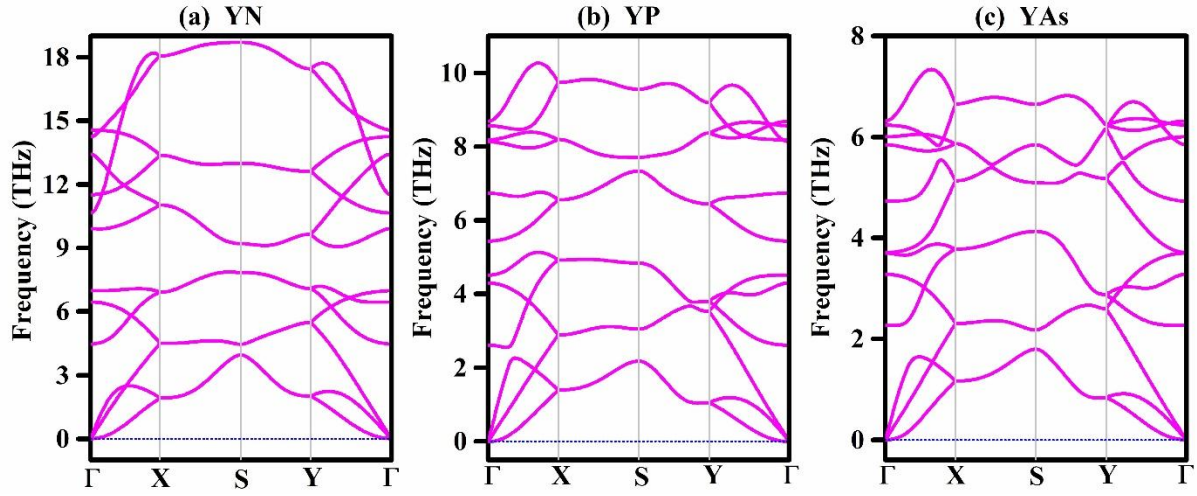


**Figure 6.3** Phonon dispersion curves of (a) YN, (b) YP and (c) YAs monolayers.

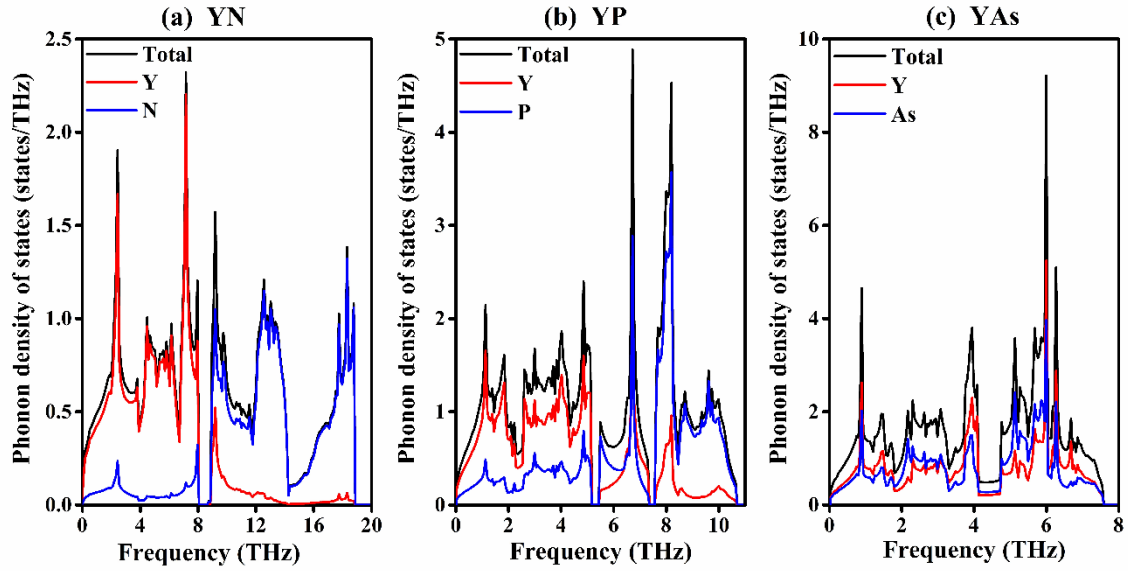


**Figure 6.4** Phonon density of states of YX (X= N, P, As) monolayers.

### 6.3.3 Electronic properties

Based on the optimized geometries and assuring the energetical, thermal, and dynamical stabilities of the studied tetragonal monolayers, we then calculated electronic properties of the systems. The band dispersion along the high symmetry  $k$ -path with the HSE06 functional of YX monolayers is illustrated in **Figure 6.5** (a)–(c). YN monolayer exhibits direct band gap character, i.e., both the valence band maximum (VBM) and conduction band minimum (CBM) present at  $\Gamma$  point. For YP and YAs, the VBM and CBM occur along the  $\Gamma$ –Y path and have an indirect character. Suitable band gaps of 0.69, 1.65, and 1.67 eV, respectively, for YN, YP, and YAs are found that can efficiently overcome the bipolar effect and hence prevent the lowering of  $S$ . These band gap values are comparable to the previously reported results [199,201,203].

The top valence bands of monolayer YP and YAs show closeness and energy degeneracy around the Fermi level. Conversely, the behaviour of the YN monolayer and conduction bands (of all three monolayers) around the Fermi level has no such similarity. These degenerate valence bands in YP and YAs monolayers will greatly increase the DOS and further increase the Seebeck coefficient [216], which directly affects the final  $ZT$ . The key finding in the vicinity of Fermi level is that the valence band and conduction band exhibit more dispersion for the case of YN monolayer than YP and YAs, leading to high carrier mobilities and, consequently, higher electrical conductivity. Our findings indicate that the structural anisotropy of these monolayers governs the anisotropy of electronic structure. Further, analyzing it, we found that the trend of the band gap, from YN to YAs, is accompanied by a flattening of the electronic bands constituting the CBM and VBM. Because the bond length in the  $x$ - and  $y$ - directions increases, resulting in weakened bonding, and, consequently, bands become less dispersive. To determine the contribution of orbitals in the formation of electronic bands, we computed DOS of YX monolayers, which is shown in **Figure 6.6**. The DOS show that the VB is almost equally contributed by the yttrium and pnictides atoms, while most of the CB arises from the yttrium atoms. Also, we have observed that the VB is primarily composed of  $X-p$  orbital characters and a significant contribution of  $Y-p$  and  $Y-d$  orbitals. The conduction band is majorly contributed by  $Y-d$  orbital in all investigated systems. The strong  $p-d$  hybridization might result in high electronic conductivities in these monolayers. The electronic DOS around the Fermi level is higher in YP and YAs compared to YN due to the presence of degenerate valence bands in YP and YAs.

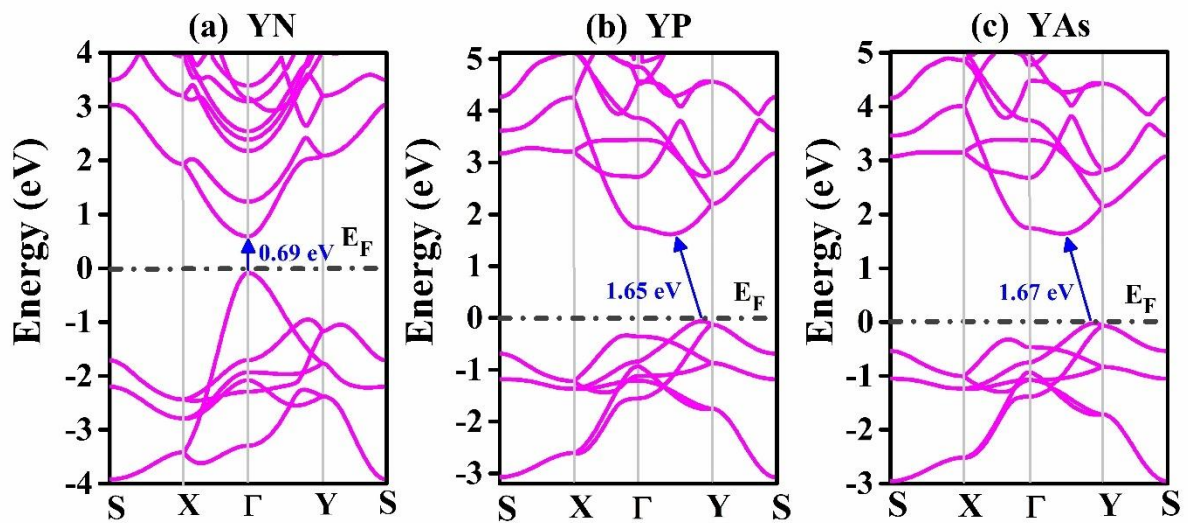


**Figure 6.5** Calculated electronic structure of (a) YN, (b) YP and (c) YAs monolayers. The Fermi level (shown by dotted black line) is set to 0 eV.



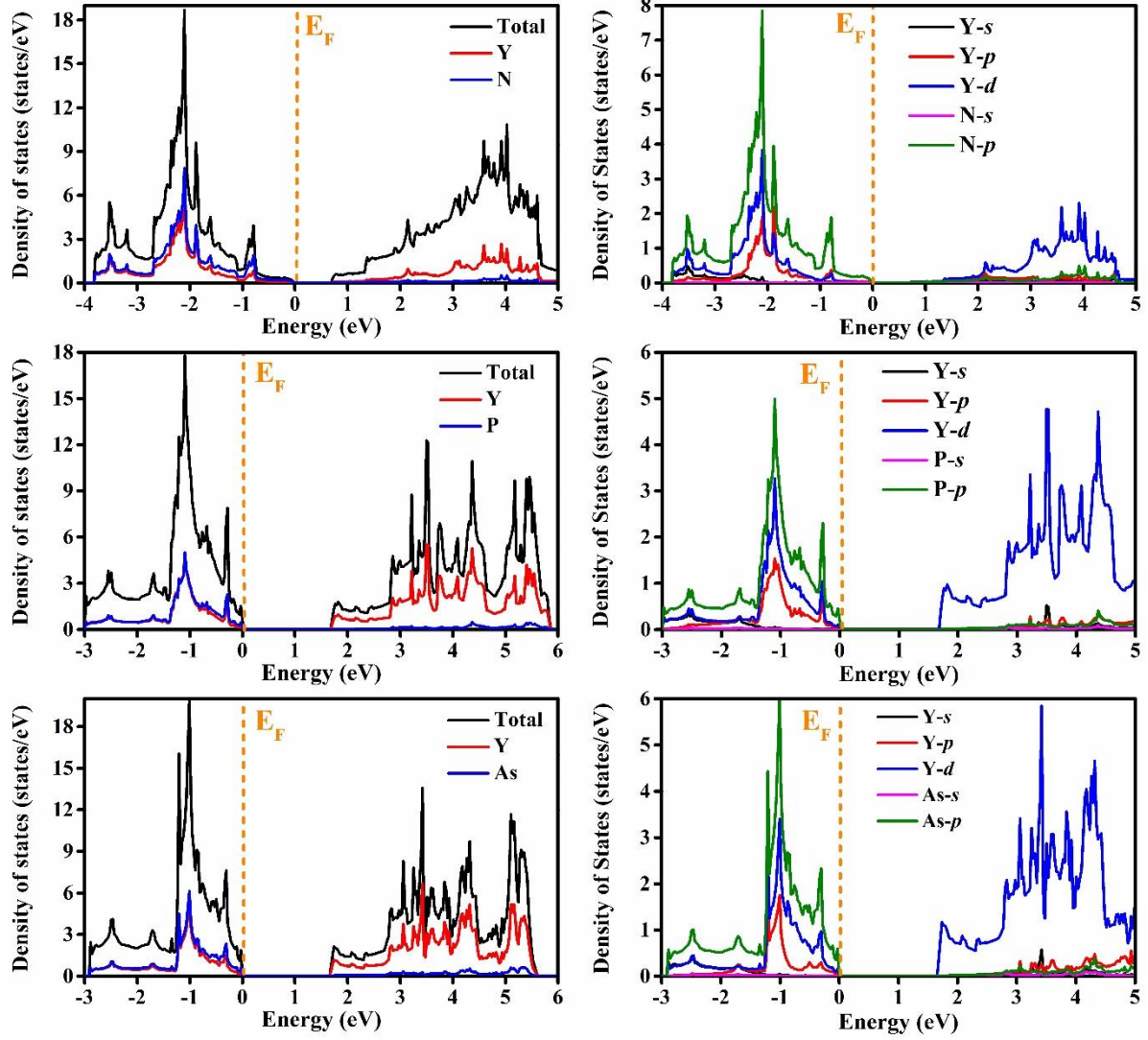


**Figure 6.6** The DOS of YX (X= N, P, As) monolayers in which contribution of different atoms and orbitals are labelled. The Fermi level (shown by dotted orange line) is set to 0 eV.

### 6.3.4 Transport properties

Turning to the TE properties, we used the semiclassical Boltzmann formalism under the CRTA and RBA for an anisotropic system to calculate the transport coefficients ( $S$ ,  $\sigma$ ,  $\kappa_e$ ) [95]. The transport coefficients show the strong dependence on the carrier concentration. Therefore, we computed  $S$ ,  $\sigma$ ,  $\kappa_e$ , and the corresponding  $PF$  and  $ZT$  as a function of carrier concentration having range from  $10^{11} \text{ cm}^{-2}$  to  $10^{14} \text{ cm}^{-2}$  in both the  $p$ -type and  $n$ -type doping. For this analysis, we consider three distinct temperatures— 300, 400, and 500 K.

#### 6.3.4.1 Seebeck coefficient

The calculated  $S$  of YX (X= N, P, As) monolayers is displayed in **Figure 6.7 (a)–(f)**. The positive and negative signs of  $S$  indicate that the dominant charge carriers are holes and

electrons, respectively. The absolute value of  $S$  linearly decreases for the whole carrier concentration range ( $10^{11} \text{ cm}^{-2}$  to  $10^{14} \text{ cm}^{-2}$ ) in both  $p$ - and  $n$ -type doping. Mahan–Sofo concept states that the  $S$  for 2D degenerate semiconductors can be expressed by [21]

$$S_{2D} = \frac{2\pi k_B^2 T}{3eh^2 n} m_d^* \quad (6.1)$$

where  $h$  represents the Planck constant,  $n$  represents the carrier concentration, and  $m_d^*$  represents the DOS effective mass around the Fermi level. Therefore, a competitive relationship exists between  $n$  and  $m_d^*$ . Our calculations indicate that the  $S$  of YX monolayers is inversely proportional to  $n$ , which aligns well with the Mahan–Sofo theory.

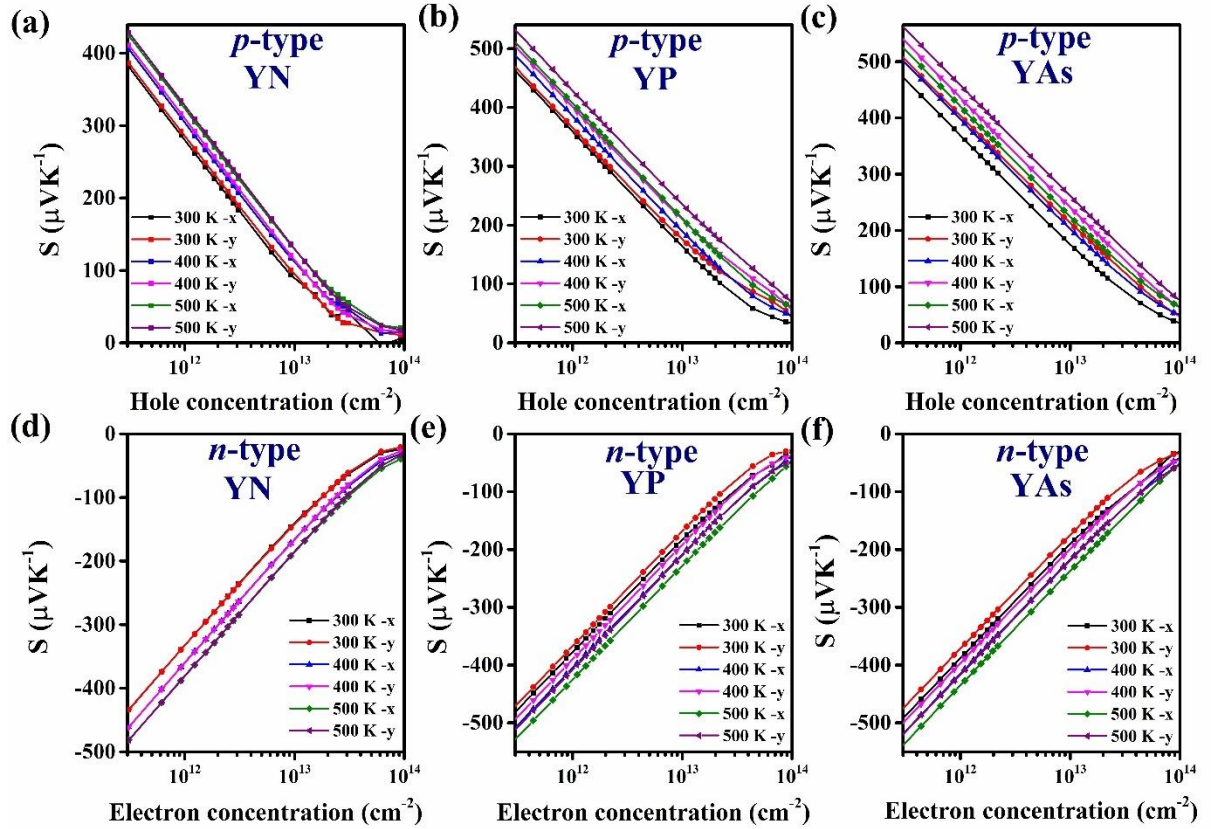


**Figure 6.7** Seebeck coefficient ( $S$ ) versus carrier concentration at 300, 400, and 500 K in both directions of (a)–(c)  $p$ -type and (d)–(f)  $n$ -type YX ( $X = \text{N, P, As}$ ) monolayers

We can find that  $S$  of the YN monolayer shows almost isotropic behaviour for both  $p$ - and  $n$ -types. However,  $S$  of YP and YAs monolayers show anisotropic behaviour for both  $p$ - and  $n$ -types. This behaviour might be attributed to the similar dispersion of the band nearby Fermi level along both  $\Gamma$ – $X$  and  $\Gamma$ – $Y$  directions for YN, whereas different dispersions are observed for the other two monolayers. In the  $p$ -type, the  $y$ -direction  $S$  value is greater than the  $x$ -

direction  $S$  value, but in the  $n$ -type, the  $x$ -direction  $S$  is greater than the  $y$ -direction  $S$  value.  $S$  of YX ( $X = \text{N, P, As}$ ) monolayers at 500 K is larger than that observed for 300 and 400 K. The highest  $|S|$  has a value of 429 (482), 558 (555), and 588 (565)  $\mu\text{VK}^{-1}$  at  $10^{11} \text{ cm}^{-2}$  carrier concentration for  $p$ -type ( $n$ -type) for YN, YP, and YAs monolayer, respectively.

#### 6.3.4.2 Electrical and Electronic Thermal Conductivity

Conventional Boltzmann transport theory gives  $\sigma$  in terms of  $\tau$  i.e.  $\sigma/\tau$ . Therefore, a method to calculate  $\tau$  should be applied suitably. Generally, the value of  $\tau$  in various materials often ranges from  $(1-2) \times 10^{-14} \text{ s}$ , but several works have employed a fixed value to tackle this problem [166,216–218]. However, numerous factors can influence the value of  $\tau$ , including acoustic phonons, nonpolar optical phonons, and ionised impurities. Acoustic phonons are widely recognised as the primary factor influencing  $\tau$ . Therefore, the  $\tau$  of charge carriers for the 2D YX monolayers can be calculated by employing DPT first proposed by Bardeen and Shockley as follows [97]:

$$\tau = \frac{2\hbar^3 C_{2D}}{3k_B T m_d^* E_d^2} \quad (6.2)$$

where  $e$  is the elementary charge,  $\hbar$  is reduced Planck constant,  $C_{2D}$  is elastic modulus,  $k_B$  is the Boltzmann constant,  $T$  is temperature, the  $m_d^* = \sqrt{m_x^* m_y^*}$  is the average effective mass in the  $x$ - and  $y$ -directions, and  $E_d$  refers to the deformation potential constant.

The effective masses of carriers obtained by parabolic fitting at the CBM and the VBM via the expression  $1/m^* = (1/\hbar^2) / \left( \left| \partial^2 E(k) / \partial k^2 \right| \right)$ , where  $E(k)$  is energy at the band edges. This expression indicates that the flat band structure around the band edges results in large effective masses of carriers. The lack in symmetry of the electronic structures around the CBM and VBM of YX monolayers results in directionally dependent effective masses  $m_e^*$  and  $m_h^*$ . As presented in Table 2, the  $m_e^*$  is much higher than  $m_h^*$  in both transport directions for all three investigated monolayers, except effective masses of YN in the  $y$ -direction that are almost equal. This indicates that electrons respond to the external field more slowly than holes might result in the mobility of electrons being lower than that of holes. This finding agrees with the electronic structures as depicted in **Figure 6.5**. The electronic structures around the CBM exhibit a more flattened appearance than those around the VBM. Also, the effective masses of electrons for YP and YAs are slightly higher than that of YN.

Elastic modulus  $C_{2D}$  for 2D structures is calculated by fitting strain-dependent energy (for detail, see **Figure 6.8** using the following formula:  $C_{2D} = (1/S_0)/(\partial^2 E/\partial \varepsilon^2)$ , where  $E$  is the total energy,  $S_0$  represents an area of the optimized unit cell, and  $\varepsilon$  denotes a uniaxial strain along the two transport directions. We investigated the elastic modulus within the uniaxial strain of  $-2\%$  to  $2\%$  along both directions.  $E_d$  is given as,  $E_d = \Delta E_{edge}/\varepsilon$  here  $E_{edge}$  stands for the shift in the energy of the band edges, and energy shifting is also explored in the uniaxial strain range of  $-2\%$  to  $2\%$  along both directions. Fitting VBM and CBM, as shown in **Figure 6.9** band energies give the deformation potential constant. Our results indicate that  $C_{2D}$  and  $E_b$  are different along the two transport directions showing anisotropic behaviour. Based on the obtained values from  $m^*$ ,  $C_{2D}$ , and  $E_d$ , we calculated  $\tau$  along two transport directions as presented in **Table 6.2**. Our obtained results indicate that  $C_{2D}$  and  $E_b$  are anisotropic along the transport directions; thereby allowing the independent tunability in the  $x$ - and  $y$ -directions. Additionally, similar anisotropy has also been reported in many 2D monolayers which leads to enhanced TE performances [219–221].

**Table 6.2** Carrier effective masses  $m^*$  in units of free electron mass ( $m_0$ ), in-plane stiffness  $C_{2D}$  ( $\text{Nm}^{-1}$ ), Deformation potential constant  $E_d$  (eV), and relaxation time  $\tau$  (s) at 300 and 500 K for YN, YP, and YAs.

System	Carrier type	$m^* (m_0)$	$C_{2D} (\text{Nm}^{-1})$	$E_d (\text{eV})$	$\tau (\text{s}) \times 10^{-14}$	
					300 K	500 K
YN	Electron (x)	1.06	109.981	1.024	124.16	74.49
	Hole (x)	0.27	109.981	17.003	0.82	0.49
	Electron (y)	0.43	39.243	1.335	26.06	15.64
	Hole (y)	0.51	39.243	2.35	15.30	9.18
YP	Electron (x)	1.63	91.496	4.852	2.30	1.38
	Hole (x)	0.41	91.496	6.259	3.53	2.12
	Electron (y)	1.12	12.148	3.801	0.50	0.30
	Hole (y)	0.68	12.148	1.869	5.26	3.16
YAs	Electron (x)	1.79	78.676	5.269	1.44	0.86
	Hole (x)	0.58	78.676	7.896	1.51	0.91
	Electron (y)	1.38	10.488	3.347	0.48	0.28
	Hole (y)	0.77	10.488	1.501	5.57	3.34



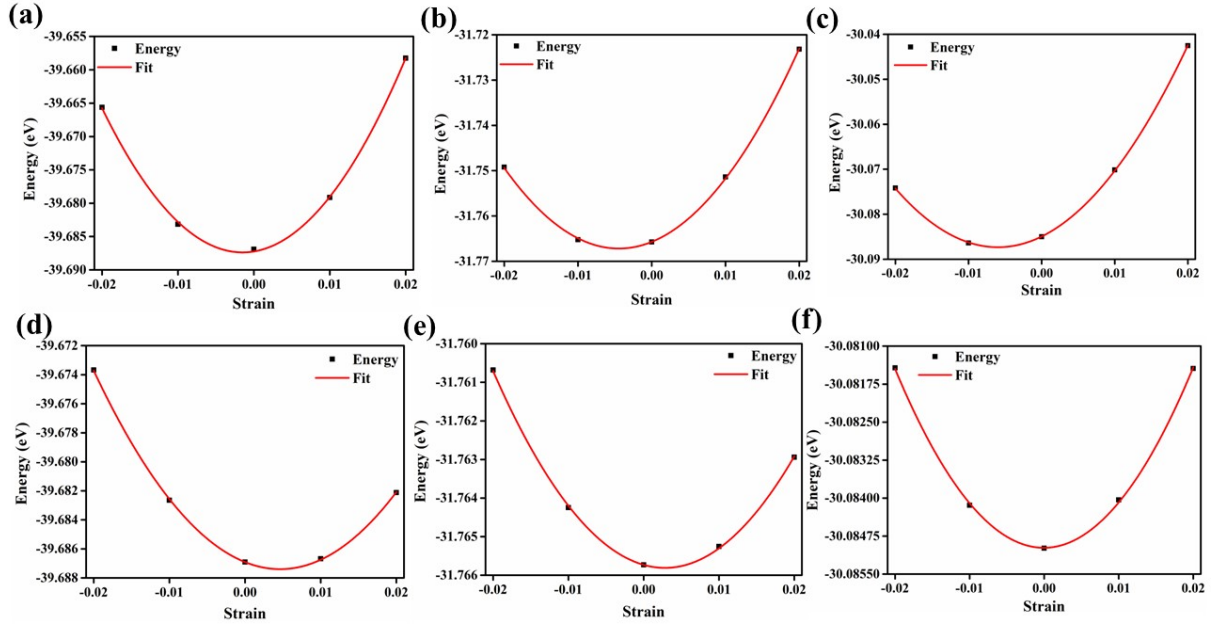


**Figure 6.8** The energy shifting as a function of uniaxial strain along the  $x$ -direction (top panel) and  $y$ -direction (bottom panel) of (a and d) YN, (b and e) YP, and (c and f) YAs. The solid lines indicate the parabolic fitting curves.

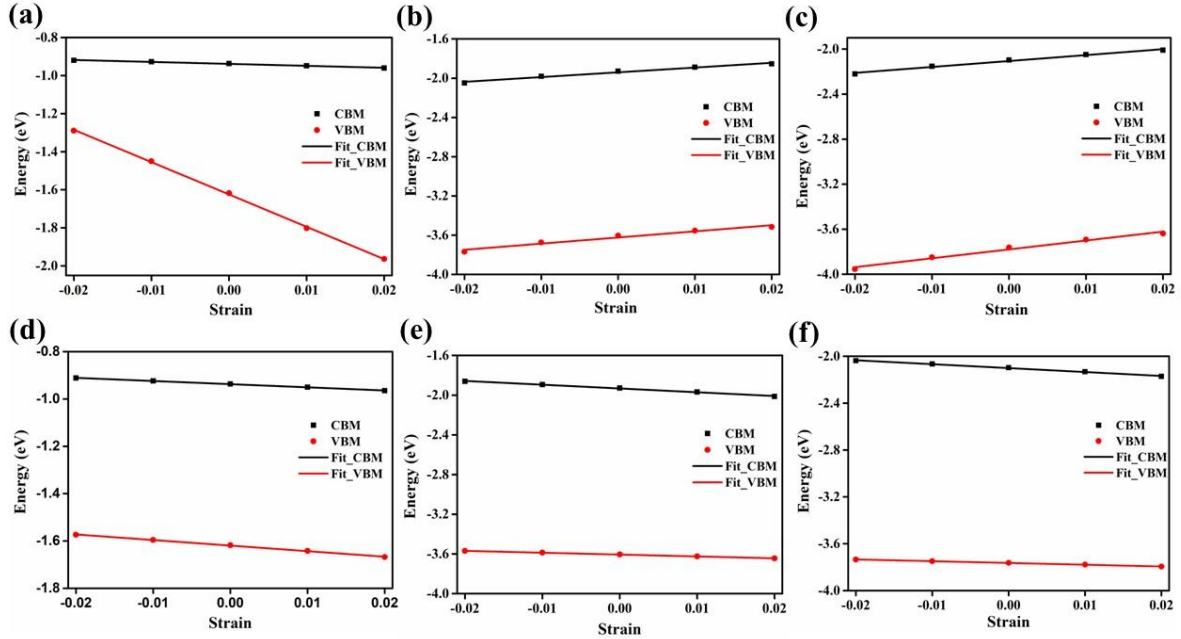


**Figure 6.9** The band edge position shifts of CBM and VBM as a function of uniaxial strain along the  $x$ -direction (top panel) and the  $y$ -direction (bottom panel) of (a and d) YN, (b and e) YP, and (c and f) YAs. The solid lines indicate the linear fitting curves.

The results for  $\sigma$  of YX monolayers with the effect of carrier concentration at respective temperatures for both  $p$ - and  $n$ -types are summarised in **Figure 6.10 (a)–(f)**. In contrary to  $S$ ,  $\sigma$  is inversely proportional to effective mass and it increases as a function of carrier concentration. When it is below  $10^{13} \text{ cm}^{-2}$ ,  $\sigma$  of 300, 400, and 500 K are comparable for both  $p$ - and  $n$ -type

YX (X=N, P, As) monolayers in both the  $x$ - and  $y$ -directions. However,  $\sigma$  of 300 K rises rapidly than of 400 and 500 K when carrier concentration is greater than  $10^{13} \text{ cm}^{-2}$ . The smaller electronic band gap of YN monolayer shows large  $\sigma$  compared to YP and YAs for  $n$ - and  $p$ -type. A large anisotropy is found in value of  $\sigma$ , with  $p$ -type monolayers exhibiting greater  $\sigma$  values in the  $y$ -direction, and  $n$ -type monolayers showing higher values in the  $x$ -direction. Further,  $\sigma$  is very high for the  $n$ -type YN monolayer because of high mobility of electrons. At hole concentration of  $10^{11} \text{ cm}^{-2}$ , the room temperature  $\sigma$  of YN, YP, and YAs are respectively 0.18, 0.03, and  $0.02 \times 10^6 \Omega^{-1}\text{m}^{-1}$ , while at electron concentrations of the same order, these are 0.82, 0.03, and  $0.02 \times 10^6 \Omega^{-1}\text{m}^{-1}$ . However, as the hole concentrations increase to  $10^{14} \text{ cm}^{-2}$ , the  $\sigma$  rises to 36.66, 13.88, and  $12.72 \times 10^6 \Omega^{-1}\text{m}^{-1}$  for YN, YP, and YAs, respectively, while for the same electron concentrations, the values are 217.84, 14.15, and  $7.15 \times 10^6 \Omega^{-1}\text{m}^{-1}$ . Similarly, the conventional Boltzmann transport theory gives  $\kappa_e$  in terms of  $\tau$  i.e.  $\kappa_e/\tau$ . Therefore, using the values of  $\tau$ , as presented in Table 2, we obtained  $\kappa_e$ . The  $\kappa_e$  shows almost similar behaviour as  $\sigma$  for the  $n$ - and  $p$ -type monolayer as illustrated in **Figure 6.11**.

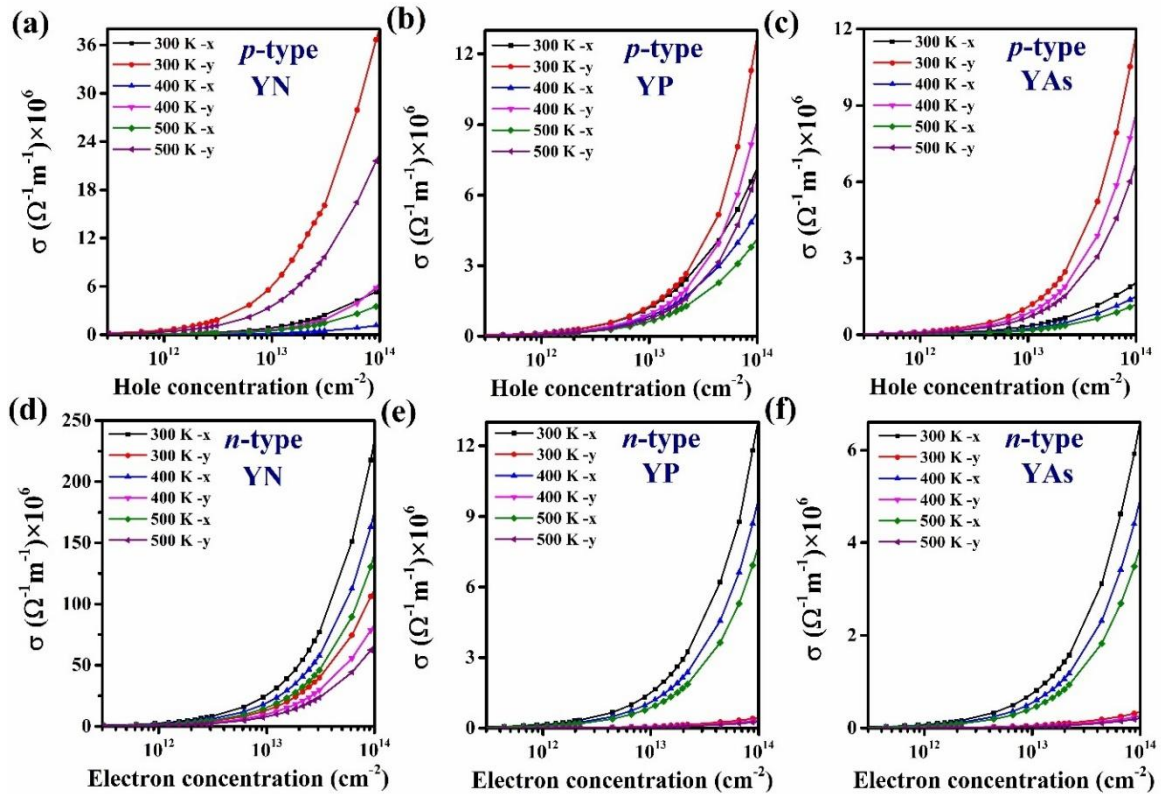


**Figure 6.10** The electrical conductivity ( $\sigma$ ) versus carrier concentration at 300, 400, and 500 K in both directions of (a)–(c)  $p$ -type and (d)–(f)  $n$ -type YX (X= N, P, As) monolayers

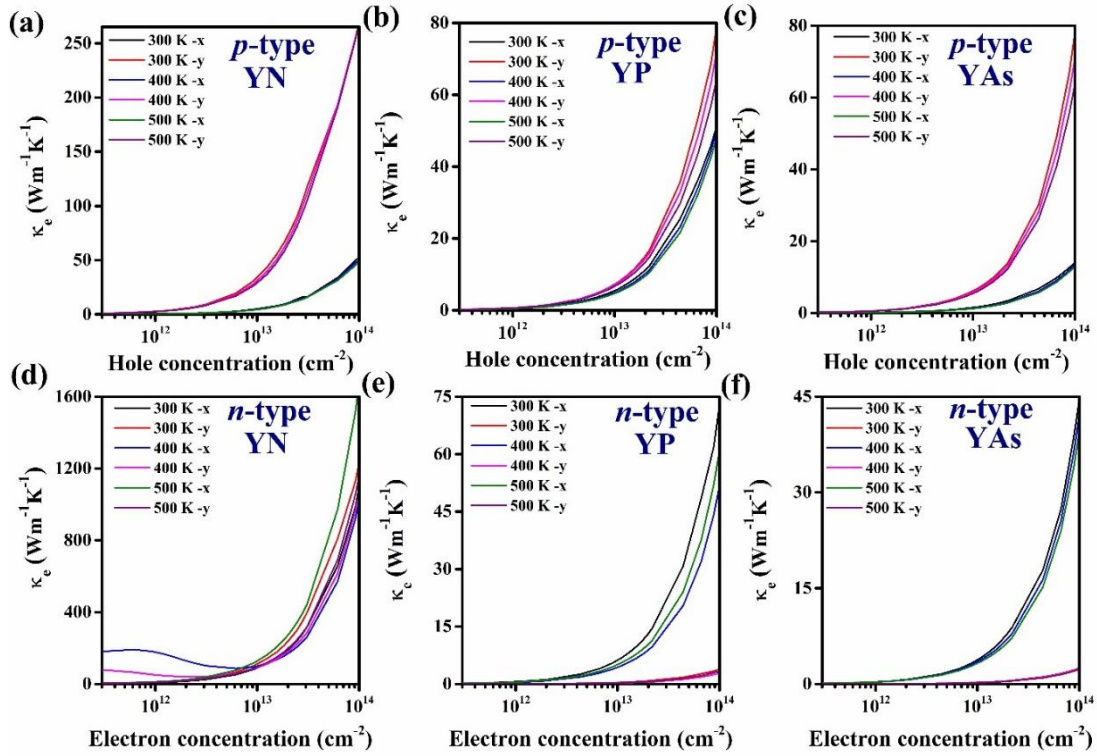


**Figure 6.11** Electronic thermal conductivity ( $\kappa_e$ ) versus carrier concentration from 300 K to 500 K in the  $x$ - and  $y$ - directions of (a)–(c)  $p$ -type and (d)–(f)  $n$ -type YX monolayers

#### 6.3.4.3 Power factor

Power factor ( $PF = S^2\sigma$ ), depends on  $S$  and  $\sigma$ .  $PF$  increases as the electron and hole concentrations rise to a peak value at ( $\sim 10^{13} \text{ cm}^{-2}$ ), then decreases. As shown in **Figure 6.12** (a)–(f), YX monolayers exhibit highly direction-dependent  $PF$ , and a high  $PF$  is obtained for hole concentration in the  $y$ -direction. Conversely, for electron concentration, a high  $PF$  is noticed in the  $x$ -direction. Also, for both the hole and electron concentration, despite large Seebeck coefficients in YP and YAs, a high  $PF$  is achieved in YN due to its high electrical conductivity. Around the hole carrier density of  $10^{13} \text{ cm}^{-2}$  the  $PF$  of YN, YP, and YAs at 500 K reach 63, 45, and 57  $\text{mWm}^{-1}\text{K}^{-2}$ , respectively, in the  $y$ -direction. On the contrary, the electron carrier density of  $10^{13} \text{ cm}^{-2}$  the  $PF$  of YN, YP, and YAs at 500 K reach 531, 49, and 27  $\text{mWm}^{-1}\text{K}^{-2}$ , respectively, in the  $x$ -direction.

#### 6.3.4.4 Lattice thermal conductivity

We obtained lattice thermal conductivities through both the solution of the fPBTE, also known as the direct solution of the linearized phonon Boltzmann equation, and based on the RTA approach. The RTA normal scattering is purely resistive and, so, generally underestimates  $\kappa_l$  in comparison to the fPBTE. In certain materials exhibiting particularly weak Umklapp scattering, such as diamond, graphene, and carbon nanotubes, RTA has been found to give qualitatively

inaccurate solutions. In most bulk materials, where the RTA approach does not completely fail it has been found to substantially limit the predictive power of the  $\kappa_l$  estimation procedure [179]. Therefore, we obtained the  $\kappa_l$  of YX monolayers, with both RTA and solving fPBTE employing Phono3py for both cases. We solved the fPBTE by directly diagonalizing the phonon collision matrices [103].

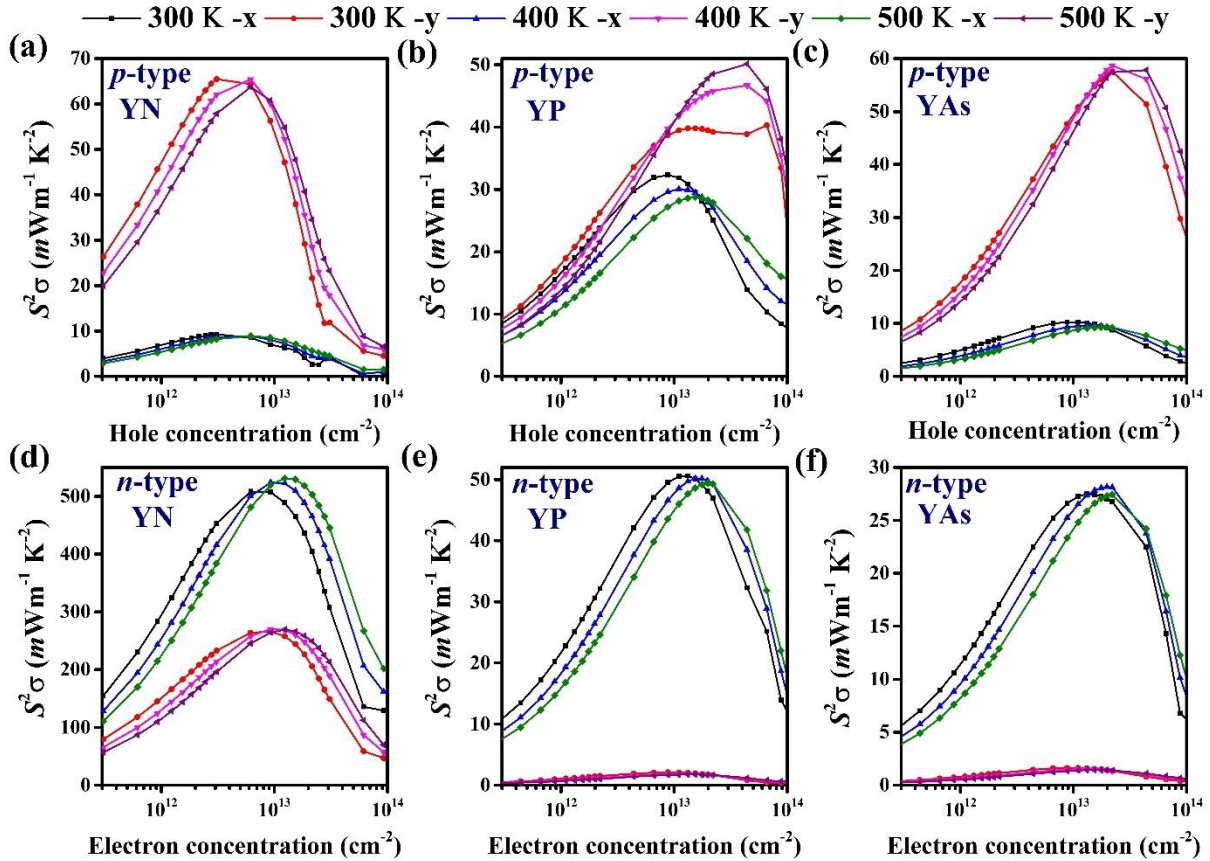


**Figure 6.12** Power factor ( $S^2\sigma$ ) versus carrier concentration at 300, 400, and 500 K in both directions of (a)–(c) *p*-type and (d)–(f) *n*-type YX (X = N, P, As) monolayers

The lattice thermal conductivities and other anharmonic phonon properties of proposed systems were evaluated at 7 representative temperatures spanning the temperature range 300 K–900 K. **Figure 6.13 (a)–(c)** shows the temperature-dependent comparative  $\kappa_l$  of the YX in the *x*- and *y*-directions calculated using both direct solution and RTA. **Figure 6.13 (d)** represents a comparison of average lattice thermal conductivities found using both approaches at 300 and 500 K. Obviously, the  $\kappa_l$  decreases as the temperature rises, in accordance with the  $T^{-1}$  relationship. The calculated  $\kappa_l$  of the rare-earth YX (X = N, P, As) monolayers at 300 and 500 K are listed in **Table 6.3**. It is clear that the RTA approach underestimated each monolayer compared to the fPBTE, consequently predicting the overestimated ZT values of these



materials. Therefore, for predicting accurate ZT and analyzing further properties, we used the  $\kappa_l$  found by the solution of fPBTE. The  $\kappa_l$  of YAs are 2.327 and 0.969  $\text{Wm}^{-1}\text{K}^{-1}$ , respectively, in the  $x$ - and  $y$ -directions at 500 K. As expected, the  $\kappa_l$  reduced as the atomic weight of the pnictide increases. We find that lattice thermal conductivity of these monolayers (2.76–5.76  $\text{Wm}^{-1}\text{K}^{-1}$ ) at 300 K is low to moderate and is comparable to or even lower than that of the other rare-earth monolayers and typical two-dimensional materials such as  $\text{RTeCl}$  ( $R = \text{La, Pr, Nd}$ ) (2.42–4.58  $\text{Wm}^{-1}\text{K}^{-1}$ ) [68]  $\text{Y}_2\text{GeX}_2$  ( $X = \text{Cl, Br, I}$ ) (5.55–25.48  $\text{Wm}^{-1}\text{K}^{-1}$ ) [194], square- $\text{Ag}_2\text{X}$  ( $X = \text{S, Se}$ ) (3.46 and 2.33  $\text{Wm}^{-1}\text{K}^{-1}$ ) [191], MX ( $M = \text{Sn, Pb}$ ;  $X = \text{S, Te}$ ) ( $\sim 3$ –1.16  $\text{Wm}^{-1}\text{K}^{-1}$ ) [222].

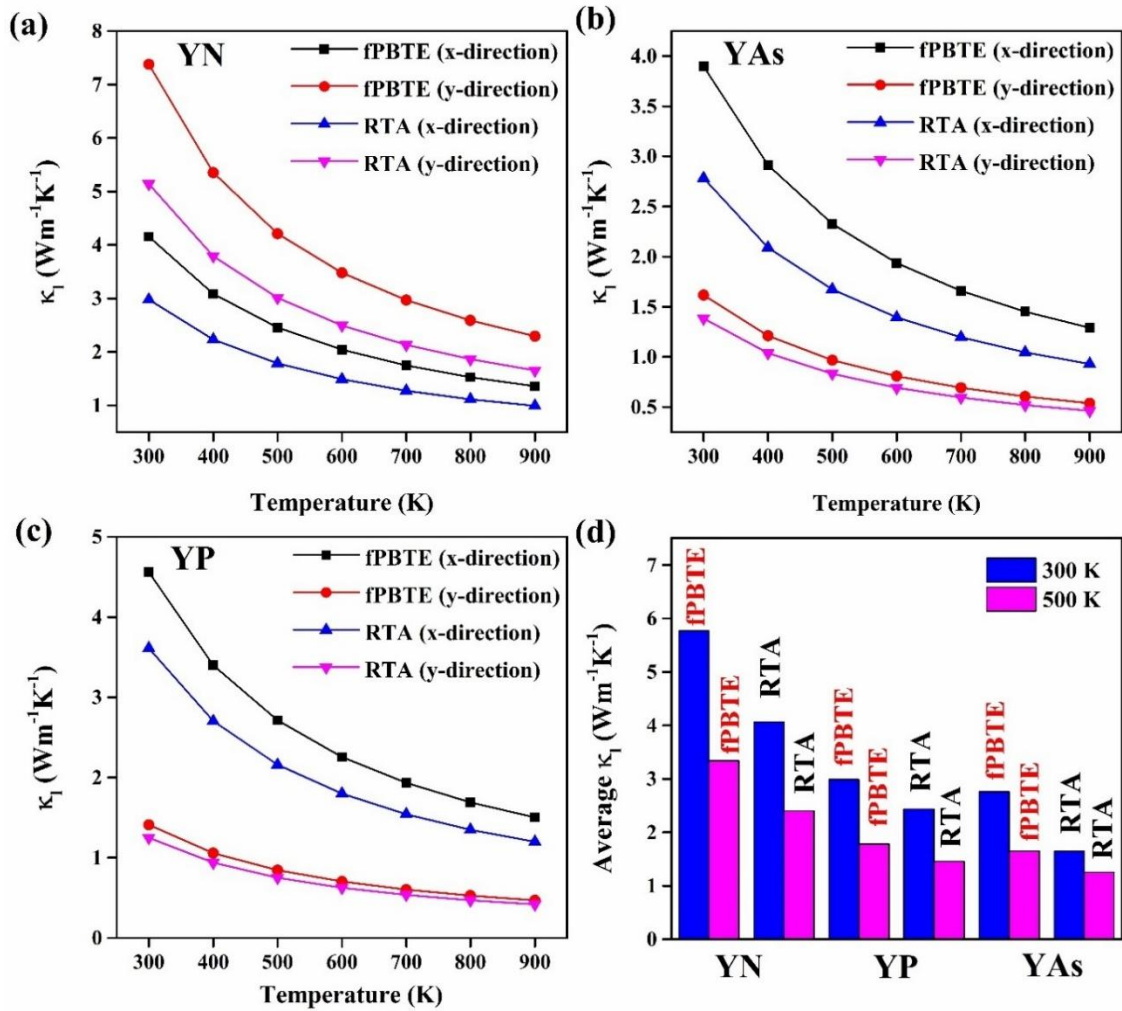


**Figure 6.13** Lattice thermal conductivities ( $\kappa_l$ ) of (a) YN, (b) YAs, (c) YP monolayers dependent on temperature in the  $x$ -direction and  $y$ -direction, and (d) Comparison of Average lattice thermal conductivities found using fPBTE and RTA approach at 300 and 500 K.

**Table 6.3** Comparison of  $\kappa_l$  (in units of  $\text{Wm}^{-1}\text{K}^{-1}$ ) for monolayer YN, YP, and YAs found by solving the fPBTE and based on the RTA approach in  $x$ -direction ( $xx$ ) and  $y$ -direction ( $yy$ ) at 300 and 500 K.

System	$\kappa_l$ ( $\text{Wm}^{-1}\text{K}^{-1}$ )	(xx) 300 K	(yy) 300 K	(xx) 500 K	(yy) 500 K
YN	fPBTE	4.157	7.374	2.457	4.213
	RTA	2.978	5.141	1.785	3.009
YP	fPBTE	4.558	1.411	2.712	0.846
	RTA	3.610	1.249	2.160	0.751
YAs	fPBTE	3.896	1.617	2.327	0.969
	RTA	2.784	1.383	1.674	0.832

To gain a deeper understanding of the fundamental process that causes significant correlation between  $\kappa_l$  and the pnictide atoms in these monolayers, we analysed the group velocity ( $v_g$ ) and phonon lifetime for the YX (X = N, P, As) monolayers as a function frequency, as displayed in **Figure 6.14**. The phonon  $v_g$  was obtained from the phonon dispersion relations, which were calculated using corrected force constants within harmonic approximation. Thus, the phonon  $v_g$  for the long wavelength modes was accurately estimated since these modes are the key heat carriers in 2D systems. As expected, and illustrated in **Figure 6.14 (a)–(c)**, the nature of pnictide atom in these systems has a substantial influence on both the  $v_g$  of phonons and the thermal transport of phonons. Consequently, when the atomic weight of pnictide atom increases, the  $v_g$  of phonons are noticeably reduced. Increasing the weight of the pnictide atom indeed results in narrower dispersions for phonon modes (which is depicted in **Figure 6.3**) and weaker bonds. To characterize the values of  $v_g$  quantitatively for each monolayer, the average  $v_g$  over phonon branches are evaluated. The average  $v_g$  of YN, YP, and YAs, respectively, comes out to 2.38, 1.57, and 1.39 ( $\text{km}^{-1}$ ). Then, we considered the phonon lifetime to analyse the phonon-phonon scattering. Similarly, the phonon lifetime at 300 K, as demonstrated in **Figure 6.14 (d)–(f)**, exhibits a consistent trend, a significant rise in phonon scattering observed as the atomic weight of the pnictide increases. Also, based on the distribution of phonon lifetimes, it is evident that the primary factor influencing  $\kappa_l$  is the acoustic branches, whereas the optical mode has a lesser impact. For the YN monolayer, at a low frequency of less than 5 THz, we can see a broad range of phonon lifetime reaches up to 50 THz. At mid to high

frequency spanning range 5-18 THz lifetime are shorter and clustered below 5 ps, indicating higher scattering. Similarly, for YP and YAs, the lifetime is shorter in the mid to high-frequency range.

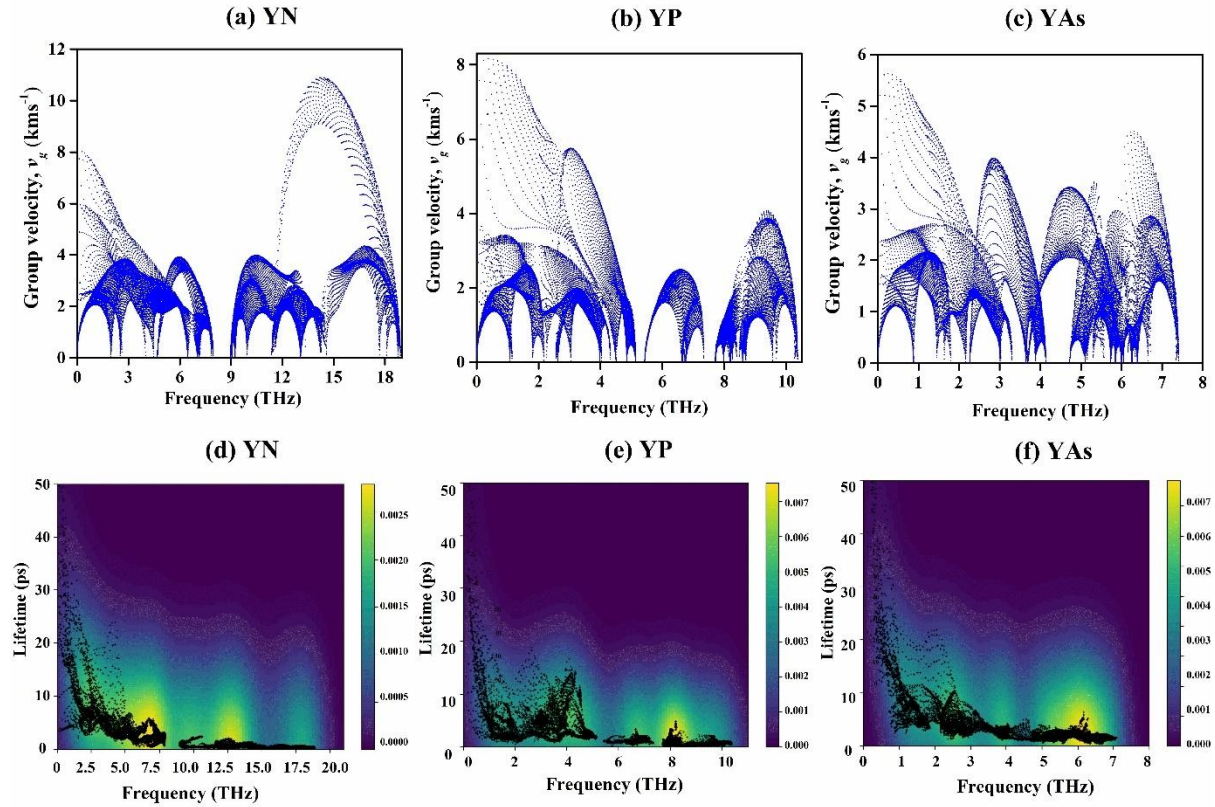


**Figure 6.14** Calculated (a)–(c) group velocity and (d)–(e) phonon lifetime of YX (X= N, P, As) monolayers as a function frequency.

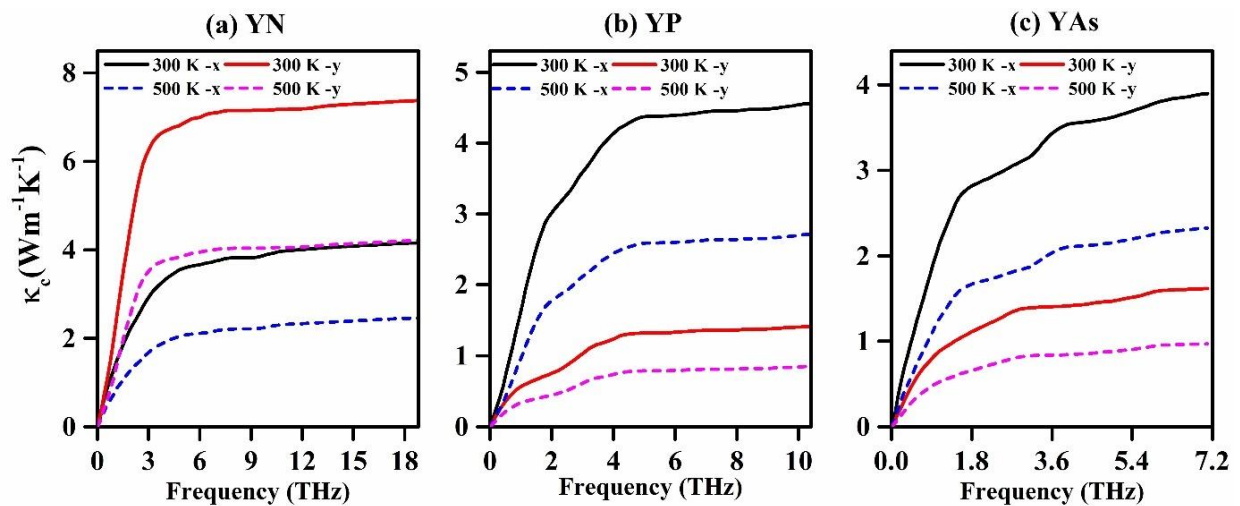


**Figure 6.15** (a)–(c) Cumulative lattice thermal conductivities ( $\kappa_c$ ) of YX (X= N, P, As) monolayers as function frequency at 300 and 500 K in both directions.

Next, the cumulative  $\kappa_l$  ( $\kappa_c$ ) of YX systems with varying frequency (**Figure 6.15 (a)–(c)**) was analyzed to determine the origin of the low  $\kappa_l$ . At 300 K, in the  $x$ - and  $y$ -direction, the  $\kappa_c$  showed a significant rise arising from the acoustic phonon modes, followed by a small rise resulting from the low-frequency optical modes, and then reached saturation. This suggests that the coupling effect between the low-lying optical and acoustic phonon modes, limiting the major contribution of acoustic phonons to the  $\kappa_l$ .

#### 6.3.4.5 Figure of merit

$ZT$  is directly proportional to the  $PF$  and inversely proportional to the thermal conductivity. The thermal conductivity consists of two parts: the electronic ( $\kappa_e$ ) and the lattice component ( $\kappa_l$ ). Using all electronic and thermal transport parameters described in above sections, we evaluated  $ZT$  at distinct temperatures (300, 400, and 500 K) as a function of carrier concentration. Combining high  $PF$  and low thermal conductivity ( $\kappa_e + \kappa_l$ ), these monolayers have high  $ZT$  values with high anisotropy in the  $x$ - and  $y$ -directions. **Figure 6.16 (a)–(f)** shows computed  $ZT$  of studied monolayers for both  $p$ -type and  $n$ -type systems. For YP and YAs, the  $ZT$  for  $p$ -type is greater than that of  $n$ -type, which indicates effectiveness of carrier doping with holes rather than electrons, whereas for YN, the  $n$ -type  $ZT$  value is higher. For  $p$ -type and  $n$ -type, respectively, we obtain highest  $ZT$  in the  $y$ -direction and the  $x$ -direction at 500 K. The highest  $ZT$  in the  $y$ -direction of YN, YP, and YAs are 0.27, 1.18, and 1.39, respectively, at optimized hole concentrations of  $6 \times 10^{12} \text{ cm}^{-2}$ ,  $8 \times 10^{12} \text{ cm}^{-2}$ , and  $1 \times 10^{13} \text{ cm}^{-2}$  at 500 K. Whereas, for  $n$ -type, the highest  $ZT$  obtained for the  $x$ -direction of YN, YP, and YAs are 2.02, 0.57, and 0.42, respectively, at optimized electron concentrations of  $3 \times 10^{12}$ ,  $1 \times 10^{13}$ , and  $1 \times 10^{13} \text{ cm}^{-2}$  at 500 K. It is evident that the  $p$ -type YP and YAs monolayers give significantly superior  $ZT$  values than the  $n$ -type doping, whereas for the case of YN  $n$ -type gives superior performance. Additionally, we also calculated the average  $ZT$  values of these monolayers. The obtained peak values of  $ZT$  in the  $y$ - and  $x$ -direction and their average at the optimized hole and electron carrier concentrations for YN, YP, and YAs monolayers at two respective temperatures i.e., 300 and 500 K are displayed in **Table 6.4**. These results show that the peak  $ZT$  of these studied monolayers is in the range of carrier doping of  $10^{12}$ – $10^{13} \text{ cm}^{-2}$ , which is a feasible range and can be achieved in real experiments. These findings suggest that the investigated rare-earth pnictide monolayers are possessing great potential for beyond and mid-temperature TE applications.



**Table 6.4** Peak figure of merit,  $ZT$  in the  $x$ -direction,  $y$ -direction, and their average values for  $p$ - and  $n$ -type YX ( $X = N, P, As$ ) monolayers at two different temperatures 300 and 500 K at optimized carrier concentration.

Monolayer		$x$ -direction		$y$ -direction		Average	
		300 K	500 K	300 K	500 K	300 K	500 K
YN	$p$ -type	0.03	0.07	0.11	0.27	0.07	0.17
	$n$ -type	1.10	2.02	0.34	0.78	0.72	1.39
YP	$p$ -type	0.15	0.25	0.35	1.18	0.20	0.76
	$n$ -type	0.23	0.57	0.03	0.08	0.13	0.33
YAs	$p$ -type	0.07	0.16	0.60	1.39	0.33	0.78
	$n$ -type	0.16	0.42	0.02	0.06	0.09	0.24

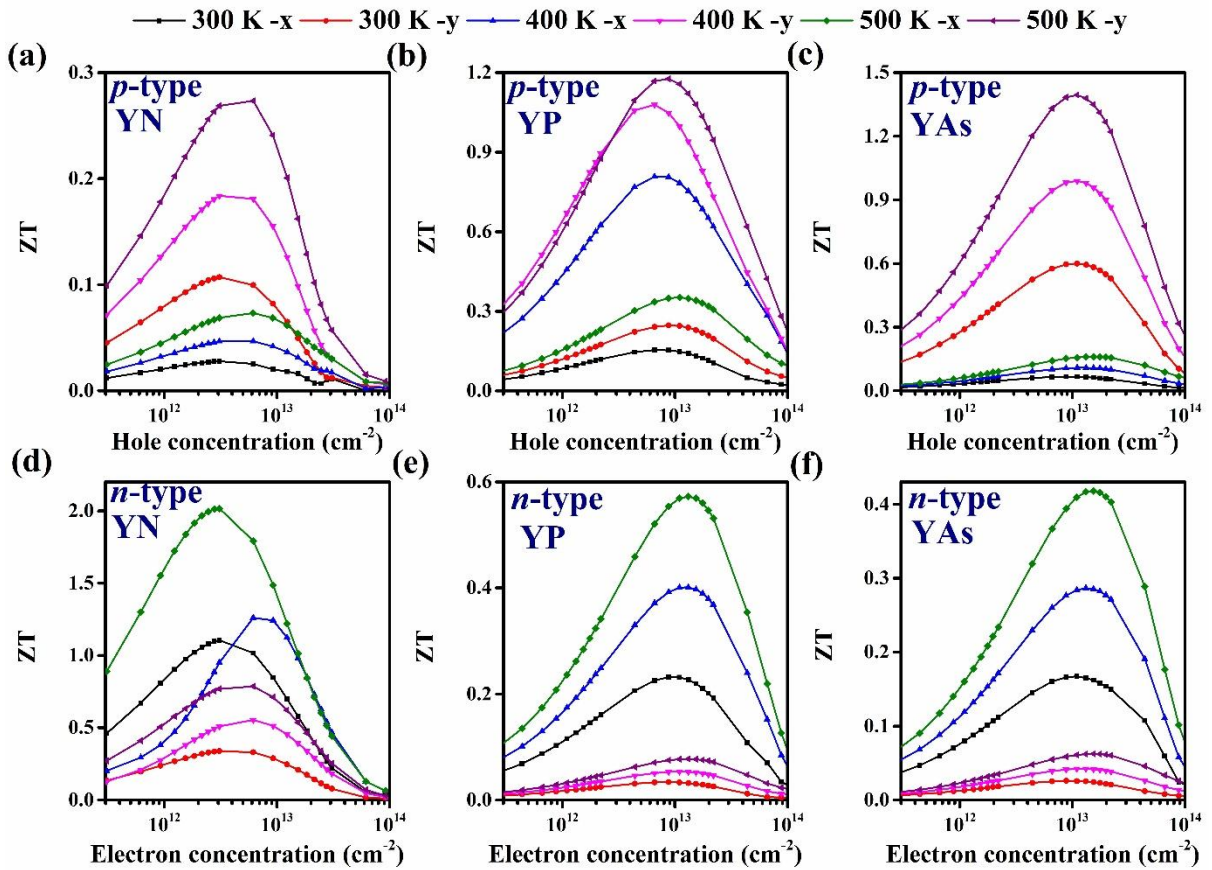


**Figure 6.16** Thermoelectric figure of merit ( $ZT$ ) with varying carrier concentrations at 300, 400, and 500 K in the  $x$ - and  $y$ - directions of (a)–(c)  $p$ -type and (d)–(f)  $n$ -type YX ( $X = N, P, As$ ) monolayers

## 6.4 Summary

We conducted extensive first-principles calculations and used semiclassical Boltzmann transport theory to explore structural, electronic, and TE properties of 2D YX ( $X = \text{N, P, As}$ ) rare-earth pnictide monolayers. We showed that these monolayers are energetically, thermally, and dynamically stable. We found that the YN, YP, and YAs monolayers are semiconductors with the HSE06 band gaps of 0.69 (direct), 1.65 (indirect), and 1.67 (indirect) eV, respectively. The monolayers are found to exhibit high anisotropy in the electronic transport properties, which is attributed to their unique crystallographic and electronic structure. The dimensionality reduction in these semiconducting materials with strong  $p$ - $d$  hybridization led to high electron conductivities thereby resulting in high  $ZT$ . The phonon band structure shows enhanced coupling between the low-frequency optical and acoustic modes. Accordingly, low  $\kappa_l$  obtained, with values 3.335, 1.779, and 1.648  $\text{Wm}^{-1}\text{K}^{-1}$  for YN, YP, and YAs monolayers, respectively at 500 K. For the  $p$ -type materials, highest  $ZT$  is achieved in the order  $\text{YN} < \text{YP} < \text{YAs}$  in the  $y$ -direction, while for  $n$ -type materials, it is in order  $\text{YN} > \text{YP} > \text{YAs}$  in the  $x$ -direction. The monolayers YN, YAs, and YP are found to exhibit a maximum figure of merit of 2.02, 1.39, and 1.18, respectively at 500 K, showing excellent TE performance. This work has demonstrated the tuning of thermoelectric parameters of rare earth pnictides monolayers for their potential use in future thermoelectric device applications.

# CHAPTER 7: CONCLUSION, FUTURE SCOPE, AND SOCIAL IMPACT

---

In this chapter, we conclude our research work entitled “*Computational Investigation of Thermoelectric Properties in Selected Two- and Three-dimensional Materials*” and provide the future prospects of this work.

## 7.1 Conclusions

The four classes of materials, *i.e.*, Zintl phase compounds, half-Heusler compounds, Li based transition metal nitrides, and two-dimensional yttrium pnictides within the framework of DFT, are reported as promising TE materials for applications over a wide temperature range. Combining first-principles calculations with the semiclassical Boltzmann transport theory, we evaluated the electronic, phonon, and transport properties of these materials to identify the promising materials with high figure of merit for TE applications. We also performed the stability analysis to confirm their phonon, mechanical, and thermodynamic viability of selected materials. Our work provides deep theoretical insights and an exhaustive data to guide future experimental work on these materials. The conclusions of each proposed series of materials are as follows:-

### 7.1.1 Thermoelectric performance in *p*-type $\text{RbZn}_4\text{P}_3$ and *n*-type $\text{RbGaSb}_2$ Zintl compounds

We analyzed the thermoelectric properties of  $\text{RbZn}_4\text{P}_3$  for various doping concentrations at different temperatures (300-700 K).  $\text{RbZn}_4\text{P}_3$  is thermodynamically, dynamically, and mechanically stable. The electronic band structure calculations reveal that  $\text{RbZn}_4\text{P}_3$  is a moderate bandgap semiconductor. Rb atom completely transfers its valence electron to the covalently bonded cluster  $[\text{Zn}_4\text{P}_3]^-$ , thus confirming the coexistence of ionic and covalent bonding. The key advantage of  $\text{RbGaSb}_2$  as a TE material is attributed to the complex crystal structure, the potential rattling of Rb cations, and the presence of heavy elements. Low thermal conductivity of  $\text{RbGaSb}_2$  allows for efficient conversion of heat into electricity, making it a potential candidate for TE applications.

### **7.1.2 Augmented thermoelectric performance of LiCaX (X = As, Sb) Half Heusler compounds via carrier concentration optimization**

The high-temperature stability and dynamical stability of these compounds are confirmed. Both LiCaAs and LiCaSb are indirect band gap semiconductors. TE performance is slightly enhanced with an increase in atomic weight of X atom owing to low  $\kappa_l$  and significant power factor. The remarkably low  $\kappa_l$  of 8-VEC half-Heusler compounds LiCaX (X = As, Sb), which we understood in terms of different phonon modes, and optimization of carrier concentration resulted in an improved  $ZT$  at higher temperatures. We are optimistic that this work could lead to future experiments to investigate the thermoelectric properties of proposed Li-based half-Heusler alloys.

### **7.1.3 Thermoelectric properties and lattice dynamics of Li<sub>2</sub>MN<sub>2</sub> (M = Zr or Hf)**

We have analyzed how replacing Zr with the relatively heavy element Hf in Li<sub>2</sub>MN<sub>2</sub> leads to an increase in thermal conductivity instead of a decrease. The anisotropic character owing to the layered structure of Li<sub>2</sub>MN<sub>2</sub> has enabled tuning their transport properties. A lower lattice thermal conductivity (1.52 Wm<sup>-1</sup>K<sup>-1</sup>), compared to Li<sub>2</sub>HfN<sub>2</sub>, along the *a*-axis at 1000 K for Li<sub>2</sub>ZrN<sub>2</sub> is attributed to the rattling behavior of Zr that leads to shorter phonon lifetimes. The high figure of merit (1.07) of Li<sub>2</sub>ZrN<sub>2</sub> along the *a*-axis has unraveled its potential for high-temperature thermoelectric application. Our findings on the electronic and lattice transport properties of Li<sub>2</sub>MN<sub>2</sub> may open new horizons for the design and synthesis of more efficient nitride-based thermoelectrics.

### **7.1.4 Realization of YX (X = N, P, As) pnictide monolayers as highly efficient thermoelectric materials**

We have explored structural, electronic, and TE properties of 2D YX (X = N, P, As) pnictide monolayers. These monolayers are energetically, thermally, and dynamically stable. The monolayers are found to exhibit high anisotropy in the electronic transport properties, which is attributed to their unique crystallographic and electronic structure. The dimensionality reduction in these semiconducting materials with strong *p-d* hybridization led to high electron conductivities thereby resulting in high  $ZT$ . The phonon band structure shows enhanced coupling between the low-frequency optical and acoustic modes. Low thermal conductivity was obtained, with values 3.335, 1.779, and 1.648 Wm<sup>-1</sup>K<sup>-1</sup> for YN, YP, and YAs monolayers, respectively, at 500 K. The monolayers YN, YAs, and YP are found to exhibit a maximum

figure of merit of 2.02, 1.39, and 1.18, respectively at 500 K, showing excellent TE performance.

## 7.2 Future Scope

The computational work presented in the present thesis provides a straightforward approach for experimentalists to design efficient TE materials by reducing the dependence on trial-and-error methods in the wet lab. Our work outlines some approaches, including carrier concentration optimization, phonon engineering, and dimensional reduction for enhancing the TE performance of bulk and 2D materials; however, several directions remain open for future work. It opens new avenues for future experimental realization of these materials for energy harvesting applications in a wide temperature range, *i.e.*, from near room temperature to high temperature. Also, the experimental validation of the proposed materials is crucial to confirm their TE performance under practical conditions. Future work could focus more deeply on phonon transport engineering, including the role of anharmonicity, considering different phonon scattering mechanisms, and defect-induced phonon changes, to further reduce lattice thermal conductivity. Also, Future studies can explore strain engineering, interface effects, and heterostructure design to enhance the  $ZT$  of the proposed materials. One can apply machine learning algorithms to predict novel high  $ZT$  TE materials and utilize high-throughput screening methods to accelerate material discovery and optimization.

## 7.3 Social Impact

The growing global demand for sustainable and clean energy has highlighted the urgent need for advanced materials that can convert waste heat into usable electricity. The present thesis focuses on the computational design and understanding of high-performance TE materials. These materials hold significant promise for enhancing energy efficiency in a variety of sectors, including industrial processes, automotive systems, and even wearable electronics for different temperature applications. By identifying and optimizing materials with high TE performance, this work contributes directly to the development of technologies that can reduce reliance on conventional energy resources. TE devices based on the materials studied here can potentially harvest waste heat, converting it to useful electricity without the need of any moving parts, thus offering a low-maintenance energy solution. The insights gained from this thesis not only advances the fundamental understanding of thermal and electronic transport in novel materials but also pave the way for their practical implementation in next-generation energy conversion devices, ultimately contributing to a more sustainable and energy-resilient society.

## REFERENCES

- [1] K.K. Jaiswal, C.R. Chowdhury, D. Yadav, R. Verma, S. Dutta, K.S. Jaiswal, SangmeshB, K.S.K. Karuppasamy, Renewable and sustainable clean energy development and impact on social, economic, and environmental health, *Energy Nexus* 7 (2022) 100118. <https://doi.org/10.1016/j.nexus.2022.100118>.
- [2] X.F. Zheng, C.X. Liu, Y.Y. Yan, Q. Wang, A review of thermoelectrics research – Recent developments and potentials for sustainable and renewable energy applications, *Renewable and Sustainable Energy Reviews* 32 (2014) 486–503. <https://doi.org/10.1016/j.rser.2013.12.053>.
- [3] A. Qazi, F. Hussain, N.Abd. Rahim, G. Hardaker, D. Alghazzawi, K. Shaban, K. Haruna, Towards Sustainable Energy: A Systematic Review of Renewable Energy Sources, Technologies, and Public Opinions, *IEEE Access* 7 (2019) 63837–63851. <https://doi.org/10.1109/ACCESS.2019.2906402>.
- [4] R. Freer, A.V. Powell, Realising the potential of thermoelectric technology: a Roadmap, *J. Mater. Chem. C* 8 (2020) 441–463. <https://doi.org/10.1039/C9TC05710B>.
- [5] T.M. Tritt, M.A. Subramanian, Thermoelectric Materials, Phenomena, and Applications: A Bird’s Eye View, *MRS Bull.* 31 (2006) 188–198. <https://doi.org/10.1557/mrs2006.44>.
- [6] S. Twaha, J. Zhu, Y. Yan, B. Li, A comprehensive review of thermoelectric technology: Materials, applications, modelling and performance improvement, *Renewable and Sustainable Energy Reviews* 65 (2016) 698–726. <https://doi.org/10.1016/j.rser.2016.07.034>.
- [7] J. He, T.M. Tritt, Advances in thermoelectric materials research: Looking back and moving forward, *Science* 357 (2017) eaak9997. <https://doi.org/10.1126/science.aak9997>.
- [8] X.-L. Shi, J. Zou, Z.-G. Chen, Advanced Thermoelectric Design: From Materials and Structures to Devices, *Chem. Rev.* 120 (2020) 7399–7515. <https://doi.org/10.1021/acs.chemrev.0c00026>.
- [9] L.E. Bell, Cooling, Heating, Generating Power, and Recovering Waste Heat with Thermoelectric Systems, *Science* 321 (2008) 1457–1461. <https://doi.org/10.1126/science.1158899>.
- [10] R. Tian, C. Wan, N. Hayashi, T. Aoi, K. Koumoto, Wearable and flexible thermoelectrics for energy harvesting, *MRS Bull.* 43 (2018) 193–198. <https://doi.org/10.1557/mrs.2018.8>.
- [11] G. Tan, M. Ohta, M.G. Kanatzidis, Thermoelectric power generation: from new materials to devices, *Phil. Trans. R. Soc. A.* 377 (2019) 20180450. <https://doi.org/10.1098/rsta.2018.0450>.
- [12] Y. Xiao, L.-D. Zhao, Seeking new, highly effective thermoelectrics, *Science* 367 (2020) 1196–1197. <https://doi.org/10.1126/science.aaz9426>.
- [13] Z. Han, J.-W. Li, F. Jiang, J. Xia, B.-P. Zhang, J.-F. Li, W. Liu, Room-temperature thermoelectric materials: Challenges and a new paradigm, *Journal of Materiomics* 8 (2022) 427–436. <https://doi.org/10.1016/j.jmat.2021.07.004>.
- [14] K.-X. Chen, M.-S. Li, D.-C. Mo, S.-S. Lyu, Nanostructural thermoelectric materials and their performance, *Front. Energy* 12 (2018) 97–108. <https://doi.org/10.1007/s11708-018-0543-5>.
- [15] D. Li, Y. Gong, Y. Chen, J. Lin, Q. Khan, Y. Zhang, Y. Li, H. Zhang, H. Xie, Recent Progress of Two-Dimensional Thermoelectric Materials, *Nano-Micro Lett.* 12 (2020) 36. <https://doi.org/10.1007/s40820-020-0374-x>.
- [16] T. Zhu, Y. Liu, C. Fu, J.P. Heremans, J.G. Snyder, X. Zhao, Compromise and Synergy in High-Efficiency Thermoelectric Materials, *Advanced Materials* 29 (2017) 1605884. <https://doi.org/10.1002/adma.201605884>.

- [17] Y. Li, K. Ma, X. Fan, F. Liu, J. Li, H. Xie, Enhancing thermoelectric properties of monolayer GeSe via strain-engineering: A first principles study, *Applied Surface Science* 521 (2020) 146256. <https://doi.org/10.1016/j.apsusc.2020.146256>.
- [18] K.H. Lee, S. Kim, H.-S. Kim, S.W. Kim, Band Convergence in Thermoelectric Materials: Theoretical Background and Consideration on Bi–Sb–Te Alloys, *ACS Appl. Energy Mater.* 3 (2020) 2214–2223. <https://doi.org/10.1021/acsaem.9b02131>.
- [19] J.L. Baker, C. Park, C. Kenney-Benson, V.K. Sharma, V. Kanchana, G. Vaitheeswaran, C.J. Pickard, A. Cornelius, N. Velisavljevic, R.S. Kumar, Pressure-Induced Enhancement of Thermoelectric Figure of Merit and Structural Phase Transition in TiNiSn, *J. Phys. Chem. Lett.* 12 (2021) 1046–1051. <https://doi.org/10.1021/acs.jpcclett.0c03609>.
- [20] M. Chen, X. Lu, L. Sun, N. Yin, Q. Shi, Y. Meng, T. Liu, P. Jiang, X. Bao, Magnetic-field-enhanced high thermoelectric performance in narrow-band-gap polycrystalline semiconductor  $\text{Ag}_{2+\delta}\text{Te}$ , *Materials Today Physics* 36 (2023) 101161. <https://doi.org/10.1016/j.mtphys.2023.101161>.
- [21] G.J. Snyder, E.S. Toberer, Complex thermoelectric materials, *Nature Mater* 7 (2008) 105–114. <https://doi.org/10.1038/nmat2090>.
- [22] J. Palraj, M. Moorthy, S. Katlakunta, S. Perumal, Isovalent Bi substitution induced low thermal conductivity and high thermoelectric performance in n-type InSb, *Ceramics International* 48 (2022) 29284–29290. <https://doi.org/10.1016/j.ceramint.2022.05.282>.
- [23] Y. Pei, H. Wang, G.J. Snyder, Band Engineering of Thermoelectric Materials, *Advanced Materials* 24 (2012) 6125–6135. <https://doi.org/10.1002/adma.201202919>.
- [24] L.D. Hicks, M.S. Dresselhaus, Effect of quantum-well structures on the thermoelectric figure of merit, *Phys. Rev. B* 47 (1993) 12727–12731. <https://doi.org/10.1103/PhysRevB.47.12727>.
- [25] M.S. Dresselhaus, G. Dresselhaus, X. Sun, Z. Zhang, S.B. Cronin, T. Koga, Low-dimensional thermoelectric materials, *Phys. Solid State* 41 (1999) 679–682. <https://doi.org/10.1134/1.1130849>.
- [26] G. Tan, L.-D. Zhao, M.G. Kanatzidis, Rationally Designing High-Performance Bulk Thermoelectric Materials, *Chem. Rev.* 116 (2016) 12123–12149. <https://doi.org/10.1021/acs.chemrev.6b00255>.
- [27] Y. Liu, M. Zhou, J. He, Towards higher thermoelectric performance of  $\text{Bi}_2\text{Te}_3$  via defect engineering, *Scripta Materialia* 111 (2016) 39–43. <https://doi.org/10.1016/j.scriptamat.2015.06.031>.
- [28] W. Wei, C. Chang, T. Yang, J. Liu, H. Tang, J. Zhang, Y. Li, F. Xu, Z. Zhang, J.-F. Li, G. Tang, Achieving High Thermoelectric Figure of Merit in Polycrystalline SnSe via Introducing Sn Vacancies, *J. Am. Chem. Soc.* 140 (2018) 499–505. <https://doi.org/10.1021/jacs.7b11875>.
- [29] W. Li, S. Lin, X. Zhang, Z. Chen, X. Xu, Y. Pei, Thermoelectric Properties of  $\text{Cu}_2\text{SnSe}_4$  with Intrinsic Vacancy, *Chem. Mater.* 28 (2016) 6227–6232. <https://doi.org/10.1021/acs.chemmater.6b02416>.
- [30] J. Li, X. Zhang, S. Lin, Z. Chen, Y. Pei, Realizing the High Thermoelectric Performance of GeTe by Sb-Doping and Se-Alloying, *Chem. Mater.* 29 (2017) 605–611. <https://doi.org/10.1021/acs.chemmater.6b04066>.
- [31] J. Tang, B. Gao, S. Lin, X. Wang, X. Zhang, F. Xiong, W. Li, Y. Chen, Y. Pei, Manipulation of Solubility and Interstitial Defects for Improving Thermoelectric SnTe Alloys, *ACS Energy Lett.* 3 (2018) 1969–1974. <https://doi.org/10.1021/acsenerylett.8b01098>.
- [32] X. Shi, A. Wu, W. Liu, R. Moshwan, Y. Wang, Z.-G. Chen, J. Zou, Polycrystalline SnSe with Extraordinary Thermoelectric Property via Nanoporous Design, *ACS Nano* 12 (2018) 11417–11425. <https://doi.org/10.1021/acsnano.8b06387>.

- [33] W. Liu, X. Shi, R. Moshwan, M. Hong, L. Yang, Z.-G. Chen, J. Zou, Enhancing thermoelectric performance of  $(\text{Cu}_{1-x}\text{Ag}_x)_2\text{Se}$  via  $\text{CuAgSe}$  secondary phase and porous design, *Sustainable Materials and Technologies* 17 (2018) e00076. <https://doi.org/10.1016/j.susmat.2018.e00076>.
- [34] W. Li, S. Lin, M. Weiss, Z. Chen, J. Li, Y. Xu, W.G. Zeier, Y. Pei, Crystal Structure Induced Ultralow Lattice Thermal Conductivity in Thermoelectric  $\text{Ag}_9\text{AlSe}_6$ , *Advanced Energy Materials* 8 (2018) 1800030. <https://doi.org/10.1002/aenm.201800030>.
- [35] L.-D. Zhao, S.-H. Lo, Y. Zhang, H. Sun, G. Tan, C. Uher, C. Wolverton, V.P. Dravid, M.G. Kanatzidis, Ultralow thermal conductivity and high thermoelectric figure of merit in  $\text{SnSe}$  crystals, *Nature* 508 (2014) 373–377. <https://doi.org/10.1038/nature13184>.
- [36] S. Lin, W. Li, S. Li, X. Zhang, Z. Chen, Y. Xu, Y. Chen, Y. Pei, High Thermoelectric Performance of  $\text{Ag}_9\text{GaSe}_6$  Enabled by Low Cutoff Frequency of Acoustic Phonons, *Joule* 1 (2017) 816–830. <https://doi.org/10.1016/j.joule.2017.09.006>.
- [37] A. Ugrinov, S.C. Sevov, Rationally Functionalized Deltahedral Zintl Ions: Synthesis and Characterization of  $[\text{Ge}_9\text{-ER}_3]^{3-}$ ,  $[\text{R}_3\text{E-Ge}_9\text{-ER}_3]^{2-}$ , and  $[\text{R}_3\text{E-Ge}_9\text{-Ge}_9\text{-ER}_3]^{4-}$  (E=Ge, Sn; R=Me, Ph), *Chemistry A European J* 10 (2004) 3727–3733. <https://doi.org/10.1002/chem.200400130>.
- [38] K. Wiesler, K. Brandl, A. Fleischmann, N. Korber, Tetrahedral  $[\text{Tt}_4]^{4-}$  Zintl Anions Through Solution Chemistry: Syntheses and Crystal Structures of the Ammoniates  $\text{Rb}_4\text{Sn}_4 \cdot 2\text{NH}_3$ ,  $\text{Cs}_4\text{Sn}_4 \cdot 2\text{NH}_3$ , and  $\text{Rb}_4\text{Pb}_4 \cdot 2\text{NH}_3$ , *Zeitschrift Anorg Allg Chem* 635 (2009) 508–512. <https://doi.org/10.1002/zaac.200801249>.
- [39] R. Nesper, The Zintl-Klemm Concept – A Historical Survey, *Zeitschrift Anorg Allg Chem* 640 (2014) 2639–2648. <https://doi.org/10.1002/zaac.201400403>.
- [40] F. Gascoin, S. Ottensmann, D. Stark, S.M. Haïle, G.J. Snyder, Zintl Phases as Thermoelectric Materials: Tuned Transport Properties of the Compounds  $\text{Ca}_x\text{Yb}_{1-x}\text{Zn}_2\text{Sb}_2$ , *Adv Funct Materials* 15 (2005) 1860–1864. <https://doi.org/10.1002/adfm.200500043>.
- [41] S.M. Kauzlarich, S.R. Brown, G. Jeffrey Snyder, Zintl phases for thermoelectric devices, *Dalton Trans.* (2007) 2099. <https://doi.org/10.1039/b702266b>.
- [42] C. Chen, Z. Feng, H. Yao, F. Cao, B.-H. Lei, Y. Wang, Y. Chen, D.J. Singh, Q. Zhang, Intrinsic nanostructure induced ultralow thermal conductivity yields enhanced thermoelectric performance in Zintl phase  $\text{Eu}_2\text{ZnSb}_2$ , *Nat Commun* 12 (2021) 5718. <https://doi.org/10.1038/s41467-021-25483-w>.
- [43] J. Zhang, L. Song, A. Mamakhel, M.R.V. Jørgensen, B.B. Iversen, High-Performance Low-Cost n-Type Se-Doped  $\text{Mg}_3\text{Sb}_2$ -Based Zintl Compounds for Thermoelectric Application, *Chem. Mater.* 29 (2017) 5371–5383. <https://doi.org/10.1021/acs.chemmater.7b01746>.
- [44] G. Yang, J. Yang, Y. Yan, Y. Wang, The relationship between the electronic structure and thermoelectric properties of Zintl compounds  $\text{M}_2\text{Zn}_5\text{As}_4$  (M = K, Rb), *Phys. Chem. Chem. Phys.* 16 (2014) 5661. <https://doi.org/10.1039/c3cp54545h>.
- [45] A. Zevalkink, W.G. Zeier, G. Pomrehn, E. Schechtel, W. Tremel, G.J. Snyder, Thermoelectric properties of  $\text{Sr}_3\text{GaSb}_3$  – a chain-forming Zintl compound, *Energy Environ. Sci.* 5 (2012) 9121. <https://doi.org/10.1039/c2ee22378c>.
- [46] S. Azam, S.A. Khan, S. Goumri-Said, Revealing the optoelectronic and thermoelectric properties of the Zintl quaternary arsenides  $\text{ACdGeAs}_2$  (A = K, Rb), *Materials Research Bulletin* 70 (2015) 847–855. <https://doi.org/10.1016/j.materresbull.2015.05.044>.
- [47] F. Heusler, Über magnetische manganlegierungen, *Verh. Dtsch. Phys. Ges* 5 (1903) 219.
- [48] O. Heusler, Kristallstruktur und Ferromagnetismus der Mangan-Aluminium-Kupferlegierungen, *Annalen Der Physik* 411 (1934) 155–201. <https://doi.org/10.1002/andp.19344110205>.



- [49] The crystal structure of the heusler alloys, *Proc. R. Soc. Lond. A* 144 (1934) 340–359. <https://doi.org/10.1098/rspa.1934.0053>.
- [50] H. Nowotny, K. Bachmayer, Die Verbindungen LiMgP, LiZnP und LiZnAs, *Monatshefte für Chemie* 81 (1950) 488–496. <https://doi.org/10.1007/BF00906437>.
- [51] R. Juza, F. Hund, Die Kristallstrukturen LiMgN, LiZnN, Li<sub>3</sub>AlN<sub>2</sub> und Li<sub>3</sub>GaN<sub>2</sub>, *Naturwissenschaften* 33 (1946) 121–122. <https://doi.org/10.1007/BF00738267>.
- [52] J.-W.G. Bos, Recent developments in half-Heusler thermoelectric materials, in: *Thermoelectric Energy Conversion*, Elsevier, 2021: pp. 125–142. <https://doi.org/10.1016/B978-0-12-818535-3.00014-1>.
- [53] T. Fang, X. Zhao, T. Zhu, Band Structures and Transport Properties of High-Performance Half-Heusler Thermoelectric Materials by First Principles, *Materials* 11 (2018) 847. <https://doi.org/10.3390/ma11050847>.
- [54] S.J. Poon, Recent Advances in Thermoelectric Performance of Half-Heusler Compounds, *Metals* 8 (2018) 989. <https://doi.org/10.3390/met8120989>.
- [55] R.J. Quinn, J.-W.G. Bos, Advances in half-Heusler alloys for thermoelectric power generation, *Mater. Adv.* 2 (2021) 6246–6266. <https://doi.org/10.1039/D1MA00707F>.
- [56] S. Anand, K. Xia, V. I. Hegde, U. Aydemir, V. Kocovski, T. Zhu, C. Wolverton, G.J. Snyder, A valence balanced rule for discovery of 18-electron half-Heuslers with defects, *Energy Environ. Sci.* 11 (2018) 1480–1488. <https://doi.org/10.1039/C8EE00306H>.
- [57] Z. Liu, S. Guo, Y. Wu, J. Mao, Q. Zhu, H. Zhu, Y. Pei, J. Sui, Y. Zhang, Z. Ren, Design of High-Performance Disordered Half-Heusler Thermoelectric Materials Using 18-Electron Rule, *Adv. Funct. Materials* 29 (2019) 1905044. <https://doi.org/10.1002/adfm.201905044>.
- [58] Vikram, B. Sahni, C.K. Barman, A. Alam, Accelerated Discovery of New 8-Electron Half-Heusler Compounds as Promising Energy and Topological Quantum Materials, *J. Phys. Chem. C* 123 (2019) 7074–7080. <https://doi.org/10.1021/acs.jpcc.9b01737>.
- [59] Y. Liu, W. Wang, J. Yang, S. Li, Recent Advances of Layered Thermoelectric Materials, *Advanced Sustainable Systems* 2 (2018) 1800046. <https://doi.org/10.1002/adsu.201800046>.
- [60] M. Samanta, T. Ghosh, S. Chandra, K. Biswas, Layered materials with 2D connectivity for thermoelectric energy conversion, *J. Mater. Chem. A* 8 (2020) 12226–12261. <https://doi.org/10.1039/D0TA00240B>.
- [61] J. Rundle, S. Leoni, Layered Tin Chalcogenides SnS and SnSe: Lattice Thermal Conductivity Benchmarks and Thermoelectric Figure of Merit, *J. Phys. Chem. C* 126 (2022) 14036–14046. <https://doi.org/10.1021/acs.jpcc.2c02401>.
- [62] Y. Hinuma, T. Hatakeyama, Y. Kumagai, L.A. Burton, H. Sato, Y. Muraba, S. Iimura, H. Hiramatsu, I. Tanaka, H. Hosono, F. Oba, Discovery of earth-abundant nitride semiconductors by computational screening and high-pressure synthesis, *Nat Commun* 7 (2016) 11962. <https://doi.org/10.1038/ncomms11962>.
- [63] P. Eklund, S. Kerdsonpanya, B. Alling, Transition-metal-nitride-based thin films as novel energy harvesting materials, *J. Mater. Chem. C* 4 (2016) 3905–3914. <https://doi.org/10.1039/C5TC03891J>.
- [64] R. Al Rahal Al Orabi, E. Orisakwe, D. Wee, B. Fontaine, R. Gautier, J.-F. Halet, M. Fornari, Prediction of high thermoelectric potential in AMN<sub>2</sub> layered nitrides: electronic structure, phonons, and anharmonic effects, *J. Mater. Chem. A* 3 (2015) 9945–9954. <https://doi.org/10.1039/C5TA00546A>.
- [65] I. Ohkubo, T. Mori, Anisotropic thermoelectric properties in layered complex nitrides with  $\alpha$ -NaFeO<sub>2</sub>-type structure, *APL Materials* 4 (2016) 104808. <https://doi.org/10.1063/1.4955399>.

- [66] S. Bandaru, A.M. Jastrzębska, M. Birowska, Recent progress in thermoelectric MXene-based structures versus other 2D materials, *Applied Materials Today* 34 (2023) 101902. <https://doi.org/10.1016/j.apmt.2023.101902>.
- [67] L. Li, W. Han, L. Pi, P. Niu, J. Han, C. Wang, B. Su, H. Li, J. Xiong, Y. Bando, T. Zhai, Emerging in-plane anisotropic two-dimensional materials, *InfoMat* 1 (2019) 54–73. <https://doi.org/10.1002/inf2.12005>.
- [68] H. Wei, X. Jin, X. Xiao, L. Shi, Y. Duan, J. Fan, R. Wang, X. Wu, Stability and thermoelectric performance of the two-dimensional rare-earth compounds  $R\text{TeCl}$  ( $R = \text{La}, \text{Pr}, \text{Nd}$ ), *Phys. Rev. Applied* 21 (2024) 054026. <https://doi.org/10.1103/PhysRevApplied.21.054026>.
- [69] G. Zhang, Y.-W. Zhang, Strain effects on thermoelectric properties of two-dimensional materials, *Mechanics of Materials* 91 (2015) 382–398. <https://doi.org/10.1016/j.mechmat.2015.03.009>.
- [70] E. Schrödinger, An Undulatory Theory of the Mechanics of Atoms and Molecules, *Phys. Rev.* 28 (1926) 1049–1070. <https://doi.org/10.1103/PhysRev.28.1049>.
- [71] M. Born, R. Oppenheimer, Zur Quantentheorie der Molekeln, *Annalen Der Physik* 389 (1927) 457–484. <https://doi.org/10.1002/andp.19273892002>.
- [72] D.R. Hartree, The Wave Mechanics of an Atom with a Non-Coulomb Central Field. Part I. Theory and Methods, *Math. Proc. Camb. Phil. Soc.* 24 (1928) 89–110. <https://doi.org/10.1017/S0305004100011919>.
- [73] V. Fock, Näherungsmethode zur Lösung des quantenmechanischen Mehrkörperproblems, *Z. Physik* 61 (1930) 126–148. <https://doi.org/10.1007/BF01340294>.
- [74] R.O. Jones, O. Gunnarsson, The density functional formalism, its applications and prospects, *Rev. Mod. Phys.* 61 (1989) 689–746. <https://doi.org/10.1103/RevModPhys.61.689>.
- [75] P. Hohenberg, W. Kohn, Inhomogeneous Electron Gas, *Phys. Rev.* 136 (1964) B864–B871. <https://doi.org/10.1103/PhysRev.136.B864>.
- [76] W. Kohn, L.J. Sham, Self-Consistent Equations Including Exchange and Correlation Effects, *Phys. Rev.* 140 (1965) A1133–A1138. <https://doi.org/10.1103/PhysRev.140.A1133>.
- [77] W. Kohn, L.J. Sham, Self-Consistent Equations Including Exchange and Correlation Effects, *Phys. Rev.* 140 (1965) A1133–A1138. <https://doi.org/10.1103/PhysRev.140.A1133>.
- [78] I.N. Yakovkin, P.A. Dowben, THE PROBLEM OF THE BAND GAP IN LDA CALCULATIONS, *Surf. Rev. Lett.* 14 (2007) 481–487. <https://doi.org/10.1142/S0218625X07009499>.
- [79] F. Herman, J.P. Van Dyke, I.B. Ortenburger, Improved Statistical Exchange Approximation for Inhomogeneous Many-Electron Systems, *Phys. Rev. Lett.* 22 (1969) 807–811. <https://doi.org/10.1103/PhysRevLett.22.807>.
- [80] J.P. Perdew, Y. Wang, Accurate and simple analytic representation of the electron-gas correlation energy, *Phys. Rev. B* 45 (1992) 13244–13249. <https://doi.org/10.1103/PhysRevB.45.13244>.
- [81] J.P. Perdew, J.A. Chevary, S.H. Vosko, K.A. Jackson, M.R. Pederson, D.J. Singh, C. Fiolhais, Atoms, molecules, solids, and surfaces: Applications of the generalized gradient approximation for exchange and correlation, *Phys. Rev. B* 46 (1992) 6671–6687. <https://doi.org/10.1103/PhysRevB.46.6671>.
- [82] J.P. Perdew, K. Burke, M. Ernzerhof, Generalized Gradient Approximation Made Simple, *Phys. Rev. Lett.* 77 (1996) 3865–3868. <https://doi.org/10.1103/PhysRevLett.77.3865>.

- [83] P. Ondračka, D. Holec, D. Nečas, L. Zajíčková, Accurate prediction of band gaps and optical properties of  $\text{HfO}_2$ , *J. Phys. D: Appl. Phys.* 49 (2016) 395301. <https://doi.org/10.1088/0022-3727/49/39/395301>.
- [84] A.D. Becke, E.R. Johnson, A simple effective potential for exchange, *The Journal of Chemical Physics* 124 (2006) 221101. <https://doi.org/10.1063/1.2213970>.
- [85] A.D. Becke, A new mixing of Hartree–Fock and local density-functional theories, *The Journal of Chemical Physics* 98 (1993) 1372–1377. <https://doi.org/10.1063/1.464304>.
- [86] J. Heyd, G.E. Scuseria, M. Ernzerhof, Hybrid functionals based on a screened Coulomb potential, *The Journal of Chemical Physics* 118 (2003) 8207–8215. <https://doi.org/10.1063/1.1564060>.
- [87] S.-H. Wei, H. Krakauer, M. Weinert, Linearized augmented-plane-wave calculation of the electronic structure and total energy of tungsten, *Phys. Rev. B* 32 (1985) 7792–7797. <https://doi.org/10.1103/PhysRevB.32.7792>.
- [88] P. Blaha, K. Schwarz, F. Tran, R. Laskowski, G.K.H. Madsen, L.D. Marks, WIEN2k: An APW+lo program for calculating the properties of solids, *The Journal of Chemical Physics* 152 (2020) 074101. <https://doi.org/10.1063/1.5143061>.
- [89] V. Heine, The Pseudopotential Concept, in: *Solid State Physics*, Elsevier, 1970: pp. 1–36. [https://doi.org/10.1016/S0081-1947\(08\)60069-7](https://doi.org/10.1016/S0081-1947(08)60069-7).
- [90] P. Schwerdtfeger, The Pseudopotential Approximation in Electronic Structure Theory, *ChemPhysChem* 12 (2011) 3143–3155. <https://doi.org/10.1002/cphc.201100387>.
- [91] P.E. Blöchl, Projector augmented-wave method, *Phys. Rev. B* 50 (1994) 17953–17979. <https://doi.org/10.1103/PhysRevB.50.17953>.
- [92] F. Bloch, Über die Quantenmechanik der Elektronen in Kristallgittern, *Z. Physik* 52 (1929) 555–600. <https://doi.org/10.1007/BF01339455>.
- [93] D.S. Sholl, J.A. Steckel, *Density Functional Theory: A Practical Introduction*, Wiley, 2011. [https://books.google.co.in/books?id=\\_f994dmAdv0C](https://books.google.co.in/books?id=_f994dmAdv0C).
- [94] H.J. Monkhorst, J.D. Pack, Special points for Brillouin-zone integrations, *Phys. Rev. B* 13 (1976) 5188–5192. <https://doi.org/10.1103/PhysRevB.13.5188>.
- [95] G.K.H. Madsen, D.J. Singh, BoltzTraP. A code for calculating band-structure dependent quantities, *Computer Physics Communications* 175 (2006) 67–71. <https://doi.org/10.1016/j.cpc.2006.03.007>.
- [96] G.K.H. Madsen, J. Carrete, M.J. Verstraete, BoltzTraP2, a program for interpolating band structures and calculating semi-classical transport coefficients, *Computer Physics Communications* 231 (2018) 140–145. <https://doi.org/10.1016/j.cpc.2018.05.010>.
- [97] J. Bardeen, W. Shockley, Deformation Potentials and Mobilities in Non-Polar Crystals, *Phys. Rev.* 80 (1950) 72–80. <https://doi.org/10.1103/PhysRev.80.72>.
- [98] A. Togo, I. Tanaka, First principles phonon calculations in materials science, *Scripta Materialia* 108 (2015) 1–5. <https://doi.org/10.1016/j.scriptamat.2015.07.021>.
- [99] T. Tadano, Y. Gohda, S. Tsuneyuki, Anharmonic force constants extracted from first-principles molecular dynamics: applications to heat transfer simulations, *J. Phys.: Condens. Matter* 26 (2014) 225402. <https://doi.org/10.1088/0953-8984/26/22/225402>.
- [100] A. Togo, L. Chaput, I. Tanaka, Distributions of phonon lifetimes in Brillouin zones, *Phys. Rev. B* 91 (2015) 094306. <https://doi.org/10.1103/PhysRevB.91.094306>.
- [101] W. Li, J. Carrete, N. A. Katcho, N. Mingo, ShengBTE: A solver of the Boltzmann transport equation for phonons, *Computer Physics Communications* 185 (2014) 1747–1758. <https://doi.org/10.1016/j.cpc.2014.02.015>.
- [102] J. Carrete, B. Vermeersch, A. Katre, A. Van Roekeghem, T. Wang, G.K.H. Madsen, N. Mingo, almaBTE: A solver of the space–time dependent Boltzmann transport equation for phonons in structured materials, *Computer Physics Communications* 220 (2017) 351–362. <https://doi.org/10.1016/j.cpc.2017.06.023>.

- [103] L. Chaput, Direct Solution to the Linearized Phonon Boltzmann Equation, *Phys. Rev. Lett.* 110 (2013) 265506. <https://doi.org/10.1103/PhysRevLett.110.265506>.
- [104] G. Kresse, J. Furthmüller, Efficiency of *ab-initio* total energy calculations for metals and semiconductors using a plane-wave basis set, *Computational Materials Science* 6 (1996) 15–50. [https://doi.org/10.1016/0927-0256\(96\)00008-0](https://doi.org/10.1016/0927-0256(96)00008-0).
- [105] G. Kresse, J. Furthmüller, Efficient iterative schemes for *ab initio* total-energy calculations using a plane-wave basis set, *Phys. Rev. B* 54 (1996) 11169–11186. <https://doi.org/10.1103/PhysRevB.54.11169>.
- [106] K.-F. Liu, S.-Q. Xia, Recent progresses on thermoelectric Zintl phases: Structures, materials and optimization, *Journal of Solid State Chemistry* 270 (2019) 252–264. <https://doi.org/10.1016/j.jssc.2018.11.030>.
- [107] L. Zheng, W. Li, C. Sun, X. Shi, X. Zhang, Y. Pei, Ternary thermoelectric AB<sub>2</sub>C<sub>2</sub> Zintls, *Journal of Alloys and Compounds* 821 (2020) 153497. <https://doi.org/10.1016/j.jallcom.2019.153497>.
- [108] Z. Lin, G. Wang, C. Le, H. Zhao, N. Liu, J. Hu, L. Guo, X. Chen, Thermal conductivities in NaSnAs, NaSnP, and NaS<sub>n</sub>As<sub>2</sub>: Effect of double lone-pair electrons, *Phys. Rev. B* 95 (2017) 165201. <https://doi.org/10.1103/PhysRevB.95.165201>.
- [109] N. Guechi, A. Bouhemadou, Y. Medkour, Y. Al-Douri, R. Khenata, S. Bin-Omran, Electronic and thermoelectric properties of the layered Zintl phase CaIn<sub>2</sub>P<sub>2</sub>: first-principles calculations, *Philosophical Magazine* 100 (2020) 3023–3039. <https://doi.org/10.1080/14786435.2020.1799101>.
- [110] Z. Feng, J. Yang, Y. Wang, Y. Yan, G. Yang, X. Zhang, Origin of different thermoelectric properties between Zintl compounds Ba<sub>3</sub>Al<sub>3</sub>P<sub>5</sub> and Ba<sub>3</sub>Ga<sub>3</sub>P<sub>5</sub>: A first-principles study, *Journal of Alloys and Compounds* 636 (2015) 387–394. <https://doi.org/10.1016/j.jallcom.2015.02.133>.
- [111] H. He, C. Tyson, S. Bobev, Eight-Coordinated Arsenic in the Zintl Phases RbCd<sub>4</sub>As<sub>3</sub> and RbZn<sub>4</sub>As<sub>3</sub>: Synthesis and Structural Characterization, *Inorg. Chem.* 50 (2011) 8375–8383. <https://doi.org/10.1021/ic2009418>.
- [112] P. Gorai, A. Ganose, A. Faghaninia, A. Jain, V. Stevanović, Computational discovery of promising new n-type dopable ABX Zintl thermoelectric materials, *Mater. Horiz.* 7 (2020) 1809–1818. <https://doi.org/10.1039/D0MH00197J>.
- [113] J. Wang, B. Owens-Baird, K. Kovnir, From Three-Dimensional Clathrates to Two-Dimensional Zintl Phases AMSb<sub>2</sub> (A = Rb, Cs; M = Ga, In) Composed of Pentagonal M–Sb Rings, *Inorg. Chem.* 61 (2022) 533–541. <https://doi.org/10.1021/acs.inorgchem.1c03217>.
- [114] F. Tran, P. Blaha, Accurate Band Gaps of Semiconductors and Insulators with a Semilocal Exchange-Correlation Potential, *Phys. Rev. Lett.* 102 (2009) 226401. <https://doi.org/10.1103/PhysRevLett.102.226401>.
- [115] G. Xing, J. Sun, Y. Li, X. Fan, W. Zheng, D.J. Singh, Electronic fitness function for screening semiconductors as thermoelectric materials, *Phys. Rev. Materials* 1 (2017) 065405. <https://doi.org/10.1103/PhysRevMaterials.1.065405>.
- [116] L. Lindsay, D.A. Broido, T.L. Reinecke, First-Principles Determination of Ultrahigh Thermal Conductivity of Boron Arsenide: A Competitor for Diamond?, *Phys. Rev. Lett.* 111 (2013) 025901. <https://doi.org/10.1103/PhysRevLett.111.025901>.
- [117] M. Born, K. Huang, M. Lax, Dynamical Theory of Crystal Lattices, *American Journal of Physics* 23 (1955) 474–474. <https://doi.org/10.1119/1.1934059>.
- [118] R. Hill, The Elastic Behaviour of a Crystalline Aggregate, *Proc. Phys. Soc. A* 65 (1952) 349–354. <https://doi.org/10.1088/0370-1298/65/5/307>.
- [119] F. Parvin, M.A. Hossain, I. Ahmed, K. Akter, A.K.M.A. Islam, First-principles calculations to investigate mechanical, optoelectronic and thermoelectric properties of

- half-Heusler p-type semiconductor BaAgP, *Results in Physics* 23 (2021) 104068. <https://doi.org/10.1016/j.rinp.2021.104068>.
- [120] O.L. Anderson, A simplified method for calculating the debye temperature from elastic constants, *Journal of Physics and Chemistry of Solids* 24 (1963) 909–917. [https://doi.org/10.1016/0022-3697\(63\)90067-2](https://doi.org/10.1016/0022-3697(63)90067-2).
- [121] A.K. Chandran, V.K. Gudelli, P.C. Sreeparvathy, V. Kanchana, Structural and thermoelectric properties of zintl-phase CaLiPn (Pn=As, Sb, Bi), *Journal of Solid State Chemistry* 243 (2016) 198–206. <https://doi.org/10.1016/j.jssc.2016.08.030>.
- [122] M. Jonson, G.D. Mahan, Mott's formula for the thermopower and the Wiedemann-Franz law, *Phys. Rev. B* 21 (1980) 4223–4229. <https://doi.org/10.1103/PhysRevB.21.4223>.
- [123] A. Putatunda, G. Xing, J. Sun, Y. Li, D.J. Singh, Thermoelectric properties of layered NaSbSe<sub>2</sub>, *J. Phys.: Condens. Matter* 30 (2018) 225501. <https://doi.org/10.1088/1361-648X/aabf5b>.
- [124] P.O. Adebambo, O.E. Osafire, J.A. Laoye, M.A. Idowu, G.A. Adebayo, Electronic fitness function, effective mass and thermoelectric properties of Rh-based (-ScTe; -TiSb; -VSn) alloys for thermoelectric generator applications, *Computational Condensed Matter* 26 (2021) e00523. <https://doi.org/10.1016/j.cocom.2020.e00523>.
- [125] G.A. Slack, The Thermal Conductivity of Nonmetallic Crystals, in: *Solid State Physics*, Elsevier, 1979: pp. 1–71. [https://doi.org/10.1016/S0081-1947\(08\)60359-8](https://doi.org/10.1016/S0081-1947(08)60359-8).
- [126] Y. Gupta, M.M. Sinha, S.S. Verma, First-principles investigation on the electronic, mechanical and lattice dynamical properties of novel AlNiX (X = As and Sb) half-Heusler alloys, *Materials Today Communications* 26 (2021) 101885. <https://doi.org/10.1016/j.mtcomm.2020.101885>.
- [127] V.N. Belomestnykh, E.P. Tesleva, Interrelation between anharmonicity and lateral strain in quasi-isotropic polycrystalline solids, *Tech. Phys.* 49 (2004) 1098–1100. <https://doi.org/10.1134/1.1787679>.
- [128] D. Bessas, I. Sergueev, H.-C. Wille, J. Perßon, D. Ebling, R.P. Hermann, Lattice dynamics in Bi<sub>2</sub>Te<sub>3</sub> and Sb<sub>2</sub>Te<sub>3</sub>: Te and Sb density of phonon states, *Phys. Rev. B* 86 (2012) 224301. <https://doi.org/10.1103/PhysRevB.86.224301>.
- [129] J.J. Kuo, S.D. Kang, K. Imasato, H. Tamaki, S. Ohno, T. Kanno, G.J. Snyder, Grain boundary dominated charge transport in Mg<sub>3</sub>Sb<sub>2</sub>-based compounds, *Energy Environ. Sci.* 11 (2018) 429–434. <https://doi.org/10.1039/C7EE03326E>.
- [130] E.S. Toberer, A. Zevkink, G.J. Snyder, Phonon engineering through crystal chemistry, *J. Mater. Chem.* 21 (2011) 15843. <https://doi.org/10.1039/c1jm11754h>.
- [131] A. El-Khouly, A. Novitskii, I. Serhienko, A. Kalugina, A. Sedegov, D. Karpenkov, A. Voronin, V. Khovaylo, A.M. Adam, Optimizing the thermoelectric performance of FeVSb half-Heusler compound via Hf–Ti double doping, *Journal of Power Sources* 477 (2020) 228768. <https://doi.org/10.1016/j.jpowsour.2020.228768>.
- [132] E. Rausch, B. Balke, T. Deschauer, S. Ouardi, C. Felser, Charge carrier concentration optimization of thermoelectric p-type half-Heusler compounds, *APL Materials* 3 (2015) 041516. <https://doi.org/10.1063/1.4916526>.
- [133] S. Ahmad Khandy, K. Kaur, S. Dhiman, J. Singh, V. Kumar, Exploring thermoelectric properties and stability of half-Heusler PtXSn (X = Zr, Hf) semiconductors: A first principle investigation, *Computational Materials Science* 188 (2021) 110232. <https://doi.org/10.1016/j.commatsci.2020.110232>.
- [134] S.A. Khandy, J.-D. Chai, Strain engineering of electronic structure, phonon, and thermoelectric properties of p-type half-Heusler semiconductor, *Journal of Alloys and Compounds* 850 (2021) 156615. <https://doi.org/10.1016/j.jallcom.2020.156615>.

- [135] J. Shen, L. Fan, C. Hu, T. Zhu, J. Xin, T. Fu, D. Zhao, X. Zhao, Enhanced thermoelectric performance in the n-type NbFeSb half-Heusler compound with heavy element Ir doping, *Materials Today Physics* 8 (2019) 62–70. <https://doi.org/10.1016/j.mtphys.2019.01.004>.
- [136] F. Serrano-Sánchez, T. Luo, J. Yu, W. Xie, C. Le, G. Auffermann, A. Weidenkaff, T. Zhu, X. Zhao, J.A. Alonso, B. Gault, C. Felser, C. Fu, Thermoelectric properties of n-type half-Heusler NbCoSn with heavy-element Pt substitution, *J. Mater. Chem. A* 8 (2020) 14822–14828. <https://doi.org/10.1039/D0TA04644B>.
- [137] S.H. Shah, S.H. Khan, A. Laref, G. Murtaza, Optoelectronic and transport properties of LiBZ (B = Al, In, Ga and Z = Si, Ge, Sn) semiconductors, *Journal of Solid State Chemistry* 258 (2018) 800–808. <https://doi.org/10.1016/j.jssc.2017.12.014>.
- [138] J. Barth, G.H. Fecher, M. Schwind, A. Beleanu, C. Felser, A. Shkabko, A. Weidenkaff, J. Hanss, A. Reller, M. Köhne, Investigation of the Thermoelectric Properties of LiAlSi and LiAlGe, *Journal of Elec Materi* 39 (2010) 1856–1860. <https://doi.org/10.1007/s11664-010-1076-9>.
- [139] Y. Dhakshayani, G. Suganya, G. Kalpana, DFT studies on electronic, magnetic and thermoelectric properties of half Heusler alloys XCaB (X = Li, Na, K and Rb), *Journal of Crystal Growth* 583 (2022) 126550. <https://doi.org/10.1016/j.jcrysgro.2022.126550>.
- [140] U. Chopra, M. Zeeshan, S. Pandey, R. Dhawan, H.K. Singh, J. Van Den Brink, H.C. Kandpal, First-principles study of thermoelectric properties of Li-based Nowotony–Juza phases, *J. Phys.: Condens. Matter* 31 (2019) 505504. <https://doi.org/10.1088/1361-648X/ab4015>.
- [141] M.K. Yadav, B. Sanyal, First principles study of thermoelectric properties of Li-based half-Heusler alloys, *Journal of Alloys and Compounds* 622 (2015) 388–393. <https://doi.org/10.1016/j.jallcom.2014.10.025>.
- [142] Anuradha, K. Kaur, R. Singh, R. Kumar, Search for thermoelectricity in Li-based half-Heusler alloys: a DFT study, *Mater. Res. Express* 5 (2018) 014009. <https://doi.org/10.1088/2053-1591/aaa507>.
- [143] A. Azouaoui, A. Hourmatallah, N. Benzakour, K. Bouslykhane, First-principles study of optoelectronic and thermoelectric properties of LiCaX (X=N, P and As) half-Heusler semiconductors, *Journal of Solid State Chemistry* 310 (2022) 123020. <https://doi.org/10.1016/j.jssc.2022.123020>.
- [144] J.-L. Xiong, F. Yu, J. Liu, X.-C. Liu, Q. Liu, K. Liu, S.-Q. Xia, LiAlTt (Tt = Si, Ge): Experimental and Theoretical Reinvestigation on the Thermoelectric Properties of 8-Valence-Electron Half-Heusler Compounds, *ACS Appl. Energy Mater.* 5 (2022) 3793–3799. <https://doi.org/10.1021/acsaem.2c00279>.
- [145] G. Kresse, J. Furthmüller, Efficiency of ab-initio total energy calculations for metals and semiconductors using a plane-wave basis set, *Computational Materials Science* 6 (1996) 15–50. [https://doi.org/10.1016/0927-0256\(96\)00008-0](https://doi.org/10.1016/0927-0256(96)00008-0).
- [146] D.J. Evans, B.L. Holian, The Nose–Hoover thermostat, *The Journal of Chemical Physics* 83 (1985) 4069–4074. <https://doi.org/10.1063/1.449071>.
- [147] K. Schwarz, P. Blaha, G.K.H. Madsen, Electronic structure calculations of solids using the WIEN2k package for material sciences, *Computer Physics Communications* 147 (2002) 71–76. [https://doi.org/10.1016/S0010-4655\(02\)00206-0](https://doi.org/10.1016/S0010-4655(02)00206-0).
- [148] K. Nakamura, S. Higuchi, T. Ohnuma, Density Functional Perturbation Theory to Predict Piezoelectric Properties, in: İ. Bakırtaş (Ed.), *Perturbation Methods with Applications in Science and Engineering*, InTech, 2018. <https://doi.org/10.5772/intechopen.76827>.
- [149] K. Kuriyama, K. Nagasawa, K. Kushida, Growth and band gap of the filled tetrahedral semiconductor LiMgN, *Journal of Crystal Growth* 237–239 (2002) 2019–2022. [https://doi.org/10.1016/S0022-0248\(01\)02249-7](https://doi.org/10.1016/S0022-0248(01)02249-7).

- [150] T. Gruhn, Comparative *ab initio* study of half-Heusler compounds for optoelectronic applications, Phys. Rev. B 82 (2010) 125210. <https://doi.org/10.1103/PhysRevB.82.125210>.
- [151] F. Birch, Finite Elastic Strain of Cubic Crystals, Phys. Rev. 71 (1947) 809–824. <https://doi.org/10.1103/PhysRev.71.809>.
- [152] H. Mehnane, B. Bekkouché, S. Kacimi, A. Hallouche, M. Djermouni, A. Zaoui, First-principles study of new half Heusler for optoelectronic applications, Superlattices and Microstructures 51 (2012) 772–784. <https://doi.org/10.1016/j.spmi.2012.03.020>.
- [153] H.Y. Wu, Y.H. Chen, C.R. Deng, X.Y. Han, Z.J. Liu, Electronic, elastic and dynamic properties of the filled tetrahedral semiconductor LiMgN under pressures, Journal of Solid State Chemistry 231 (2015) 1–6. <https://doi.org/10.1016/j.jssc.2015.07.047>.
- [154] X. Ye, Z. Feng, Y. Zhang, G. Zhao, D.J. Singh, Low thermal conductivity and high thermoelectric performance via Cd underbonding in half-Heusler PCdNa, Phys. Rev. B 105 (2022) 104309. <https://doi.org/10.1103/PhysRevB.105.104309>.
- [155] S.N.H. Eliassen, A. Katre, G.K.H. Madsen, C. Persson, O.M. Løvvik, K. Berland, Lattice thermal conductivity of  $\text{Ti}_x\text{Zr}_y\text{Hf}_{1-x-y}\text{NiSn}$  half-Heusler alloys calculated from first principles: Key role of nature of phonon modes, Phys. Rev. B 95 (2017) 045202. <https://doi.org/10.1103/PhysRevB.95.045202>.
- [156] H. Zhu, J. Mao, Y. Li, J. Sun, Y. Wang, Q. Zhu, G. Li, Q. Song, J. Zhou, Y. Fu, R. He, T. Tong, Z. Liu, W. Ren, L. You, Z. Wang, J. Luo, A. Sotnikov, J. Bao, K. Nielsch, G. Chen, D.J. Singh, Z. Ren, Discovery of TaFeSb-based half-Heuslers with high thermoelectric performance, Nat Commun 10 (2019) 270. <https://doi.org/10.1038/s41467-018-08223-5>.
- [157] S. Ju, T. Shiga, L. Feng, J. Shiomi, Revisiting PbTe to identify how thermal conductivity is really limited, Phys. Rev. B 97 (2018) 184305. <https://doi.org/10.1103/PhysRevB.97.184305>.
- [158] M.-K. Han, Y. Jin, D.-H. Lee, S.-J. Kim, Thermoelectric Properties of Bi<sub>2</sub>Te<sub>3</sub>: CuI and the Effect of Its Doping with Pb Atoms, Materials 10 (2017) 1235. <https://doi.org/10.3390/ma1011235>.
- [159] A. Yadav, S. Kumar, M. Muruganathan, R. Kumar, Thermoelectric properties of half Heusler topological semi-metal LiAuTe, EPL 132 (2020) 67003. <https://doi.org/10.1209/0295-5075/132/67003>.
- [160] Sangeeta, M. Singh, Augmented thermoelectric performance of LiCaX (X = As, Sb) Half Heusler compounds via carrier concentration optimization, Journal of Physics and Chemistry of Solids 174 (2023) 111182. <https://doi.org/10.1016/j.jpcs.2022.111182>.
- [161] T. Hadji, H. Khalfoun, H. Rached, A. Azzouz-Rached, Spin gapless semiconductor and nearly spin semimetal antiferromagnets: The case of the inverse Heusler compounds Mn<sub>2</sub>LiZ (Z = Al and Ga), Materials Research Bulletin 143 (2021) 111461. <https://doi.org/10.1016/j.materresbull.2021.111461>.
- [162] S.M. Kauzlarich, S.R. Brown, G. Jeffrey Snyder, Zintl phases for thermoelectric devices, Dalton Trans. (2007) 2099. <https://doi.org/10.1039/b702266b>.
- [163] Sangeeta, R. Kumar, M. Singh, Realizing high thermoelectric performance in p-type RbZn<sub>4</sub>P<sub>3</sub> Zintl compound: a first-principles investigation, J Mater Sci 57 (2022) 10691–10701. <https://doi.org/10.1007/s10853-022-06953-y>.
- [164] X. Li, B. Yang, H. Xie, H. Zhong, S. Feng, Y. Zhang, Y. Ma, J. Zhang, H. Su, Synergistic effects of Mg vacancy and Ag doping on thermoelectric transport properties of p-type Mg<sub>3</sub>Sb<sub>2</sub>, Materials Research Bulletin 159 (2023) 112106. <https://doi.org/10.1016/j.materresbull.2022.112106>.
- [165] E. Suprayoga, W.B.K. Putri, K. Singsoog, S. Paengson, M.Y. Hanna, A.R.T. Nugraha, D.R. Munazat, B. Kurniawan, M. Nurhuda, T. Seetawan, E.H. Hasdeo, Investigation of

- electron and phonon transport in Bi-doped CaMnO<sub>3</sub> for thermoelectric applications, *Materials Research Bulletin* 141 (2021) 111359. <https://doi.org/10.1016/j.materresbull.2021.111359>.
- [166] R. Kumar, R. Kumar, M. Singh, D. Meena, A. Vij, Carrier concentration mediated enhancement in thermoelectric performance of various polymorphs of hafnium oxide: a plausible material for high temperature thermoelectric energy harvesting application, *J. Phys. D: Appl. Phys.* 55 (2022) 495302. <https://doi.org/10.1088/1361-6463/ac9986>.
- [167] Md.T. Rahman, E. Haque, M.A. Hossain, Elastic, electronic and thermoelectric properties of Sr<sub>3</sub>MN (M = Sb, Bi) under pressure, *Journal of Alloys and Compounds* 783 (2019) 593–600. <https://doi.org/10.1016/j.jallcom.2018.12.339>.
- [168] R. Deng, B.D. Ozsdolay, P.Y. Zheng, S.V. Khare, D. Gall, Optical and transport measurement and first-principles determination of the ScN band gap, *Phys. Rev. B* 91 (2015) 045104. <https://doi.org/10.1103/PhysRevB.91.045104>.
- [169] M.E. McGahay, B. Wang, J. Shi, D. Gall, Band gap and electron transport in epitaxial cubic Cr<sub>1-x</sub>Al<sub>x</sub>N (001), *Phys. Rev. B* 101 (2020) 205206. <https://doi.org/10.1103/PhysRevB.101.205206>.
- [170] S. Kerdsonpanya, N. Van Nong, N. Pryds, A. Žukauskaitė, J. Jensen, J. Birch, J. Lu, L. Hultman, G. Wingqvist, P. Eklund, Anomalous high thermoelectric power factor in epitaxial ScN thin films, *Applied Physics Letters* 99 (2011) 232113. <https://doi.org/10.1063/1.3665945>.
- [171] P.V. Burmistrova, J. Maassen, T. Favaloro, B. Saha, S. Salamat, Y. Rui Koh, M.S. Lundstrom, A. Shakouri, T.D. Sands, Thermoelectric properties of epitaxial ScN films deposited by reactive magnetron sputtering onto MgO(001) substrates, *Journal of Applied Physics* 113 (2013) 153704. <https://doi.org/10.1063/1.4801886>.
- [172] B. Saha, J.A. Perez-Taborda, J.-H. Bahk, Y.R. Koh, A. Shakouri, M. Martin-Gonzalez, T.D. Sands, Temperature-dependent thermal and thermoelectric properties of n -type and p -type Sc<sub>1-x</sub>Mg<sub>x</sub>N, *Phys. Rev. B* 97 (2018) 085301. <https://doi.org/10.1103/PhysRevB.97.085301>.
- [173] M. Zebarjadi, Z. Bian, R. Singh, A. Shakouri, R. Wortman, V. Rawat, T. Sands, Thermoelectric Transport in a ZrN/ScN Superlattice, *Journal of Elec Materi* 38 (2009) 960–963. <https://doi.org/10.1007/s11664-008-0639-5>.
- [174] I. Ohkubo, T. Mori, Anisotropic Anomalies of Thermoelectric Transport Properties and Electronic Structures in Layered Complex Nitrides AMN<sub>2</sub> (A = Na, Cu; M = Ta, Nb), *Chem. Mater.* 27 (2015) 7265–7275. <https://doi.org/10.1021/acs.chemmater.5b02015>.
- [175] P.-F. Liu, T. Bo, J. Xu, W. Yin, J. Zhang, F. Wang, O. Eriksson, B.-T. Wang, First-principles calculations of the ultralow thermal conductivity in two-dimensional group-IV selenides, *Phys. Rev. B* 98 (2018) 235426. <https://doi.org/10.1103/PhysRevB.98.235426>.
- [176] S.K. Saha, Exploring the origin of ultralow thermal conductivity in layered BiOCuSe, *Phys. Rev. B* 92 (2015) 041202. <https://doi.org/10.1103/PhysRevB.92.041202>.
- [177] M.U. Farooq, S. Butt, K. Gao, X.L. Pang, X. Sun, Asfandiyar, F. Mohamed, A. Ahmad, A. Mahmood, N. Mahmood, Improved thermoelectric performance of BiCuSeO by Ag substitution at Cu site, *Journal of Alloys and Compounds* 691 (2017) 572–577. <https://doi.org/10.1016/j.jallcom.2016.08.236>.
- [178] J. Shen, X. Zhang, Z. Chen, S. Lin, J. Li, W. Li, S. Li, Y. Chen, Y. Pei, Substitutional defects enhancing thermoelectric CuGaTe<sub>2</sub>, *J. Mater. Chem. A* 5 (2017) 5314–5320. <https://doi.org/10.1039/C6TA10770B>.
- [179] A. Togo, First-principles Phonon Calculations with Phonopy and Phono3py, *J. Phys. Soc. Jpn.* 92 (2023) 012001. <https://doi.org/10.7566/JPSJ.92.012001>.
- [180] R. Niewa, H. Jacobs, H.M. Mayer, eds., Re-evaluation of the crystal structure of lithium zirconium nitride, Li<sub>2</sub>ZrN<sub>2</sub>, by neutron powder diffraction, *Zeitschrift Für*



- Kristallographie - Crystalline Materials 210 (1995) 513–515.  
<https://doi.org/10.1524/zkri.1995.210.7.513>.
- [181] N. Tapia-Ruiz, M. Segalés, D.H. Gregory, The chemistry of ternary and higher lithium nitrides, *Coordination Chemistry Reviews* 257 (2013) 1978–2014.  
<https://doi.org/10.1016/j.ccr.2012.11.008>.
- [182] R. Kumar, R. Kumar, A. Vij, M. Singh, A first-principle study of electronic, thermoelectric, and optical properties of sulfur doped c-HfO<sub>2</sub>, *Phys. Scr.* 97 (2022) 075813. <https://doi.org/10.1088/1402-4896/ac7678>.
- [183] L. Debache, Y. Medkour, F. Djeghloul, K. Haddadi, S. Berri, M. Kharoubi, N. Bouarissa, N. Guechi, A. Roumili, Elastic, electronic, optical and thermoelectric properties of Ca<sub>5</sub>Si<sub>2</sub>N<sub>6</sub> and Sr<sub>5</sub>Ge<sub>2</sub>N<sub>6</sub> ternary nitrides, *Journal of Physics and Chemistry of Solids* 179 (2023) 111405. <https://doi.org/10.1016/j.jpcs.2023.111405>.
- [184] Insights into structural, Electronic and Thermoelectric properties of ZnTMN<sub>2</sub> (TM= Zr and Hf): A First-Principles study, *IJPAP* (2023).  
<https://doi.org/10.56042/ijpap.v61i11.3151>.
- [185] M. Tachibana, T. Kolodiazhnyi, E. Takayama-Muromachi, Thermal conductivity of perovskite ferroelectrics, *Applied Physics Letters* 93 (2008) 092902.  
<https://doi.org/10.1063/1.2978072>.
- [186] X. Yu, H. Shao, X. Wang, Y. Zhu, D. Fang, J. Hong, Anomalous lattice thermal conductivity in layered MNCl (M = Zr, Hf) materials driven by lanthanide contraction, *J. Mater. Chem. A* 8 (2020) 3128–3134. <https://doi.org/10.1039/C9TA12600G>.
- [187] D. Parker, X. Chen, D.J. Singh, High Three-Dimensional Thermoelectric Performance from Low-Dimensional Bands, *Phys. Rev. Lett.* 110 (2013) 146601.  
<https://doi.org/10.1103/PhysRevLett.110.146601>.
- [188] K.S. Novoselov, A.K. Geim, S.V. Morozov, D. Jiang, Y. Zhang, S.V. Dubonos, I.V. Grigorieva, A.A. Firsov, Electric Field Effect in Atomically Thin Carbon Films, *Science* 306 (2004) 666–669. <https://doi.org/10.1126/science.1102896>.
- [189] B. Luo, Y. Yao, E. Tian, H. Song, X. Wang, G. Li, K. Xi, B. Li, H. Song, L. Li, Graphene-like monolayer monoxides and monochlorides, *Proc. Natl. Acad. Sci. U.S.A.* 116 (2019) 17213–17218. <https://doi.org/10.1073/pnas.1906510116>.
- [190] Q.H. Wang, K. Kalantar-Zadeh, A. Kis, J.N. Coleman, M.S. Strano, Electronics and optoelectronics of two-dimensional transition metal dichalcogenides, *Nature Nanotech* 7 (2012) 699–712. <https://doi.org/10.1038/nnano.2012.193>.
- [191] F. Zhang, B. Zhu, H. Guo, J. Qiu, K. Zheng, X. Chen, J. Yu, Monolayer square-Ag<sub>2</sub>X (X = S, Se): Excellent n-type thermoelectric materials with high power factors, *Applied Surface Science* 550 (2021) 149230. <https://doi.org/10.1016/j.apsusc.2021.149230>.
- [192] Y. Wang, T. Guo, Z. Tian, K. Bibi, Y. Zhang, H.N. Alshareef, MXenes for Energy Harvesting, *Advanced Materials* 34 (2022) 2108560.  
<https://doi.org/10.1002/adma.202108560>.
- [193] K. Zheng, X. Yang, H. Cui, Q. Yang, H. Ye, D. Xiong, S. Ingebrandt, X. Chen, Intriguing electronic insensitivity and high carrier mobility in monolayer hexagonal YN, *J. Mater. Chem. C* 6 (2018) 4943–4951. <https://doi.org/10.1039/C8TC00558C>.
- [194] N. Mehak, B. Rani, A.F. Wani, S.A. Khandy, A.S. Verma, A.M. Ali, M.A. Sayed, S. Dhiman, K. Kaur, First principle examination of two dimensional rare-earth metal germanide halides Y<sub>2</sub>GeX<sub>2</sub> (X = Cl, Br, I) for thermoelectric applications, *Materials Science in Semiconductor Processing* 171 (2024) 107995.  
<https://doi.org/10.1016/j.mssp.2023.107995>.
- [195] D. Vahedi Fakhrabad, M. Yeganeh, Investigation of the effect of lattice thermal conductivity on the thermoelectric performance of ScN monolayer, *Materials Science in*

- Semiconductor Processing 148 (2022) 106770.  
<https://doi.org/10.1016/j.mssp.2022.106770>.
- [196] K. Kaur, D. Murali, B.R.K. Nanda, Stretchable and dynamically stable promising two-dimensional thermoelectric materials: ScP and ScAs, *J. Mater. Chem. A* 7 (2019) 12604–12615. <https://doi.org/10.1039/C9TA01393H>.
- [197] M. Loyal, B. Biswas, P. Das, B. Saha, Coexistence of infrared plasmon and thermoelectricity in rare-earth semiconducting ytterbium nitride, *Applied Physics Letters* 123 (2023) 042101. <https://doi.org/10.1063/5.0160396>.
- [198] D. Liang, T. Jing, M. Deng, S. Cai, Two-dimensional ScN with high carrier mobility and unexpected mechanical properties, *Nanotechnology* 32 (2021) 155201. <https://doi.org/10.1088/1361-6528/abd8af>.
- [199] J. Liu, X.-B. Li, H. Zhang, W.-J. Yin, H.-B. Zhang, P. Peng, L.-M. Liu, Electronic structures and optical properties of two-dimensional ScN and YN nanosheets, *Journal of Applied Physics* 115 (2014) 093504. <https://doi.org/10.1063/1.4867515>.
- [200] S. Kerdsonpanya, O. Hellman, B. Sun, Y.K. Koh, J. Lu, N. Van Nong, S.I. Simak, B. Alling, P. Eklund, Phonon thermal conductivity of scandium nitride for thermoelectrics from first-principles calculations and thin-film growth, *Phys. Rev. B* 96 (2017) 195417. <https://doi.org/10.1103/PhysRevB.96.195417>.
- [201] B. Xu, H. Xiang, J. Yin, Y. Xia, Z. Liu, A two-dimensional tetragonal yttrium nitride monolayer: a ferroelastic semiconductor with switchable anisotropic properties, *Nanoscale* 10 (2018) 215–221. <https://doi.org/10.1039/C7NR05679F>.
- [202] S. Babaei Touski, M. Hosseini, A. Kokabi, Anti-reflective MX (M = Sc and Y; X = N, P, As, Sb and Bi) monolayers: structural, electronic and optical study, *Semicond. Sci. Technol.* 39 (2024) 015002. <https://doi.org/10.1088/1361-6641/ad0f4d>.
- [203] J.-H. Yuan, G.-Q. Mao, K.-H. Xue, J. Wang, X.-S. Miao, A new family of two-dimensional ferroelastic semiconductors with negative Poisson's ratios, *Nanoscale* 12 (2020) 14150–14159. <https://doi.org/10.1039/C9NR10114D>.
- [204] F. Eriksson, E. Fransson, P. Erhart, The Hiphive Package for the Extraction of High-Order Force Constants by Machine Learning, *Advcd Theory and Sims* 2 (2019) 1800184. <https://doi.org/10.1002/adts.201800184>.
- [205] A. Taheri, S. Pisana, C.V. Singh, Importance of quadratic dispersion in acoustic flexural phonons for thermal transport of two-dimensional materials, *Phys. Rev. B* 103 (2021) 235426. <https://doi.org/10.1103/PhysRevB.103.235426>.
- [206] C. Cui, Y. Zhang, T. Ouyang, C. Tang, C. He, J. Li, M. Chen, J. Zhong, Machine learning interatomic potentials as efficient tools for obtaining reasonable phonon dispersions and accurate thermal conductivity: A case study of typical two-dimensional materials, *Applied Physics Letters* 123 (2023) 152201. <https://doi.org/10.1063/5.0173967>.
- [207] T. Zhang, J.-H. Lin, X.-L. Zhou, X. Jia, Stable two-dimensional pentagonal tellurene: A high ZT thermoelectric material with a negative Poisson's ratio, *Applied Surface Science* 559 (2021) 149851. <https://doi.org/10.1016/j.apsusc.2021.149851>.
- [208] Y. Aierken, D. Çakır, C. Sevik, F.M. Peeters, Thermal properties of black and blue phosphorenes from a first-principles quasiharmonic approach, *Phys. Rev. B* 92 (2015) 081408. <https://doi.org/10.1103/PhysRevB.92.081408>.
- [209] S. Cahangirov, M. Topsakal, E. Aktürk, H. Şahin, S. Ciraci, Two- and One-Dimensional Honeycomb Structures of Silicon and Germanium, *Phys. Rev. Lett.* 102 (2009) 236804. <https://doi.org/10.1103/PhysRevLett.102.236804>.
- [210] X. Qiu, W. Xu, W. Kong, X. Xiao, R. Wang, J. Fan, X. Wu, High hole mobilities in two dimensional monolayer  $\text{MSi}_2\text{Z}_4$  (M = Mo/W; Z = P, As, Sb) for solar cells, *J. Mater. Chem. C* 10 (2022) 15483–15490. <https://doi.org/10.1039/D2TC03403D>.

- [211] N.R. Abdullah, Y.H. Azeez, C.-S. Tang, V. Gudmundsson, High thermal conductivity of orthorhombic BC<sub>2</sub>N semiconductor: DFT study of electronic, phonon, AIMD, and optical properties, *Diamond and Related Materials* 148 (2024) 111455. <https://doi.org/10.1016/j.diamond.2024.111455>.
- [212] Sangeeta, M. Singh, Computational study of the thermoelectric properties and lattice dynamics of Li<sub>2</sub>MN<sub>2</sub> (M = Zr or Hf), *Materials Research Bulletin* 172 (2024) 112650. <https://doi.org/10.1016/j.materresbull.2023.112650>.
- [213] S. Ramawat, S. Kukreti, A. Dixit,  $\beta$  - SrZrS<sub>3</sub> : A superior intermediate temperature thermoelectric through complex band geometry and ultralow lattice thermal conductivity, *Phys. Rev. Materials* 7 (2023) 085403. <https://doi.org/10.1103/PhysRevMaterials.7.085403>.
- [214] S. Tang, M. Wu, S. Bai, D. Luo, J. Zhang, D. Wan, X. Li, SnSe<sub>2</sub> monolayer with square lattice structure: a promising p-type thermoelectric material with an indirect bandgap and low lattice thermal conductivity, *J. Mater. Chem. C* 10 (2022) 16116–16125. <https://doi.org/10.1039/D2TC03587A>.
- [215] Sangeeta, R. Kumar, M. Singh, Realizing high thermoelectric performance in p-type RbZn<sub>4</sub>P<sub>3</sub> Zintl compound: a first-principles investigation, *J Mater Sci* 57 (2022) 10691–10701. <https://doi.org/10.1007/s10853-022-06953-y>.
- [216] Z. Gao, J.-S. Wang, Thermoelectric Penta-Silicene with a High Room-Temperature Figure of Merit, *ACS Appl. Mater. Interfaces* 12 (2020) 14298–14307. <https://doi.org/10.1021/acsami.9b21076>.
- [217] G.K.H. Madsen, Automated Search for New Thermoelectric Materials: The Case of LiZnSb, *J. Am. Chem. Soc.* 128 (2006) 12140–12146. <https://doi.org/10.1021/ja062526a>.
- [218] A. Yadav, S. Kumar, M. Muruganathan, R. Kumar, Topological phase transition associated with structural phase transition in ternary half Heusler compound LiAuBi, *J. Phys.: Condens. Matter* 34 (2022) 145501. <https://doi.org/10.1088/1361-648X/ac49c8>.
- [219] T. Li, P.-H. Du, L. Bai, Q. Sun, P. Jena, Thermoelectric Figure of Merit of a Superatomic Crystal Re<sub>6</sub>Se<sub>8</sub>I<sub>2</sub> Monolayer, *Phys. Rev. Applied* 18 (2022) 064067. <https://doi.org/10.1103/PhysRevApplied.18.064067>.
- [220] Z. Gao, T. Zhu, K. Sun, J.-S. Wang, Highly Anisotropic Thermoelectric Properties of Two-Dimensional As<sub>2</sub>Te<sub>3</sub>, *ACS Appl. Electron. Mater.* 3 (2021) 1610–1620. <https://doi.org/10.1021/acsaelm.0c01100>.
- [221] S. Sharma, S. Kumar, U. Schwingenschlögl, Arsenene and Antimonene: Two-Dimensional Materials with High Thermoelectric Figures of Merit, *Phys. Rev. Applied* 8 (2017) 044013. <https://doi.org/10.1103/PhysRevApplied.8.044013>.
- [222] A. Pandit, B. Hamad, Thermoelectric and lattice dynamics properties of layered MX (M = Sn, Pb; X = S, Te) compounds, *Applied Surface Science* 538 (2021) 147911. <https://doi.org/10.1016/j.apsusc.2020.147911>.

# LIST OF PUBLICATIONS AND THEIR PROOFS

## THESIS WORK

*J Mater Sci* (2022) 57:10691–10701

### Computational Materials Design



## Realizing high thermoelectric performance in p-type $\text{RbZn}_4\text{P}_3$ Zintl compound: a first-principles investigation

Sangeeta<sup>1</sup>, Ramesh Kumar<sup>2</sup>, and Mukhtiyar Singh<sup>1,\*</sup>

<sup>1</sup> Department of Applied Physics, Delhi Technological University, Delhi 110042, India

<sup>2</sup> Department of Physics, Guru Jambheshwar University of Science and Technology, Hisar 124001, India

Received: 30 November 2021

Accepted: 25 January 2022

Published online:

9 February 2022

© The Author(s), under exclusive licence to Springer Science+Business Media, LLC, part of Springer Nature 2022

### ABSTRACT

This work presents structural, elastic, electronic, and thermoelectric properties of a tetragonal Zintl compound  $\text{RbZn}_4\text{P}_3$ , using the Density Functional Theory and Boltzmann transport equation. The computed structural parameters and bond lengths agree well with available experimental data. We use the density functional perturbation theory approach to obtain the Phonon dispersion curve to prove its dynamical stability. The charge density analysis confirms the coexistence of ionic and covalent bonding in the system. The calculated electronic structure shows the semiconducting nature of  $\text{RbZn}_4\text{P}_3$  with a direct bandgap of 1.02 eV using the TB-mBJ approach. We analyze its thermoelectric properties for various hole doping concentrations at different temperatures (300 K–700 K). We obtained a high value of Seebeck coefficient ( $760.00 \mu\text{VK}^{-1}$ ) at 700 K and ( $641.72 \mu\text{VK}^{-1}$ ) at 300 K. The lattice thermal conductivity is estimated using Slack's equation to get the true value of total thermal conductivity. We obtain an ultra-low total thermal conductivity, which in conjunction with high power factor, results in enhanced thermoelectric efficiency or figure of merit (ZT). The maximum ZT value is found to be 0.78 for optimum hole doping concentration of  $2 \times 10^{20} \text{ cm}^{-3}$  at 700 K. This study reveals that  $\text{RbZn}_4\text{P}_3$  possesses excellent potential as thermoelectric energy harvesting material.

### Introduction

A continuously increasing global energy demand resulted in an unprecedented consumption of fossil fuels, leading to harmful effects on the environment.

To avoid the over usage of fossil fuels and safeguard the environment, clean and sustainable energy alternatives become the need of the hour. Various such options have been proposed in the recent past, such as piezoelectric, optoelectronics, thermoelectrics,

Handling Editor: M. Grant Norton.

Address correspondence to E-mail: mukhtiyarsingh@dtu.ac.in; msphysik09@gmail.com

<https://doi.org/10.1007/s10853-022-06953-y>

Springer



# Augmented thermoelectric performance of LiCaX (X = As, Sb) Half Heusler compounds via carrier concentration optimization

Sangeeta, Mukhtiyar Singh\*

Department of Applied Physics, Delhi Technological University, Delhi, 110042, India

## ARTICLE INFO

**Keywords:**  
Half Heusler compounds  
DFT  
Thermoelectrics  
AIMD  
Lattice thermal conductivity

## ABSTRACT

The present study is focussed on the detailed physical insight into the structural, thermal, and dynamical properties of 8-valence electron Half Heusler (HH) compounds LiCaX (X = As, Sb) using Density functional theory. The thermal and dynamic stabilities of the compounds are assessed via *ab-initio* molecular dynamic simulations and phonon dispersion calculations, respectively. The Tran-Blaha modified Becke Johnson potential is used to accurately predict the band gap of investigated compounds. It is found that they are indirect band gap semiconductors with band gaps of 2.52 eV (LiCaAs) and 2.09 eV (LiCaSb). The transport parameters are obtained for *p*-type and *n*-type doping at temperatures ranging from 300 K to 800 K by solving the Boltzmann Transport equation. The deformation potential theory is employed to calculate the temperature dependent relaxation time for both compounds. The results of the various thermoelectric parameters obtained using actual values of time-dependent relaxation time are compared with that calculated under constant relaxation time approximation. The maximum power factor is  $10.95 \times 10^{11}$  ( $4.99 \times 10^{11}$ )  $\text{Wm}^{-1}\text{K}^{-2}\text{s}^{-1}$  for *p*-type (*n*-type) LiCaAs and  $12.53 \times 10^{11}$  ( $5.30 \times 10^{11}$ )  $\text{Wm}^{-1}\text{K}^{-2}\text{s}^{-1}$  for *p*-type (*n*-type) LiCaSb at optimized carrier concentration. The obtained low lattice thermal conductivities for LiCaSb ( $0.66 \text{ Wm}^{-1}\text{K}^{-1}$ ) and LiCaAs ( $0.88 \text{ Wm}^{-1}\text{K}^{-1}$ ) are explicated in terms of different phonon modes. The Figure of Merit at 800 K for *p*-type (*n*-type) LiCaAs is as high as 0.90 (0.73) and 0.93 (0.84) for LiCaSb at optimum carrier concentration  $\sim 10^{20} \text{ cm}^{-3}$  ( $\sim 10^{19} \text{ cm}^{-3}$ ), which has been experimentally realized in other 8-valence electron Li-based HH compounds. The good thermoelectric performance of *p*-type LiCaX in comparison to *n*-type suggests that *p*-type LiCaX alloys are viable candidates for high temperature energy harvesting applications.

## 1. Introduction

Thermoelectric (TE) materials based solid-state electronic devices convert waste heat into useable electrical energy. These materials have been shown to hold great potential for clean and green energy harvesting [1–3] over other renewable energy resources such as wind, geothermal, and solar which have their own constraints pertaining to location and weather [4]. The efficiency of a TE material is given by a dimensionless quantity known as the Figure of Merit (FOM), which is defined by  $ZT = S^2\sigma T / \kappa_e + \kappa_{\text{lattice}}$ , where  $\sigma$ ,  $S$ ,  $\kappa_{\text{lattice}}$ , and  $\kappa_e$ , respectively, represents the electrical conductivity, Seebeck coefficient, lattice thermal conductivity, and electronic thermal conductivity. An efficient TE material should possess a high ZT value [5,6]. The tuning of  $S$ ,  $\sigma$ , and  $\kappa_e$  to maximize the ZT is a tedious task as these parameters are mutually dependent [7]. It is established that enhancement in ZT can be achieved by tuning these parameters independently in two ways: one is to

increase the power factor (PF i.e.,  $S^2\sigma$ ) through carrier concentration optimization [8], and another is to suppress the  $\kappa_{\text{lattice}}$  by increasing phonon scattering [9].

Most of the traditional TE materials are based upon lead chalcogenides and bismuth tellurides. Although these materials possess high ZT [10] but they are not eco-friendly. The plausible alternatives are Zintl materials [11], skutterudites [12], and Half Heusler (HH) compounds [13–15]. The HH compounds have attracted major scientific attention in recent years owing to their excellent band structure tunability, as well as high mechanical and thermal stability [16–18]. These compounds exist in chemical composition XYZ (or, 1:1:1 ratio), where X and Y are transition metal elements, and Z is a p-block element. Numerous studies are existing in the literature that shows enhancement in TE performance of HH alloys realized through optimization of the carrier concentration via doping [19], heavy element substitution [20,21], and strain [22]. Rausch et al. [20] have synthesized *p*-type HH alloy

\* Corresponding author.

E-mail addresses: [msphysik09@gmail.com](mailto:msphysik09@gmail.com), [mukhtiyarsingh@dtu.ac.in](mailto:mukhtiyarsingh@dtu.ac.in) (M. Singh).

<https://doi.org/10.1016/j.jpcs.2022.111182>

Received 26 September 2022; Received in revised form 17 November 2022; Accepted 10 December 2022

Available online 16 December 2022

0022-3697/© 2022 Elsevier Ltd. All rights reserved.



## Unravelling the Ultralow Thermal Conductivity of Ternary Antimonide Zintl Phase RbGaSb<sub>2</sub>: A First-principles Study

Sangeeta, Rajesh Kumar, Ramesh Kumar, Kulwinder Kumar & Mukhtiyar Singh\*  
Department of Applied Physics, Delhi Technological University, Delhi 110 042, India

Received 28 June 2023; accepted 14 August 2023

The recent discovery of antimonide based Zintl phase compounds has sparked the research in finding high-performance thermoelectric materials. In present study, a ternary antimonide Zintl phase RbGaSb<sub>2</sub> is investigated using First-principles calculations. A good agreement observed between our computed results, such as lattice parameter and thermal conductivity, with the experimental report validating our theoretical framework. A direct band gap of 1.17 eV is obtained using Tran Blaha modified Becke Johnson approach. The negative value of Seebeck coefficient indicates its n-type character. We purpose a strategy for enhancing power factor via carrier concentration optimization. The calculated results reveal the anisotropic transport properties. The intrinsic ultralow lattice thermal conductivity about 0.094 Wm<sup>-1</sup>K<sup>-1</sup> along the x-direction, and 0.019 Wm<sup>-1</sup>K<sup>-1</sup> along z-direction at room temperature is obtained. The ZT value can reach 0.90 (in x-direction) and 0.85 (in z-direction) for n-type doping at 900 K, indicating RbGaSb<sub>2</sub> as promising thermoelectric material.

**Keywords:** RbGaSb<sub>2</sub>; Ternary Antimonide Zintl Phase; Thermal Conductivity; DFT

### 1 Introduction

Thermoelectric (TE) materials incorporate an approach that transform thermal energy into electricity without any moving parts and have been identified as highly promising candidates for energy harvesting<sup>1,2</sup>. The efficiency of these materials relies on the figure of merit, ZT, which is represented as  $S^2 \sigma T / (k_e + k_l)$ . Here,  $S$ ,  $\sigma$ ,  $k_e$ , and  $k_l$  denote the Seebeck coefficient, electrical conductivity, electronic thermal conductivity, and lattice thermal conductivity, respectively. Currently, extensive research has been taking pace on various materials<sup>3-5</sup> to explore their potential application in thermoelectricity. Among these, Zintl compounds possess intriguing properties like mix chemical bonding, narrow band gap, and high density of material. Their complex structure leads to low lattice thermal conductivity due to large phonon scattering. Also, these compounds exhibit Phonon-Glass Electron-Crystal behaviour<sup>6,7</sup>. Motivated by the recent experimental synthesis of ternary antimonide RbGaSb<sub>2</sub><sup>8</sup>, we examine the structural, electronic and transport properties. This work presents an effective n-type Zintl compound with remarkable promise as a future TE material across a large temperature range.

### 2 Computational Methods

The properties of RbGaSb<sub>2</sub>, were analysed using density functional theory based wien2k code<sup>9</sup>. The optimisation of the structure was performed using generalised gradient approximation method proposed by Perdew-Burke-Ernzerhof<sup>10</sup>. An energy convergence of 0.0001 Ry was achieved when the Kohn-Sham equations were solved in a self-consistent manner. For Brillouin zone sampling, a Monkhorst-Pack k-mesh of 17×17×9 was used. The Tran Blaha modified Becke Johnson (TB-mBJ) approach was chosen to perform calculations pertaining to the electronic and transport properties<sup>11</sup>. The transport properties were obtained via solving Boltzmann Transport equation (BTE) as implemented in BoltzTraP code<sup>12</sup>. The phono3py code was used for the computation of anharmonic third-order inter atomic force constants<sup>13</sup>. The lattice thermal conductivity was obtained by solving phonon BTE employing a dense 13 × 13 × 7 q-mesh.

### 3 Results and Discussion

#### 3.1 Structural and electronic properties

RbGaSb<sub>2</sub> ternary antimonide Zintl phase crystallizes in tetragonal structure with space group P4<sub>2</sub>/nmc (space group no. 137). The crystal structure as shown in Fig. 1(a) inset, of the investigated compound comprises of two-dimensional [GaSb<sub>2</sub>]

\*Corresponding authors: (E-mail: msphysik09@gmail.com)



## Research Papers

Computational study of the thermoelectric properties and lattice dynamics of  $\text{Li}_2\text{MN}_2$  ( $\text{M} = \text{Zr}$  or  $\text{Hf}$ )

Sangeeta, Mukhtiyar Singh\*

Department of Applied Physics, Delhi Technological University, Delhi 110042, India

## ARTICLE INFO

## Keywords:

Nitrides  
Layered compounds  
Lattice dynamics  
Thermoelectrics  
Thermal conductivity

## ABSTRACT

This study systematically examines the lattice dynamics of  $\text{Li}_2\text{MN}_2$  ( $\text{M} = \text{Zr}$  or  $\text{Hf}$ ), with the aim of unraveling the factors contributing to its unique thermal transport properties using first-principles calculations. Both compounds are found to be energetically and dynamically stable, and our results for their lattice parameters and bond lengths are in good agreement with the available experimental data. The transport properties exhibit strong anisotropic behavior due to the layered structure.  $\text{Li}_2\text{ZrN}_2$  possesses a low lattice thermal conductivity ( $1.52 \text{ W m}^{-1} \text{ K}^{-1}$ ) along the  $a$ -axis at 1000 K, owing to the significant reduction in phonon lifetime caused by the rattling behavior of Zr. The present study may provide valuable insights when exploring the role of lattice dynamics in minimizing the lattice thermal conductivity of transition metal nitrides and their prospective energy harvesting applications.

## 1. Introduction

Thermoelectric (TE) materials have gained significant attention worldwide in recent years due to the potential for application of these materials in green and sustainable energy technology that relies on recovering useful power from waste heat [1–4]. These materials produce an electric current upon the application of a thermal gradient, without the need for any external inputs or moveable mechanical components. The efficiency of any TE material can be gauged by a dimensionless quantity called the figure of merit, denoted as  $ZT$ , which is equal to  $S^2 \sigma T / (\kappa_e + \kappa_l)$ , where  $S$ ,  $\sigma$ ,  $T$ ,  $\kappa_e$ , and  $\kappa_l$  are the Seebeck coefficient, electrical conductivity, absolute temperature, and electronic and thermal contributions to the thermal conductivity, respectively. An enhancement in  $ZT$  can be achieved through two methods: by increasing the power factor ( $PF = S^2 \sigma$ ), or by decreasing the total thermal conductivity,  $\kappa_l$  [5,6]. However, it is difficult to manipulate these two parameters simultaneously, due to their interdependence, and researchers are therefore constantly looking for new materials with high  $ZT$  and/or effective strategies that can enhance the TE performance of existing materials [7]. Intense research is ongoing into Heusler alloys [8–10], Zintl compounds [11–13], oxides and nitrides [14–17] in terms of their TE properties. Of these, nitride semiconductors are particularly attractive owing to their potential for environmental sustainability, the ready availability of these elements, and their desirable electronic properties

[18]. Extensive research has been conducted to explore the early transition metal nitrides, such as  $\text{ScN}$  and  $\text{CrN}$ , and various methods have been implemented to enhance their performance for potential use in TE applications [19–21]. Investigations have been carried out into the TE properties of epitaxial  $\text{ScN}$  films deposited by magnetron sputtering onto  $\text{MgO}$  (001) substrates [22]. Enhanced transport properties have been achieved for  $\text{ScN}$  through electronic structure engineering via stoichiometry tuning and doping. Saha et al. examined the temperature-dependent thermal and TE properties of  $n$ - and  $p$ -type  $\text{Sc}_{1-x}\text{Mg}_x\text{N}$  thin film alloys up to 850 K [23]. A high  $ZT$  value of 1.5 has also been attained for a  $\text{ZrN/ScN}$  superlattice [24]. These studies shed light on the crucial role of nitride semiconductors in TE applications, and offer potential improvements in energy conversion efficiency and sustainability. Layered nitrides are of great interest for TE energy conversion, as they have anisotropic properties that ultimately enable the tuning of transport properties [25,26]. In one study, Ohkubo et al. found that the transport properties of  $\text{NaTaN}_2$ , which exhibits an anisotropic character, were potentially superior to those of isotropic  $\text{KTaO}_3$  [27].

The present study aims to investigate the TE properties of  $\text{Zr}$ - and  $\text{Hf}$ -based nitrides (i.e.,  $\text{Li}_2\text{MN}_2$ ) in order to analyze their structural properties, electronic structures, transport properties, and potential for utilization in TE applications. We also explore the effect of using  $\text{Hf}$  to replace the transition metal ( $\text{M}$ )  $\text{Zr}$ . In general, heavy elements result in a reduced frequency of acoustic phonons [28,29], decreased group

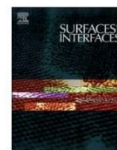
\* Corresponding author.

E-mail address: [mukhtiyarsingh@dtu.ac.in](mailto:mukhtiyarsingh@dtu.ac.in) (M. Singh).<https://doi.org/10.1016/j.materresbull.2023.112650>

Received 12 July 2023; Received in revised form 26 November 2023; Accepted 12 December 2023

Available online 13 December 2023

0025-5408/© 2023 Elsevier Ltd. All rights reserved.



# *In-silico* realization of YX (X = N, P, As) pnictide monolayers as highly efficient thermoelectric materials

Sangeeta, Rajesh Kumar, Mukhtiyar Singh\*

Computational Quantum Materials Design (CQMD) Laboratory, Department of Applied Physics, Delhi Technological University, Delhi, 110042, India

## ARTICLE INFO

### Keywords:

First-principles calculation  
Thermoelectric  
Monolayers  
Rare earth pnictides  
Figure of merit  
Lattice thermal conductivity

## ABSTRACT

Exploiting the changes in the electronic and vibrational properties accompanying the reduction of dimensionality from 3D to 2D has now become a widely established strategy for developing materials breaking the figure of merit ( $ZT$ )  $\sim 1$  barrier that was experienced in much of the last century. Several studies have suggested the possibility of developing rare earth pnictides into a new family of prospective thermoelectric (TE) materials owing to the strong p-d hybridization in these materials, leading to dispersive band edges and, consequently, high carrier mobilities in these semiconductors. Motivated by the above developments, we explored the electronic and transport properties of three yttrium pnictide monolayers. We present a detailed investigation highlighting the merit of YX (X = N, P, As) monolayer-based materials for TE applications. We found a high power factor for p-type (n-type) YX monolayers in the y-direction (x-direction). This, in conjunction with low to moderate lattice thermal conductivities 3.335, 1.779, and 1.648  $\text{Wm}^{-1}\text{K}^{-1}$  of the YN, YP, and YAs monolayers, respectively, at 500 K, leads to high  $ZT$ s in optimally doped YN, YAs and YP of 2.02, 1.39, and 1.18. The finding of high TE performance adds further evidence in support of the conjecture that dimensionality reduction in semiconducting materials with strong p-d hybridization can lead to particularly high electrical conductivities (reaches up to  $217.84 \times 10^6 \Omega^{-1}\text{m}^{-1}$  for YN), thereby resulting in excellent  $ZT$ . The high TE performance of these materials at 500 K suggests the prospect of developing rare-earth-based materials for energy applications.

## 1. Introduction

Thermoelectric (TE) materials are functional and green materials that can be used to convert waste heat directly into useful electrical energy using the Seebeck effect. These materials have a great potential to provide sustainable solutions to the increasing energy crisis by reducing our dependence on fossil fuels and the devastating problem of global warming. The TE generators possess unprecedented advantages, including eco-friendly, long working life, silent, containing no moving parts, easy maintenance, and high reliability [1,2]. The other renewable energy sources, like geothermal, solar, and wind, have their own constraints regarding weather and location [3]. The efficiency of a TE material is characterized by a dimensionless quantity called the figure of merit, denoted as  $ZT$ , which is equal to  $S^2\sigma T / (\kappa_e + \kappa_l)$ , where  $\sigma$ ,  $S$ ,  $T$ ,  $\kappa_e$ , and  $\kappa_l$  are the electrical conductivity, Seebeck coefficient, absolute temperature, and electronic and lattice thermal conductivity, respectively [4]. The high  $ZT$  value is proportional to the high TE conversion ability of a material but the interdependence of transport parameters, making it quite challenging to achieve high  $ZT$  of a material. Reducing

the dimensionality has been considered an important approach for enhancing TE performance, which was proposed first by Hicks and Dresselhaus [5,6]. The low dimensionality improves the density of states (DOS) near the Fermi level, resulting in enhanced  $S$  value. Since the discovery of graphene, two-dimensional (2D) systems have gained extensive attention because of their interesting electronic, mechanical, transport, and optical properties and their promising applications in optoelectronics, energy storage and conversion devices [7–10]. 2D materials can demonstrate lower  $\kappa_l$ , making them highly promising for TE devices. In general, decreasing the dimensionality of materials can significantly reduce the average distance that phonons can travel freely and increase the scattering of phonons at interfaces. This ultimately limits the ability of these materials to transport heat and, consequently, good TE performance.

The 2D systems, such as transition metal chalcogenides, MXenes, and h-BN, rare-earth monolayers with anisotropic properties have gained extensive consideration as efficient TE materials [10–17]. Beginning from the later part of the last decade, several computational studies have suggested the potential for developing d<sup>1</sup> transition metal pnictides into

\* Corresponding author.

E-mail address: [mukhtiyarsingh@dtu.ac.in](mailto:mukhtiyarsingh@dtu.ac.in) (M. Singh).

<https://doi.org/10.1016/j.surfin.2024.105442>

Received 13 July 2024; Received in revised form 25 October 2024; Accepted 12 November 2024

Available online 14 November 2024

2468-0230/© 2024 Elsevier B.V. All rights are reserved, including those for text and data mining, AI training, and similar technologies.



## PUBLICATIONS OTHER THAN THESIS WORK



Indian Journal of Pure & Applied Physics  
Vol. 61, November 2023, pp. 910-914  
DOI: 10.56042/ijpap.v61i11.3151



### Insights into Structural, Electronic and Thermoelectric Properties of $\text{ZnTMN}_2$ (TM= Zr and Hf): A First-Principles Study

Rajesh Kumar, Ramesh Kumar, Sangeeta, Kulwinder Kumar & Mukhtiyar Singh\*

Department of Applied Physics, Delhi Technological University (DTU), Delhi 110 042 India

Received 28 June 2023; accepted 14 August 2023

We employ first-principles calculations combined with semi classical Boltzmann transport theory to investigate the structural, electronic, and thermoelectric properties of  $\text{ZnTMN}_2$  (TM= Zr and Hf). The negative value of formation energy confirms the stability of these compounds. We used Tran Blaha modified Becke Johnson approximation to calculate electronic properties.  $\text{ZnZrN}_2$  and  $\text{ZnHfN}_2$  are having indirect bands of magnitude 2.77 eV and 3.31 eV, respectively. The positive value of the Seebeck Coefficient at all studied temperatures confirms its p-type nature. The thermal conductivity slightly decreases with a rise in temperature in  $\text{ZnHfN}_2$  as compared to  $\text{ZnZrN}_2$ . The observed value of the figure of merit is 0.80 and 0.81 at 500 K and 600 K for  $\text{ZnZrN}_2$  and  $\text{ZnHfN}_2$ , respectively. The high figure of merit of Hf and Zr-based nitrides make them a potential material for thermoelectric energy harvesting applications.

**Keywords:** DFT; Becke johnson approximation; Electronic properties; Seebeck coefficient; Thermoelectric energy harvesting

#### 1 Introduction

The unprecedented demand of energy led to over-consumption of natural resources resulting in devastating natural calamities in recent times. The green energy harvesting techniques are emerging as an alternate to conventional energy resources to safeguard the environment. Thermoelectric (TE) materials have been considered as one of the potential candidates for the green energy harvesting given its peculiar merits over the other conventional energy resources *i.e.*, wind energy and solar energy<sup>1,2</sup>. The efficiency these materials characterized by a dimensionless quantity<sup>1</sup>, figure of merit which is represented as  $ZT = S^2\sigma T / \kappa_e + \kappa_l$ . Here,  $S$ ,  $\sigma$ ,  $\kappa_e$ , and  $\kappa_l$  denote the Seebeck coefficient, electrical conductivity, electronic thermal conductivity, and lattice thermal conductivity, respectively. To find effective TE material the extensive research has been carried out on various materials, including oxide<sup>3</sup>, Zintl<sup>4</sup>, and nitrides<sup>5</sup>. Among the semiconductors, nitrides are considered as the promising candidate owing to their high radiation resistance, high chemical stability and thermal stability which are advantageous for TE applications<sup>6,7</sup>. We examined the structural, electronic and transport properties using first-principles calculation in combination with Boltzmann

transport theory of  $\text{ZnTMN}_2$  (Tm = Zr, Hf) as a potential TE material.

#### 2 Computational Methods

The ab-initio calculations were performed using Density Functional Theory (DFT) based wien2k code<sup>8</sup>. The generalized gradient approximation (GGA) scheme of Perdew-Burke-Ernzerhof (PBE) was used to optimize the lattice parameters of the studied systems<sup>9</sup>. As GGA scheme underestimate the band gap, so for realistic prediction of various properties, we were employed Tran-Blaha modified Becke-Johnson (TB-mBJ) potential<sup>10</sup> which incorporates exchange and correlation energy that uses semi local quantities. The strict energy convergence of 0.0001 Ry was used. A  $\Gamma$ -centred k-mesh of  $15 \times 15 \times 11$  was employed to sample the Brillouin zone. The transport properties were obtained by solving semi classical Boltzmann transport equation under constant relaxation time approximation which are implemented in the BoltzTraP code<sup>11</sup>. A denser k-mesh of  $45 \times 45 \times 33$  was used for transport calculations.

#### 3 Results and Discussion

##### 3.1 Structural and Electronic Properties

The  $\text{ZnTMN}_2$  (Tm = Zr, Hf) exist in hexagonal structure with space group  $P3m1$ <sup>12</sup>. The crystal structure exists in  $\text{TM}^{4+}$ ,  $\text{Zn}^{2+}$ , and  $\text{N}^{3-}$  environment.

\*Corresponding author: (E-mail: msphysik09@gmail.com)

## Pressure Induced Surface States and Wannier Charge Centers in Ytterbium Monoarsenide

Ramesh Kumar, Rajesh Kumar, Sangeeta & Mukhtiyar Singh\*

Department of Applied Physics, Delhi Technological University, New Delhi, Delhi 110 042, India

Received 28 June 2023; accepted 14 August 2023

We demonstrate that the XMR material ytterbium monoarsenide (YbAs) shows transitions from a trivial to a non-trivial topological phase with hydrostatic pressure of 20 GPa and maintains its topological character up to structural phase transition pressure. We observed band inversions close to the Fermi level at the X high symmetry point at 20 GPa and band parities are used to confirm the same with consideration of Spin-orbit coupling (SOC) effect. The evolution of the surface states and the bulk band structure in YbAs are discussed.

**Keywords:** Ytterbium monoarsenide; Topological phase; Fermi level; Spin-orbit coupling

### 1 Introduction

The  $Z_2$  topological semimetals are a subclass of topological materials. These can be distinguished from trivial insulator via  $Z_2$  topological invariant and requires time-reversal symmetry (TRS) to protect their nontrivial topological characteristics. These topological systems do not exhibit a gap in the bulk band structure *e.g.*, rare earth mononpnictide LnPn (Ln = Ce, Pr, Sm, Gd, Yb; Pn = Sb, Bi)<sup>1</sup>. These systems have shown the  $Z_2$  topological character at ambient pressure. However, LaAs<sup>2</sup>, LaSb<sup>3</sup>, TmSb<sup>4</sup>, PbTe, PbS, PbSe, GeTe<sup>5</sup> exhibited inversion when external pressure is applied. Similarly, the rare earth mononpnictide family also includes YbAs, which was experimentally reported to be a topologically trivial semimetal under ambient pressure<sup>6</sup> and theoretically demonstrated to show band inversion under applied pressure of 6 GPa<sup>7</sup>, turning it into a  $Z_2$  topological insulator. In this study, we discussed the effect of pressure on topological phase of YbAs by implementing a more accurate hybrid functional with density functional theory (DFT). The invariants, calculated from the parity table of wave functions on high symmetry points, and Wannier Charge Centres (WCCs) along with existence of odd number of gapless topological surface states confirm the topological phase in YbAs.

### 2 Computational Details

Our calculations were based on the projector augmented wave (PAW) approach<sup>8</sup> as implemented

in the VASP code<sup>10</sup>. The screened hybrid functional of HSE06<sup>11</sup> was used to calculate the exchange-correlation potential. The plane wave basis set had a kinetic energy cutoff of 380 eV and 7x7x7 k-mesh applied to sample the Brillouin zone (BZ). The maximally localised Wannier functions (MLWFs)<sup>12</sup> were used to construct the TB Hamiltonian and surface band structure. The Wannier charge centers (WCCs) were obtained using the Wannier Tools code<sup>13</sup>.

### 3 Result & Discussions

At ambient pressure, the NaCl-type (space group  $Fm\bar{3}m$ ) structure of YbAs have (0, 0, 0) and (1/2, 1/2, 1/2) position coordinates for As and Yb, respectively, as illustrated in Fig. 1(a). The optimized lattice parameter (5.722 Å), structural phase transition (SPT) and dynamical stability of NaCl-type structure of YbAs with applied hydrostatic pressure is discussed in our previous report<sup>7</sup>. The band structure of YbAs at normal pressure is shown in Fig. 1(c). K-path for band structure includes the Time Reversal Invariant Momenta (TRIM) points in the BZ (*i.e.*, X,  $\Gamma$  and L). A small overlap between the valance and conduction bands around the Fermi level (Fig. 1(b)), in the orbital projected density of states (PDOS), demonstrated that YbAs is semimetallic in nature which is fully agree with previous experimental study<sup>6</sup>. The band structure, Fig. 1(c), indicates that YbAs is a topologically trivial and the *p*-orbital of As dominate in valance band and the *d*-orbital of Yb dominate in

\*Corresponding author: (E-mail: mukhtiyarsingh@dtu.ac.in)



## An ab-initio study of induced half metallic ferromagnetism in Hf–Nb alloy oxides

Rajesh Kumar<sup>1</sup>, Sangeeta<sup>1</sup>, Ramesh Kumar<sup>1</sup>, Ramesh K. Bibiyan<sup>2</sup>, Mukhtiyar Singh<sup>1,a</sup> , Ankush Vij<sup>3</sup>

<sup>1</sup> Department of Applied Physics, Delhi Technological University, Delhi 110042, India

<sup>2</sup> Department of Physics, Guru Jambheshwar University of Science and Technology, Hisar 125001, India

<sup>3</sup> Department of Physics and Astrophysics, Central University of Haryana, Mahendergarh, Haryana 123031, India

Received: 28 October 2022 / Accepted: 9 June 2023

© The Author(s), under exclusive licence to Società Italiana di Fisica and Springer-Verlag GmbH Germany, part of Springer Nature 2023

**Abstract** We used ab-initio calculations to examine the structural, mechanical, electronic, and magnetic properties of  $\text{Hf}_{1-x}\text{Nb}_x\text{O}_2$  ( $x = 0, 0.25, 0.50$ , and  $0.75$ ). The thermodynamical and mechanical stability of the Hf–Nb alloy are ascertained through formation energy and elastic properties, respectively. We used the Tran–Blaha modified Becke–Johnson approximation to obtain a band structure that shows no band gap in the spin-up configuration but a significant band gap in the spin-down channel. This establishes the half-metallic ferromagnetic nature of the studied systems. We also calculated their Curie Temperatures within the mean field approximation and the obtained values of  $T_C$  are 520.34 K, 397.91 K, and 346.89 K for  $x = 0.25, 0.50$ , and  $0.75$  doping concentrations. The calculated total magnetic moments are 1.018  $\mu_B$ , 1.975  $\mu_B$ , 2.978  $\mu_B$  per formula unit for  $\text{Hf}_{0.75}\text{Nb}_{0.25}\text{O}_2$ ,  $\text{Hf}_{0.50}\text{Nb}_{0.50}\text{O}_2$ ,  $\text{Hf}_{0.25}\text{Nb}_{0.75}\text{O}_2$ , respectively, which are very close to the integer values. The origin of magnetism in the Hf–Nb alloy oxides is understood with the help of crystal field splitting. Our theoretical calculations may be helpful for the experimentalist to design the new high spin polarized materials at room temperature, and also provide a precise understanding of the origin of magnetism in the Hf–Nb alloy oxides.

### 1 Introduction

Spintronics or spin electronics is referred to the use of charge and spin of electrons to manipulate and store information. The research in this field has evolved at a tremendous rate in recent times due to its peculiar merits over conventional electronics such as low power usage, non-volatility of data, and being smaller in size [1]. Integration of spin-based conduction with semiconductor has shown great utility in the semiconductor industry. Expertise has been grown regarding how to integrate ferromagnetism into semiconductor materials which are capable of generating and manipulating electronic spin at room temperature [2, 3]. Half-metallicity is a novel property, responsible for high spin polarization, associated with any spintronics material [4]. The dilute magnetic semiconductors (DMS) [5], oxide based compounds [6, 7], and Heusler alloy based materials [8–10] are considered as the potential candidates for the spintronics devices as they have shown the signature of half-metallicity with ferromagnetism and are known as half-metallic ferromagnets (HMF).

Generally, DMS have a low Curie temperature ( $T_C$ ) which hinders their applicability in spintronics devices [11]. Transition metal (TM) oxide based DMS, on the other hand, are more suitable for this purpose because of having a high  $T_C$  [12–14]. The experimental and theoretical calculations have predicted half-metallic ferromagnetism in Mn-doped ZnO [12]. Ostanin et al. have predicted that at 500 K, Mn-doping in *c*-ZrO<sub>2</sub> makes it a HMF [13]. The semiconductor oxides based on hosts such as TiO<sub>2</sub> [15], SnO<sub>2</sub> [16], ZrO<sub>2</sub> [17], CeO<sub>2</sub> [18], and HfO<sub>2</sub> [19] have been reported to show room temperature ferromagnetism. Among the above listed semiconductor oxides, HfO<sub>2</sub> has been considered as a promising candidate due to its wide band gap, high dielectric constant and thermal stability [20]. HfO<sub>2</sub> used in industrial applications like laser mirror [21], sensing [22], optical and protective coatings [23]. It acquires a cubic phase at high temperature [24].

HfO<sub>2</sub> exhibits the phase dependent room temperature ferromagnetism which has been ascribed to oxygen vacancies or some structural defects [25]. Seema et al. have investigated the effect of transition metal (V, Cr, Mn) doped *m*-HfO<sub>2</sub> for its electronic and magnetic properties [14]. A similar study has also reported on the emergence of half-metallic ferromagnetism via V and Mn doping in *c*-HfO<sub>2</sub> [26, 27]. Zhang et al. have found that co-doping of C and F can create half-metallic ferromagnetism in *c*-HfO<sub>2</sub> and ZrO<sub>2</sub> [28, 29]. The oxygen vacancies can induce ferromagnetism in Ni doped HfO<sub>2</sub> as shown by Sharma et al. [30]. Han et al. and Singhal et al. have analysed that Co and Fe doping in the thin film of HfO<sub>2</sub> leads to magnetic properties at ambient temperature [31, 32]. The Nb doping has been done in amorphous HfO<sub>2</sub> thin films to enhance the electrical properties of a capacitor [33].

<sup>a</sup> emails: msphysik09@gmail.com; mukhtiyarsingh@dtu.ac.in (corresponding author)





## Optimizing carrier concentration for enhanced thermoelectric performance in AgSbS<sub>2</sub> monolayer

Stephen Shaiju Mathew<sup>1</sup> · Sangeeta<sup>1</sup> · Rajesh Kumar<sup>1</sup> · Mukhtiyar Singh<sup>1</sup> · Manish K. Kashyap<sup>2</sup>

Received: 10 August 2024 / Revised: 9 September 2024 / Accepted: 19 September 2024  
© The Author(s), under exclusive licence to Springer-Verlag GmbH Germany, part of Springer Nature 2024

### Abstract

This work investigates the structural, electronic, elastic, and transport properties of the AgSbS<sub>2</sub> monolayer, using density functional theory in conjunction with semiclassical Boltzmann transport theory. In this study, we proposed a strategy to enhance the figure of merit ( $ZT$ ) by optimizing the carrier concentrations. The monolayer of AgSbS<sub>2</sub> is found to be both mechanically and thermodynamically stable. The phonon bandstructure and *ab-initio* molecular dynamics are also used to verify its excellent dynamical and thermal stability. The calculated electronic bandstructure shows a semiconducting nature of AgSbS<sub>2</sub> with an indirect band gap of 1.31 eV using the Heyd-Scuderia-Ernzerhof (HSE06) exchange–correlation functional. The investigated monolayer is found to be anisotropic, hence we analyzed its thermoelectric properties at various carrier concentrations along  $a$ - and  $b$ -directions at 300 K. It attained a high value of Seebeck coefficient of 360  $\mu\text{VK}^{-1}$  and 370  $\mu\text{VK}^{-1}$  in the  $a$ - and  $b$ - directions at room temperature, respectively. The low thermal conductivity and high power factor result in an appreciable  $ZT$  value. The maximum  $ZT$  of AgSbS<sub>2</sub> monolayer at an optimized carrier concentration of  $2 \times 10^{19} \text{ cm}^{-3}$  is found to be 0.54 in the  $b$ -direction for the n-type monolayer at 300 K. The present work supports the potential use of AgSbS<sub>2</sub> in room-temperature energy harvesting applications.

**Keywords** Thermoelectrics · DFT · Electronic Transport · Thermal Conductivity

### Introduction

In a challenging era of excessive fossil fuels consumption and their consequential environmental impacts, achieving a net zero target requires minimum reliance on conventional energy sources. To achieve this, developing clean and secure energy alternatives is imperative. New technologies can play a pivotal role in energy generation and storage. These encompass diverse areas such as photovoltaics, wind and water turbines, and energy-efficient technologies like low-loss electronics, piezoelectrics, and thermoelectrics (TEs). TE materials, for instance, can efficiently convert waste

heat into usable electrical energy, powering TE generators. TE devices show unique advantages as compared to other energy conversion devices, including stability, long service life, and noiselessness [1–3]. The dimensionless figure of merit ( $ZT$ ) represents the efficiency of a TE material and can be calculated from the formula  $ZT = S^2 \sigma T / \kappa$ , where  $T$  is the absolute temperature,  $S$  denotes the Seebeck coefficient,  $\sigma$  represents electrical conductivity, and  $\kappa$  encompasses the combined effects of electronic ( $\kappa_e$ ) and lattice ( $\kappa_l$ ) contributions to thermal conductivity [4, 5]. Achieving a high  $ZT$  necessitates a significant power factor ( $S^2 \sigma$ ) and reduced  $\kappa$  value. A significant challenge lies in optimizing  $S^2 \sigma$  and  $\kappa_e$ , as they are interdependent through the carrier concentration [6, 7]. Various strategies have been devised to overcome this challenge to decouple these parameters. These include increasing the power factor (PF) via carrier concentration adjustments, tuning bandstructures, and reducing lattice thermal conductivity through dimensional reduction or introducing defects [8–12].

Two-dimensional (2D) semiconductors are highly effective for TE applications and possess exceptional electronic, thermal, and transport properties over bulk materials, along

✉ Mukhtiyar Singh  
mukhtiyarsingh@dtu.ac.in; msphysik09@gmail.com

✉ Manish K. Kashyap  
manishdft@gmail.com; mkkashyap@mail.jnu.ac.in

<sup>1</sup> Computational Quantum Materials Design Laboratory,  
Department of Applied Physics, Delhi Technological  
University, Delhi 110042, India

<sup>2</sup> Renewable Energy Laboratory, School of Physical Sciences,  
Jawaharlal Nehru University, New Delhi 110067, India



# DELHI TECHNOLOGICAL UNIVERSITY

(Formerly Delhi College of Engineering)

Shahbad Daulatpur, Main Bawana Road, Delhi-42

## PLAGIARISM VERIFICATION

Title of the Thesis Computational Investigation of Thermoelectric Properties in Selected Two- and Three-Dimensional Materials.

Total Pages 158 Name of the Scholar Sangeeta.

Supervisor Dr. Mukhtiyar Singh.

Department of Applied Physics.

This is to report that the above thesis was scanned for similarity detection. Process and outcome is given below:

Software used: TURNITIN Similarity Index: 7%,

Total Word Count: 41,800.

Date: 30-04-2025

Candidate's Signature

Signature of Supervisor

## **CURRICULUM VITAE**

### **SANGEETA**

Date of Birth: 1<sup>st</sup> August, 1996

Designation: Research Scholar

Department of Applied Physics

Delhi Technological University (DTU), India

### **CONTACT INFORMATION**

Computational Quantum Materials Design Laboratory

Department of Applied Physics

Delhi Technological University

Delhi – 110 042, India

Email – dhullsangeeta0108@gmail.com, sangeetadhull\_2k20phdap02@dtu.ac.in

Phone - +91 8708578591

### **EDUCATION**

**Ph.D.** (August 2020 to Present)

Thesis Title: Computational Investigation of Thermoelectric Properties in Selected Two- and Three-Dimensional Materials

Department of Applied Physics,

Delhi Technological University, Delhi, India

CGPA: 8.54/10

**M.Sc** in Physics (2017-19) Department of Physics,

Kurukshetra University Kurukshetra, Haryana, India

Percentage: 84.09/100

**B.Sc** with Physics, Chemistry and Mathematics (2014-17)

University College Kurukshetra,

Kurukshetra University Kurukshetra, Haryana

Percentage: 82.06/100

**10<sup>+2</sup>** with Physics, Chemistry, Mathematics, English and Physical Education (2014)

Central Board of Secondary Education, Delhi, India

Percentage: 84.80/100

**10<sup>th</sup>** with Science, Mathematics, Social Sciences, English, and Hindi (2012)

Central Board of Secondary Education, Delhi, India

CGPA: 10/10

### **RESEARCH INTERESTS**

Computational Material Science (First-principles calculations using Density Functional Theory, Ab Initio Molecular Dynamics, Thermoelectric materials: layered materials and two-dimensional materials their electronic and phononic properties, Energy and Quantum Materials, Spintronics, Optoelectronics)

## AWARDS

**GATE AIR-993** (2019)

**GATE AIR-1023** (2020)

**Research Excellence Award** in 2022, 2023 (awarded by DTU)

**Best Poster Award** WIEN2k Hands-On Workshop for New and Existing Users (08 - 19 April 2024) ICTP, Trieste, Italy

## SKILLS

**Operating systems:** Linux, Windows

**Programming skills:** Python, FORTRAN 90, Scripting

**Software Packages:** Vienna ab initio simulation package (VASP), WIEN2k, Quantum espresso, Phonopy, Phono3py, BoltzTraP2, AMSET,

**Experience of working on High-Performance computers (HPC)**

**Graphical software:** Xmgrace, Origin, Vesta, Xcrysden, Gnuplot

## PEER-REVIEWED PUBLICATIONS

1. Sangeeta, Rajesh Kumar, Mukhtiyar Singh, “In-silico realization of YX (X = N, P, As) pnictide monolayers as highly efficient thermoelectric materials”, *Surfaces and Interfaces* 55, 105442 (2024). <https://doi.org/10.1016/j.surfin.2024.105442>.
2. Stephen Shaiju Mathew, Sangeeta, Rajesh Kumar, Mukhtiyar Singh, Manish K. Kashyap, “Optimizing carrier concentration for enhanced thermoelectric performance in AgSbS<sub>2</sub> monolayer. *Ionics* 30, 8647–8657 (2024). <https://doi.org/10.1007/s11581-024-05844->
3. Sangeeta, Mukhtiyar Singh, “Computational study of the thermoelectric properties and lattice dynamics of Li<sub>2</sub>MN<sub>2</sub> (M = Zr or Hf)”, *Material Research Bulletin* 172, 112650 (2024). <https://doi.org/10.1016/j.materresbull.2023.112650>.
4. Sangeeta and Mukhtiyar Singh, “Augmented thermoelectric performance of LiCaX (X = As, Sb) Half Heusler compounds via carrier concentration optimization”, *Journal of Physics and Chemistry Solids* 174, 111182 (2023). <https://doi.org/10.1016/j.jpcs.2022.111182>.
5. Sangeeta, Rajesh Kumar, Ramesh Kumar, Kulwinder Kumar, and Mukhtiyar Singh, “Unravelling the ultralow Thermal Conductivity of Ternary Antimonide Zintl Phase RbGaSb<sub>2</sub>: A First-principles Study”, *Indian Journal of Pure & Applied Physics* 61, 731 (2023). <https://doi.org/10.56042/ijpap.v61i9.3152>.
6. Rajesh Kumar, Sangeeta, Ramesh Kumar, Ramesh K. Bibiyan, Mukhtiyar Singh, and Ankush Vij, “An ab-initio study of induced half metallic ferromagnetism in Hf–Nb alloy oxides”, *European Physical Journal Plus* 138, 561 (2023). <https://doi.org/10.1140/epjp/s13360-023-04179-8>.
7. Rajesh Kumar, Ramesh Kumar, Sangeeta, Kulwinder Kumar, and Mukhtiyar Singh, “Insights into Structural, Electronic and Thermoelectric Properties of ZnTMN<sub>2</sub> (TM= Zr and Hf): A First-Principles Study”, *Indian Journal of Pure & Applied Physics* 61, 910 (2023). <https://doi.org/10.56042/ijpap.v61i11.3151>.
8. Ramesh Kumar, Rajesh Kumar, Sangeeta, and Mukhtiyar Singh, “Pressure Induced Surface States and Wannier Charge Centers in Ytterbium monoarsenide”, *Indian*

Journal of Pure & Applied Physics 61 735, 2023.  
<https://doi.org/10.56042/ijpap.v61i9.3148>.

9. Sangeeta, Ramesh Kumar, and Mukhtiyar Singh, “Realizing high thermoelectric performance in p-type  $\text{RbZn}_4\text{P}_3$  Zintl compound: a first-principles investigation”, *Journal of Materials Science* 57, 10691 (2022). <https://doi.org/10.1007/s10853-022-06953-y>.

## WORK PRESENTED IN CONFERENCES/ WORKSHOPS

1. Participated and presented the paper as a poster titled “Computational Study of Two-Dimensional  $\text{Sc}_2\text{B}_2\text{O}_2$ : Insights into Electronic and Thermoelectric properties” in the International Conference on 60 Years of DFT: Advancements in Theory and Computation held at IIT Mandi, Himachal Pradesh, India from 21–26 July 2024.
2. Participated and presented a poster titled “Thermoelectric Performance of Li-based Half-Heusler Alloys: A First-Principles Investigation” at the WIEN2K Hands-On Workshop for New and Existing Users held at the International Centre for Theoretical Physics (ICTP), Trieste, Italy, from 08–19 April 2024.
3. Attended and presented a poster titled “Exploring the Thermoelectric Potential of  $\text{CsGaSb}_2$  Zintl Phase Compound: A Computational Study” in the International Conference on Materials Genome–III (ICMG–III) held at SRM University AP, Andhra Pradesh, India from 22–24 February 2024.
4. Attended and presented a poster “Effect of lattice dynamics on thermoelectric performance of Li-based transition metal nitrides” at International conference Vienna Ab-Initio Simulation Package (VASP) and Applications virtually organized by The High Performance Computing (HPC) Centre–University of Évora from 14–15 February 2024.
5. Participated and presented a poster titled “Effect of strain on the thermoelectric properties of Zintl compound  $\text{KZn}_4\text{P}_3$ : A first-principles study” at International Conference on Atomic, Molecular, Material, Nano & Optical Physics with Applications (ICAMNOP-2023) held at Delhi Technological University, Delhi, India during 20–22 December 2023.
6. Participated and presented a poster titled “Carrier Concentration Optimisation Enhances Thermoelectric Performance of  $\text{LiCaAs}$  and  $\text{LiCaSb}$  Half Heusler Alloys” in the New Approaches and Machine learning Methods for Ab initio calculations (NAMMA) Psi-k Workshop held at Jawaharlal Nehru Centre for Advanced Scientific Research and Indian Institute of Science, Bengaluru, India from 24–28 July 2023.
7. Participated and presented a paper as poster titled “Unravelling the ultralow thermal conductivity of ternary antimonide Zintl phase  $\text{RbGaSb}_2$ : A first-principles study” in the National Workshop on Materials Design and processing organized by the School of Physical Sciences, Jawaharlal Nehru University (JNU), New Delhi and India Association of Physics Teachers (IAPT) from 08–10 May 2023.
8. Participated and presented a poster titled “First-principles Investigation of the structural, electronic, dynamic and thermoelectric properties of Zintl phase,  $\text{RbZn}_4\text{P}_3$ ” at the 33rd AGM of MRSI and 4th Indian Material Conclave IUMRS-ICA 2022 held at Indian Institute of Technology, Jodhpur, India from 19–23 December 2022.



## **ATTENDED CONFERENCES, WORKSHOPS, SEMINARS, AND FDP**

1. Contributed in Young Scientists Conference as a part of 9th India International Science Festival 2023 organized by Government of India's Ministry of Science and Technology held from 17–20 January 2024.
2. Participated in the Workshop on Materials and Computational Chemistry Applications on HPC platform (MSCC) organized by Centre for Development of Advance Computing (C-DAC), Pune, Maharashtra, India held from 09–11 October 2023.
3. Participated in one week short term training program on Introduction to high performance Computing (HPC) and its applications in Artificial intelligence (AI) organized by Delhi Technological University, Delhi, India held from 07–11 August 2023.
4. Participated in one day national seminar on National Science Day (NSD-2023) organized by Delhi Technological University on 28 February 2023.
5. Attended one day national seminar on Recent advancements in semiconductor devices and materials RASDM-2023 organized by Delhi Technological University, Delhi, India on 30 January, 2023.
6. Participated in two days workshop “Hands-on Training on Latex” organized by Delhi Technological University, Delhi, India held from 26–27 September 2022.
7. Participated in the Pacific Rim International Conference on the Superconducting Materials: Fundamental and Applications- PRISM organized by SRM, Chennai, India held on 22-23 September, 2022.
8. Participated in value added Workshop: Smart Nanotechnology for Societal Applications organized by Amity Institute of Nanotechnology, Amity University Uttar Pradesh, Noida, India held from 27–30 June 2022.
9. Attended the one day online workshop on “Research and Publication Ethics” organized by University of School of Management and Entrepreneurship, Delhi Technological University held on 28 January, 2022
10. Participated in the International Workshop on Energy Technology and Sensor Systems TENSYS-2021 virtually organized by Universiti Malaya from 21–22 December 2021.
11. Participated in two weeks of the International Facility Development Program on “Pursuit of Excellence in Research and Advanced Technology” through virtual mode organized by the Department of Applied Physics, Sathyabama Institute of Science and Technology, Chennai, India held from 20–30 October 2021.
12. Participated in International Symposium on “Emerging Smart Materials for the Advancement of Science and Technology (ESMAST-2021)” organized by Department of Applied Science, Faculty of Science, Invertis University, Bareilly, India held from 11–12 June 2021.
13. Participated in and completed online the “2D materials for Spin-Orbitronics” organised by International Centre for Theoretical Physics (ICTP), Trieste, Italy, from 03–05 May 2021.
14. Attended the online course on “Basics of High-Performance Computing” conducted jointly by JNU and C-DAC under the aegis of National Supercomputing Mission held from 19–30 April 2021.

## TEACHING ASSISTANTSHIP

1. Physics-II Lab (AP102) (B.Tech. 1st year: Jan'2021 - May'2021)
2. Physics-I Lab (AP101) (B.Tech. 1st year: Aug'2021 - Dec'2021)
3. Physics-II Lab (AP102) (B.Tech. 1st year: Jan'2022 - May'2022)
4. Physics-I Lab (AP101) (B.Tech. 1st year: Aug'2022 - Dec'2022)
5. Physics-II Lab (AP102) (B.Tech. 1st year: Jan'2023 - May'2023)
6. Physics Lab (AP101) (B.Tech. 1st year: Aug'2023 - Dec'2023)
7. Computational Methods Tutorial (EP208) (B.Tech. 2nd year: Jan'2024 -May'2024)  
Lectured by Dr. Mukhtiyar Singh, DTU
8. Physics Lab (AP102) (B.Tech. 1st year: Jan'2024 - May'2024)
9. Physics Theory (AP101) Summer Semester (B.Tech. 1st year: June'2024 -July'2024)
10. Physics Lab (AP101) (B.Tech. 1st year: Aug'2024 -Dec'2024)
11. Quantum Mechanics Tutorial (MSPH105) (M.Sc. 1st year: Aug'2024 -Dec'2024)  
Lectured by Dr. Mukhtiyar Singh, DTU
12. Physics Lab (AP102) (B.Tech. 1st year: Jan'2025 – Apr'2025)

## LIST OF REFEREES

### **Dr. Mukhtiyar Singh**

Assistant Professor

Department of Applied Physics

Delhi Technological University, Delhi, India

Email: mukhtiyarsingh@dtu.ac.in

Mobile: +91 8295975147

### **Prof. Manish K Kashyap**

Professor

School of Physical Sciences

Jawaharlal Nehru University, Delhi, India

Email: mkkashyap@jnu.ac.in

Mobile: +91 9467210306